Investigating Cloud-Cloud Collisions and Hub-Filament Systems: Pathways to Massive Star Formation

a thesis submitted

in partial fulfilment of the requirements

for the degree of

Doctor of Philosophy

by

Arup Kumar Maity

(Roll No. 20330004)

under the supervision of

Dr. Lokesh Kumar Dewangan

Associate Professor

Astronomy & Astrophysics Division

Physical Research Laboratory, Ahmedabad, India

Department of Physics

INDIAN INSTITUTE OF TECHNOLOGY GANDHINAGAR

2025

This thesis is dedicated to my beloved grandparents, who raised me as their own child with unconditional love and support.

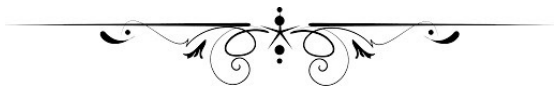

DECLARATION

I, **Arup Kumar Maity (IITGN Roll No. 20330004)**, declare that this thesis titled **"Investigating Cloud-Cloud Collisions and Hub-Filament Systems: Pathways to Massive Star Formation"**, submitted to the Indian Institute of Technology Gandhinagar in partial fulfillment of the requirements for the award of **Doctor of Philosophy** in **Physics**, is my original work. This research was conducted under the supervision of **Dr. Lokesh Kumar Dewangan** at the Physical Research Laboratory, Ahmedabad, India. I have adhered to academic integrity and ethical research practices. Any external information, statements, or results referenced in this thesis have been properly cited with appropriate acknowledgment to the relevant sources.

Date: 13th June, 2025

Arup Kumar Maity

CERTIFICATE

This is to certify that the thesis titled **"Investigating Cloud-Cloud Collisions and Hub-Filament Systems: Pathways to Massive Star Formation"**, submitted by **Arup Kumar Maity (IITGN Roll No. 20330004)** to the Indian Institute of Technology Gandhinagar, has been completed under my supervision. I declare that this thesis has not been submitted for the conferment of any degree or diploma at any other university or institution.

Date: 13th June, 2025

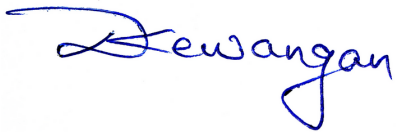

Dr. Lokesh Kumar Dewangan

(Thesis Supervisor)

Associate Professor

Astronomy & Astrophysics Division

Physical research Laboratory

Ahmedabad, India

Contents

ACKNOWLEDGEMENT

I am grateful to my thesis supervisor, Dr. Lokesh Kumar Dewangan, for his exceptional guidance and constant support. His patience, dedication, and commitment to my PhD work have been genuinely inspiring. I sincerely thank the Director, Dean, and Registrar of the Physical Research Laboratory (PRL) for providing the necessary resources for my research work. I also acknowledge the support of Dr. Bhushit Vaishnav, Head of Academic Services, PRL, in all my academic activities.

I extend my gratitude to all the DSC members, Dr. Manash Samal, Dr. Amitava Guharay, and Dr. Rohan Eugene Louis, for their valuable feedback and insightful discussions that enriched my research. I appreciate the Academic Committee members for carefully reviewing my progress, which enhanced the quality of my work. My heartfelt thanks go to all the Astronomy and Astrophysics (A&A) division faculties and coursework instructors for teaching the fundamentals related to my PhD work. I would like to express my gratitude to Dr. Lokesh Kumar Dewangan, Prof. Sachindra Naik, Dr. Aveek Sarkar, and Dr. Kinsuk Acharyya for allowing me to do project work under their supervision. I sincerely thank Prof. Sachindra Naik, Deputy Head (A&A division), and Prof. Abhijit Chakraborty, Chair (A&A division), for their constant support in all the official works. I am grateful for the encouragement and positive feedback from Dr. Aveek Sarkar and Dr. Arvind Singh Rajpurohit during my PhD tenure. I am also indebted to the Computer Center, Library, Dispensary, and all other members of PRL for their assistance and support throughout my PhD journey. I am grateful to the Department of Space (India), the Department of Science and Technology (India), Observatório Nacional (Brazil), and the International Astronomical Union for financially supporting my oral presentations at national and international conferences.

I want to acknowledge the invaluable contributions of all my collaborators: Dr. L. K. Dewangan (thesis supervisor), Prof. Y. Fukui, Prof. T. Inoue, Prof. D. K. Ojha, Prof. Z. Chen, Dr. H. Sano, Dr. K. Tachihara, Dr. Saurabh Sharma, Dr. Ram Kesh Yadav, Dr. N. K. Bhadari, Dr. A. Haj Ismail, Dr. R. Pandey, Mr. O. R. Jadhav, and Mr. R. I. Yamada. Their expertise has significantly contributed to my research work. A special mention goes to Prof. Y. Fukui and Dr. H. Sano for arranging an in-person meeting on very short notice in Nagoya, Japan. I regard my senior, Dr. N. K. Bhadari (Naval da), as an elder brother, and I have received impressive academic and personal support from him. He is still a major source of motivation for me. I am thankful to my junior Mr. O. R. Jadhav (Sr. Omkar) for his invaluable contribution in proof reading of the thesis. I sincerely thank Dr. A. Men'shchikov and Dr. Sabyasachi Pal for all of our scientific discussions.

I acknowledge all my seniors of PRL – Sushant da, Abhijit da, Vipin da, Naval da, Vineet da, Birendra da, Saumya da, Namita di, Aravind da, Akanksha di, Vikas da, Kimi di, Neha di, and energetic juniors – Narendra, Goldy, Arijit, Soumik, Dibyendu, Anupam, Sr. Omkar, Shubhendra, Swagata, Barsha, Kiran, Ashish, Ritik, Priyadarshee, Kushagra, for their significant contributions to office work and hostel life. I am thankful to all my batchmates: Sanjay, Trinesh, Aditya, other Arup, Wafikul, Debashis, Gurucharan, Dharmendra, Kamran, Sandeep, Mansi, Malika, Ananya, Chandrima and Akanksha. I appreciate the patience of Sanjay, Aditya and Trinesh, who are the primary subjects of my funny comments.

As PhD comes at the top of the academic degrees, thus I can not forget the contributions of those who stood with me to build the necessary foundation up to the master degree. I thank all my teachers at JC Primary School, MGS Siksha Niketan, Tamluk Hamilton High School, Tamralipta Mahavidyalaya, and the University of Calcutta. I am thankful to Gautam and Jaydev sir for their support in my school days, which continues to inspire my pursuit of a better education.

I am grateful to have friends like Raju, Pappu, Babai, Santu, Tanmay, Atanu, Debmalya, Subhasis, and Trinesh at different phases of life, from my school days to the Master degree.

Finally, I am forever grateful to my father for his unwavering support, encouragement, and patience. His belief in me has been a constant source of motivation and strength during this journey.

Arup Kumar Maity

ABSTRACT

Although the influence of massive stars ($\gtrsim 8M_{\odot}$) on galactic evolution and interstellar chemistry is well-documented, the fundamental physical processes behind their formation remain unknown. Since massive stars reach the main sequence while accreting material, the radiation pressure becomes significant and can halt further mass accretion. The observational study of massive star-forming regions (MSFRs) is challenging because they are statistically rare and located at large distances ($>$ 1 kpc). Earlier works have well established that massive star formation (MSF) requires high mass accretion rates ($\sim 10^{-3}$ $M_{\odot}\,\mathrm{yr}^{-1}$) to overcome the radiation pressure, thus, massive stars form exclusively in high-density regions, having column density, $N(\mathrm{H_2}) > 10^{22}$ cm^{-2}. Such high column density regions are commonly found at the junction of several filaments or the interface of colliding molecular clouds. The former scenario is based on accretion through filaments to their common junctions (i.e., hubs), and such systems are known as HFSs. Although the potential of HFSs in the context of MSF is well recognized, their origin remains elusive. The latter scenario is based on the collision of molecular clouds, which is known as cloud-cloud collision (CCC). Several simulation-based studies have previously shown that CCC can drive filament formation. However, whether these filaments eventually converge to form an HFS remains unexplored. One of the obstacles in observing CCC is the angle (θ_{col}) between the collision axis and the line of sight. For θ_{col} is 90°, it is impossible to detect CCC with existing methods in the literature, highlighting the need for new signatures for higher viewing angles.

This thesis explores various aspects of MSF through observational investigations and using numerical simulation data. The primary focus is understanding the physical processes involved in MSF, detecting multiple HFSs in the same molecular cloud, and examining their origins and evolutionary stages. Addition-

ally, magnetohydrodynamic (MHD) simulation data obtained from Inoue et al. 2018 are analyzed using supercomputer VIKRAM-100 to explore whether CCC can lead to the formation of HFSs and examine the roles of collision, gravity, turbulence, and magnetic fields. Another key objective of this thesis is to search for new observational CCC signatures applicable at higher viewing angles. For the observational investigations we selected four MSFRs: the W31 complex ($d \sim 3.55$ kpc), AFGL 5180 and AFGL 6366S ($d \sim 1.5$ kpc), G321.93–0.01 ($d \sim 1.98$ kpc) and the infrared dark cloud hosting the N59-North bubble ($d \sim 4.66$ kpc). MSFRs exhibit diverse environments, from cold molecular clumps/cores to extended H II regions. Therefore, we utilized multi-wavelength and multi-scale observational data in this thesis work to understand the ongoing physical processes.

The major outcomes of this thesis include the detection of two HFSs using the tool *getsf* on *Herschel* 250 μm image of W31 complex. The analysis of ^{13}CO(J = 2–1) data favors the applicability of CCC to explain the formation of massive stars and the existence of HFSs. The far-infrared dust continuum emission reveals that AFGL 5180, and AFGL 6366S reside at the opposite edges of an elongated filamentary cloud. We have identified one HFS toward both the sites using *getsf* on the *Herschel* 160 μm image. The analysis of ^{13}CO(J = 1–0) data toward AFGL 5180 and AFGL 6366S suggests a CCC event to explain the observed MSF and HFSs. The ^{13}CO(J = 2–1) data toward the molecular cloud G321.93–0.01 reveal multiple HFSs, namely, HFS-1, HFS-2, and a candidate HFS. HFS-1 and HFS-2 exhibit significant mass accretion rates ($> 10^{-3}$ $M_{\odot}$ yr^{-1}) to their hubs. The detection of compact H II regions in HFS-1 and candidate HFS using MeerKAT radio continuum data indicates that they are in relatively evolved stages of MSF compared to HFS-2, which shows no signs of ionized gas. Additionally, a thorough analysis of ^{13}CO data shows that the collision and merging of filaments led to the formation of HFSs in G321.93–0.01. Based on

the analysis of MHD simulation data, we have found that CCC can lead to the formation of HFSs, which is a combined effect of turbulence, shock compression, magnetic fields, and gravity. After highlighting the major challenges of detecting CCC, this thesis proposes that CCC events at higher viewing angles can be confirmed based on their characteristic position-velocity diagrams, distribution of YSOs, and magnetic field morphology. The existence of the infrared-dark filament (hosting N59-North) observed in *Spitzer* 8 μm image is confirmed using ^{13}CO($J = 1$–0) and ^{13}CO($J = 3$–2) data. The *Spitzer* image reveals an embedded HFS candidate toward the filament's central region at the early stages of MSF. Finally, a comparison of the position-velocity diagram of the filament with the results of our simulation-based work attributes the filament's formation and gas motion to CCC.

Overall, this thesis highlights that mass accretion through filaments in HFSs is an active process of MSF. We have investigated multiple HFSs within a single molecular cloud at various stages of evolution. In our observational investigations, the detection of simultaneous signatures of both CCC and HFSs suggests that CCC may play a role in HFS formation, which is further confirmed using MHD simulation data. In this thesis, we also propose new signatures for identifying CCC at higher viewing angles, which are unique in the existing literature.

List of Publications

Part of this Thesis

1. **A. K. Maity**, L. K. Dewangan, H. Sano, K. Tachihara, Y. Fukui, and N. K. Bhadari, 2022, "Unraveling the observational signatures of cloud-cloud collision and hub-filament systems in W31", *The Astrophysical Journal*, Volume 934, Issue 1, https://doi.org/10.3847/1538-4357/ac7872.

2. **A. K. Maity**, L. K. Dewangan, N. K. Bhadari, D. K. Ojha, Z. Chen, and Rakesh Pandey, 2023, "AFGL 5180 and AFGL 6366S: sites of hub-filament systems at the opposite edges of a filamentary cloud", *Monthly Notices of the Royal Astronomical Society*, Volume 523, Issue 4, pp.5388-5407, https://doi.org/10.1093/mnras/stad1644.

3. **A. K. Maity**, T. Inoue, Y. Fukui, L. K. Dewangan, H. Sano, R. I. Yamada, K. Tachihara, N. K. Bhadari, and O. R. Jadhav, 2024, "Cloud-Cloud Collision: Formation of Hub-Filament Systems and Associated Gas Kinematics. Mass-collecting Cone—A New Signature of Cloud–Cloud Collision", *The Astrophysical Journal*, Volume 974, Issue 2, https://doi.org/10.3847/1538-4357/ad7098.

4. **A. K. Maity**, L. K. Dewangan, N. K. Bhadari, Y. Fukui, A. Haj Ismail, O. R. Jadhav, Saurabh Sharma, and H. Sano, 2024, "G321.93–0.01: A Rare Site of Multiple Hub-Filament Systems with Evidence of Collision and Merging of Filaments", *The Astronomical Journal*, Volume 169, Issue 2, https://doi.org/10.3847/1538-3881/ad98ff.

5. **A. K. Maity**, L. K. Dewangan, O. R. Jadhav, Saurabh Sharma, Ram Kesh Yadav, Y. Fukui, H. Sano, and T. Inoue, "Investigating embedded

structures and gas kinematics in the infrared-dark cloud hosting bubble N59-North", *The Astronomical Journal*, Volume 169, Issue 6, https://doi.org/10.3847/1538-3881/adcedd.

Contributory

6. N. K. Bhadari, L. K. Dewangan, D. K. Ojha, L. E. Pirogov, and **A. K. Maity**, 2022, "Simultaneous evidence of edge collapse and hub-filament configurations: A rare case study of a Giant Molecular Filament G45.3+0.1", *The Astrophysical Journal*, Volume 930, Issue 2, https://doi.org/10.3847/1538-4357/ac65e9.

7. L. K. Dewangan, L. E. Pirogov, N. K. Bhadari, and **A. K. Maity**, 2023, "Ionized filaments and ongoing physical processes in star-forming sites around l = 345.5 degree", *Monthly Notices of the Royal Astronomical Society*, Volume 516, Issue 2, pp.2988-3005, https://doi.org/10.1093/mnras/stac2334.

8. L. K. Dewangan, N. K. Bhadari, A. Men'shchikov, E. J. Chung, R. Devaraj, C. W. Lee, **A. K. Maity**, and T. Baug, 2023, "IC 5146 Dark Streamer: The First Reliable Candidate of Edge Collapse, Hub-filament Systems, and Intertwined Sub-filaments", *The Astrophysical Journal*, Volume 946, Issue 1, https://doi.org/10.3847/1538-4357/acbccc.

9. N. K. Bhadari, L. K. Dewangan, L. E. Pirogov, A. G. Pazukhin, I. I. Zinchenko, **A. K. Maity**, and Saurabh Sharma, 2023, "Fragmentation and dynamics of dense gas structures in the proximity of massive young stellar object W42-MME", *Monthly Notices of the Royal Astronomical Society*,

Volume 526, Issue 3, pp.4402-4417, https://doi.org/10.1093/mnras/stad2981.

10. L. K. Dewangan, N. K. Bhadari, **A. K. Maity**, Rakesh Pandey, Saurabh Sharma, T. Baug, and C. Eswaraiah, 2023, "Star-forming site RAFGL 5085: Is a perfect candidate of hub-filament system?", *Journal of Astrophysics and Astronomy*, Volume 44, Article number 23, https://doi.org/10.1007/s12036-022-09907-7.

11. L. K. Dewangan, **A. K. Maity**, Y. D. Mayya, N. K. Bhadari, Suman Bhattacharyya, Saurabh Sharma, and Gourav Banerjee, 2023, "New Insights in the Bubble Wall of NGC 3324: Intertwined Substructures and a Bipolar Morphology Uncovered by JWST", *The Astrophysical Journal*, Volume 958, Issue 1, https://doi.org/10.3847/1538-4357/ad004b.

12. L. K. Dewangan, N. K. Bhadari, **A. K. Maity**, C. Eswaraiah, Saurabh Sharma, and O. R. Jadhav, 2024, "Galactic 'Snake' IRDC G11.11-0.12: a site of multiple hub-filament systems and colliding filamentary clouds", *Monthly Notices of the Royal Astronomical Society*, Volume 527, Issue 3, pp.5895-5915, https://doi.org/10.1093/mnras/stad3384.

13. L. K. Dewangan, O. R. Jadhav, **A. K. Maity**, N. K. Bhadari, Saurabh Sharma, M. Padovani, T. Baug, Y. D. Mayya, and Rakesh Pandey, 2024, "Deciphering the hidden structures of HH 216 and Pillar IV in M16: results from JWST and HST", *Monthly Notices of the Royal Astronomical Society*, Volume 528, Issue 3, pp.3909-3926, https://doi.org/10.1093/mnras/stae150.

14. L. K. Dewangan, N. K. Bhadari, **A. K. Maity**, O. R. Jadhav, Saurabh Sharma, and A. Haj Ismail, 2025, "Mon R2: A Hub-Filament System with

an Infrared Bubble at the Hub center", *The Astronomical Journal*, Volume 169, Issue 2, https://doi.org/10.3847/1538-3881/ad9b22.

15. O. R. Jadhav, L. K. Dewangan, Aayushi Verma, N. K. Bhadari, **A. K. Maity**, Saurabh Sharma, and A. Haj Ismail, 2025, "Uncovering the hidden physical structures and protostellar activities in the Low-Metallicity S284-RE region: results from ALMA and JWST", *The Astrophysical Journal*, Volume 980, Issue 1, https://doi.org/10.3847/1538-4357/ada388.

16. N. K. Bhadari, L. K. Dewangan, O. R. Jadhav, Ariful Hoque, L. E. Pirogov, Paul F. Goldsmith, **A. K. Maity**, Saurabh Sharma, A. Haj Ismail, and Tapas Baug, 2025, "JWST-ALMA Study of a Hub-Filament System in the Nascent Phase", *Astronomy & Astrophysics Letters*, Volume 694, Article Number L18 https://doi.org/10.1051/0004-6361/202452189.

17. O. R. Jadhav, L. K. Dewangan, A. Haj Ismail, N. K. Bhadari, **A. K. Maity**, Ram Kesh Yadav, Moustafa Salouci, Sanhueza, Patricio, and Saurabh Sharma, "Unveiling Physical Conditions and Star Formation Processes in the G47 Filamentary Cloud", Volume 986, Issue 1, *The Astrophysical Journal*, https://doi.org/10.3847/1538-4357/adcee4

Abbreviations

AFGL	Air Force Geophysical Laboratory
ALMA	Atacama Large Millimeter/submillimeter Array
AU	Astronomical Unit
ATLASGAL	APEX Telescope Large Area Survey of the Galaxy
CCC	Cloud-Cloud Collision
CCD	Color-Color Diagram
CFHT	Canada-France-Hawaii Telescope
CHIMPS	^{13}CO/C^{18}O (J = 3→2) Heterodyne Inner Milky Way Plane Survey
CMD	Color-Magnitude Diagram
DSS	Digitized Sky Survey
EDC	End-Dominated Collapse
FIR	Far-Infrared
FWHM	Full Width at Half Maximum
GPS	Galactic Plane Survey
GMRT	Giant Metrewave Radio Telescope
GHC	Global Hierarchical Collapse

GLIMPSE	*Spitzer* Galactic Legacy Infrared Mid-Plane Survey Extraordinaire
GRS	Galactic Ring Survey
HFS	Hub-Filament System
HMSC	High-Mass Starless Core
Hi-GAL	*Herschel* Infrared Galactic Plane Survey
HC	Hypercompact
IR	Infrared
IRDC	Infrared-Dark Cloud
ISM	Interstellar Medium
IRAS	Infrared Astronomical Satellite
JCMT	James Clerk Maxwell Telescope
JWST	James Webb Space Telescope
LMR	Line-mass ratio
LMC	Large Magellanic Cloud
LSR	Local Standard of Rest
MHD	Magneto-Hydrodynamic
MIR	Mid-Infrared
MME	Methanol Maser Emission
mm	Millimeter
MOST	Molonglo Observatory Synthesis Telescope
MSF	Massive Star Formation
MSFR	Massive Star-Forming Region

MIPSGAL	MIPS Inner Galactic Plane Survey
MWISP	Milky Way Imaging Scroll Painting
NIR	Near-Infrared
NN	Nearest Neighbor
NVAS	NRAO Very Large Array Archive Survey
NVSS	NRAO VLA Sky Survey
PACS	Photoconductor Array Camera and Spectrometer
PAH	Polycyclic Aromatic Hydrocarbon
pc	parsec
PDR	Photo Dissociation Region
PV	Position-Velocity
PPV	Position-Position-Velocity
PP	Position-Position
PPP	Position-Position-Position
PMO	Purple Mountain Observatory
PSF	Point Spread Function
RMS	Root Mean Square
SED	Spectral Energy Distribution
SPICY	*Spitzer*/IRAC Candidate YSO
SPIRE	Spectral and Photometric Imaging Receiver
sub-mm	Sub-Millimeter
SUMSS	Sydney University Molonglo Sky Survey

2MASS	Two Micron All Sky Survey
UC	Ultracompact
uGMRT	Upgraded Giant Metrewave Radio Telescope
UV	Ultraviolet
UKIDSS	UKIRT Infrared Deep Sky Survey
VLT	Very Large Telescope
WFCAM	Wide Field Camera
WIRCam	Wide-field InfraRed Camera
WISE	Wide Field Infrared Survey Explorer
YSO	Young Stellar Object

List of Constants and Units

Constant	Description	In SI Units	In CGS Units
c	Vaccum light speed	$2.998 \times 10^{8}\ \mathrm{m\,s^{-1}}$	$2.998 \times 10^{10}\ \mathrm{cm\,s^{-1}}$
G	Gravitation constant	$6.673 \times 10^{-11}\ \mathrm{m^{3}\,kg^{-1}\,s^{-2}}$	$6.673 \times 10^{-8}\ \mathrm{dyn\,cm^{2}\,g^{-3}}$
h	Planck constant	$6.626 \times 10^{-34}\ \mathrm{J\,s}$	$6.626 \times 10^{-27}\ \mathrm{erg\,s}$
m_{H}	Mass of hydrogen atom	$1.673 \times 10^{-27}\ \mathrm{kg}$	$1.673 \times 10^{-24}\ \mathrm{g}$
k	Boltzmann constant	$1.381 \times 10^{-23}\ \mathrm{J\,K^{-1}}$	$1.381 \times 10^{-23}\ \mathrm{erg\,K^{-1}}$
Units	Description	In SI Units	In CGS Units
AU	Astronomical unit	$1.496 \times 10^{11}\ \mathrm{m}$	$1.496 \times 10^{13}\ \mathrm{cm}$
pc	Parsec	$3.086 \times 10^{16}\ \mathrm{m}$	$3.086 \times 10^{18}\ \mathrm{cm}$
pc	Parsec	$3.086 \times 10^{16}\ \mathrm{m}$	$3.086 \times 10^{18}\ \mathrm{cm}$
$M_{\odot}$	Solar mass	$1.989 \times 10^{30}\ \mathrm{kg}$	$1.989 \times 10^{33}\ \mathrm{g}$
$L_{\odot}$	Solar luminosity	$3.845 \times 10^{26}\ \mathrm{W}$	$3.845 \times 10^{33}\ \mathrm{erg\ s^{-1}}$

List of Figures

List of Tables

Chapter 1

Introduction

Since the dawn of civilization, stars have fascinated human minds through their significant roles in mythology, navigation, and timekeeping. In the last few centuries, we have obtained a basic understanding of their origin, characteristics, and evolution. However, the complete picture of star formation is still illusive and demands further studies. Therefore, this thesis is an addition to our continuous effort to better understand the origin of stars, particularly the massive[1] ones ($\gtrsim 8 M_{\odot}$). Massive stars are rare compared to their low-mass counterparts. The number of stars within the unit mass interval is proportional to $M^{-2.35}$, where M denotes the stellar mass (Salpeter, 1955; Kroupa, 2002) having a wide range value from 0.08 to a few hundred Solar masses (e.g., Zinnecker & Yorke, 2007). This suggests that massive stars make up less than 1% of all-stars. However, despite being rare, they greatly influence the evolution of their host galaxies through immense radiative and mechanical feedback (Motte et al., 2018, and references therein). They are also responsible for the chemical enrichment of the interstellar medium (ISM; Dunne et al., 2003; Du, 2021). Although the impact of massive

[1]They are also called "high-mass stars." However, they are mentioned as "massive stars" throughout this thesis.

stars on galactic evolution and interstellar chemistry is well-documented (Zinnecker & Yorke, 2007; Du, 2021, and references therein), various aspects of their formation mechanisms remain poorly understood. Significant progress has been achieved in the last few decades using advanced telescopes and computing facilities for observational and theoretical/numerical works in this field. However, a complete understanding of the physical processes behind massive star formation (MSF) remain elusive (e.g., Zinnecker & Yorke, 2007; Tan et al., 2014; Krumholz, 2015a; Motte et al., 2018).

The structure of this chapter is as follows: Section 1.1 introduces the ISM and its components. Next, Sections 1.2 and 1.3 discuss the fundamental processes of star formation and how MSF differs from its low-mass counterparts, respectively. The evolutionary stages of both low-mass and massive star formation are outlined in Section 1.4. We then explore the possible physical processes driving MSF in Sections 1.5, 1.6, and 1.7. Section 1.8 presents the motivation and objectives of this thesis, followed by an introduction to the target sites for our observational studies in Section 1.9. Finally, Section 1.10 provides an overview of the subsequent chapters.

1.1 Molecular clouds

Stars form in the ISM, which is composed of hydrogen (∼70%), helium (∼28%), other heavier elements (Draine, 2011; Girichidis et al., 2020). The lighter elements predominantly remain in the gaseous phase. In comparison, a significant amount of the heavier elements are locked in dust grains, comprising about 1% of the total mass of the ISM. The gas in the ISM exists in three phases: ionized (H II), atomic (H I), and molecular (H_2). These phases are classified based on the ionization state and chemical properties of hydrogen, the most abundant element in the

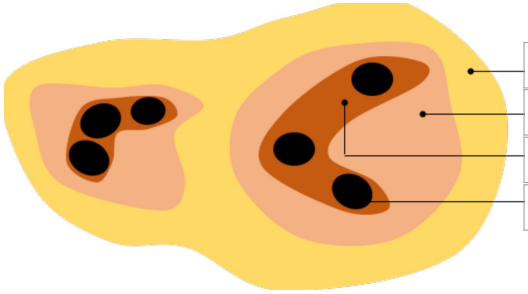

	Size [pc]	Density [cm $^{-3}$]
Cloud	~1 – 10	~10^2–10^3
Clump	~1	~10^3–10^4
Filament	~0.1 (Width)	~10^4–10^5
Core	~0.05 – 0.1	> 10^5

Figure 1.1: A schematic diagram showing the hierarchical structure of molecular clouds, from the cloud to the core scale. The typical sizes and densities of the structures are mentioned on the right side of the image. The image is adopted from Owen et al. (2023).

ISM. The temperature of the inonized gas ranges from 10^4 to 10^6 K, while the density varies from 10^{-1} to 10^{-2} cm^{-3}. Molecular gas has a temperature of about 10–20 K and a density exceeding 10^2 cm^{-3} (see Table 1 in Girichidis et al., 2020). Therefore, molecular gas is the densest and coolest region within the ISM. It occupies only 2–4% of the ISM's volume but contains nearly 48% of its total mass (Smith, 2004). The molecular gas in the ISM exists as clouds, typically tens of parsecs in size and with masses exceeding 10^3 $M_\odot$, known as molecular clouds. Although molecular clouds primarily consist of H_2, they also include a small amount of other molecules such as CO, OH, and H_2O. Due to the presence of cold molecular gas and dust, molecular clouds can block infrared (IR) radiation from the Galactic background. As a result, they may appear as dark features in IR images and are also referred to as IR-dark clouds (IRDC; Draine, 2003).

As shown in Figure 1.1, molecular clouds exhibit a hierarchical density structure consisting of the overall cloud (∼1-10 pc), smaller clumps (∼1 pc), and dense cores (∼0.05-0.1 pc). The elongated structures in molecular clouds with an aspect ratio (i.e., A = length/width) > 3 are known as filaments (Myers, 2009; André et al., 2010). These structures are ubiquitous in the molecular clouds

and have gained significant importance in recent years in star formation studies. More details about the role of filaments in star formation are described in Section 1.5. The cores are the densest ($n > 10^5$ cm^{-3}) regions of the molecular cloud. Their high density makes them conducive to star formation, which is primarily driven by gravity (e.g., Shu, 1977). However, magnetic fields and non-thermal gas motion due to turbulence also play significant roles in the formation of density structures within molecular clouds and, consequently, in star formation (Schulz, 2005; Federrath et al., 2010). Turbulence is a common feature in molecular clouds (Larson, 1981), potentially arising from larger-scale flow collisions, Galactic shear, supernova explosions, expanding H II regions, protostellar outflows, and stellar winds (e.g., Vázquez-Semadeni et al., 2003; Hennebelle & Falgarone, 2012; Padoan et al., 2016; Orkisz et al., 2017). According to Larson's law, the velocity dispersion of molecular clouds of radius R is proportional to $\sqrt{R}$ (Larson, 1981; Ward-Thompson & Whitworth, 2015). Thus, the Full Width at Half Maximum (FWHM) for a molecular cloud with $R = 10$ pc is about a few km s^{-1}, significantly higher than the isothermal sound speed of about 0.2–0.3 km s^{-1}. Therefore, generally, molecular clouds are supersonically turbulent. Several studies, such as Federrath et al. (2010) and Padoan et al. (2020), indicate that supersonic turbulence is responsible for the formation of structures in molecular clouds. The typical magnetic field strength in molecular clouds is about 10 μG for low-density gas ($n_{\rm H} < 300$ cm^{-3}); however, for higher densities, magnetic field strength scales as $n_{\rm H}^{2/3}$ (Crutcher, 2012). Molecular clouds do not interact directly with the magnetic fields as they are mostly neutral. However, there is a small fraction of ions, primarily due to the ionization of the molecular gas by cosmic rays (Krumholz, 2015b). Tielens (2005) has shown that for a density of about $n_{\rm H}$ ($= n({\rm H\,I}) + n({\rm H\,II})$) $\sim 100\,{\rm cm}^{-3}$, the ionization fraction is about 10^{-6}. These ions interact with the magnetic fields and are collisionally coupled with

the neutral components of the molecular cloud. Thus, magnetic fields indirectly influence gas motion and the formation of substructures (i.e., clumps, filaments, and cores) in molecular clouds (e.g., Hennebelle & Inutsuka, 2019). In general, thermal pressure, turbulence, and magnetic fields counteract the gravitational collapse of the substructures in the molecular clouds (e.g., Smith, 2004; Schulz, 2005). However, as soon as gravity overcomes the opposing forces, gas collapses to form stars.

1.2 Gravitational collapse and Jeans mass

In 1902, Sir James Jean formulated the condition for the gravitational collapse of interstellar gas, considering the self-gravity and thermal pressure of the gas. For a spherical cloud of radius R, mass M, and having uniform density (ρ_0), gravitational potential energy is $\mathcal{U} \approx -\frac{3}{5}GM^2/R$, where G is the gravitational constant. Whereas total kinetic energy is $\mathcal{K} = \frac{3}{2}\mathcal{N}kT$ at temperature T, where k is the Boltzmann constant and $\mathcal{N}$ is the number of molecules in the cloud. For a cloud of mass M, $\mathcal{N} = M/\mu m_{\rm H}$, where μ is the mean molecular weight and $m_{\rm H}$ is the mass of hydrogen atom. According to the virial theorem, a molecular cloud of kinetic energy $\mathcal{K}$ and gravitational potential energy $\mathcal{U}$ remains stable and gravitationally bound if:

$$2\,\mathcal{K} + \mathcal{U} = 0. \tag{1.1}$$

Once $2\,\mathcal{K} < |\mathcal{U}|$, the thermal pressure falls short of the gravitational pressure. As a result, the cloud collapses under the influence of gravity. This condition provides a critical mass known as the Jeans mass (M_J), and the cloud will undergo a gravitational collapse only if $M > M_J$. The expression for M_J can be derived from Equation 1.1 as (e.g., Jeans, 1902; Shu et al., 1987),

$$M_J = \left(\frac{5kT}{\mu m_{\rm H} G}\right)^{3/2} \left(\frac{3}{4\pi\rho_0}\right)^{1/2}. \tag{1.2}$$

For instance, a cloud with $T = 20\,\mathrm{K}$ and $n = 10^5\,\mathrm{cm}^{-3}$ has a Jeans mass of $M_J \sim 3\ M_\odot$ (Ward-Thompson & Whitworth, 2015). In contrast, for $T = 50\,\mathrm{K}$ and $n = 10^3\,\mathrm{cm}^{-3}$, M_J is about 120 $M_\odot$. This comparison naturally explains why a cooler and denser environment is favorable for star formation. As a cloud undergoes isothermal gravitational collapse, its density increases, which results in a decrease in M_J according to Equation 1.2. This leads the cloud to fragment into additional condensations (e.g., Girichidis et al., 2020). It is important to note that turbulence, magnetic fields, and rotation are not considered in the formulation of Jeans mass. However, the Jeans condition offers valuable insights into the early stages of gravitational collapse. The low gas density in the early stages of collapse enables efficient cooling, maintaining a constant temperature. As a result, there is no increase in thermal pressure, and the cloud undergoes an essentially free-fall collapse. The free-fall timescale for a spherical cloud of density ρ_0 is given by (e.g., Lequeux, 2005),

$$t_{\rm ff} = \sqrt{\frac{3\pi}{32 G \rho_0}}. \tag{1.3}$$

For $\rho_0 \sim 4 \times 10^{-20}$ g cm^{-3} (i.e., $n \sim 10^4$ cm^{-3}), $t_{\rm ff}$ is about $\sim 3 \times 10^5$ yr.

1.3 Low-mass star formation and the challenges of MSF

This section presents our general understanding of low-mass star formation and why this mechanism is not directly applicable to massive stars. As mentioned in the previous sections, molecular clouds have hierarchical density structures, and

cores are suitable locations for star formation due to their cooler and denser environments. Gravitationally bound cores likely to collapse are known as prestellar cores. The collapse begins when gravity dominates over thermal and non-thermal (i.e., magnetic and turbulent) pressures. Interestingly, $t_{\rm ff}$ (see Equation 1.3) depends solely on the density. Hence, for a core with uniform density, the free-fall collapse will result in an uniform increase in density through out the region. However, isothermal cores are centrally condensed (i.e., $\rho(r) \propto r^{-2}$; Schulz, 2005) and as a result, the central region collapses more rapidly than the outer portion at the onset of gravitational collapse. Over a timescale of about 10^4 yr, the density at the central region increases to 10^{13} g cm^{-3}, making it optically thick and adiabatic. As a result, the internal temperature and pressure increase, and a stable core with a radius of a few AU forms, known as the "first hydrostatic core." The dust grains evaporate at temperatures of about 1000 K, and the hydrogen molecules begin to dissociate at about 2000 K. The dissociation of hydrogen molecules causes a second collapse. With increasing temperature, several such collapse occures due to the ionization of H, He, and heavier elements above 10^4 K, resulting in the formation of a highly dense core ($\rho \sim$0.1 g cm^{-3}). This is know as protostellar core and it accretes materials from the envelope (Smith, 2004). Over time, it will form an accretion disk as a result of the conservation of angular momentum and show outflow activity due to magnetic acceleration from the disk (Zinnecker & Yorke, 2007; McKee & Ostriker, 2007; Cai et al., 2008). According to Shu (1977), the mass accretion rate is constant and can be expressed as,

$$\dot{M} \sim \frac{c_{\rm s}^3}{G} \approx 10^{-6} \left(\frac{T}{10\,{\rm K}}\right)^{3/2} M_\odot\,{\rm yr}^{-1}, \tag{1.4}$$

where $c_{\rm s}$ is the isothermal sound speed of the medium. However, including effects of rotation and magnetic fileds provides higher $\dot{M}$ ($\sim 50\,\frac{c_{\rm s}^3}{G}$) at initial stages which decreases to about $\sim 0.06\,\frac{c_{\rm s}^3}{G}$ at the very later stages of protostellar evolution (e.g., Basu, 1998; Schulz, 2005). The typical value of average $\dot{M}$ for the formation of

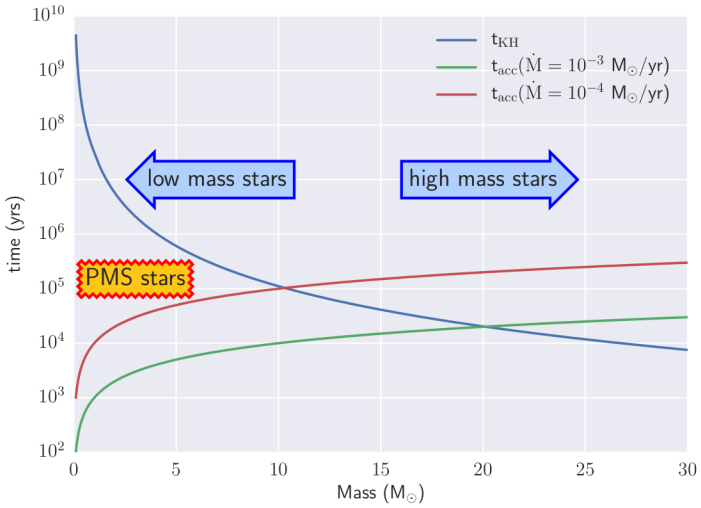

Figure 1.2: The Kelvin-Helmholtz timescale vs. accretion timescale for $\dot{M} = 10^{-4}$ and $10^{-3}\ M_\odot\,\mathrm{yr}^{-1}$ (from Schilke, 2015).

Solar mass stars is about $10^{-5}\,M_\odot\,\mathrm{yr}^{-1}$ (Stahler, 1983; Schulz, 2005; Haemmerlé et al., 2016).

The accretion timescale for a star of mass M is given by $t_{\mathrm{acc}} \sim M/\dot{M}$. Whereas the timescale related to the evolution of protostars to main-sequence stars is known as Kelvin-Helmholtz timescale and expressed as $t_{\mathrm{KH}} = GM^2/RL$, where, M, R, L are mass, radius, and luminosity of the star. For a Sun-like stars, t_{acc} is about 10^5 yr (for $\dot{M} \sim 10^{-5}\,M_\odot\,\mathrm{yr}^{-1}$) and t_{KH} is about 3×10^7 yr (Smith, 2004; Schulz, 2005). Hence, $t_{\mathrm{acc}} \ll t_{\mathrm{KH}}$ and as a result, such stars accumulate their entire mass well before reaching the main sequence and undergo a pre-main sequence phase (Schilke, 2015). As shown in Figure 1.2, t_{KH} decreases with incresing stellar mass. Interstingly, for stellar masses above $8\,M_\odot$, t_{acc} with $\dot{M} \sim 10^{-5}\,M_\odot\,\mathrm{yr}^{-1}$ exceeds t_{KH}. Therefore, such stars begin hydrogen fusion while they are accreting mass and they do not have pre-main sequence phase (Schilke, 2015). As a result, the accreting materials face the radiation pressure of the stars (Wolfire & Cassinelli, 1987). The high luminosity of those stars

(i.e., $> 10^3\ L_\odot$) is sufficient to stop further accretion as the accretion rate in Equation 1.4 is not adequate to overcome the radiation pressure (e.g., Palla & Stahler, 1993; Keto & Wood, 2006). Therefore, the mechanism of low-mass star formation is not directly applicable for the massive stars. Such stars can only form with a high mass accretion rate (Zinnecker & Yorke, 2007). The comparison between $t_{\rm acc}$ and $t_{\rm KH}$ is shown in Figure 1.2 for mass accretion rate of 10^{-4} and $10^{-3}\,M_\odot\,{\rm yr}^{-1}$. The higher mass accretion rate provides two key advantages: first, it allows for the accumulation of more mass before radiation pressure becomes significant. For instance, with $\dot{M} = 10^{-3}\,M_\odot\,{\rm yr}^{-1}$, $t_{\rm acc}$ exceeds $t_{\rm KH}$ for stellar masses above $20\,M_\odot$. Second, the increased mass accretion rate have higher ram pressure, which can effectively overcome the effects of radiation pressure to form massive stars (Zinnecker & Yorke, 2007; Ward-Thompson & Whitworth, 2015). An extensive review of low-mass star formation and MSF can be found in the recent article Beuther et al. (2025).

In addition to the theoretical challenge of radiation pressure and mass accretion rates, there are several observational difficulties associated with the study of MSF. These stars are extremely rare, form over a short timescale of about 10^5 yr, and are often located at distances (d) greater than 1 kpc (Zinnecker & Yorke, 2007, and references therein). Their rarity and rapid formation make it challenging to observe them in the embedded phase. Moreover, their greater distances limit the smallest physical scales that can be observed.

1.4 The evolutionary stages of low-mass and massive star formation

In the case of the formation of Solar mass stars, the protostellar cores to pre-main sequence stars are collectively referred to as young stellar objects (YSOs), which

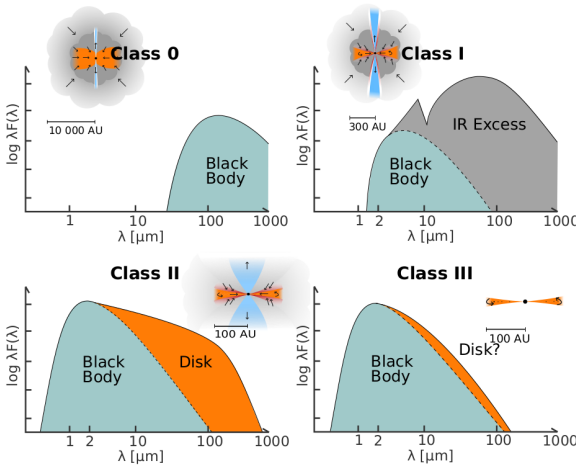

Figure 1.3: A schematic diagram illustrating the structural components and SEDs of different classes of YSOs. Image Credit: M. V. Persson and N. K. Bhadari.

emit in near-infrared (NIR) to sub-millimeter (sub-mm) wavelengths. Based on their evolutionary stages, YSOs are classified into Class 0, I, II, and III, which show distinct spectral energy distributions (SEDs; see Smith, 2004; André, 2015). Figure 1.3 presents the structural components, such as envelope, accretion disk, protostar, and outflows for different classes of YSOs and their SEDs. Class 0 YSOs are protostars surrounded by a dusty infalling envelope, which causes their SEDs to peak in the sub-mm range. The objects are identified as Class I YSOs once half of the envelope's mass has been transferred to the protostar. They show IR excess due to their envelopes and circumstellar disks (Povich et al., 2011). The Class II YSOs, commonly referred to as classical T Tauri stars, do not have an envelope. Instead, the protostar accretes materials solely through an accretion disk. Class 0, I, and II YSOs are associated with outflow activity. In contrast, Class III YSOs – also known as weak-lined T Tauri stars – represent a post-accretion stage and do not exhibit outflow activity.

As mentioned earlier in Section 1.3, massive stars start burning hydrogen while actively accreting material. As a result, they remain deeply embedded

within dense molecular gas even when they reach the main sequence. That is why, observationally, it is challenging to establish an evolutionary sequence for MSF compared to their lower-mass counterparts. However, observational signatures of various objects provide a general idea of the evolutionary sequence of MSF (e.g., Churchwell, 1999; Zinnecker & Yorke, 2007), which is discussed in the following sections.

1.4.1 Early stages of MSF

IRDCs are considered promising sites for MSF due to their high density ($n > 10^5$ cm^{-3}), significant mass reservoirs (10^3–10^5 $M_\odot$), and cooler environments ($T < 20$ K) (Rathborne et al., 2006; Ragan et al., 2009). MSF typically begins when a high-mass starless core (HMSC) undergoes gravitational collapse inside the clumpy molecular clouds. Figure 1.4 shows a schematic diagram of a clumpy molecular cloud and the cold collapsing core. Due to their low-temperature, HMSCs are detectable through the molecular line and dust continuum emissions in the mm/sub-mm domain (e.g., Tan et al., 2013). However, it is difficult to observationally catch them because of their brief lifetime (e.g., Ragan et al., 2012). The gravitational collapse of HMSCs leads to the formation of high-mass protostellar objects (HMPOs). As the core collapses, material accretes onto the protostar, increasing its temperature (T = 20-90 K) and density ($n > 10^6$ cm^{-3}) (Motte et al., 2007, 2018; Molet et al., 2019). HMPOs are also characterized by strong outflow activity.

Next, due to the radiative heating from the central protostar, temperature over an extent of about 2000 AU exceeds 100 K (see Figure 1.4). At such elevated temperatures complex molecules, such as CH_3OH, CH_3OCHO, $HC(O)NH_2$ are released from ice mantles and grain surfaces through thermal desorption (Csengeri et al., 2019, and references therein). This stage is known as hot molecular

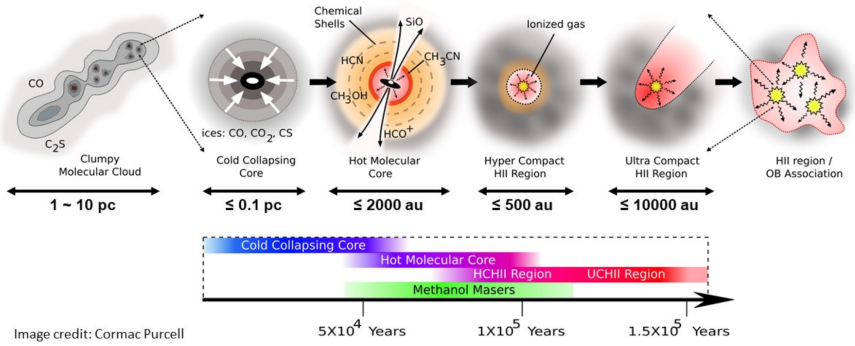

Figure 1.4: A schematic representation of the evolutionary stages of MSF from a clumpy molecular cloud to extended H II region. The time scales related to different stages are indicated at the bottom of the diagram. Image credit: Dr. Cormac Purcell, Macquarie University.

core (HMC) and just preceeds the stars begining to ionize their surrounding gas (Kurtz et al., 2000). HMCs are characterized by their complex molecular line emission and molecular outflow signature (Herbst & van Dishoeck, 2009; Csengeri et al., 2019). They are widely recognized as sources of astronomical masers. The term 'maser' stands for 'Microwave Amplification by Stimulated Emission of Radiation.' Some common examples of astronomical masers are OH, H_2O, SiO, CH_3OH, and NH_3. Numerous observational studies and theoretical models of CH_3OH (methanol) excitation show that Class II 6.7 GHz methanol maser emission (MME) is radiatively pumped and serves as an exclusive tracer of the early stages of MSF (Menten, 1991; Caswell et al., 1995; Sobolev et al., 1997; Walsh et al., 1998; Cragg et al., 2005).

1.4.2 Evolved stages of MSF

As soon as hydrogen burning begins inside the massive stars, they emit copious amounts of ultraviolet (UV) radiation above the Lyman limit (i.e., $>$ 13.6

Table 1.1: The size and electron density for different classes of H II regions (from Kurtz, 2005).

H II region	Size (pc)	Electron density (cm^{-3})
HC	≤ 0.03	$\geq 10^6$
UC	≤ 0.1	$\geq 10^4$
Compact	≤ 0.5	$\geq 5 \times 10^3$
Classical	$\sim$10	$\geq 10^2$

eV). This highly energetic radiation ionizes the surrounding medium to form H II regions (Churchwell, 2002; Hoare et al., 2007). The H II regions traces newly formed massive stars and are observed in radio and IR wavelengths due to free-free emission from the electrons and warm dust emission, respectively. Based on their size and electron density, H II regions are classified into hypercompact (HC), ultracompact (UC), compact and classical H II regions, respectively (Kurtz, 2005). Figure 1.4 shows the HC, UC, and an extended (i.e., compact/classical) H II region. As the H II regions evolve from HC to classical, their size increases and electron density decreases. The typical values of size and electron density for different classes of H II regions are listed in Table 1.1.

Considering the differences in size and electron density, HC H II regions are linked to photoevaporating disks (Kurtz, 2005; Keto, 2007), while in UC H II regions, the gas is likely ionized up to the envelopes (Hoare, 2005). Now, the thermal pressure of the H II regions is greater than that of the molecular gas (Goicoechea et al., 2016). As a result, they expand over time and give rise to compact and subsequently classical H II regions. Therefore, the compactness of the H II regions serves as a proxy to detect young massive stars. It is important to note that no sharp boundary exists between the successive evolutionary stages

of MSF, which is indicated by the overlap of these stages in the time domain in Figure 1.4.

1.5 Possible scenarios of MSF

As discussed in Section 1.3, the core collapse scenario of low-mass star formation cannot account for the formation of massive stars due to insufficient mass accretion rate ($\sim 10^{-5}\,M_\odot\,\mathrm{yr}^{-1}$). To address this limitation, the monolithic collapse scenario of MSF (McKee & Tan, 2002; Hosokawa & Omukai, 2009) extends the core collapse model to accommodate significantly higher mass accretion rates ($\sim 10^{-4}$–$10^{-3}\,M_\odot\,\mathrm{yr}^{-1}$). In this scenario, the formation of massive stars begins with the collapse of an isolated prestellar massive core ($> 30\,M_\odot$), supported by mainly turbulent pressure. For this reason, the model is also referred to as the turbulent core/"core-fed" model (McKee & Tan, 2003; Rosen et al., 2020). Considering the thermal, non-thermal gas motion and effect of the magnetic field, the mass accretion rate can be expressed as $\dot{M} \sim c_{\rm eff}^3/G \approx 2.5\times10^{-4}\left(\frac{c_{\rm eff}}{1\,\mathrm{km\,s^{-1}}}\right)^3 M_\odot\,\mathrm{yr}^{-1}$ (Hosokawa & Omukai, 2009; Fukui et al., 2018a). Here, $c_{\rm eff}$ is the effective sound speed, defined as, $c_{\rm eff} = \sqrt{c_{\rm s}^2 + \sigma_{\rm NT}^2 + c_{\rm A}^2}$, where $\sigma_{\rm NT}$ is the non-thermal velocity dispersion, and $c_{\rm A} = \sqrt{B/4\pi\rho}$ is the Alfvén velocity. Therefore, the supersonic turbulence inside the massive cores increases the effective sound speed and, consequently, the mass accretion rate. In this context, Krumholz et al. (2007a) demonstrated through radiation-hydrodynamical simulations that the mass accretion rate in a turbulent core of $100\,M_\odot$ can exceed $10^{-4}\,M_\odot\,\mathrm{yr}^{-1}$ to form massive stars. Similar to low-mass stars, the infalling gas from the molecular core leads to the formation of an accretion disk around the massive protostar. The disk-mediated accretion will also result in outflow activity (Zinnecker & Yorke, 2007). However, the observational detection of outflow activity and accretion

disk is limited up to the late O-type sources ($< 25\,M_{\odot}$; Cesaroni et al., 1999; Wu et al., 2005; Arce et al., 2007). Another significant limitation of the monolithic collapse scenario is the scarcity of identified massive prestellar core candidates (Morii et al., 2023; Mai et al., 2024, and references therein). Therefore, the absence of evidence of disk-mediated accretion for early O-type sources and the scarcity of massive prestellar cores raise doubts about the applicability of the monolithic collapse model for MSF (Zinnecker & Yorke, 2007).

Bonnell et al. (2001, 2004) proposed an alternative model for MSF based on the concept of competitive accretion. In this model, star formation begins with the creation of a large number of low-mass seeds within a shared gas reservoir. These low-mass seeds compete with each other to accrete gas from the surrounding medium. Thus, it is called a "clump-fed" scenario as the mate-

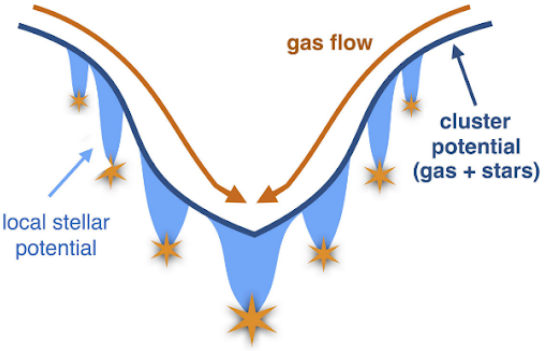

Figure 1.5: A schematic representation of competitive accretion. Image credit: Dr. Paul Clark, Cardiff University.

rial gets accreted from regions beyond the core scale (Rosen et al., 2020). Due to the combined gravitatinal effect of the gas and the stars, gas preferentially moves toward the central regions of the cluster, where the gravitational pull is strongest. Consequently, the seeds located closer to the cluster's center are in a more favorable position to accumulate larger amounts of gas. This advantage

allows these seeds to grow rapidly compared to those in the outer regions, eventually forming massive stars. The cluster potential and corresponding gas flow are shown in Figure 1.5. In competitive accretion, the mass accretion rate can be estimated as $\dot{M} \sim 4\pi\rho \frac{(G\,M)^2}{v^3}$, where M is the seed mass and v is the relative velocity between the gas and the seed (Krumholz & Bonnell, 2009). Depending upon various values of ρ, M, and v, $\dot{M}$ can varies from 10^{-9}–$10^{-4}\,M_\odot\,\mathrm{yr}^{-1}$. In competitive accretion, only a few stars acquire a high mass accretion rate of about $10^{-4}\,M_\odot\,\mathrm{yr}^{-1}$ and become massive stars (Krumholz & Bonnell, 2009). According to Krumholz (2008), the close encounters among the massive stars at the center of the cluster will truncate the disk (up to ∼30 AU), and therefore, the disk mass and the fraction of massive stars with disks expected to be lower in competitive accretion model than monolithic collapse mode. Competitive accretion occurs in a clustered environment, therefore it cannot explain the origin of isolated massive O-type stars.

The monolithic collapse and competitive accretion scenarios do not account for large-scale (i.e., cloud-scale) gas motions that supply materials to the clumps and, subsequently, to the cores (Vázquez-Semadeni et al., 2024a). The large-scale gas motions can be driven by gravity, as discussed in the global hierarchical collapse (GHC) model (Vázquez-Semadeni et al., 2017, 2019, and references therein), or by turbulence, as described in the inertial-inflow model (Padoan et al., 2020). In Rosen et al. (2020), GHC and inertial-inflow models are also referred as "clump-fed" scenarios. It is important to note that "clump-fed" scenarios refer to clustered star formation, which produces both low-mass and massive stars. According to the GHC model, gravitational contraction extends beyond the core-scale (∼0.1 pc) and can occur throughout the entire cloud (e.g., Vázquez-Semadeni et al., 2009, 2017, 2019). Thus, the gravitational collapse of the cloud contributes to the accumulation of mass in clumps, while the collapsing

clumps feed mass into cores. Using smoothed particle hydrodynamics, Gómez & Vázquez-Semadeni (2014) showed that the large-scale gravitational contraction of a molecular cloud can be anisotropic, potentially leading to the formation of filamentary structures (see Figure 1.1), which are primarily responsible for channeling material from cloud to the clump-scale. On the other hand, in the inertial-inflow model, Padoan et al. (2020) proposed that large-scale gas motion in the molecular clouds is primarily driven by supersonic turbulence. In this model, energy related to turbulent gas motion is significantly higher than the energy of gravitational interaction and thermal gas motion. Supersonic turbulence generates shocks in the molecular cloud, creating sheet-like structures that interact with each other to form filaments (Pineda et al., 2023). Filaments appear as dark or absorption features at shorter wavelengths (i.e., optical to mid-infrared (MIR)) because of the extinction of the background emissions (e.g., Lynds & Oneil, 1985; Wang et al., 2014; Santos et al., 2016; Dewangan, 2022). In contrast, at longer wavelengths (i.e., far-infrared (FIR) to sub-mm/mm), they are observed as bright or emission features due to molecular rotational transitions and thermal emission from cold dust (e.g., Panopoulou et al., 2014; Ragan et al., 2014; Bhadari et al., 2022). Although filamentary structures in molecular clouds have been known for many years (e.g., Schneider & Elmegreen, 1979; Bally et al., 1987), *Herschel* data demonstrate that these filaments are indeed ubiquitous and are associated with star-forming regions (André et al., 2010; Molinari et al., 2010a).

1.5.1 Role of filaments in MSF

The star formation activity in a filament begins with gravitational collapse. The stability of filaments during this process depends on their line mass ($M_{\rm line,obs}$), which is calculated as the ratio of their mass to their length. If $M_{\rm line,obs} > M_{\rm line,cri}$, then the filament becomes supercritical and undergoes gravitational collapse.

Here, $M_{\rm line,cri}$ is referred to as the critical line mass, which can be estimated as $M_{\rm line,cri} \sim 2c_{\rm s}^2/G \simeq 16\,(T/10\,K)\,M_\odot\,{\rm pc}^{-1}$ considering only thermal gas pressure at temperature T (Ostriker, 1964). To incorporate the effect of non-thermal gas motion and magnetic filed, c_s can be substituted with the effective sound speed. Thus, the critical line mass becomes (e.g., Fiege & Pudritz, 2000; Henshaw et al., 2014),

$$M_{\rm line,cri} = \frac{2c_{\rm eff}^2}{G} \simeq 465 \left(\frac{c_{\rm eff}}{1\ {\rm km\ s^{-1}}}\right)^2 M_\odot\,{\rm pc}^{-1}. \tag{1.5}$$

Observationally, Busquet et al. (2013) found that most filaments in the molecular cloud G14.225–0.506 have $M_{\rm line,obs} \gtrsim M_{\rm line,cri}$. Consequently, these filaments are unstable and are undergoing fragmentation, which is consistent with their clumpy structure. According to Bastien (1983) and Pon et al. (2012), differential gravitational acceleration along the longer axis of an isolated filament (typically with $A \gtrsim 5$) causes massive fragments suitable for MSF to form exclusively at its edges. This process, known as end-dominated collapse (EDC), has only a handful of reported candidates in the literature (e.g., Wang et al., 2019; Bhadari et al., 2020, 2022; Verma et al., 2023).

Observational studies have revealed that multiple filaments often converge at common junctions (e.g., Myers, 2009; Schneider et al., 2012; Dewangan et al., 2017a; Kumar et al., 2022). The junctions where three or more filaments meet are referred to as hubs, and together, these structures are known as hub-filament systems (HFSs; Myers, 2009). Figure 1.6a presents a three-color composite image of a HFS, Monoceros R2 (Treviño-Morales et al., 2019). The filaments and their common junction (i.e., hub) can be observed in red, displaying the H_2 column density (i.e., $N(H_2)$) map. Hubs are characterized by higher $N(H_2)$ ($\gtrsim 10^{22}$ cm^{-2}) values and lower aspect ratios compared to the filaments. The $N(H_2)$ map of the HFS, RAFGL 5085, clearly shows the higher $N(H_2)$ values toward the hub than the filaments (Dewangan et al., 2023a).The filaments channel material from

large-scale to the hubs, leading to significant mass accumulation, which facilitates the formation of massive stars (e.g., Treviño-Morales et al., 2019; Motte et al., 2018). Consequently, the proxies of MSF, such as H II regions and/or Class II 6.7

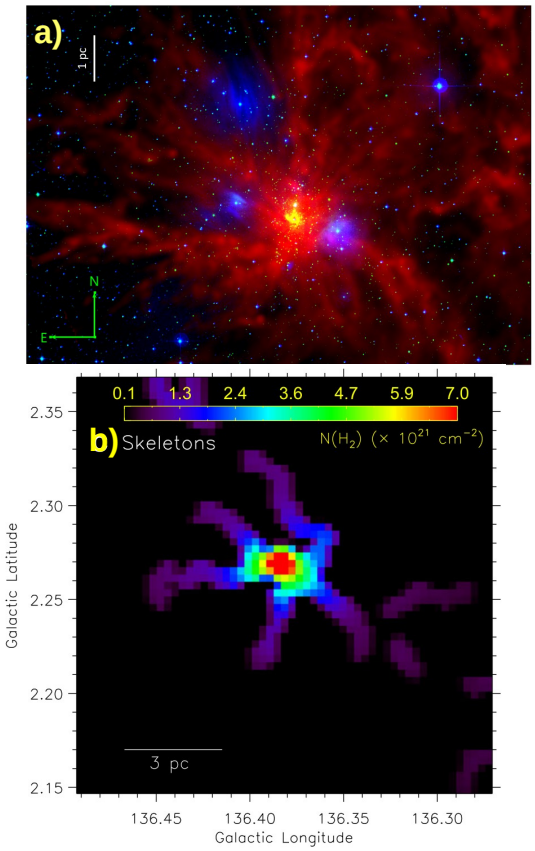

Figure 1.6: (a) Three-color composite image of the HFS, Monoceros R2, obtained from Treviño-Morales et al. (2019). The colors red, green, and blue represent the *Herschel* $N(H_2)$ map, 2MASS 1.65 μm band image, and Digitized Sky Survey (DSS) 560 nm band image, respectively. (b) This panel displays the *Herschel* $N(H_2)$ map of RAFGL 5085, masked using filaments identified by *getsf* on the *Herschel* 250 μm map (from Dewangan et al., 2023a).

GHz MMEs are commonly observed toward hubs (Schneider et al., 2012; Tigé et al., 2017; Dewangan et al., 2017a, 2020a). A recent study by Kumar et al.

(2020) identified nearly 3700 candidate HFSs in the Galactic plane. Considering the widespread presence and importance of HFSs, more details about them are provided in Section 1.6.

Interestingly, recent studies based on numerical simulations indicate that the collision of molecular clouds can also lead to the formation of filaments as well as massive cores (e.g., Inoue & Fukui, 2013; Balfour et al., 2017; Inoue et al., 2018). Molecular clouds in the Galactic disk often collide with each other due to cloud-to-cloud velocity dispersion ($\sim$6 km s^{-1}; e.g., Jog & Ostriker, 1988; Stark & Lee, 2005; Dobbs et al., 2015; Inutsuka et al., 2015), which primarily arises from the gravitational interactions between molecular clouds and the Galactic disk, as well as supernova explosions (Fukui et al., 2021a). In the case of supersonic collisions, the effective sound speed increases at the shock-compressed interface of the colliding clouds (Habe & Ohta, 1992; Anathpindika, 2010; Fukui et al., 2014, 2018b). This increase in effective sound speed results in a higher mass accretion rate, ranging from 10^{-4} to 10^{-3} $M_{\odot}$ yr^{-1} (Inoue & Fukui, 2013), making the collision scenario an efficient mechanism for MSF. This scenario is known as cloud-cloud collision (CCC) in the literature. Figure 1.7 illustrates a schematic representation of CCC. Given the significance of CCC in the formation of large-scale structures and massive stars, further details are provided in Section 1.7.

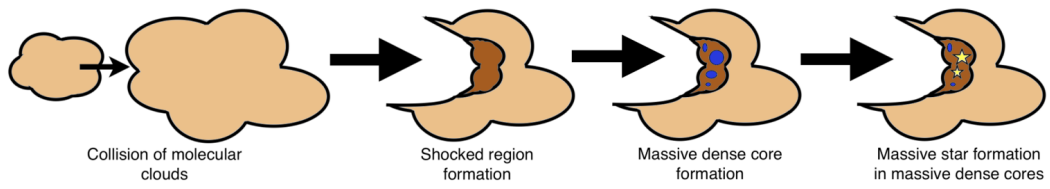

Figure 1.7: A schematic representation of CCC between two clouds of different sizes. The collision results in the formation of a shock-compressed layer at the interface of the colliding clouds, leading to the formation of massive dense cores and subsequently massive stars. Image credit: Dr. Nirmit Deepak Sakre, Hokkaido University.

1.6 Hub-filament systems (HFSs)

As mentioned in Section 1.5, HFSs are important structures within molecular clouds. Hubs accumulate a large amount of material through the filaments and are commonly associated with massive star-forming activity. A recent study of gas kinematics toward more than 100 HFSs by Zhou et al. (2022) revealed that mass accretion through filaments to their hubs is primarily driven by gravity on small scales (i.e., < 1 pc). On larger scales (i.e., > 1 pc), however, both turbulence as inertial flow and gravitational contraction contribute to the process. The mass accretion rate ($\dot{M}_{||}$) along the filament is a key parameter for the HFSs and can be estimated by assuming that filaments are uniform-density cylinders, as described by Kirk et al. (2013):

$$\dot{M}_{||} = \frac{\nabla V_{||}^{\rm obs} M^{\rm Fil}}{\tan(\alpha)}, \tag{1.6}$$

where, $\nabla V_{||}^{\rm obs}$ represents the observed velocity gradient along the filament, $M^{\rm Fil}$ is the mass of the filament and α is its angle relative to the plane of the sky. Several observational studies have found that filaments can have significantly high longitudinal gas flow rates ($\sim 10^{-4}$–10^{-3} $M_\odot$ yr^{-1}) to their central hubs (e.g., Chen et al., 2019; Treviño-Morales et al., 2019; Yang et al., 2023; Seshadri et al., 2024). Such high gas flow rates are sufficient for the formation of massive stars. Kumar et al. (2020) identified about 11% of their target clumps as the part of HFS candidates using *DisPerSE* algorithm (Sousbie, 2011) on *Herschel* 250 μm data. Typically, the hubs were found to have 3–7 skeletons joining them. Their study found that filaments forming the HFSs had a mean length of about 10–20 pc. Interestingly, their study also revealed that all the clumps with luminosity greater than 10^4 and 10^5 $L_\odot$, at distances within 2 kpc and 5 kpc, respectively, are located in the hubs of HFSs.

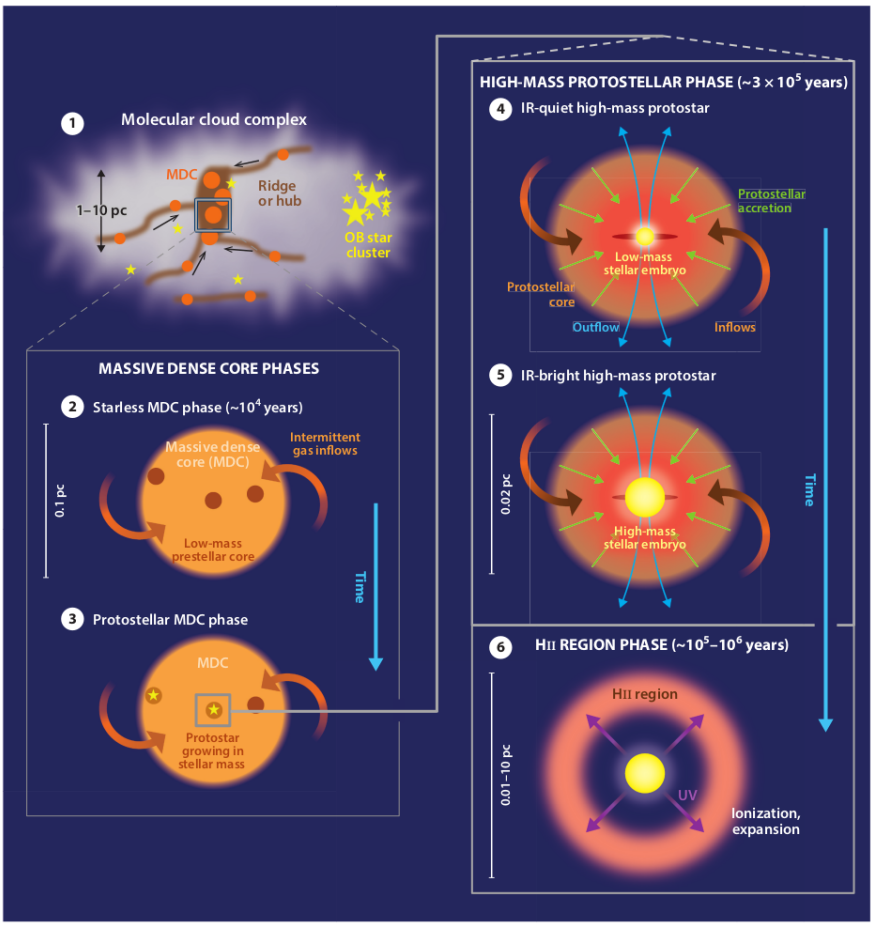

Figure 1.8: The schematic diagram illustrates the evolutionary stages of MSF from HFS, as proposed by Motte et al. (2018). (1) Hubs contain MDCs. (2) These MDCs initially host low-mass prestellar cores, (3) which develop into low-mass stellar embryos. Gravitational inflows feed the protostellar envelopes, supporting the formation of high-mass protostars. The stellar embryos evolve from a (4) IR-quiet state to a (5) IR-bright state as their mass increases. (6) Finally, the accretion phase concludes as the UV radiation from the massive stars ionizes the protostellar envelope and creates an H II region. The figure is obtained from Motte et al. (2018).

Concerning the observed hub-filament configurations, Motte et al. (2018) proposed the evolutionary stages of MSF from HFS, which are shown in Figure 1.8.

The process begins with the formation of density-enhanced hubs at the junctions of several filaments. These hubs contain several massive dense cores (MDCs). These MDCs initially host low-mass prestellar cores that gradually evolve into low-mass stellar embryos ($< 8\,M_{\odot}$). Gravitational inflows channel material into the protostellar envelopes, driving the growth of high-mass protostars ($> 8\,M_{\odot}$). As the stellar embryos gain mass, they transit from an IR-quiet stage to an IR-bright stage, reflecting their increased luminosity. Eventually, the accretion phase concludes when UV radiation from the massive stars ionizes the surrounding protostellar envelope, leading to the formation of an H II region. This scenario supports the picture of a mass accumulation from the large-scale to the dense core-scale through filaments (Tigé et al., 2017; Motte et al., 2018; Treviño-Morales et al., 2019).

Although the potential of HFSs in the context of MSF is well recognized, their origin remains elusive. In this context, Kumar et al. (2020) put forward the idea of overlapping or merging of gravitationally unbound flow-driven filaments to explain the origin of HFSs. The overlapping of filaments and the formation of HFSs is shown in Figure 1.9. The relative motion between the filaments, causing them to overlap, is possibly driven by intra-molecular cloud velocity dispersions ($\sim$1 km s^{-1}), stellar winds, and expansion of the H II regions. According to Kumar et al. (2020), low-mass star formation may occur both prior to and during the formation of the hub. However, overlapping filaments amplify the gas density in the hubs, and the increased gravitational potential begins to drag material along the filaments into the hubs. As a result, massive stars form exclusively within the hub. The scenario of overlapping filaments effectively explains the origin of the HFS at G083.097+03.270 (Panja et al., 2023). However, reconciling the complex morphologies of HFSs observed in studies, such as Monoceros R2 (Treviño-Morales et al., 2019), G45.3+0.1 (Bhadari et al., 2022), N159E-Papillon

(Fukui et al., 2019) and N159W-South (Tokuda et al., 2019) with the model of Kumar et al. (2020) can be challenging.

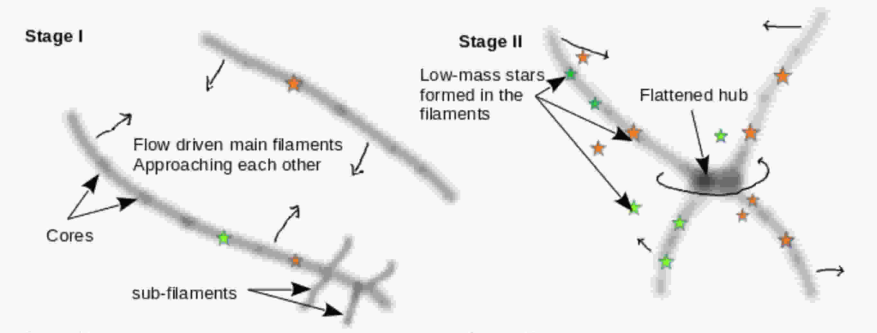

Figure 1.9: A schematic diagram showing the formation of HFSs due to the overlap of flow-driven filaments (from Kumar et al., 2020). The star symbols show the positions of the low-mass stars.

1.7 Cloud-cloud collision (CCC)

Smith (1980) conducted simulations of one-dimensional colliding flows, taking into account the effects of radiative gas cooling as well as the formation and dissociation of molecules. His findings indicated that a dense layer of molecular gas develops when atomic clouds collide and a slower collision speed is more favorable for gravitational instability in the layer. Later, Gilden (1984) carried out two-dimensional numerical simulations of two identical colliding molecular clumps, demonstrating that these interactions create dense, gravitationally unstable gas layers. Habe & Ohta (1992) argued that the possibility of collisions between non-identical clouds is higher than identical clouds. Then, they successfully demonstrated that collisions between non-identical clouds are conducive to the formation of gravitationally unstable massive cores, which are essential for MSF. In recent years, CCC has emerged as a potential mechanism for MSF, successfully explaining the origin of superstar clusters that contain tens of massive

stars, as well as H II regions driven by isolated massive stars (Fukui et al., 2021a, and references therein).

Observationally, CCC sites can be identified through the analysis of spatial distribution and velocity of the molecular gas. In general, CCC sites show the bridge feature and complementary distribution in the position-velocity (PV) and position-position (PP) space, respectively (e.g., Torii et al., 2011; Fukui et al., 2014, 2015; Dewangan, 2017; Sano et al., 2018; Fujita et al., 2021). The bridge feature is a subtle connection of the colliding cloud components in PV space (e.g., Haworth et al., 2015a; Torii et al., 2017; Dewangan & Ojha, 2017; Priestley & Whitworth, 2021). In PP space, the spatial fit of "intensity-enhancement/key" and "intensity-depression/keyhole" regions of the cloud components is known as the complementary distribution (Fukui et al., 2021a). Figure 1.10 shows the bridge feature and complementary distribution resulting from a head-on collision between two non-identical clouds, using synthetic observations of ^{12}CO(J = 1–0) emission by Takahira et al. (2014). The colliding clouds in this case have radii (masses) of 3.5 pc (417 $M_{\odot}$) and 7.2 pc (1635 $M_{\odot}$), and they collide with a relative velocity of 5 km s^{-1}. Figures 1.10a–1.10h show how the gas distribution varies with velocity when the angle ($\theta_{\rm col}$) between the relative motion of the clouds and the line of sight is 0°. The PV diagrams in Figures 1.10j and 1.10k clearly reveal two velocity components at approximately 0 and −5 km s^{-1}. These velocity components are connected by the bridge feature. The complementary spatial distribution between these velocity components is shown in Figure 1.10i. The image presents the larger cloud component, while the contour displays the smaller cloud component.

It is important to note that the complementary distribution between two cloud components can be displaced, as shown in Figure 1.11 for the Orion Molecular Cloud (Fukui et al., 2021a). This displacement occurs when $\theta_{\rm col}$ is not 0° (Fukui

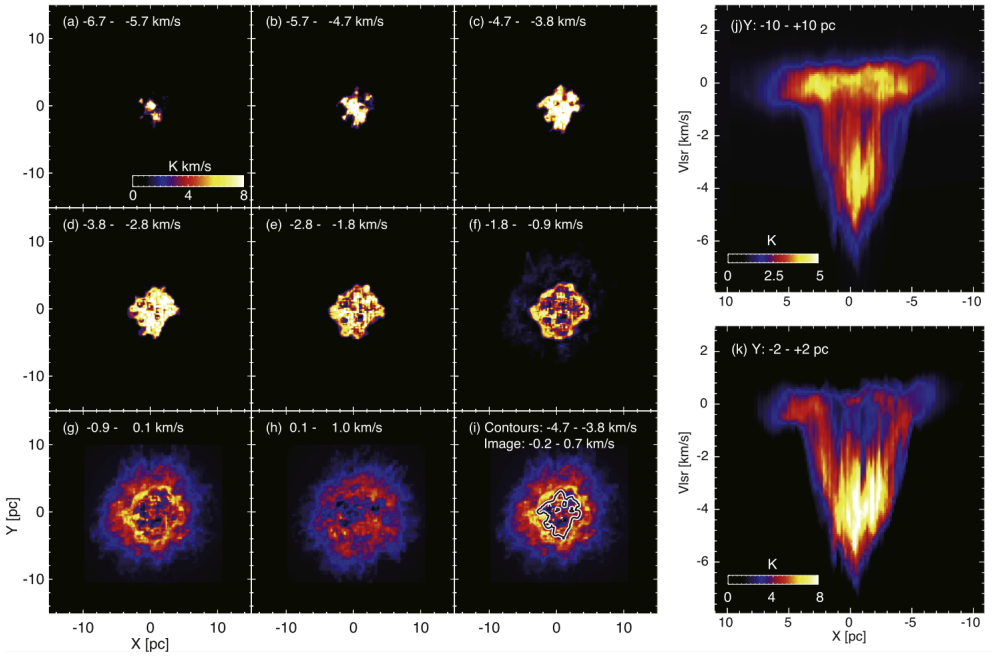

Figure 1.10: The distribution of molecular gas for CCC at $\theta_{\rm col} = 0°$ based on synthetic observations of ^{12}CO(J = 1–0) emission by Takahira et al. (2014). This image is obtained from Fukui et al. (2018b). Panels (a)–(h) show the integrated intensity maps for the velocity intervals specified in each panel. Panel (i) shows a complementary distribution between the large cloud (integrated intensity image for velocity $[-0.2, 0.7]$ km s^{-1}) and the small cloud (contour at 4 K km s^{-1} for the image shown in panel (c)). Panels (j) and (k) present the PV diagrams for Y: $[-10, 10]$ and $[-2, 2]$ pc, respectively.

et al., 2018b). A detailed observational overview of CCC can be found in Fukui et al. (2021a), which also includes a list of more than 50 observationally detected CCC sites and their corresponding physical parameters. They determined that the average relative velocity of the colliding clouds is about 5 km s^{-1}. Interestingly, several theoretical and numerical studies estimated the rate of CCC to be once in every 100 years for our Galaxy (e.g., Tasker & Tan, 2009; Dobbs et al., 2015). Despite the large theoretical expectations, the observational record of CCC is limited. The primary challenge in observing CCC lies in $\theta_{\rm col}$ (see Fukui

et al., 2018b; Fujita et al., 2021, for details). When $\theta_{\rm col}$ is 90°, colliding clouds become indistinguishable in the velocity space (e.g., Takahira et al., 2014; Priestley & Whitworth, 2021), making it impossible to test for CCC. This limitation highlights the need for new diagnostic signatures to detect CCC at higher values of $\theta_{\rm col}$.

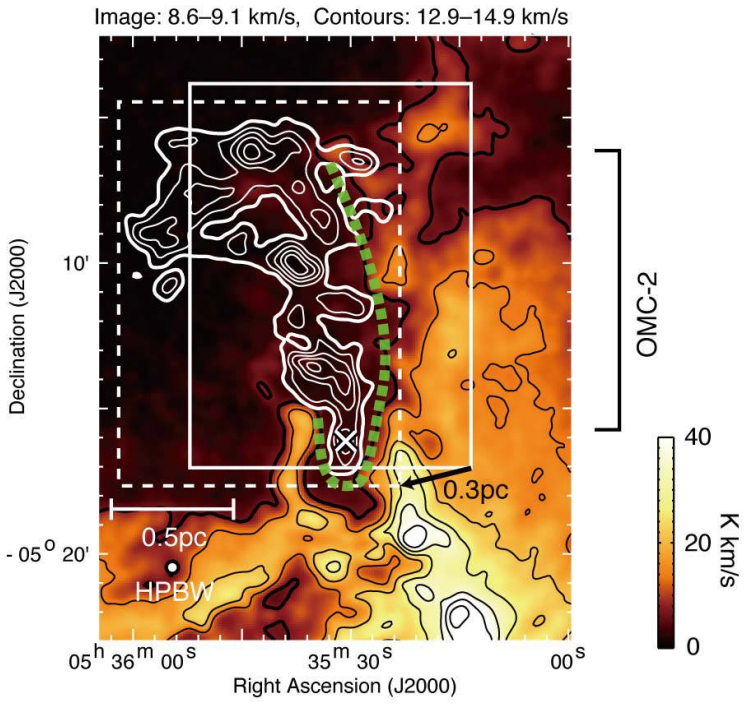

Figure 1.11: The image shows the complementary distribution of two velocity components toward the Orion Molecular Cloud using ^{12}CO(J = 1–0) data (from Fukui et al., 2021a). The image and black contours represent the blue-shifted component, while the white contours display the red-shifted component. The velocity ranges of the blue- and red-shifted components are indicated at the top of the image. A better complementary fit between these two velocity components is achieved with a linear shift of 0.3 pc, as indicated by the black arrow. The solid rectangle represents the initial position of the red-shifted component, while the dashed rectangle shows its position after the displacement. The green dashed line marks the contact surface between the two cloud components, and the white cross marks the position of a B3-type star.

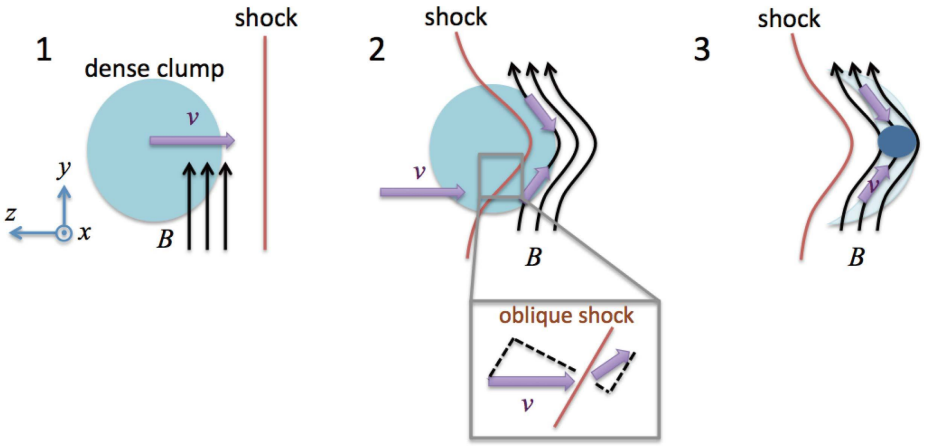

Figure 1.12: A schematic diagram showing the formation of filaments perpendicular to the magnetic field due to shock-compression of dense structures (from Inoue et al., 2018). In this case, the filament is oriented perpendicular to the plane of the page.

As mentioned earlier in Section 1.5.1, CCC can also lead to the formation of filaments. Using hydrodynamic simulations Balfour et al. (2015) showed that lower collision velocities of uniform density clouds with subsonic turbulence form radially converging filaments, while relatively higher collision velocities lead to a complex network of filaments resembling a spider's web. The distinction between the radially converging filaments and the spider's web structure becomes blurred for the collisions of molecular clouds with internal substructure (Balfour et al., 2017). The formation of filaments in the CCC scenario was extensively explored using magneto-hydrodynamic (MHD) simulations by Inoue & Fukui (2013) and Inoue et al. (2018). The physical process of filament formation based on the model proposed by Inoue & Fukui (2013) is depicted in Figure 1.12. In molecular clouds, inhomogeneous dense structures form as a result of turbulence (see Phase 1). These dense structures are compressed during collisions (see Phase 2), leading to the formation of filaments. As compression is more efficient along magnetic field lines, high-density filaments develop perpendicular to the magnetic field lines

(see Phase 3). However, it has yet to be explored whether these filaments converge over time to form a HFS and what potential factors influence this process.

1.8 Objectives of the thesis

As mentioned in earlier sections, MSF is a complex mechanism that involves many physical processes spanning from cloud to the core scales. Observational investigations of massive star-forming regions (MSFRs) provide insights into the ongoing physical processes and help to assess the applicability of the proposed scenarios of MSF. In addition, such studies can reveal completely new aspects of the existing physical processes – such as the simultaneous occurrence of various physical processes and the presence of multiple HFSs within same MSFR at different evolutionary stages. On the other hand, numerical simulations can help to uncover the processes involved in the formation of structures (i.e., filaments and cores) within molecular gas. Specifically, in the context of CCC, simulations offer an opportunity to evaluate the potential formation of HFSs from CCC events. Furthermore, studies of numerically simulated data can improve our understanding of existing observational signatures of CCC reported in the literature, examine how these signatures evolve over time, and guide the search for new ones.This thesis explores various aspects of MSF through observational studies and the use of numerically simulated data. The primary objectives of the thesis are as follows:

1. To understand the physical processes involved in MSF by conducting multi-wavelength observational investigations of Galactic MSFRs at different stages of evolution i.e., from cold molecular clump to extended H II regions.

2. To investigate the simultaneous signatures of various physical processes of MSF within the same MSFR. This thesis also involves detecting multiple

HFSs in a single molecular cloud and investigating their origins and evolutionary stages.

3. To explore whether CCC can lead to the formation of HFSs and examine the roles of collision, gravity, turbulence, and magnetic fields in the origin of HFSs.

4. To search for new observational signatures of CCC that will be applicable at higher values of $\theta_{\rm col}$ (i.e., $\sim 90^{\circ}$), where the signatures, such as the bridge feature and complementary spatial distribution, are not effective. The new signatures will be useful for detecting CCC sites that might otherwise remain undetected.

1.9 Target selection

The first two objective of this thesis is related to the observational investigations of the structure formation and gas kinematics toward Galactic MSFRs. Therefore, several MSFRs are selected within a distance of 5 kpc, which are at different stages of evolution. As described in Sections 1.4.1 and 1.4.2, the presence/absence of radio continuum emission (indicating the presence/absence of H II regions), the compactness of the H II region, and the detection of Class II 6.7 GHz MMEs help to identify MSFRs and to infer their evolutionary stages. To understand the formation of massive O-type stars, we selected one of the most luminous ($> 10^6$ $L_{\odot}$; Beuther et al., 2011) MSFRs of our galaxy, the W31 complex ($d \sim$ 3.55 kpc; Chapter 3, Maity et al., 2022). It hosts two extended H II regions driven by multiple O-type stars, one of which is referred to as a "giant H II region" in the literature, as it emits more than 10^{50} Lyman continuum photons per second (Blum et al., 2001). In contrast to W31, which represents an evolved stage of MSF, we selected AFGL 5180 and AFGL 6366S for our observational

investigation of the early stages of MSF (Chapter 4, Maity et al., 2023). These target sites were chosen due to their proximity ($d \sim 1.5$ kpc; Devine et al., 2008) and the earlier detection of Class II 6.7 GHz MMEs toward both AFGL 5180 and AFGL 6366S (Szymczak et al., 2018). Additionally, AFGL 5180 is a well-known massive MSFR, having been featured as the NASA/ESA Hubble Space Telescope Picture of the Week[2]. Next, we selected the nearby molecular cloud G321.93–0.01 ($d \sim 1.98$ kpc; Chapter 5, Maity et al., 2025a), which contains several cold, molecular massive clumps at the earliest stages of MSF. A visual inspection of G321.93–0.01 reveals the presence of numerous filaments (∼2–10 pc in length). Therefore, this molecular cloud became a unique target for investigating multiple HFSs and exploring their origins and relative evolutionary stages. Finally, to illustrate how the results from our simulation-based study of CCC (see Chapter 6) can improve the understanding of the spatial distribution and large-scale gas motion in MSF, we have examined the IRDC hosting the N59-North bubble ($d \sim 4.66$ kpc; Chapter 7, Maity et al., 2025b). This region was previously proposed as a site of CCC (Chen et al., 2024).

1.10 Outline of upcoming chapters

The outline of the upcoming chapters is detailed below.

Chapter 2: Data, tools and techniques

This chapter provides an overview of the observational and MHD simulation data used in this thesis. We discuss the origin of multi-wavelength emissions from star-forming regions and their significance in studying MSF. Details of the

[2] https://esahubble.org/images/potw/page/11/

observational data, including the survey names, telescopes, wavelengths, and resolutions, are provided in this section. The fundamentals of MHD in the context of molecular clouds are also explained. Finally, we discuss the tools and techniques employed in this thesis to derive various physical parameters related to star formation studies.

Chapter 3: Unraveling the observational signatures of cloud-cloud collision and hub-filament systems in W31

This chapter presents an observational study of the W31 complex, which hosts two extended H II regions: W31-N and W31-S, powered by a cluster of O-type stars. The *Herschel* 250 μm continuum map shows the presence of HFS toward both W31-N and W31-S. In the direction of W31-S, analysis of the NANTEN2 ^{12}CO(J = 1–0) and SEDIGISM ^{13}CO(J = 2–1) data reveals the presence of two cloud components, which show a complementary distribution. Based on these results, the applicability of the CCC scenario is discussed for the formation of HFSs and the O-type stars in the W31 complex. The outcomes of this chapter are published in Maity et al. (2022).

Chapter 4: AFGL 5180 and AFGL 6366S: sites of hub-filament systems at the opposite edges of a filamentary cloud

In this chapter, we present a multi-scale and multi-wavelength observational study of AFGL 5180 and AFGL 6366S, both of which host a Class II 6.7 GHz MME. The application of the *getsf* utility on *Herschel* far-infrared images reveals a HFS toward each target site, found to be located at opposite edges of a filamentary cloud. Based on the analysis of the MWISP ^{13}CO(J = 1–0) data, signatures of CCC are detected. Finally, the possible role of CCC in the formation of these HFSs is discussed. This chapter is based on the published work, as presented in Maity et al. (2023).

Chapter 5: G321.93–0.01: A rare site of multiple hub-filament systems

with evidence of collision and merging of filaments

This chapter presents an observational investigation of the molecular cloud G321.93–0.01. The SEDIGISM ^{13}CO(J = 2–1) data reveal multiple HFSs. Two of them exhibit significant mass accretion rates ($> 10^{-3}$ $M_{\odot}$ yr^{-1}) to their hubs. We utilized *astrodendro* on ATLASGAL 870 μm and ALMA Band-7 images to explore the hierarchical structures, ranging from clump- to core-scale. The MSF activity of the HFSs is compared based on Kauffmann & Pillai's criteria and the detection of MeerKAT 1.28 GHz radio continuum emission. Futhermore, the analysis of ^{13}CO data indicates the formation of HFSs through the collision and merging of filaments. The key findings of this chapter are published in Maity et al. (2025a).

Chapter 6: Cloud-cloud collision: Formation of hub-filament systems and associated gas kinematics

Our observational studies of the MSFRs, G321, AFGL 5180 & 6366S, and W31 complex, suggest a possible connection between CCC and the formation of HFSs. In this chapter, we analyzed the MHD simulation data from Inoue et al. (2018) to understand the connection between CCC and the formation of HFSs, focusing on the distinct roles of turbulence, shock compression, magnetic fields, and gravity. Additionally, this chapter highlights the challenges in observing CCC signatures at $\theta_{\rm col} = 0°$ and proposes new possible signatures for $\theta_{\rm col} = 90°$. The results discussed in this chpater are published in Maity et al. (2024).

Chapter 7: Investigating embedded structures and gas kinematics in the IRDC hosting bubble N59-North

This chapter presents a multi-wavelength study of an extended area covering the bubble N59-North to investigate embedded structures and large-scale gas flow in light our simulation work. The *Spitzer* 8 μm image reveals an IR-dark filament and its existance is further confirmed using GRS ^{13}CO(J = 1–0) and CHIMPS

^{13}CO(J = 3–2) data. A new HFS candidate is investigated toward the central part of the filament at early stage of MSF. Comparisons of the outcomes of this study with MHD simulations indicate that gas is converging toward the HFS candidate. Finally, the possibility of CCC is discussed in the context of filament formation and large-scale gas motion. The important results of this chapter are published in Maity et al. (2025b).

Chapter 8: Summary and future prospects

This chapter provides a detailed summary of the major outcomes of this thesis. It further highlights the the limitations of the overall work and provides immediate future prospects.

Chapter 2

Data, tools and techniques

This thesis integrates both observational and MHD simulation data to obtain a comprehensive understanding of MSF. Observational studies enable us to infer the ongoing mechanisms of MSF, such as the physical conditions, kinematics, and environmental factors influencing MSFRs. On the other hand, simulations provide essential insights into the evolution of molecular clouds with time and the underlying physics of MSF, including the role of gravity, turbulence, and magnetic fields. In Chapters 3, 4, and 5, we present detailed observational studies of Galactic MSFRs, W31 complex, AFGL 5180 & AFGL 6366S, and G321.93–0.01, respectively. These observational studies of the MSFRs aim to uncover the key processes driving MSF by identifying their observational signatures. In Chapter 6, we complement the observational findings by utilizing MHD simulation data to explore the interplay between gas dynamics, gravity, turbulence, and magnetic fields. The observational investigation of the IRDC hosting N59-North bubble in Chapter 7 demonstrates how the results of Chapter 6 improve the understanding of the spatial distribution and large-scale kinematics of the molecular gas. The observational data, details of MHD simulation, and the analysis tools and techniques utilized in this thesis are described in the following

sections.

2.1 Multi-wavelength observational data

The importance of multi-wavelength observations in the investigation of MSFRs, along with the data utilized in this thesis, is presented in the following sections.

2.1.1 Importance of multi-wavelength observations

MSFRs exhibit diverse environments, from cold molecular clumps/cores to extended H II regions. Also, they manifest across a wide range of spatial scales, from large molecular clouds ($>$ 10 pc) to small dense cores ($<$ 0.1 pc). As a result, observational studies require multi-wavelength and high-resolution data to characterize the ongoing physical processes. A basic classification of the electromagnetic spectrum relevant to star formation studies is provided in Table 2.1.

Molecular clouds are the coolest ($\sim$10 K) and densest region of the ISM. The density in the molecular cloud varies from about 10^{2-3} cm^{-3} at the cloud scale to as high as 10^{6} cm^{-3} at the core scale. Unfortunately, the main constituents of the molecular cloud, H_2 and He do not radiate in such cold environments. Due to the lack of electric dipole moment, rotational transitions with $\Delta J = \pm 1$ are not allowed for H_2. The permitted quadrupole transitions ($\Delta J = \pm 2$) are improbable, as they require temperatures above 510 K, which are much higher than typical temperatures of molecular clouds. Interestingly, CO possess electric dipole moment, which allows $\Delta J = \pm 1$ transitions. The higher reduced mass of CO makes the transitions J = 1–0, J = 2–1, and J = 3–2 ideal for cold molecular gas (e.g., 5 to 40 K). The rotational transitions of CO, and other molecules such as CO, CS, HCN, and SiO, are typically detected in the mm/sub-mm wavelength regime. We can infer the gas velocity by comparing the observed

Table 2.1: Wavelength ranges and their contributions to star formation studies. The regime and corresponding wavelength ranges are obtained from Smith (2004).

Regime	Wavelength Range	Contribution
Radio/ millimeter	**0.1 – 1000 cm**	• Traces H II regions and masers • Detects molecular rotational transitions. • Probes dense cores and molecular outflows. • Offers insights into cloud dynamics.
Sub-millimeter	**300 – 1000 μm**	• Traces cold dust and dense molecular gas. • Crucial for studying the earliest stages of star formation.
Mid/Far-infrared	**10 – 300 μm**	• Penetrates dust to reveal embedded protostars. • Probes warm dust emission.
Near-infrared	**0.8 – 10 μm**	• Probes YSOs • Detects hot dust, Polycyclic Aromatic Hydrocarbons (PAH) emission, and outflows.

frequencies of these transitions to their rest frequencies, which is essential to understand kinematics of the molecular cloud. The CO rotational transitions are ideal for large-scale study due to its high abundance ratio ($\sim 10^{-4}$ times that of the H_2). In particular, ^{12}CO(J = 1–0) traces low density ($n \gtrsim 10^2$ cm^{-3}) gas, which is ideal to reveal large scale molecular distribution. Whereas ^{13}CO/C^{18}O(J = 2–1) exhibit significantly lower optical depths compared to ^{12}CO(J = 1–0),

making them effective tracers for moderately dense molecular gas in the ISM, with densities around $n \sim 10^3$ cm^{-3} (Schuller et al., 2017a). The ^{13}CO/C^{18}O (J = 3–2) transitions traces relatively more dense gas ($n \gtrsim 10^4$ cm^{-3}; Rigby et al., 2016). The CS and HCN molecular line data are useful to prove densities above 10^5 cm^{-3} (Smith, 2004; Krumholz et al., 2007b). SiO emission serves as evidence for high-velocity shocks generated by protostellar jets (Liu et al., 2021).

The ISM contains dust particles that represent around 1% of its total mass (Smith, 2004; Schulz, 2005), which makes thermal dust emission a valuable proxy for studying both the ISM and molecular clouds. The thermal continuum in mm/sub-mm regime traces cold dust emission. Depending upon the resolution and sensitivity of the telescopes, mm/sub-mm continuum emission is useful to observe cloud-to-core scale structures. The MIR/FIR continuum emission from the warm dust, heated by UV photons from massive stars, reveals the Photo-Dissociation Regions (PDRs). The NIR/MIR domain includes several Polycyclic Aromatic Hydrocarbon (PAH) emission features at 3.3, 6.2, 7.7, 8.6, and 11.3 μm (Schulz, 2005; Tielens, 2008). Interestingly, the molecular clouds exhibit dark absorption features in the NIR/MIR domain against strong background emission from PAHs and thermal dust emission in the Galactic plane (Ragan et al., 2009). NIR continuum data are particularly useful for detecting YSOs (Hartmann et al., 2005; Getman et al., 2007; Gutermuth et al., 2009). The radio continuum emission indicates the presence of ionized gas in H II regions (e.g., Terzian, 1965; Churchwell, 2002). This phenomenon, known as free-free emission, occurs due to the deceleration of electrons (Condon & Ransom, 2016). The maser emissions from molecules such as OH, H_2O, and CH_3OH in the radio/mm domain indicate the ongoing star-forming activity (Bartkiewicz & van Langevelde, 2012). As mentioned in Section 1, the Class II 6.7 GHz MME traces the early stages of MSF (Menten, 1991; Minier et al., 2001). The multi-wavelength data utilized in

this thesis are mentioned in the following section.

2.1.2 Multi-wavelength data utilized in this thesis

To reveal the physical mechanisms behind MSF, this thesis describes detailed observational studies of several Galactic MSFRs. These studies involved exploring and analyzing multi-wavelength and multi-scale data from NIR to radio. Table 2.2 provides an overview of all the observational data analyzed in this thesis, detailing the data sources, observing telescopes, wavelengths, and resolutions. The radio continuum data at different resolutions enables us to detect classical to HC H II regions, which were obtained from both national (GMRT) and international facilities (MOST, VLA, and MeerKAT). This thesis focuses on exploring cloud-scale gas morphology and kinematics; hence, ^{12}CO, ^{13}CO and C^{18}O line data were utilized from several international facilities such as NANTEN2, MWISP, SEDIGISM, GRS, and CHIMPS. In the mm/sub-mm domain, ALMA provides an unprecedented resolution of about 0.″3, which enables us to core scale study toward AFGL 5180 (Chapter 4) and G321.93–0.01 (Chapter 5). In addition to the NIR data from ground-based observatories, data from space-based telescopes such as *HST*, *Spitzer*, *Herschel*, and *Planck* in the NIR/MIR/FIR domains are also utilized in this thesis. Additional details about the data, including instruments, reduction pipelines, and sensitivity, are provided in the relevant chapters.

2.2 MHD simulation data

To achieve our objective of understanding the possibility of formation of HFSs from CCC and the physical processes behind it, we conducted an extensive analysis of the MHD simulation data (in Section 6). The MHD simulation data of CCC were collected from Inoue et al. (2018), which incorporated ideal isothermal

Table 2.2: An overview of all observational data analyzed in this thesis.

	Data source	Telescope/Diameter	Wavelength/Transitions	Resolution	Reference
Radio	Giant Metrewave Radio Telescope (GMRT)	GMRT/45 m (NA[a]: 30)	93 cm	$\sim13''$	Proposal Code: 23_024
	Sydney University Molonglo Sky Survey (SUMSS)	Molonglo Observatory Synthesis Telescope (MOST)[b]	36 cm	$\sim63''$	Bock et al. (1999)
	SARAO MeerKAT Galactic Plane Survey (SMGPS)	MeerKAT/13.5 m (NA: 64)	23 cm	$\sim8''$	Goedhart et al. (2024)
	NRAO VLA Sky Survey (NVSS)	Very Large Array (VLA)/25 m (NA: 25)	21 cm	$\sim45''$	Condon et al. (1998)
	Multi-Array Galactic Plane Imaging Survey (MAGPIS)	VLA	20 cm	$\sim6''$	Helfand et al. (2006)
	NRAO VLA Archive Survey (NVAS)	VLA	4 cm	$\sim3''$	Crossley et al. (2007)
mm/Sub-mm	NANTEN2	NANTEN2 (mm)/sub-mm telescope/4 m	2.6 mm; ^{12}CO(J = 1–0)	$\sim180''$	Fukui et al. (2006)
	Milky Way Imaging Scroll Painting (MWISP)	Purple Mountain Observatory (PMO)/13.7 m	2.6 mm; ^{12}CO(J = 1–0)	$\sim50''$	Su et al. (2019)
	^{13}CO/C^{18}O (J = 3→2) Heterodyne Inner Milky Way Plane Survey (CHIMPS)	James Clerk Maxwell Telescope (JCMT)/15 m	$\sim$0.9 mm; ^{13}CO(J = 3–2)	$\sim15''$	Rigby et al. (2016)
	Atacama Large Millimeter/submillimeter Array (ALMA)	ALMA/12 m (NA: 54), 7 m (NA: 12)	$\sim$0.88 and 1.3 mm	$\sim0\farcs3$ and $0\farcs3$	Ids: 2013.1.00960.S and 2015.1.01454.S
	APEX Telescope Large Area Survey of the Galaxy (ATLASGAL)	Atacama Pathfinder Experiment (APEX) Telescope/12 m	870 μm	$\sim19\farcs2$	Schuller et al. (2009)
Sub-mm/FIR	*Planck* Survey	Planck Telescope/1.5 m	850 μm	$\sim4\farcm8$	Planck Collaboration et al. (2014)
	Submillimeter High Angular Resolution Camera II (SHARC-II)	Caltech Submillimeter Observatory/10.4 m	350 μm	$\sim8\farcs5$	Merello et al. (2015)
	Herschel Infrared Galactic Plane Survey (Hi-GAL)	Herschel Space Observatory/3.5 m	70, 160, 250, 350, and 500 μm	$6''$, $12''$, $18''$, $25''$, and $37''$	Molinari et al. (2010a)
MIR	*Spitzer* MIPS Inner Galactic Plane Survey (MIPSGAL)	Spitzer Space Telescope/0.85 m	24 μm	$\sim6''$	Carey et al. (2009)
NIR	*Spitzer* Galactic Legacy Infrared Mid-Plane Survey Extraordinaire 360 (GLIMPSE360)	Spitzer Space Telescope	3.6, 4.5, 5.8, 8.0 μm	$\sim2''$	Benjamin et al. (2003); Whitney et al. (2011)
	Survey of extended H_2 emission	Canada-France-Hawaii Telescope (CFHT)/ 3.6m	2.12 μm	$\sim0\farcs7$	Navarete et al. (2015)
	UKIRT near-infrared Galactic Plane Survey (GPS)	United Kingdom Infrared Telescope (UKIRT)/3.8 m	1.25–2.2 μm	$\sim0\farcs8$	Lawrence et al. (2007)
	Two Micron All Sky Survey (2MASS)	Fred Lawrence Whipple Observatory/1.3 m & Cerro Tololo Inter-American Observatory/1.3 m	1.25–2.2 μm	$\sim2\farcs5$	Skrutskie et al. (2006)
	Hubble Space Telescope (HST)	HST/2.4 m	1.10–1.64 μm	$\sim0\farcs1$–$0\farcs2$	Kimble et al. (2008)

[a]NA: Number of Antenna

[b]MOST consists of two 778 m × 12 m cylindrical paraboloids that are separated by 15 meters.

MHD with self-gravity and utilized adaptive mesh refinement and sink particle techniques (developed by Matsumoto, 2007; Matsumoto et al., 2015). The basic equations for the MHD simulation with self gravity and the concept of sink particles are presented in the following sections, which are mostly taken from Matsumoto (2007), Federrath et al. (2010), and Matsumoto et al. (2015). However, other details, such as the numerical setup for the simulation, boundary conditions, and the resolution of the data, are presented in the respective chapter.

2.2.1 Ideal MHD equations with self-gravity

As mentioned earlier in Section 1.1, magnetic fields influence gas motion in the molecular cloud due to the small fraction of ions in the gas. For an ionization fraction of about 10^{-6}, the resistivity ($\mathcal{R}$) of the molecular cloud is about $10^{22} - 10^{23}$ cm^2 s^{-1} (Krumholz, 2015b). Hence, the magnetic Reynolds number, Rm $= LV/\mathcal{R} \gg 1$, at molecular cloud scales for $L \sim 10$ pc and $V \sim$ a few km s^{-1}. Therefore, magnetic diffusion is not significant in the molecular cloud. Similarly, it has been shown in (Krumholz, 2015b) that the viscous forces are unimportant in the cloud scale. Therefore, ideal MHD equations are applicable for the study of molecular clouds.

The ideal MHD equations in the conservative form are presented in Equations 2.1–2.4. The components of F_x given in Equation 2.3 can be rotated by the right-hand rule to obtain F_y and F_z. In Equations 2.2–2.4, $\vec{v}$, $\vec{B}$, $\vec{g}$ and ρ present velocity, magnetic field, gravity, and density, respectively. Total energy is, $E = |\vec{v}|^2/2 + (\gamma-1)^{-1}P/\rho + \left|\vec{B}\right|^2/8\pi\rho$ and the pressure is P. Here, γ is the adiabatic index (also known as the ratio of specific heats). The self-gravity can be introduced in the simulation using Poisson's equation, $\nabla^2\Phi = 4\pi G\rho$, where Φ denotes gravitational potential, and G is the gravitational constant as defined earlier.

In the case of molecular clouds, the cooling timescale ($\sim 10^3$ yr) is negligible when compared to the crossing timescale ($\sim 10^6$ yr) (Krumholz, 2015b). Thus, gas driven away from thermal equilibrium by any reason will restore its equilibrium temperature well before any significant mechanical movement occurs. Hence, molecular clouds can be treated as isothermal, and then the eighth components of Equations 2.1, 2.2, and 2.4 need to be excluded. It is important to note that the ideal MHD approximation is not valid at small scales (i.e., $\lesssim 0.05$ pc; Krumholz, 2015b). In such cases, gas can flow across magnetic field lines, which is known as ambipolar diffusion.

$$\frac{\partial U}{\partial t} + \frac{\partial F_x}{\partial x} + \frac{\partial F_y}{\partial y} + \frac{\partial F_z}{\partial z} = S, \tag{2.1}$$

where,

$$U = \left(\rho, \rho v_x, \rho v_y, \rho v_z, B_x, B_y, B_z, \rho E\right)^T, \tag{2.2}$$

$$F_x = \begin{pmatrix} \rho v_x \\ \rho v_x^2 + P + \left|\vec{B}\right|^2/8\pi - B_x^2/4\pi \\ \rho v_x v_y - B_x B_y/4\pi \\ \rho v_x v_z - B_x B_z/4\pi \\ 0 \\ v_x B_y - v_y B_x \\ -v_z B_x + v_x B_z \\ (\rho E + P + \left|\vec{B}\right|^2/8\pi) v_x - B_x(\vec{B}\cdot\vec{v})/4\pi \end{pmatrix}, \text{and} \tag{2.3}$$

$$S = \left(0, \rho g_x, \rho g_y, \rho g_z, 0, 0, 0, \rho\vec{g}\cdot\vec{v}\right)^T. \tag{2.4}$$

2.2.2 Sink particles

The simulation introduces sink particles to follow star formation activity for regions above the density threshold ($\rho_{\rm sink}$), following the criteria detailed in Federrath et al. (2010). The criteria include a local gravitational potential minimum, negative velocity divergence, negative eigenvalues of the velocity gradient tensor, and negative total energy within the sink radius. The last condition ensures that the gas is gravitationally bound. The sink radius is $r_{\rm sink} = 4\Delta x$ (Krumholz et al., 2004), where Δx is the highest grid resolution.

The sink particles interact with the surrounding gas through accretion and gravity. For the i-th sink particle, the amount of mass accreted in each timestep (Δt) can be estimated as,

$$\dot{M}\Delta t = \int_{|\vec{r}-\vec{r}_i|<r_{\rm sink}} \Delta\rho(\vec{r})\, dV, \tag{2.5}$$

where, $\Delta\rho(\vec{r}) = \max\left[\rho(\vec{r}) - \rho_{\rm sink}, 0\right]$. The $\dot{M}$, $\vec{r}$, and dV denote the mass accretion rate, position vector, and volume element, respectively. The mass accretion of the sink particles also results in changes in their momentum by an amount of

$$\int_{|\vec{r}-\vec{r}_i|<r_{\rm sink}} \Delta\rho(\vec{r})\vec{v}(\vec{r})\, dV, \tag{2.6}$$

in the timestep Δt for the i-th particle.

The equation for the gravitational force acting on the i-th sink particle is

$$\vec{g}_i = \vec{g}_{{\rm gas},i} + \sum_{j\neq i} \vec{g}_{{\rm sink},j}(r_i), \tag{2.7}$$

where the first term represents the gravitational force from the gas, and the second term accounts for the gravitational forces exerted by all other sink particles on the i-th sink particle.

2.3 Tools and techniques

This section provides a brief overview of the tools and techniques utilized in this thesis. These include molecular line data analysis, determination of $N(H_2)$ and the dust temperature (T_d), detection of filaments, cores, and clumps, their mass estimation, and identification of YSOs. Results obtained through these methods are important for addressing the objectives of this work. A detailed description of these tools and techniques is provided in the respective chapters.

2.3.1 Analysis of molecular line data

Molecular line data are obtained using mm/sub-mm telescopes. The spectrometers in the backend provide intensities (I) at different frequency channels, which are then converted to velocity using the rest frequency of the line (Roelfsema, 1989). Therefore, the observations produce a data cube, i.e., $I(x, y, v)$, where x

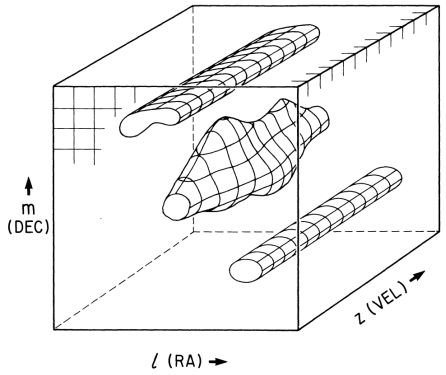

Figure 2.1: A shematic diagram showing structure of a data cube (Roelfsema, 1989). RA-DEC is plane of the sky and VEL is the velocity axis.

and y are the two spatial dimensions representing the sky coordinates, and the third dimension, v corresponds to the line-of-sight velocity[1]. The structure of

[1]This velocity is relative to Local Standard of Rest (LSR)

a data cube is shown using a schematic diagram in Figure 2.1. The integrated intensity (moment-0) map, which is defined as $\mathrm{M}_0(x,y) = \int I(x,y,v)\,dv$, shows the molecular gas distribution. The intensity-weighted velocity map (moment-1) map, $\mathrm{M}_1(x,y) = \int v\,I(x,y,v)\,dv/\mathrm{M}_0(x,y)$ provides information of overall gas velocity. The intensity-weighted velocity variance (moment-2) map is calculated as $\mathrm{M}_2(x,y) = \int(v - \mathrm{M}_1(x,y))^2\,I(x,y,v)\,dv/\mathrm{M}_0(x,y)$. The FWHM line-width map is related to the $\mathrm{M}_2(x,y)$ map as, $\mathrm{FWHM}(x,y) = \sqrt{8\ln 2\,\mathrm{M}_2(x,y)}$. The moment maps utilized in this thesis are produced using the Python package `SpectralCube`[2]. This package also generates the peak intensity map along with the corresponding velocity.

From a molecular line data, we can estimated the column density of that molecule using equation form Mangum & Shirley (2015),

$$N = \frac{3h}{8\pi^3\mu_{\rm dm}^2 S}\frac{Q_{\rm rot}}{g_J}\frac{\exp\left(\frac{E_{\rm up}}{kT_{\rm ex}}\right)}{\exp\left(\frac{h\nu}{kT_{\rm ex}}\right)-1} \times\frac{1}{J(T_{\rm ex})-J(T_{\rm bg})}\frac{\tau}{1-\exp(-\tau)}\int I\,dv, \tag{2.8}$$

where, $T_{\rm ex}$ and $T_{\rm bg}$ stand for the excitation temperature related to our target source and the cosmic microwave background temperature, respectively. I represents intensity/the main beam temperature of the line emission. $J(T)$ is the Rayleigh-Jeans equivalent temperature, which is defined as $(h\nu/k)/(\exp(h\nu/kT)-1)$. The energy of the upper state, its degeneracy, and the line strength are denoted with $E_{\rm up}$, $g_{\rm J}$, and S, respectively. $Q_{\rm rot}$, $\mu_{\rm dm}$, and τ are the rotational partition function, dipole moment, and optical depth, respectively. Now, the knowledge of $T_{\rm ex}$, τ, and other parameters allows the determination of N. We have produced the $N(^{13}\mathrm{CO})$ map using $^{13}\mathrm{CO}/\mathrm{C}^{18}\mathrm{O}(J=2\text{–}1)$ data in Chapter 5, where more details are provided.

[2] https://spectral-cube.readthedocs.io/en/latest/moments.html

2.3.2 Use of *hires* to produce $N(\mathrm{H_2})$ and T_d maps

The multi-wavelength *Herschel* images allow the computation of $N(\mathrm{H_2})$ and T_d maps. A pixel-by-pixel spectral energy distribution (SED) fitting with a modified blackbody spectra provides the desired physical parameters (i.e., $N(\mathrm{H_2})$ and T_d) at each pixel. With the assumption of optically thin thermal emission the modified blackbody spectra can be expressed as (Men'shchikov, 2021),

$$I_\nu = B_\nu(T_\mathrm{d})\, N(\mathrm{H_2})\, \kappa_\nu\, \eta\, \mu\, m_\mathrm{H}, \tag{2.9}$$

where, I_ν is the observed flux density, B_ν is the Planck function. The dust absorption coefficient can be parameterized as $\kappa_\nu = \kappa_0\,(\nu/\nu_0)^\beta$ with $\beta = 2$, $\lambda_0 = 300\,\mu$m, and $\kappa_0 = 9.31\,\mathrm{cm^2 g^{-1}}$ (Men'shchikov, 2021). Dust-to-gas mass ratio, η is 0.01 (Weingartner & Draine, 2001a). The mean molecular weight per $\mathrm{H_2}$ molecule, $\mu = 2.8$ (Kauffmann et al., 2008) and m_H is the hydrogen mass. Before the SED fitting, the *Herschel* images must be converted to identical units (Jy pixel^{-1}), as well as to the same pixel scale and resolution. Unit conversion is essential because the *Herschel* 250, 350, and 500 μm data are calibrated in MJy sr^{-1}.

Hereafter, $N(\mathrm{H_2})$ and T_d are referred to as N and T, respectively, in this section for simplicity. $\{N|T\}_{\{2|3|4\}}$ can be derived by fitting of two (i.e., 160 and 250 μm), three (i.e., 160–350 μm), and four (i.e., 160–500 μm) *Herschel* images at resolutions, $\Theta_{\{2|3|4\}} \sim 18''$, $25''$, and $37''$, respectively. The *Herschel* 70 μm image is excluded from SED fitting because it typically tends to be too noisy and is often contaminated by PAH emission or UV-heated dust emission. Interestingly, achieving high-resolution $\{N|T\}$ maps comes at the cost of reduced image accuracy, as fewer *Herschel* images are used in the fitting process. In this context, Palmeirim et al. (2013) provided a simple concept to produce reliable high resolution ($\Theta_\mathrm{P} \sim 18''$) column density map by using lower-resolution images of higher accuracy together with higher-resolution images of lower accuracy. The

method is also applicable for producing reliable high resolution dust temperature map, and mathematically can be expressed as,

$$\{N|T\}_{\Theta_{\rm P}} = \{N|T\}_4 + \delta\{N|T\}_3 + \delta\{N|T\}_2, \tag{2.10}$$

where, the last two terms (i.e., $\delta\{N|T\}_{\{2|3\}}$) add the higher-resolution informations to $\{N|T\}_4$ and are derive by the method of unsharp masking,

$$\delta\{N|T\}_{\{2|3\}} = \{N|T\}_{\{2|3\}} - \mathcal{G}_{\{3|4\}} * \{N|T\}_{\{2|3\}}, \tag{2.11}$$

where $\mathcal{G}_{\{3|4\}}$ are the Gaussian kernels to convolve $\{N|T\}_{\{2|3\}}$ to the next lower resolutions, i.e., $\Theta_{\{3|4\}}$, respectively. Now, *hires* uses $\{T\}_{\{2|3|4\}}$ produced by the above-mentioned method and *Herschel* images (I_ν) with the resolutions $\Theta_\lambda \sim 6''-37''$ to create several column density maps as,

$$N_{\Theta_\lambda\{2|3|4\}} = \frac{I_\nu}{B_\nu(T_{\{2|3|4\}})\,\kappa_\nu \eta\mu m_{\rm H}}, \tag{2.12}$$

following Equation (2.9). Then the high-resolution column density image is computed as

$$N_{\Theta_{\rm H}} = N_{\Theta 4} + \sum_{\lambda=\lambda_{\rm H}}^{500} \max\left(\delta N_{\Theta_\lambda 2}, \delta N_{\Theta_\lambda 3}, \delta N_{\Theta_\lambda 4}\right), \tag{2.13}$$

where $\Theta_{\rm H}$ is the desired angular resolution and equal to the resolution of the *Herschel* image $I_{\lambda_{\rm H}}$. Corresponding high-resolution dust temperature maps are computed inverting the Planck function,

$$T_{\Theta_{\rm H}} = B_{\nu_{\rm H}}^{-1}\left(\frac{I_{\nu_{\rm H}}}{N_{\Theta_{\rm H}}\kappa_{\nu_{\rm H}}\eta\mu m_{\rm H}}\right), \tag{2.14}$$

where $\nu_{\rm H} = c/\lambda_{\rm H}$ and c is the speed of light in free space. Figure 2.2 displays the *Herschel* column density maps of Cygnus X, produced with *hires*, at two distinct resolutions. We have utilized *hires* in Chapters 5 and 4 to generate $N(\rm H_2)$ and $T_{\rm d}$ maps.

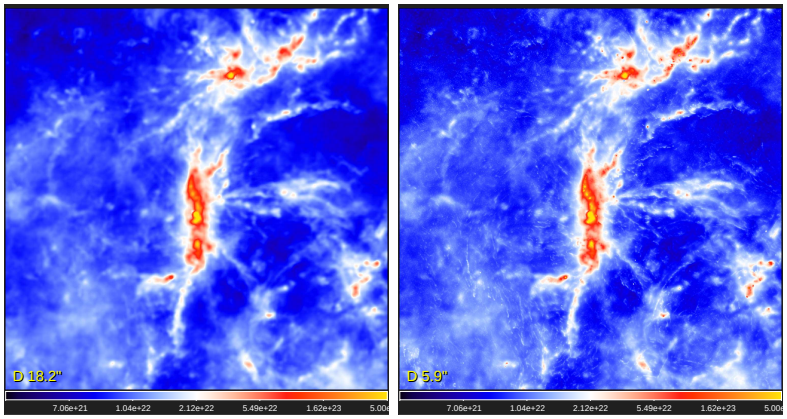

Figure 2.2: The left and right panels show *hires*-generated $N(H_2)$ maps of Cygnus X at $\Theta_H \sim 18''$ and $6''$, respectively (from Men'shchikov, 2021).

2.3.3 Detection of filaments and cores using *getsf*

Filaments play a significant role in star formation. However, reliable detection of filaments (i.e., their skeletons) from astronomical images is extremely challenging. In this context, visual inspection of filaments is inherently biased by the observer. Therefore, filament identification algorithms, such as *DisPerSE* (Sousbie, 2011), *filfinder* (Koch & Rosolowsky, 2015), and *getsf* (Men'shchikov, 2021) offer unbiased alternatives. Interestingly, *Herschel* images demonstrate the physical association of the sources/cores and filaments. However, *DisPerSE* and *filfinder* do not account for sources while detecting filaments. Therefore, we utilized the newly developed *getsf*, which simultaneously detects sources and filaments. The *getsf* requires four input parameters: the distance of the source, the angular resolution of the image, and the maximum sizes of the filaments and sources. The maximum sizes of the filaments and cores are estimated by placing circular regions that cover the width of the largest filament and core using DS9[3]. First, *getsf* spatially decomposes the image using successive unsharp masking.

[3] https://sites.google.com/cfa.harvard.edu/saoimageds9

Maximum sizes of the filaments and sources are required to set a cutoff during successive unsharp masking to prevent decomposition to a very large scale. The decomposed images are then broken down into their structural components, distinguishing sources and filaments and isolating them from each other and their backgrounds. The sources and filaments are separated based on their elongations. The *getsf* catalogs provide important information about the filaments, such as the coordinates of their skeletons, lengths, and position angles. Interestingly, *getsf* can deblend overlapping sources and provide the position, size, and total flux of the deblended sources. Additional information about this algorithm is available in Men'shchikov (2021).

2.3.4 Detection of clumps using *clumpfind* and *astrodendro*

The IDL-based algorithm *clumpfind* is used to detect clumps. This algorithm is applicable to both 2D and 3D (position-position-velocity) data. A schematic diagram illustrating how *clumpfind* works is provided in Figure 2.3. The algorithm starts by contouring the data at multiples of the root mean square (RMS) noise, then identifies peaks of emission (labeled A, B, C, and D in Figure 2.3). These peak emissions correspond to the clump locations, and the algorithm subsequently traces them down to lower intensities to determine their boundaries. The rejection criteria for the data are defined by the input parameter, which is the lowest contour level. We utilized *clumpfind* in Chapter 4. However, it is important to note that *clumpfind* is a single-scale algorithm that does not trace hierarchical density structures.

To detect the hierarchical density structures, we performed dendrogram analysis using the Python-based tool *astrodendro*[4]. The basic idea behind the dendrogram analysis was presented in the studies of Houlahan & Scalo (1992) and

[4] https://dendrograms.readthedocs.io/en/stable/index.html

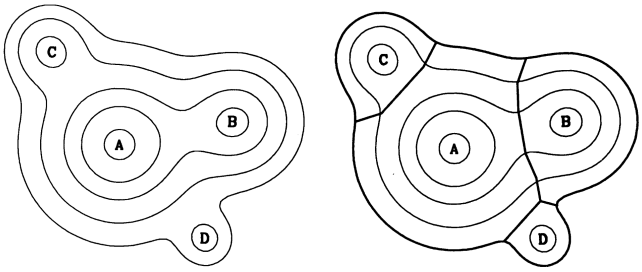

Figure 2.3: Left: A contour map. A, B, C, and D are peaks of emission. Right: Clumps identified in *clumpfind* for the contour map shown in the left panel (Williams et al., 1994).

Rosolowsky et al. (2008). Burkhart et al. (2013) described the dendrogram technique in simple words as "an underwater mountain chain." The *astrodendro* can be applied to astronomical 2D images as well as 3D data cubes (Rosolowsky et al., 2008; Goodman et al., 2009; Burkhart et al., 2013). For 2D images, *astrodendro* requires three input parameters: 1. `min_value`, the minimum flux density for pixels to be included in a structure, 2. `min_delta`, the minimum peak density difference required between two potential structures to consider them separate entities, and 3. `min_npix`, the minimum number of pixels necessary to form the smallest possible structure. The physical interpretation of these input parameters is illustrated in Figure 2.4. Based on the inputs, *astrodendro* provides a hierarchical tree structure composed of branches and leaves. Branches, which are larger and fainter structures, are positioned lower in the tree and can break down into new branches and leaves. Leaves are small, bright structures at the tips of the tree that do not subdivide. The *astrodendro* is utilized in Chapter 5 to detect the hierarchical density structures from ATLASGAL and ALMA dust continuum maps.

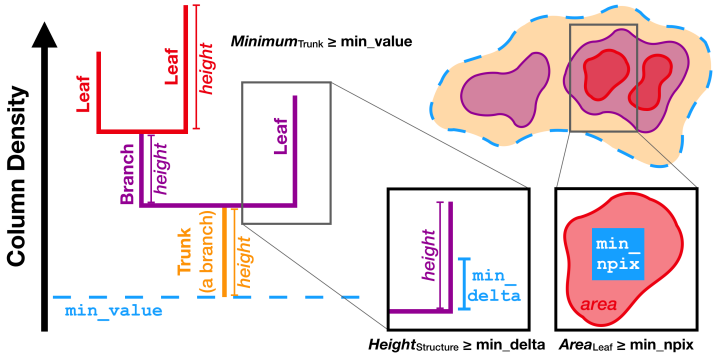

Figure 2.4: A schematic diagram showing how the criteria (i.e., `min_value`, `min_delta`, and `min_npix`) are used in the computation of a dendrogram tree in *astrodendro* (from Chen et al., 2019).

2.3.5 Estimation of mass

Mass is one of the fundamental physical parameters for all the structural components of a molecular cloud. It can be calculated from the dust continuum emission or derived from the $N(\mathrm{H_2})$ map.

2.3.5.1 Using dust continuum emission

The mass of clump/core can be estimated based on their dust continuum emission at frequency ν using the formula from Hildebrand (1983),

$$M = \frac{S_\nu \; d^2 \; R_t}{B_{(\nu,T_\mathrm{d})} \; k_\nu}, \tag{2.15}$$

where S_ν, T_d, and d are total flux density, dust temperature, and distance of the clump/core, respectively. $B_{(\nu,T_\mathrm{d})}$, R_t, and k_ν are Planck function, gas-to-dust mass ratio, and dust absorption coefficient, respectively.

2.3.5.2 Using $N(H_2)$ map

Once the $N(H_2)$ map is available the mass of any structure, such as clump/core/filament can be estimated using,

$$M = \mu_{H_2}\, m_H\, \mathrm{Area}_{\mathrm{pixel}}\, \Sigma N(H_2). \tag{2.16}$$

Here, m_H is the mass of a hydrogen atom, μ_{H_2} is the mean molecular weight, $\mathrm{Area}_{\mathrm{pixel}}$ is the area subtended by one pixel, and $\Sigma N(H_2)$ is the total column density for the structure of interest.

2.3.6 Dectection of YSOs

The star-forming activity can be inferred from the detection of YSOs. Their envelopes and dusty circumstellar disks result in IR excess (Povich et al., 2011; Sharma et al., 2017). In this thesis, we have utilized NIR photometric data from VVV, UKIDSS-GPS, 2MASS, and GLIMPSE for point-like sources to detect YSOs in our regions of interest. YSOs can be distinguished from other sources in the color-color diagram (CCD) and color-magnitude diagram (CMD) because of their IR excess (Hartmann et al., 2005; Getman et al., 2007; Lucas et al., 2008; Gutermuth et al., 2009). Our analysis for detecting YSOs involves the examination of the CCD (i.e., [4.5]–[5.8] vs. [3.6]–[4.5]) and the dereddened CCD (i.e., $[[3.6]-[4.5]]_0$ vs. $[K-[3.6]]_0$). Additionally, we examined the $H-K$ vs. K CMD to identify potential YSO candidates.

2.3.7 Related to the simulation data

- The $N(H_2)$ in the x-y plane can be estimated as,

$$N(H_2) = \frac{\Delta z}{\mu m_H} \sum_{k=1}^{N_z} \rho(k), \tag{2.17}$$

where Δz is the pixel or grid size in the z-direction. N_z is the number of pixels summed over the z-direction. All other symbols are as previously defined. Similarly, $N(H_2)$ maps in the y-z and z-x planes can also be calculated.

- The mass-weighted average value for any physical quantity (say, ψ) is defined as,

$$< \psi >= \frac{\sum_{k=1}^{N} \rho\psi}{\sum_{k=1}^{N} \rho}, \tag{2.18}$$

where N is the number of pixels of interest.

Chapter 3

Unraveling the observational signatures of cloud-cloud collision and hub-filament systems in W31[†]

3.1 Introduction

As discussed in Section 1, massive O-type stars play a crucial role in shaping galaxy structure and influencing the formation of the next generation of stars. However, their formation process is not fully understood (Zinnecker & Yorke, 2007). To explore the potential formation mechanisms of massive O-type stars, this chapter examines the W31 complex, which hosts two extended H II regions: G10.3-0.15 (hereafter, W31-N) and G10.15-0.34 (hereafter, W31-S) (Wood & Churchwell, 1989; Kim & Koo, 2001).

[†]**A. K. Maity**, L. K. Dewangan, H. Sano, K. Tachihara, Y. Fukui, N. K. Bhadari, 2022, *The Astrophysical Journal*, Volume 934, Issue 1, https://doi.org/10.3847/1538-4357/ac7872

The W31-N H II region, associated with the MIR bubble CN 148, is excited by O-type stars (Bik et al., 2005; Dewangan et al., 2015). The location of one such exciting O-type star is highlighted in the top-left panel of Figure 1 in Beuther et al. (2011). Meanwhile, the W31-S H II region emits more than 10^{50} Lyman continuum photons per second, indicating the presence of multiple O-type stars (Blum et al., 2001). Also, it is one of the largest H II regions in our galaxy. Despite numerous studies, no existing work, to our knowledge, has successfully explained the birth of O-type stars in W31. Therefore, this chapter aims to uncover the physical processes driving the formation of these massive stars.

In this context, a thorough and detailed study of dust continuum emission and the distribution of molecular gas is essential. Therefore, multi-wavelength data have been carefully examined for W31 (see Table 3.1). Specifically, to investigate the molecular gas, we analyzed new ^{12}CO(J = 1–0) line data from the NANTEN2 telescope, along with publicly available ^{13}CO(J = 2–1) line data from the SEDIGISM (Schuller et al., 2017a) survey. Various distance estimates for W31 have been reported in the literature, including 3.4 kpc (Blum et al., 2001), 6 kpc (Wilson, 1974; Downes et al., 1980), and 14.5 kpc (Corbel et al., 1997). In this study, we adopt a distance of 3.55 kpc for W31-N and W31-S, based on the measured distances of the ATLASGAL dust clumps associated with W31 (see Section 3.3.1).

Section 3.2 describes the observational data sets analyzed in this study. The key findings are presented in Section 3.3, which are thoroughly discussed in Section 3.4. Finally, Section 3.5 provides a summary of this chapter.

3.2 Data sets

3.2.1 New molecular line data: NANTEN2 ^{12}CO(J = 1–0)

Observations of ^{12}CO(J = 1–0) line emission at 115.27 GHz were conducted in 2012 December and 2013 January using the NANTEN2 millimeter (mm)/submm radio telescope of Nagoya University installed at an altitude of 4865 m in the Atacama Desert in Chile. We mapped an area of $0.^{\circ}7 \times 0.^{\circ}7$ centered at W31 using on-the-fly mapping mode with Nyquist sampling. The front end was a double-sideband heterodyne receiver equipped with a 4 K-cooled Nb superconductor-insulator-superconductor mixer. The back end was a digital Fourier-transform spectrometer with a bandwidth of 1 GHz and a channel spacing of 61 kHz, corresponding to a velocity coverage of ∼2600 km s^{-1} and a velocity resolution of ∼0.16 km s^{-1} at 115 GHz. The typical system temperature was ∼190–240 K in the DSB, including the atmosphere. After convolution with a two-dimensional Gaussian function of 90″ (FWHM), we obtained a data cube with a beam size of ∼180″ (FWHM). The absolute intensity was calibrated by observing Orion-KL [$\alpha_{2000} = 05^h35^m14.^s48$; $\delta_{2000} = -05^{\circ}22'27.''55$] and Infrared Astronomical Satellite (IRAS) 16239-2422 [$\alpha_{2000} = 16^h32^m23.^s3$; $\delta_{2000} = -24^{\circ}28'39.''2$] (Ridge et al., 2006). The pointing accuracy was checked every two hours to achieve an offset within 2″, verified by observing IRC+10216 and the edge of the Sun. The typical noise fluctuation is ∼1.0 K at the velocity resolution of 0.16 km s^{-1}.

3.2.2 Archive data sets

In this study, we analyzed multiple data sets sourced from various publicly available surveys, as listed in Table 3.1. The *Herschel* dust temperature and column

density maps (with a resolution of ∼12″) were obtained from Marsh et al. (2017). These maps were generated using the PPMAP algorithm (Marsh et al., 2015, 2017) applied to *Herschel* FIR images. The velocity and distance of the ATLASGAL clumps in our selected target region were obtained from Urquhart et al. (2018). The properties of the ATLASGAL clumps linked to the ^{13}CO outflows were taken from Yang et al. (2022). We have applied Gaussian smoothing with a width of 3 pixels (∼28.″5) to the SEDIGISM ^{13}CO(J = 2–1) line data, resulting in a final angular resolution of $\sqrt{30^2 + 28.5^2} \approx 41.''4$. We obtained the photometric magnitudes of point-like sources at 3.6, 4.5, and 5.8 μm from the highly reliable GLIMPSE-I Spring ′07 photometric catalog to identify protostars in this study.

Table 3.1: List of archive data sets utilized in this work.

Survey	Wavelength/Frequency/line(s)	Resolution (″)	Reference
NRAO VLA Sky Survey (NVSS)	1.4 GHz	∼45	Condon et al. (1998)
SEDIGISM	^{13}CO(J = 2–1)	∼30	Schuller et al. (2017a)
ATLASGAL	870 μm	∼19	Schuller et al. (2009)
Herschel Infrared Galactic Plane Survey (Hi-GAL)	250, 350, 500 μm	∼18, 25, 37	Molinari et al. (2010b)
Spitzer Galactic Legacy Infrared Mid-Plane Survey Extraordinaire (GLIMPSE)	3.6, 4.5, 5.8 μm	∼2	Benjamin et al. (2003)

3.3 Results

3.3.1 Dust clumps, ionized regions, and embedded protostars in W31

To infer the distribution of ionized gas and thermal dust emission, we have created a three-color composite map using NVSS 1.4 GHz (red), *Herschel* 500 μm (green), and 350 μm (blue) images (see Figures 3.1a and 3.1b). The *Herschel* images show extended structures of dust emission toward W31-N and W31-S,

and each extended structure surrounds the ionized gas detected in the NVSS 1.4 GHz radio continuum emission. Figure 3.1a is overlaid with ATLASGAL 870 μm dust continuum emission contour (in yellow) and the positions of 49 ATLASGAL clumps. These clumps, spanning a velocity range of [8.9, 15.3] km s^{-1}, are situated at a distance of 3.55 kpc (Urquhart et al., 2018). The spatial distribution of ATLASGAL clumps suggests a single, extended physical system encompassing both W31-N and W31-S. The southern region contains a higher concentration of ATLASGAL clumps compared to the northern region. Out of the 49 identified clumps, 25 are associated with molecular outflows (marked by asterisks in Figure 3.1a). Yang et al. (2022) provided the velocity ranges for the ^{13}CO(J = 2–1) blue wing-like and red wing-like components corresponding to these outflow-associated clumps. In this connection, we find 9 and 16 clumps associated with outflows toward W31-N and W31-S, respectively. In general, the detection of a molecular outflow is known as a reliable signature of star formation activity. Hence, ongoing star-forming activities are traced in both regions, W31-N and W31-S.

The detection of embedded protostars or YSOs serves as key indicators of star-forming activity. Typically, YSOs can be identified based on their IR color-excess, which arises from dusty circumstellar disks and envelopes. To locate the young protostars toward W31, we identified Class I YSOs based on the color criteria $[4.5] - [5.8] \geq 0.7$ and $[3.6] - [4.5] \geq 0.7$ using *Spitzer* 3.6–5.8 μm photometric data of point-like sources (see Hartmann et al., 2005; Getman et al., 2007, for more details). Previous study by Evans et al. (2009) estimated the mean age of Class I YSOs to be about 0.44 Myr. In Figure 3.1b, the identified Class I YSOs are overlaid on the color composite image, highlighting the presence of protostars in both W31-N and W31-S. Notably, relatively more number of Class I YSOs are detected in W31-N compared to W31-S.

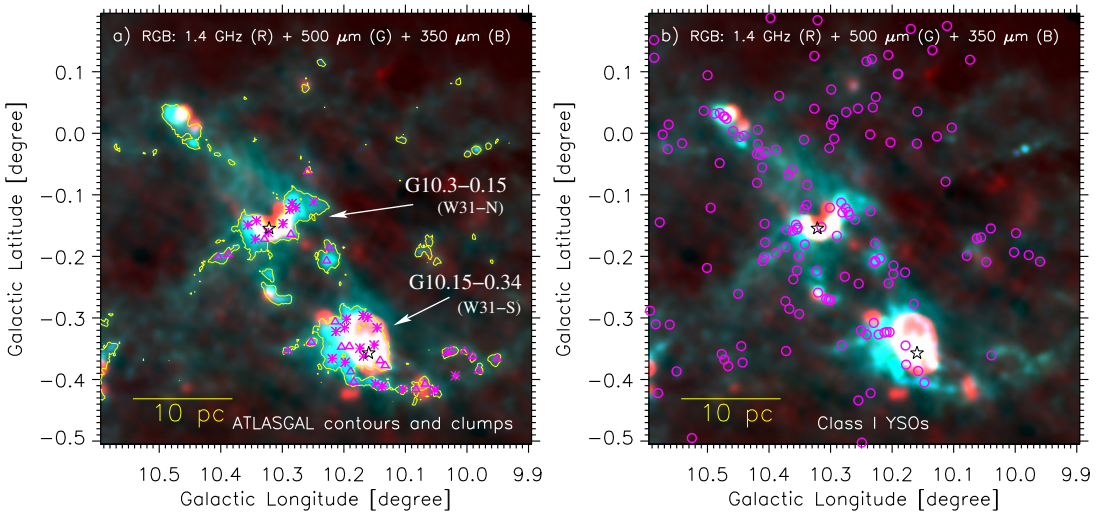

Figure 3.1: A multi-wavelength view of an area hosting the W31 complex (size ∼0.°7 × 0.°695; centered at l = 10.°247; b = −0.°156). a) Overlay of the positions of the ATLASGAL clumps (see triangles and asterisks; Urquhart et al., 2018) and the ATLASGAL 870 μm continuum emission contour (at the level of 0.25 Jy beam^{-1}) on a three-color composite map. The color composite map is made of the NVSS 1.4 GHz (red), *Herschel* 500 μm (green), and 350 μm (blue) images. The asterisk symbols highlight the ATLASGAL clumps associated with molecular outflows. Two sites, G10.3−0.15 (or W31-N) and G10.15−0.34 (or W31-S), are indicated in the color composite map. b) Overlay of the positions of Class I YSOs (see circles) on the three-color composite map. In each panel, stars indicate the NVSS radio continuum peaks. A scale bar corresponding to 10 pc (at d = 3.55 kpc) is shown in each panel.

In Figure 3.1a, the *Herschel* and ATLASGAL dust continuum maps indicate the presence of elongated filamentary structures in W31-N and W31-S. These structures exhibit higher $N(\mathrm{H_2})$ values in the *Herschel* column density map shown in Figure 3.2a, ranging from ∼10^{22} to 10^{23} cm^{-2}. In Figure 3.2b, the *Herschel* dust temperature map is presented, and the site W31-S is found to be prominently extended compared to the site W31-N. Both the H II regions are seen with the warm dust emission (i.e., $T_{\rm d}$ ∼21–32 K), while the elongated filamentary features seem to be associated with the relatively cold dust emission (i.e., $T_{\rm d}$ ∼17–20 K). This suggests that O-type stars contribute to heating the dust in W31-N and W31-S.

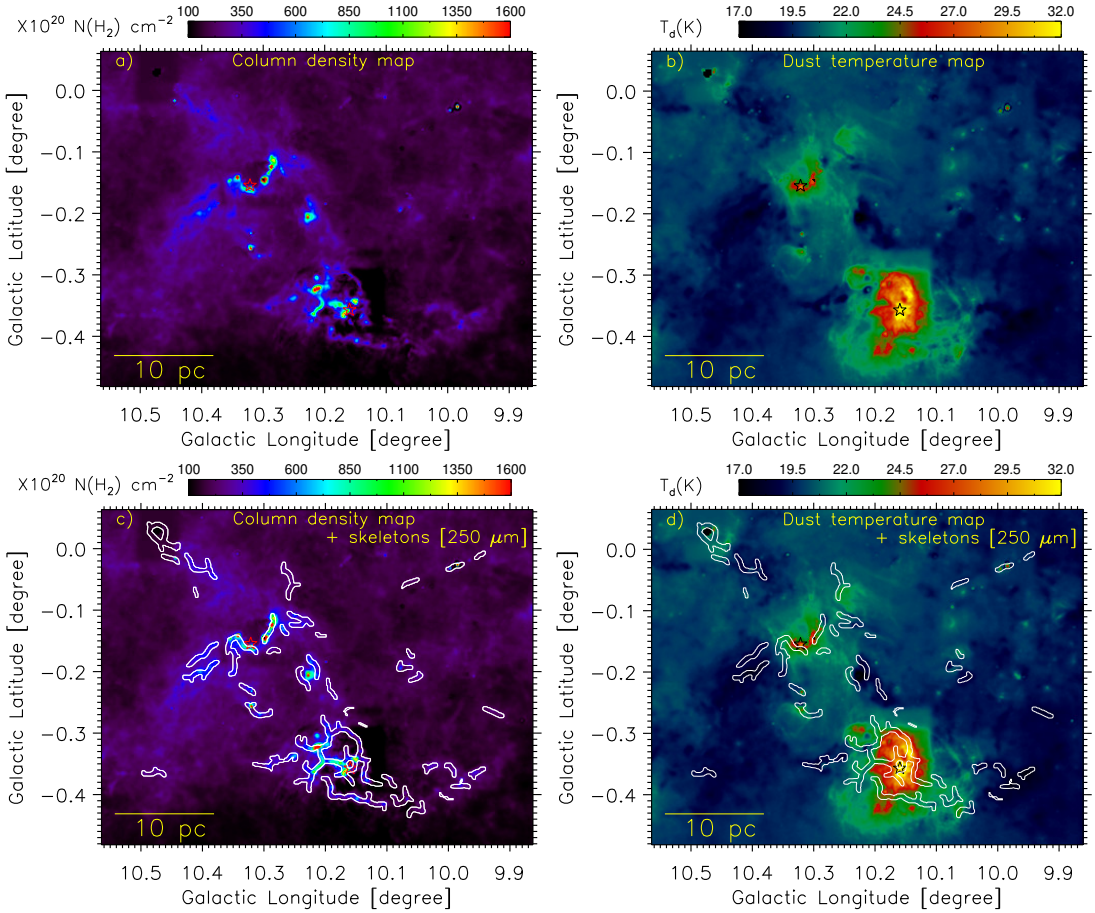

Figure 3.2: Panels (a) and (b) display *Herschel* column density (i.e., $N(\mathrm{H_2})$) and dust temperature (i.e., T_d) maps. The *getsf*-identified filament skeletons are highlighted in panels (c) and (d) over the $N(\mathrm{H_2})$ and T_d maps, respectively. These filament skeletons are detected using *getsf* over the *Herschel* 250μm image.

3.3.2 Hub-filament systems in W31

In general, identifying an HFS in a MSFR hosting multiple O-type stars is challenging due to the intense energetic feedback from these stars (i.e., stellar winds, ionized emission, and radiation pressure), which can significantly impact their surroundings. A similar scenario applies to W31, which contains several O-type stars and exhibits a complex structure, as revealed in multi-wavelength images (see Figures 3.1a and 3.2a).

To identify the filament skeletons in W31, we employed *getsf* (Men'shchikov, 2021) on the *Herschel* 250 μm image (resolution $\sim$18$''$). Details of this algorithm are provided in Section 2.3.3. In this work, the filament skeletons are extracted with maximum source size and filament width of 40$''$ and 220$''$, respectively. Several parsec-scale filaments have been identified in our target area, which are highlighted over the *Herschel* column density and dust temperature maps in Figures 3.2c and 3.2d, respectively. These filaments appear to be directed toward the W31-N and W31-S H II regions, which exhibit higher column density values and warm dust emission. Such configurations suggest the presence of HFSs associated with each H II region.

3.3.3 Distribution of molecular gas in W31

3.3.3.1 Spatial and velocity structures of molecular cloud associated with W31

We analyzed the NANTEN2 ^{12}CO(J = 1–0) and SEDIGISM ^{13}CO(J = 2–1) emissions to investigate the cloud morphology of the W31 complex. Figure 3.3a presents the moment-0 map of the NANTEN2 ^{12}CO emission for an extended area toward W31, where molecular emission is integrated for [0.16, 20.3] km s^{-1}. The moment-0 map reveals a molecular cloud extending from the north-east to the south-west, with the moment-0 peaks aligning closely with the NVSS radio emission peaks associated with W31-N and W31-S (see stars in Figure 3.3a). Figure 3.3b displays the moment-1 map of the NANTEN2 ^{12}CO emission, providing insights into the velocity distribution of the gas. A clear velocity gradient is observed across the cloud, particularly between W31-N and W31-S. The moment-2 map, shown in Figure 3.3c, highlights regions of high velocity dispersion (greater than 5 km s^{-1}) toward W31-N and W31-S. Additionally, Figure 3.3d provides a

zoomed-in view of the molecular cloud associated with W31-S (see the dashed box in Figure 3.3c). The NANTEN2 ^{12}CO line data reveal the overall distribution and kinematics of the molecular cloud associated with the W31 complex; however, they are limited by resolution. In contrast, the SEDIGISM ^{13}CO(J = 2–1) line data (beam size $\sim$41$''$.4) offer better resolution compared to the NANTEN2 molecular line data. The moment-0 map of the SEDIGISM ^{13}CO(J = 2–1) emission over the velocity range [0, 21] km s^{-1} is shown in Figure 3.3e. This map provides greater insight into the cloud morphology associated with the W31 complex, enabling a more detailed examination of the molecular structures around W31-N and W31-S. Additionally, Figure 3.3f presents the moment-1 map of the SEDIGISM ^{13}CO emission, which reveals a significant velocity gradient in the direction of W31-N and W31-S.

To investigate the velocity distribution of the molecular cloud associated with W31, we have generated several PV diagrams. Figures 3.4a, 3.4b, and 3.4c present the PV diagrams extracted from the NANTEN2 ^{12}CO(J = 1–0) line data along the arrows labeled "fn1," "fn2," and "fn3" as shown in Figure 3.3a. Each PV diagram was extracted using a slice width of 1 pixel (= 60$''$). The arrow "fn1" extends through both W31-N and W31-S, while "fn2" and "fn3" are positioned toward W31-N. Similarly, Figures 3.4d, 3.4e, and 3.4f display PV diagrams along the arrows "fs1," "fs2," and "fs3," respectively, as indicated in Figure 3.3d. In each panel of Figure 3.4, one or two arrows indicate the associated velocity gradients. The velocity gradients measured along the arrows in panels (a), (b), and (c) are [+0.53 (for A1) and −0.69 (for A2)], −0.28, and +0.40 km s^{-1}pc^{-1}, respectively. Similarly, in the last three panels (d), (e), and (f), the velocity gradient values along the arrows are estimated to be [−0.48 (A1) and −1.29 (A2)], [+0.48 (A1) and +1.54 (A2)], and [+0.45 (A1) and +1.40 (A2)] km s^{-1}pc^{-1}, respectively. Note that several ATLASGAL clumps associated with molecular

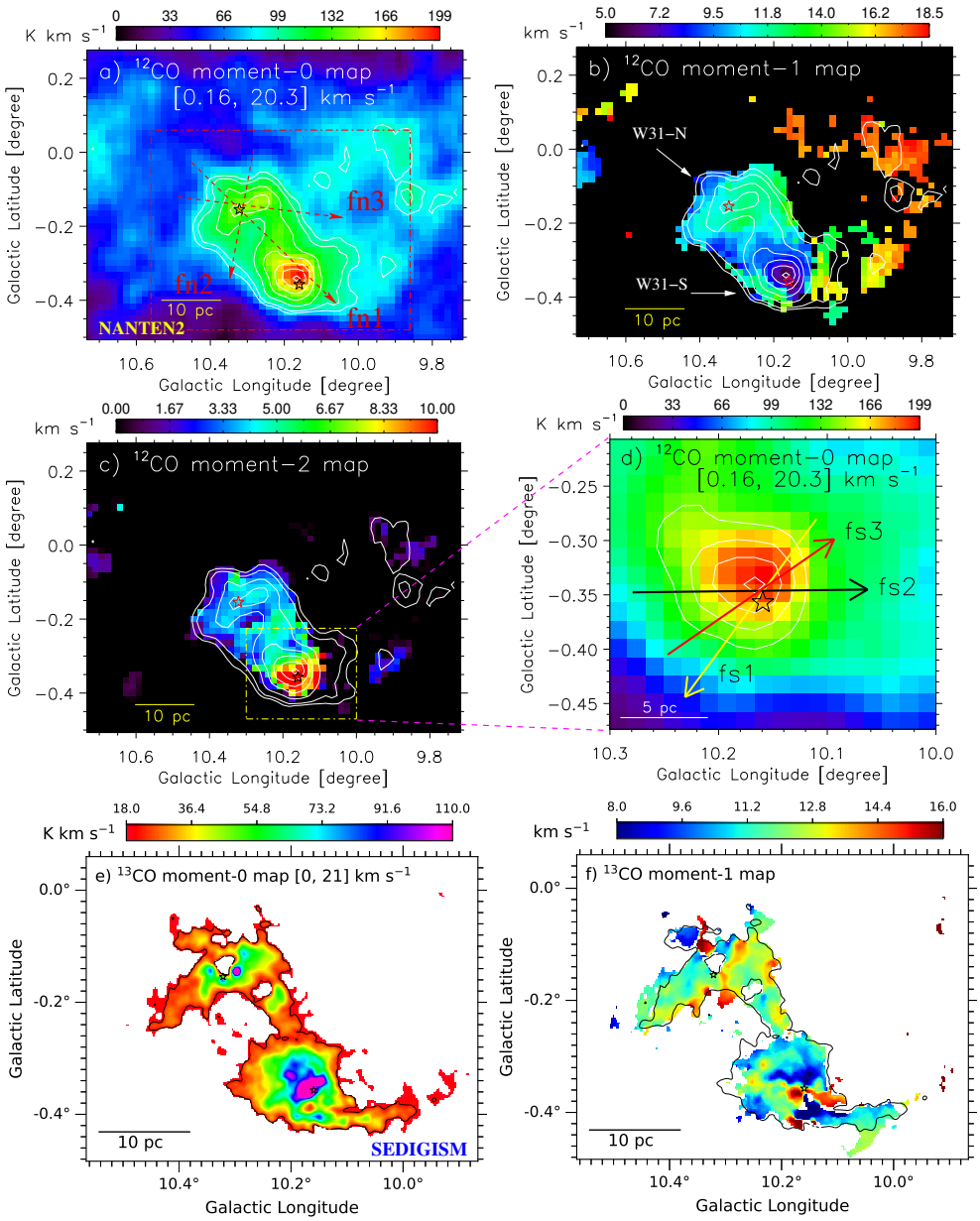

Figure 3.3: a) The NANTEN2 ^{12}CO(J = 1–0) moment-0 map (at [0.16, 20.3] km s^{-1}) of an area hosting the W31 complex. A dotted dashed box (in red) highlights the area shown in Figure 3.2a. The molecular map is also overlaid with the molecular emission (in contours). Three arrows "fn1", "fn2", and "fn3" are shown in the panel, where the PV diagrams are produced (see Figures 3.4a–3.4c). b) Overlay of the molecular emission contours on the NANTEN2 ^{12}CO moment-1 map. c) Overlay of the molecular emission contours on the NANTEN2 ^{12}CO moment-2 map. A dotted-dashed box (in yellow) represents an area presented in Figure 3.3d. In panels "a–c", the molecular integrated emission contours are shown with the levels of 45, 50, 60, 70, 80, 90, and 98% of the peak value (i.e., 198.7 K km s^{-1}). d) A zoomed-in view of the NANTEN2 moment-0 map at [0.16, 20.3] km s^{-1} toward W31-S (see a dotted dashed box in Figure 3.3c). The levels of the contours are 70, 80, 90, and 98% of the peak integrated emission value (i.e., 198.7 K km s^{-1}). Three arrows "fs1", "fs2", and "fs3" are marked in the panel, where the PV diagrams are generated (see Figures 3.4d–3.4f). e) The panel displays the SEDIGISM ^{13}CO moment-0 map at [0, 21] km s^{-1} toward the W31 complex hosting both W31-N and W31-S. The ^{13}CO emission contour at 22.0 K km s^{-1} is also overplotted on the SEDIGISM moment-0 map. f) The SEDIGISM moment-1 map of the ^{13}CO emission toward the W31 complex. The ^{13}CO data contour, as shown in Figure 3.3e, is also overplotted on the moment-1 map. In each panel, stars are the same as shown in Figure 3.1a.

outflows and young protostars are detected toward W31-N and W31-S. Hence, star-forming activities may be one of the factors to explain the observed velocity gradients. Furthermore, the observed velocity gradients could also suggest the existence of multiple velocity components. In the direction of W31-S, the NANTEN2 ^{12}CO line data hint at the presence of two velocity components and higher values of velocity dispersion. Such observed results are further investigated using the SEDIGISM ^{13}CO line data in Section 3.3.3.2. However, we do not find a clear signature of the presence of multiple velocity components toward W31-N (see also section 3.4.2).

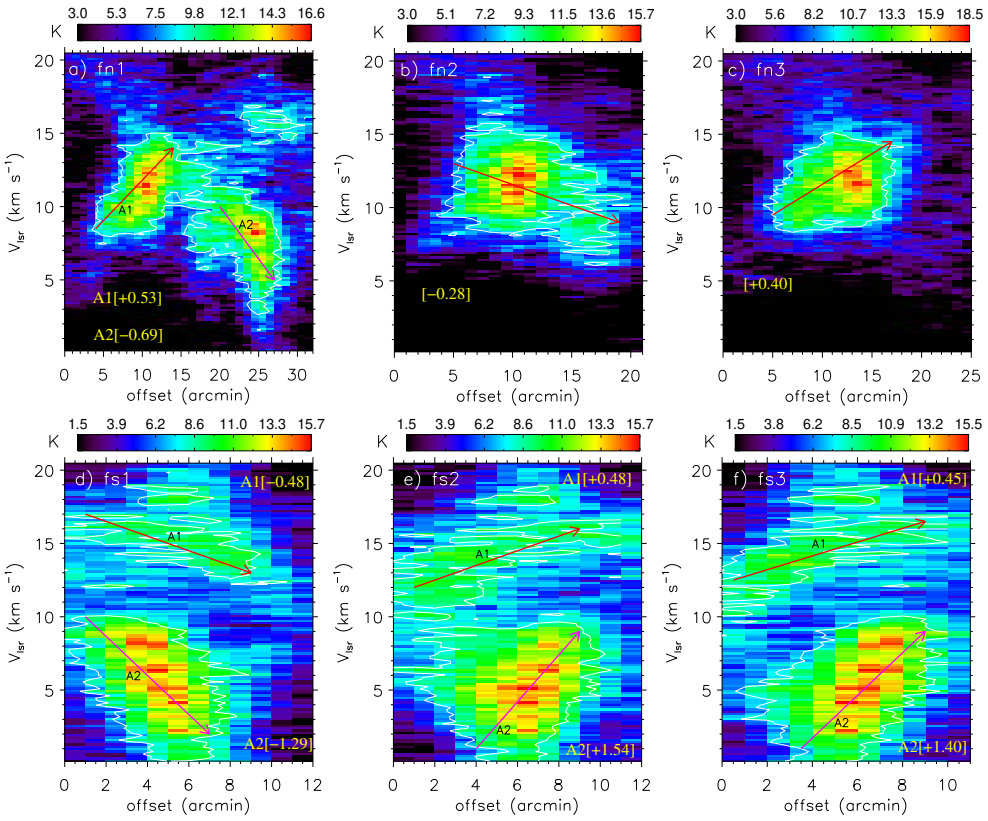

Figure 3.4: PV diagrams of NANTEN2 ^{12}CO(J = 1–0) data along arrows (a) "fn1," (b) "fn2," (c) "fn3," (d) "fs1," (e) "fs2," and (f) "fs3" (see the arrows in Figures 3.2a and 3.2d). In each panel, a contour is shown with a level of 53% of its corresponding peak value. In all panels, a velocity gradient is computed along the arrow(s), and is mentioned in the unit of km s^{-1}pc^{-1}.

3.3.3.2 Velocity components toward W31-S

Toward W31-S, Figures 3.5a, 3.5b, and 3.5c present the moment-0, moment-1, and moment-2 maps of the SEDIGISM ^{13}CO(J = 2–1) emission, respectively, for the area highlighted by the dotted-dashed box in Figure 3.3c. In the moment-0 map, the molecular emission is integrated over a velocity range of 0 to 21 km s^{-1}. The contours of the moment-0 map, along with the position of the NVSS radio continuum peak, are overlaid on all the SEDIGISM moment maps. Notably, the molecular integrated emission peak coincides with the NVSS radio peak. The moment-1 map reveals a distinct velocity gradient within the region marked by a circle in Figure 3.5b, where the NVSS radio peak is located. This map suggests the presence of two distinct velocity components, around 8 and 16 km s^{-1}, along with an intermediate component near 12 km s^{-1} in the same region. In the moment-2 map, higher velocity dispersion values (i.e., 13–16 km s^{-1}) are observed within the circled area (see Figure 3.5c), consistent with the NANTEN2 ^{12}CO moment-2 map. Interestingly, the velocity dispersion appears to gradually decrease toward the outer regions of the molecular cloud associated with W31-S.

The velocity channel maps of ^{13}CO(J = 2–1) are presented in Figure 3.6. A total of 21 panels have been generated, covering a velocity range from 0 to 21 km s^{-1}, with an integration interval of 1 km s^{-1}. The position of NVSS radio peak is marked in each panel of Figure 3.6. The channel maps appear to support the presence of two velocity components toward W31-S, particularly in the panels corresponding to [10, 11] and [14, 15] km s^{-1}. Figure 3.7a presents the ^{13}CO moment-0 map of W31-S, where ten arrows are marked (five vertical: "l1–l5" and five horizontal: "b1–b5") to indicate the positions from which PV diagrams are extracted. The width of the slices used for extracting the PV diagrams is 1 pixel (= 9.″5). Additionally, magenta hexagons overlaid on Figure 3.7a denote the positions of clumps associated with outflows (see the asterisks in Figure 3.1a). In

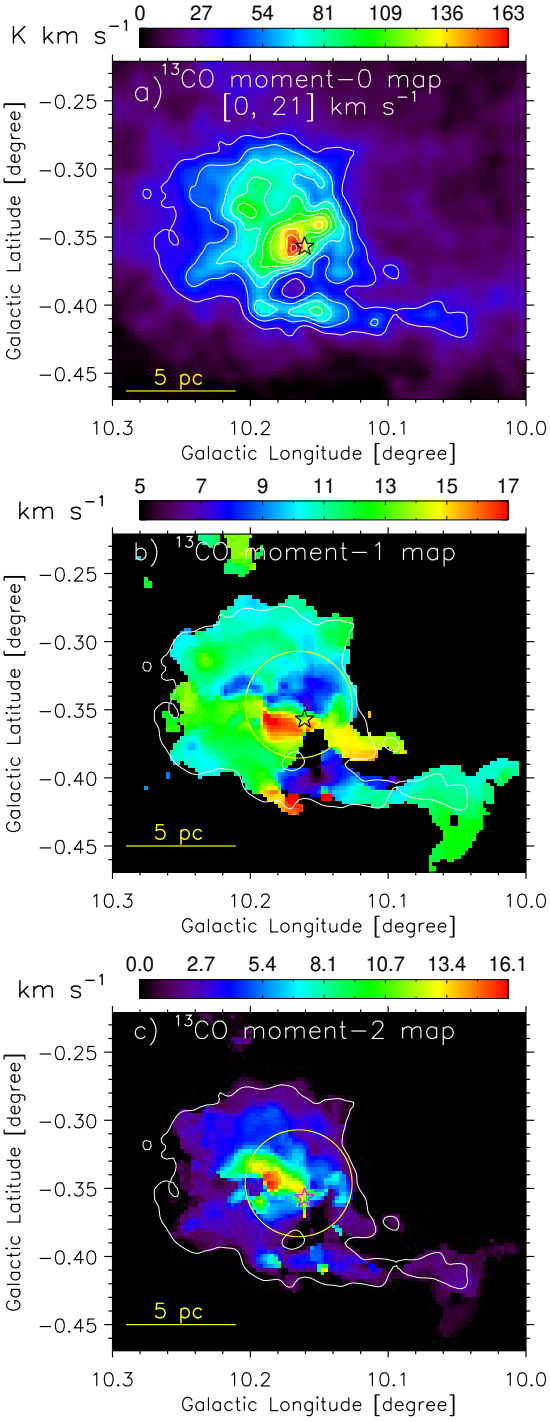

Figure 3.5: Moment maps of the SEDIGISM ^{13}CO(J = 2–1) data toward W31-S for the area highlighted by the dotted-dashed box in Figure 3.3c. (a) Moment-0 map at [0, 21] km s^{-1}. (b) Moment-1 map. (c) Moment-2 map. In each moment map, the ^{13}CO integrated emission contour is displayed at a level of 32.6 K km s^{-1}. A circle is marked in the moment-1 and moment-2 maps to highlight the region where the NVSS 1.4 GHz emission is primarily distributed toward W31-S. The star symbol remains consistent with the one shown in Figure 3.3d.

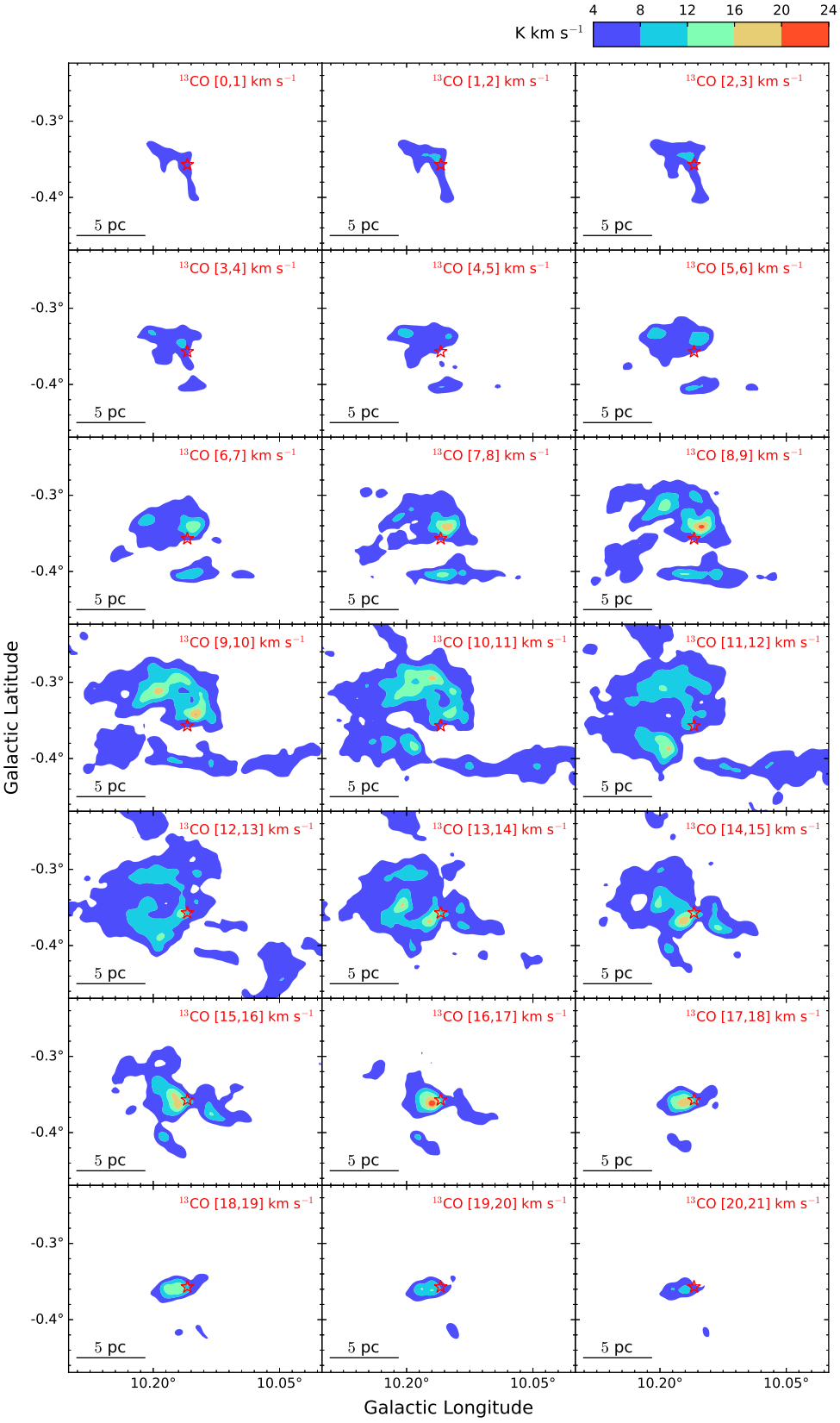

Figure 3.6: Velocity channel maps of the SEDIGISM ^{13}CO data with a velocity interval of 1 km s^{-1}, covering a range from 0 to 21 km s^{-1} toward W31-S. A color bar is shown in the top right corner. The star symbol is the same as marked in Figure 3.3d.

Figures 3.7b–3.7k, we present the PV diagrams of the ^{13}CO data along the ten marked arrows. Additionally, Figure 3.7l displays the Galactic latitude-velocity diagram for the ^{13}CO data, where the molecular emission is integrated over the longitude range of [10.°12, 10.°22]. We also examine the extents of the blue wing-like and red wing-like velocity components of a molecular outflow associated with ATLASGAL clumps in the W31-S region (see Figures 3.8a and 3.8b). Figures 3.8a and 3.8b exhibit the velocity ranges of outflow wings against Galactic latitude and longitude of each ATLASGAL clump distributed toward W31-S, respectively (see hexagons in Figure 7a). We find that the knowledge of the velocity ranges of outflow wings is useful for exploring the complex velocity structure observed in the PV diagrams (see Figures 3.7b–3.7l). In Figures 3.7c, 3.7d, 3.7e, and 3.7i, we suspect the presence of two velocity components along the directions of arrows "l2," "l3," "l4," and "b3" respectively. These arrows pass through regions with higher velocity dispersions and areas associated with radio continuum emission in W31-S. Given the locations of these arrows, Figure 3.7l is generated to examine the velocity distribution, revealing a possible connection between the two velocity components toward W31-S. No spike or outflow signature is detected in Figure 3.7l. However, in panel "i" (corresponding to arrow "b3"), both a spike (or outflow signature) and two velocity components may be present. Therefore, our analysis indicates the existence of two velocity components along with outflow signatures toward W31-S.

Based on the PV diagrams, we have produced two integrated maps of ^{13}CO for two distinct velocity ranges: [0, 11] and [12, 21] km s^{-1}. To analyze the morphology of each cloud component, the corresponding integrated intensity maps and contours are presented in Figures 3.8c and 3.8d, respectively. Figure 3.8e displays a two-color composite image, where the ^{13}CO maps at [0, 11] and [12, 21] km s^{-1} are shown in cyan and red, respectively, overlaid with NVSS radio

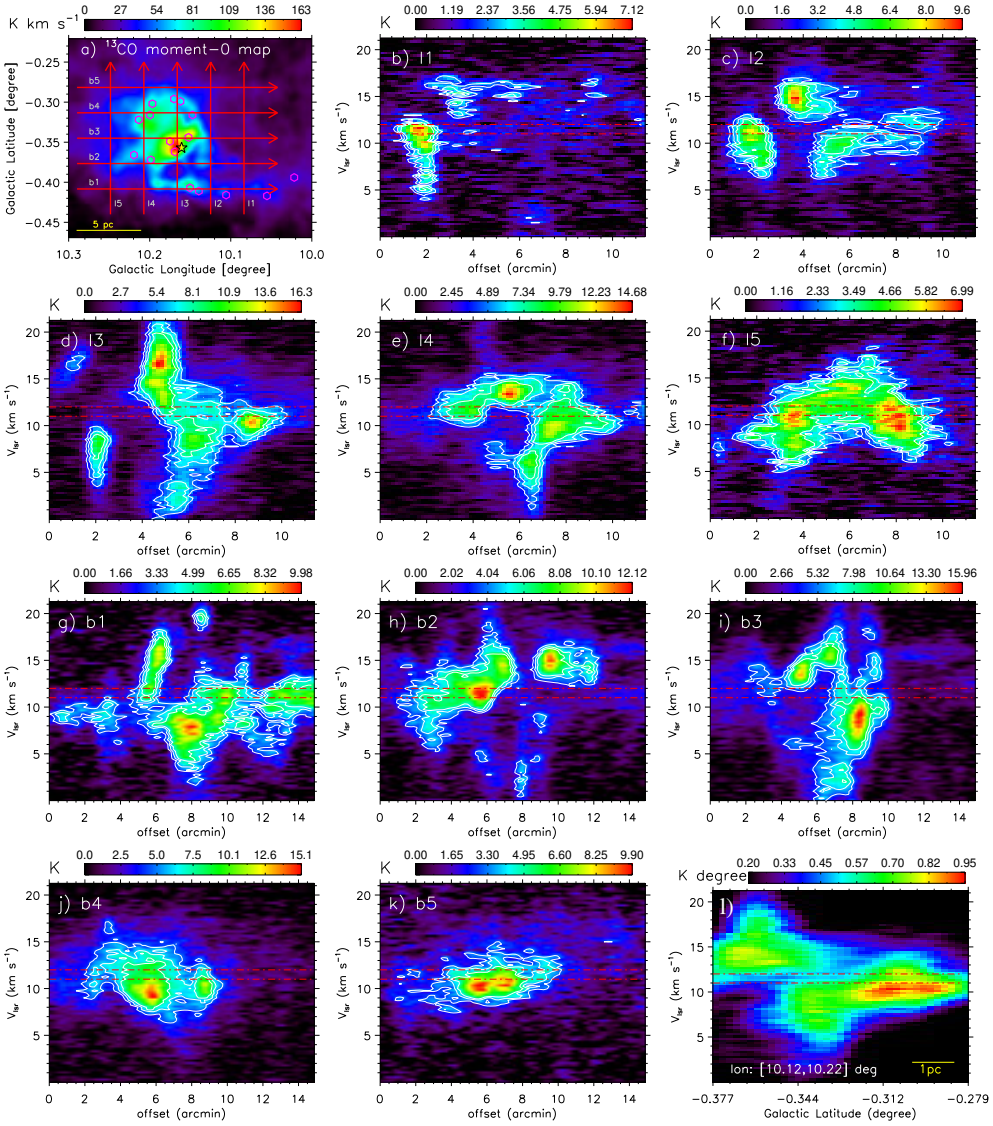

Figure 3.7: (a) Moment-0 map of the SEDIGISM ^{13}CO data in the direction of W31-S. The star symbol is the same as Figure 3.3d. The magenta Hexagons indicate the positions of the ATLASGAL clumps associated with the molecular outflows. Ten arrows (5 vertical: "l1–l5" and 5 horizontal: "b1–b5") are also indicated in the panel, where the PV diagrams are extracted. PV diagrams along the vertical arrows "l1," "l2," "l3," "l4," and "l5" are shown in panels (b), (c), (d), (e), and (f), respectively. PV diagrams along the horizontal arrows "b1," "b2," "b3," "b4," and "b5" are shown in panels (g), (h), (i), (j), and (k), respectively. (l) The panel shows the Galactic latitude-velocity diagram of the SEDIGISM ^{13}CO data. The longitude range used in the integration is indicated in the panel. In panels (b)–(k), the PV diagrams are overplotted with the contours with the levels of 30, 40 and 50% of corresponding peak values. In each PV diagram, two dotted dashed lines (in red) at V_{lsr} = 11 and 12 km s^{-1} are marked.

continuum emission contours. The ionized emission is primarily concentrated in the overlapping regions of these two cloud components. Figure 3.8f is identical to Figure 3.8e but includes the same arrows from Figure 3.7a, allowing us to assess the presence of two cloud components along these directions. From the channel maps of ^{13}CO, we find an "intensity-enhancement" feature in the map at [14, 15] km s^{-1} and an "intensity-depression" feature in the map at [10, 11] km s^{-1}. Figure 3.9a shows a two color-composite image using the ^{13}CO maps at [10, 11] and [14, 15] km s^{-1} in cyan and red, respectively. Figure 3.9b is the same as Figure 3.9a but is superimposed with the NVSS radio continuum emission contours. In Figure 3.9a, we find a spatial match of the "intensity-enhancement" and "intensity-depression" features, which can be referred to as a complementary distribution of clouds. Figure 3.9b displays the presence of the NVSS radio continuum emission toward the complementary distribution of clouds.

The implication of all these findings is discussed in Section 3.4.

3.4 Discussion

3.4.1 W31-S: A site of CCC

The distribution of ATLASGAL clumps (at a distance of 3.55 kpc) and the molecular gas presented in this work confirms the existence of a single extended star-forming complex W31 containing two H II regions, W31-N and W31-S, which are excited by a cluster of O-type stars. Using the *Herschel* 250 μm image, we have demonstrated the existence of HFSs toward both W31-N and W31-S for the first time in the literature (see Section 3.3.1). In the case of HFSs, filaments channel molecular gas and dust toward their central hub. Thus, hubs become the densest part of the system, which eventually forms massive stars (Myers, 2009; André et al., 2010; Schneider et al., 2012; Motte et al., 2018).

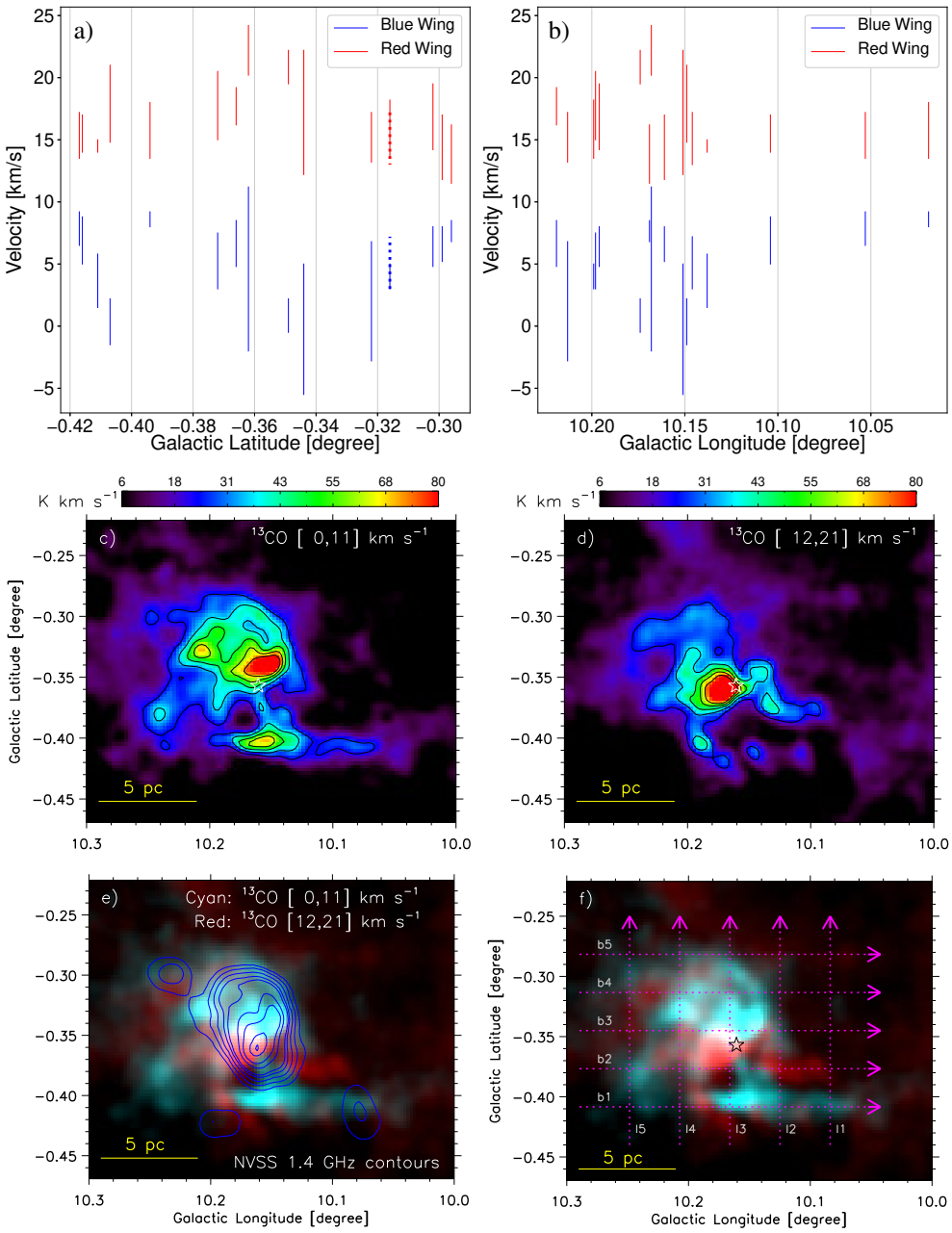

Figure 3.8: (a) Velocity ranges of the ^{13}CO(J = 2–1) blue wing-like component and red wing-like component of molecular outflows associated with ATLASGAL clumps are shown against their Galactic latitudes (two clumps sharing the same latitude −0.°316 are differentiated with solid and dotted lines). These clumps are distributed toward W31-S (see hexagons in Figure 3.7a. (b) Same as panel (a), but velocity ranges are presented against Galactic longitudes of the clumps. (c) Moment-0 map at [0, 11] km s^{-1} for the SEDIGISM ^{13}CO data toward W31-S. (d) Moment-0 map at [12, 21] km s^{-1} for the ^{13}CO data toward the same region. In panels (a) and (b), the SEDIGISM ^{13}CO data contours are at 24, 36, 48, 60, and 72 K km s^{-1}. (e) The panel displays a two-color composite image made, using the SEDIGISM ^{13}CO map at [12, 21] km s^{-1} (in red) and the SEDIGISM ^{13}CO map at [0, 11] km s^{-1} (in cyan), overlaid with the NVSS radio continuum contours having the levels of 0.02, 0.08, 0.2, 0.4, 0.6, 1.4, 2.2, 3.7 and 4.4 Jy beam^{-1} ($1\sigma \sim 0.45$ mJy beam^{-1}). (f) The panel is the same as Figure 3.8c, but overlaid with the arrows as shown in Figure 3.7a. In panels (c), (d), and (f), the star symbol is the same as marked in Figure 3.3d.

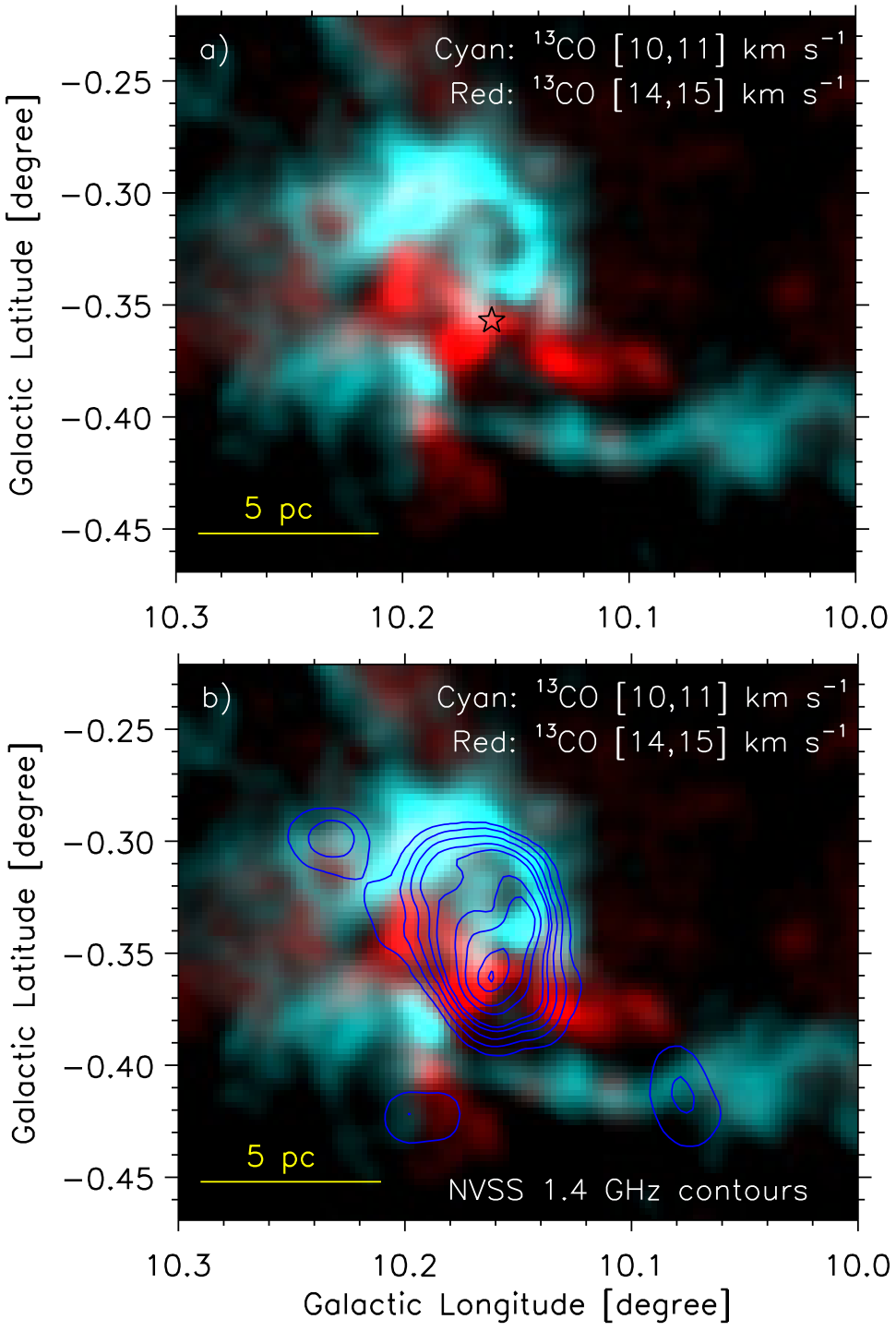

Figure 3.9: (a) The panel presents a two-color composite image made using the SEDIGISM ^{13}CO map at [14, 15] km s^{-1} (in red) and the SEDIGISM ^{13}CO map at [10, 11] km s^{-1} (in cyan). The star symbol is the same as marked in Figure 3.3d. (b) The panel is the same as Figure 3.9a, but overlaid with the NVSS radio continuum contours as mentioned in Figure 3.8c.

The analysis of the NANTEN2 ^{12}CO(J = 1–0) line data has disclosed new insights about the molecular gas associated with W31, particularly revealing the presence of two velocity components toward W31-S (see Section 3.3.3.1). This finding is further investigated using the SEDIGISM ^{13}CO(J = 2–1) line data, allowing for a detailed examination of the cloud's kinematics. While tracing the outflow kinematics of individual clumps in the PV diagrams is challenging, the overall kinematics of the cloud can still be observed (see Section 3.3.3.2). Toward W31-S, the SEDIGISM ^{13}CO(J = 2–1) line data confirm the presence of two velocity components at ∼8 and 16 km s^{-1}, which are also connected in the velocity space. Additionally, we propose the existence of outflow signatures in this region. Furthermore, the ^{13}CO maps reveal a complementary distribution toward W31-S, characterized by a spatial fit between "key/intensity-enhancement" and "cavity/keyhole/intensity-depression" features of the blue- and red-shifted cloud components (see Section 3.3.3.2).

As described in Chapter 1, a connection of two cloud components in physical and velocity space is considered as a reliable characteristic of CCC (e.g., Fukui et al., 2014, 2018b; Dewangan, 2017; Nishimura et al., 2017; Hayashi et al., 2018; Sano et al., 2018; Fujita et al., 2021; Torii et al., 2021). Two colliding clouds show a complementary distribution in PP space (e.g., Fukui et al., 2018b; Dewangan et al., 2018b; Fujita et al., 2021) and a bridge feature in PV space (e.g., Haworth et al., 2015a; Torii et al., 2017; Dewangan & Ojha, 2017; Priestley & Whitworth, 2021). We also highlight some works on CCC concerning extragalactic objects, such as R136 (Fukui et al., 2017a) and N44 (Tsuge et al., 2019) in Large Magellanic Cloud (LMC), Antennae galaxies (Tsuge et al., 2021), and M33 (Sano et al., 2021). The signatures of CCC, i.e., the complementary distribution and bridge feature together, may be observed as a V-shaped gas distribution in the PV space (e.g., Hayashi et al., 2018; Fukui et al., 2018b, 2021a; Torii et al., 2021).

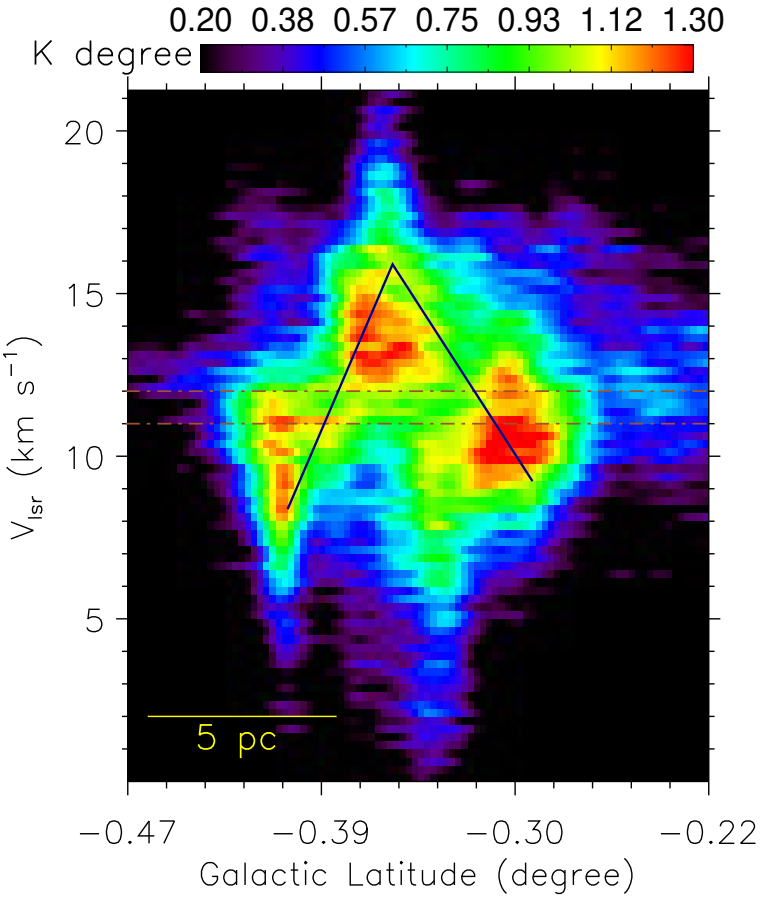

Figure 3.10: Galactic latitude-velocity diagram of the ^{13}CO data. An inverted "V" like structure is also indicated in the figure. Two dotted dashed lines at V_{lsr} = 11 and 12 km s^{-1} are marked in the figure.

For inclined viewing angles to the collision axis, the V-shaped gas distribution becomes skewed (Fukui et al., 2018b, see Figure 5 therein). Interestingly, almost a V-like gas distribution is observed in the Galactic latitude-velocity diagram of ^{13}CO toward W31-S (see Figure 3.10). In the Galactic latitude-velocity diagram, the V-shaped gas distribution is not skewed. Therefore, it suggests that the inclination of our line of sight with the collision axis is very small.

The H II regions powered by O-type stars (Blum et al., 2001) and the signatures of star-forming activities are traced toward the collision interface of two cloud components (see Figures 3.8e and 3.9b). Hence, a possible connection be-

tween the birth of the O-type stars and CCC is likely. As previously discussed, the inclination angle between our line of sight and the collision axis is very small. Hence, we assume this value to be ∼10° to estimate the collision time scale. The size of the overlapping region between the cloud components is found to be ∼2.5 pc; hence, its value along the axis of collision is 2.5 pc/sin(10°) ≈ 14.3 pc. The velocity difference between two clouds in our line of sight is ∼8 km s^{-1} and its value along the axis of collision is 8 km s^{-1}/cos(10°) ≈ 8.12 km s^{-1}. Therefore, the collision time scale is about 14.3 pc/8.12 km s^{-1} ∼1.7 Myr. The formation of an O-type star of 30 $M_{\odot}$ requires nearly 10^5 yr for a mass accretion rate of ∼3 × $10^{-4} M_{\odot}$ yr^{-1} (Wolfire & Cassinelli, 1987; Inoue & Fukui, 2013). Such a high value of mass accretion rate is necessary to overcome the enormous radiation pressure of the massive stars and continue further mass accumulation. By comparing the collision time scale with the formation time scale of the massive O-type stars and the typical age of Class I YSOs (∼0.44 Myr), we suggest that CCC possibly triggered the star-forming activity toward W31-S.

3.4.2 A larger picture of CCC in W31?

Earlier, Dewangan et al. (2015) and Beuther et al. (2011) suggested that W31-N is relatively younger than W31-S due to the presence of 6.7 GHz MMEs in the boundary of the MIR bubble, CN 148 toward W31-N. However, previous studies based on the NIR spectroscopic observations of point-like sources (e.g., Blum et al., 2001; Bik et al., 2005) and radio continuum data (Kim & Koo, 2002) suggest almost similar ages of about 1 Myr for both regions, W31-N and W31-S. Additionally, the detection of several Class I YSOs and ATLASGAL clumps associated with outflow activities indicates an earlier stage of star-forming activities around a relatively evolved H II region in both the sites (see Figures 3.1a and 3.1b, respectively). Altogether, these results hint at the common origin of

W31-N and W31-S and encourage exploring the detailed gas kinematics of the entire W31 complex.

In the moment-1 map of SEDIGISM ^{13}CO data, a noticeable velocity variation is also observed toward W31-N (see Figure 3.3f), indicating the presence of similar cloud components in the direction of W31-N as detected toward W31-S. Figures 3.11b, 3.11c, and 3.11d present the PV diagrams extracted from ^{13}CO

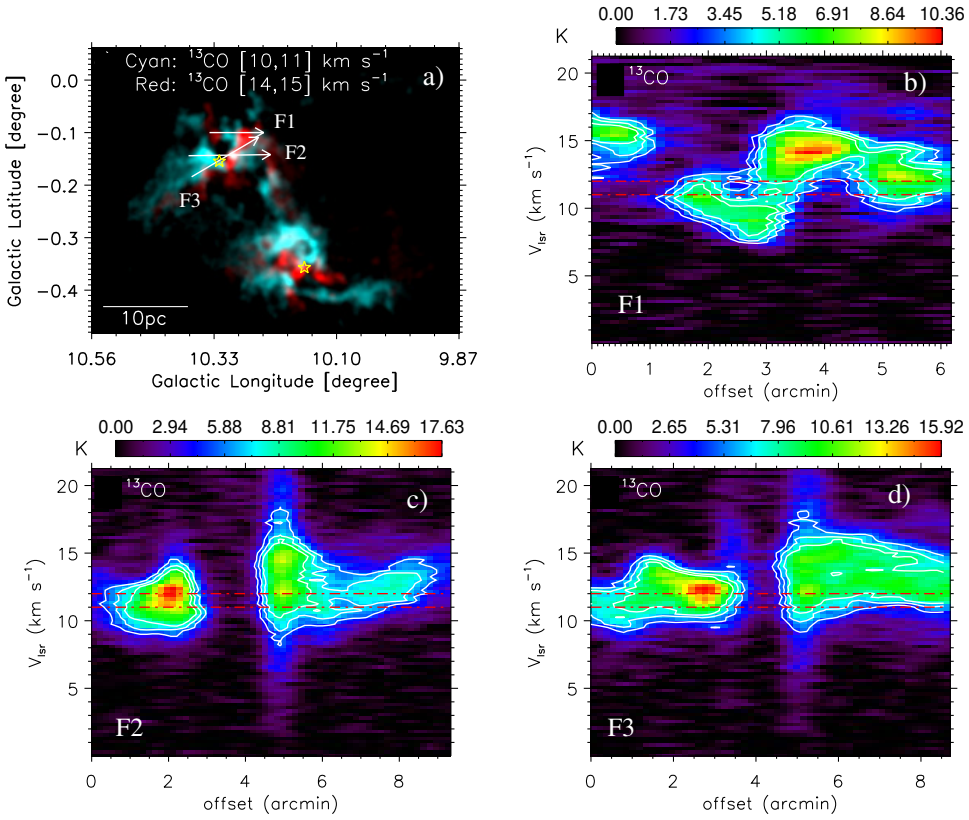

Figure 3.11: (a) The panel shows a two-color composite image made using the SEDIGISM ^{13}CO map at [14, 15] km s^{-1} (in red) and the SEDIGISM ^{13}CO map at [10, 11] km s^{-1} (in cyan) toward the W31 complex. Star symbols are the same as marked in Figure 3.1a. Three arrows "F1," "F2," and "F3" are marked in the direction of W31-N, where the PV diagrams are produced (see Figures 3.11b–3.11d). PV diagrams along the arrows "F1," "F2," and "F3" are shown in panels (b), (c), and (d), respectively. Two dotted dashed lines (in red) at V_{lsr} = 11 and 12 km s^{-1} are marked in each PV diagram.

line data along the arrows "F1," "F2," and "F3," respectively. In Figure 3.11b, there is a hint of two velocity components, but it is not as convincing as observed

toward W31-S. Together, the PV diagrams of ^{12}CO line data toward W31-N do not show a clear signature of two cloud components (see Section 3.4.1). It is quite possible that the signature of CCC in W31-N is diminished by the feedback of O-type stars, which is evident by the presence of MIR bubble CN 148. Taking into account the age difference between young protostars and H II regions, there was a suggestion of triggered star formation through the feedback of massive O-type stars in W31-N (e.g., Beuther et al., 2011; Dewangan et al., 2015). Therefore, the outcomes of our observational investigation indicate that the possibility of CCC cannot be completely ruled out in W31-N. It is important to note that this chapter does not focus on the impact of massive stars on their surroundings. Hence, such a study is beyond the scope of this work.

Furthermore, as described in Section 1.7, CCC can lead to the formation of filaments, which serve as the building blocks of HFSs. This occurs either through the fragmentation of the shock-compressed layer or the shock-compression of inhomogeneous density structures present in the colliding cloud components. (see Balfour et al., 2015, 2017; Inoue & Fukui, 2013; Inoue et al., 2018). Observationally, Beltrán et al. (2022) studied a MSFR and found a deep connection between CCC in the formation of HFS and the massive protocluster associated with the hot molecular core at G31.41+0.31 using N_2H^+(1–0) observations. In addition, the work of Dewangan (2022) on the IRDC G333.73+0.37 based on the SEDIGISM ^{13}CO and C^{18}O line data and the study of Fukui et al. (2019) on N159E-Papillon Nebula located in LMC (distance ∼50 kpc) provided observational results in favor of CCC or converging flows, explaining the presence of HFSs and massive stars. Interestingly, our observational investigation of the W31 complex reveals signatures of CCC and the simultaneous presence of HFSs. Therefore, based on the findings of the theoretical and observational studies discussed above, our proposed collision process may provide a plausible explanation for the presence of

HFSs and the formation of massive stars in our target region. The presence of HFSs indicates gas inflow from the large-scale toward the central hubs through the filaments. Determining the gas motion along these filaments (see Figure 3.2) requires dense gas kinematic data, which remains an observational limitation of this chapter.

3.5 Summary

The present chapter focuses on observationally uncovering the physical process behind O-type star formation in the W31 complex. ln this context, we have analyzed multi-wavelength data sets, including new NANTEN2 ^{12}CO and archival SEDIGISM ^{13}CO line data in the direction of the W31 complex. The key findings of the present study are summarized below.

1. A total of 49 ATLASGAL 870 μm dust clumps and several Class I protostars are traced toward W31-N and W31-S. All these dust clumps in a velocity range of [8.9, 15.3] km s^{-1} are situated at a distance of 3.55 kpc, illustrating that W31-N and W31-S belong to a single extended physical system. Out of 49, 25 ATLASGAL clumps are associated with molecular outflow signatures, which supports the ongoing star-forming activity.

2. The application of *getsf* on the *Herschel* 250 μm image reveals several filaments toward W31-N and W31-S. In both cases, filaments are observed to converge at the common junctions, hosting the H II regions. These findings indicate the presence of HFSs in regions W31-N and W31-S.

3. The molecular gas distribution in the PV and PP space indicates the applicability of CCC toward W31-S. The observed Galactic latitude-velocity diagram suggests a small inclination angle between the line of sight and the

axis of collision, which is assumed to be about 10°. The size of the overlapping zone of the cloud components along the collision axis and the relative velocity are computed to be ∼14.3 pc and ∼8.1 km s^{-1}, respectively. These parameters yield a collision timescale of ∼2 Myr.

4. Signposts of star formation, including massive O-type stars in W31-S, are concentrated toward the overlapping areas of the two cloud components. The derived collision timescale is sufficiently large enough to have influenced MSF in the W31 complex. In the direction of W31-N, the signatures of CCC are not as promising as W31-S and are possibly destroyed by the feedback of the massive stars.

Overall, our observational study of W31 reveals concurrent signatures of both CCC and HFSs. This is a significant finding, as only a few sources in the literature report their simultaneous presence.

Chapter 4

AFGL 5180 and AFGL 6366S: sites of hub-filament systems at the opposite edges of a filamentary cloud[†]

4.1 Introduction

The last chapter presents an observational investigation of the W31 complex, hosting two extended H II regions, to understand the origin of massive O-type stars. We have revealed signatures of CCC and HFSs simultaneously in W31. However, the presence of the extended H II regions in W31 suggests that the strong radiative feedback of the O-type stars has been influencing the parental molecular environment of MSF. Therefore, understanding the physical processes

[†]**A. K. Maity**, L. K. Dewangan, N. K. Bhadari, D. K. Ojha, Z. Chen, and Rakesh Pandey, 2023, *Monthly Notices of the Royal Astronomical Society*, Volume 523, Issue 4, pp.5388-5407, https://doi.org/10.1093/mnras/stad1644

responsible for MSF in the parental molecular environment requires extensive observational study of the MSFRs in their early stages.

The presence of young massive stars is often evident through the detection of HC/UC H II regions in the radio continuum emission (Sharpless, 1959) and/or the detection of Class II 6.7 GHz MMEs (Menten, 1991; Caswell et al., 1995; Walsh et al., 1998). The 6.7 GHz MMEs exclusively trace the early stages of MSF (Minier et al., 2001; Breen et al., 2013), which are very promising to reveal the parental molecular environment of the MSF. In this context, this chapter examines a target area hosting two MSFRs, AFGL 5180 and AFGL 6366S, each associated with a 6.7 GHz MME.

AFGL 5180 is also referred to as G188.946+00.886 or IRAS 06058+2138 (hereafter, T1), while AFGL 6366S is known as G189.030+0.784 or IRAS 06056+2131 (hereafter, T2). In the literature, different distances (d) have been reported to T1 and T2, which are 1.0–1.5 kpc (Bik et al., 2005), 1.76 kpc (Oh et al., 2010), 2.1 kpc (Reid et al., 2009), 2.2 kpc (Koempe et al., 1989), and 3.5 kpc (Saito et al., 2007). Previously, Leistra et al. (2006) and Devine et al. (2008) used the distance of 1.5 kpc as an average estimation between the proposed values of Bik et al. (2005) and Koempe et al. (1989). Following Leistra et al. (2006) and Devine et al. (2008), we have adopted the distance of 1.5 kpc in this work for T1 and T2.

Toward T1 and T2, the 6.7 GHz MMEs were detected with systemic velocities of 2.8 and 1.7 km s^{-1}, respectively (Szymczak et al., 2018). In addition to the MMEs, other star formation indicators–such as, outflow activity, H_2O maser, and YSOs–were observed toward both the sites, along with several dense clumps (e.g., Koempe et al., 1989; Davis et al., 1998; Ghosh et al., 2000; Klein et al., 2005; Wu et al., 2010; Shimoikura et al., 2013; Navarete et al., 2015). These sites are located close to an H II region Sh2-247 (hereafter, S247), which is excited by a massive O9.5 star *LS V +21° 27* (Roman-Lopes & Roman-Lopes, 2019). This star

is also referred to as ALS 8736 or CGO 115 (hereafter, cgo115).

In the direction of T1, high-resolution NIR images from the Integral Field Spectrograph (SINFONI) at the Very Large Telescope (VLT) (Vasyunina, 2010) and mm maps from ALMA have been examined (e.g., Mutie et al., 2021). Based on the ground-based NIR observations, the age of the NIR cluster toward T1 was reported to be ∼2.5 Myr (Devine et al., 2008). Later, Vasyunina (2010) estimated a similar age of 1-3 Myr for T1 using their NIR spectroscopic study. Earlier studies also suggested that T1 is younger than T2 (Kurtz et al., 1994; Ghosh et al., 2000). T1 and T2 were found to be connected by a filamentary feature in the JCMT 850 μm dust continuum map (see Figure 1 in Klein et al., 2005). The filamentary feature were also detected in the molecular gas emission (see Figures 1b and 1c in Shimoikura et al., 2013). Previously, Carpenter et al. (1995a,b) proposed a triggered star formation scenario for the Gemini OB1 molecular cloud complex, which includes our selected target sites. Using molecular line data, Shimoikura et al. (2013) identified two velocity components in the ranges [−3, 5] and [5, 13] km s^{-1} (see Figure 3b in their paper) and suggested that the CCC process could explain the observed star formation activities at both sites.

The target sites of this chapter, T1 and T2, are in early phases of MSF and connected with a filamentary feature traced in dust continuum and molecular line data. However, despite numerous studies on T1 and T2, no attempt has been made to study embedded filaments and their role in the mass accumulation for MSF. Therefore, this chapter aims to examine the role of filament in MSF and the applicability of the previously proposed CCC scenario. Additionally, this study explores the influence of cgo115 on T1 and T2. To accomplish the objectives of this chapter, a detailed multi-scale and multi-wavelength observational study has been conducted. Embedded features are analyzed across spatial scales ranging from ∼0.01 to ∼1 pc using continuum images spanning NIR to radio wavelengths.

Embedded features are examined from the small- to the large-scale (i.e., 0.01–1 pc) using continuum images covering NIR to radio wavelengths. Additionally, molecular line data are utilized to analyze the spatial distribution and kinematics of molecular gas.

This chapter is organized as follows. Section 4.2 details the data sets used in this work. The results are outlined in Section 4.3 and discussed in Section 4.4. Finally, Section 4.5 summarizes the key findings of this work.

4.2 Data sets

We collected multi-scale and multi-wavelength data sets from various surveys for the target area of $19\farcm58 \times 18\farcm33$ (centred at $l = 188\fdg98$, $b = 0\fdg83$). A brief overview of all the datasets analyzed in this study is provided below.

4.2.1 NIR data

Deep NIR photometric magnitudes of point-like sources in H and K band were collected from UKIDSS-GPS (Lawrence et al., 2007) and 2MASS (Skrutskie et al., 2006). We only selected sources with photometric errors < 0.1 mag in both bands. The K band image for our target area was also obtained from UKIDSS GPS (resolution $\sim 0\farcs8$). The observations for the UKIDSS-GPS were conducted with the Wide Field Camera (WFCAM) installed on the 3.8 m UK Infra-Red Telescope. (Casali et al., 2007). The *Spitzer* IRAC images at 3.6 and 4.5 μm (with a resolution of $\sim 2''$) along with the photometric magnitudes of point-like sources were obtained from the Warm-*Spitzer* Glimpse 360 survey (Whitney et al., 2011). Only the point-like sources that have a photometric magnitude error $<$0.2 mag were selected for further analysis. We also acquired the HST pipeline-calibrated NIR imaging data (with a resolution of $\sim 0\farcs1$ –$0\farcs2$) in the J (WFC3/F110W)

and H (WFC3/F160W) wide band filters, as well as in the [Fe II] (WFC3/F164N) narrow band filter. These images are exclusively available for site T1.

4.2.2 H_2 narrow band image

Our selected target area was included in the survey of extended H_2 emission conducted by Navarete et al. (2015). This survey was carried out using the Wide-field InfraRed Camera (WIRCam) mounted on the Canada-France-Hawaii Telescope (CFHT), with an average seeing of about 0.″7. We utilized the continuum-subtracted H_2 image ($\lambda = 2.122\,\mu$m, $\Delta\lambda = 0.032\,\mu$m) from this survey (see Navarete et al., 2015, for more details).

4.2.3 Dust continuum data

We obtained FIR/sub-mm dust continuum images (70–500 μm) from the Hi-GAL Survey (Molinari et al., 2010b). The resolution of the *Herschel* images at 70, 160, 250, 350, and 500 μm are about 6″, 12″, 18″, 25″, and 37″, respectively. We also utilized a high-resolution (∼8.″5) dust continuum map at 350 μm obtained with Submillimeter High Angular Resolution Camera II (SHARC-II; Merello et al., 2015). Additionally, we collected the *Planck* 353 GHz (i.e., 850 μm) dust continuum polarization data, comprising of Stokes I, Q, and U maps (resolution ∼5′) for our target area (Planck Collaboration et al., 2014). These data were extracted from the *Planck* Public Data Release 3 of Multiple Frequency Cutout Visualization (PR3 Full Mission Map with PCCS2 Catalog). The results derived using the *Planck* polarization data can be found in APPENDIX A.1.

The high-resolution ALMA 1.3 mm dust continuum images (project id: 2015.1.01454.S, PI: Zhang, Yichen) at two different resolutions (i.e., 0.″18 × 0.″28 and 0.″63 × 1.″23) were collected toward the site T1 from the ALMA FITS Archive. It is important to note that there were no ALMA observations toward site T2.

The analysis of the high-resolution HST/UKIDSS images and the ALMA dust continuum map are presented in APPENDIX A.2

4.2.4 Molecular CO line data

We examined the ^{12}CO/^{13}CO/C^{18}O($J = 1$–0) line data toward our selected target area to explore the gas kinematics. These data were obtained as a part of the MWISP[1] project, led by the Purple Mountain Observatory (PMO), using the 13.7 m telescope at Delingha, China. The beam size of the data is $\sim$55″ and the pointing accuracy is better than 5″. The velocity channel widths are $\sim$0.16 km s^{-1} for ^{12}CO and $\sim$0.17 km s^{-1} for ^{13}CO and C^{18}O data. The RMS noise level for ^{12}CO is $\sim$0.5 K and for ^{13}CO and C^{18}O is $\sim$0.3 K. These molecular line data were reduced using the software, GILDAS (Pety, 2005). Details about the telescope and receiver used in the MWISP project is available in Su et al. (2019) and the references cited therein.

4.2.5 Radio continuum data

For our target area, the 1.4 GHz radio continuum map was collected from NVSS (Condon et al., 1998), having resolution and sensitivity of $\sim$45″ and $\sim$0.45 mJy beam^{-1}, respectively. We acquired Band-3 low-frequency (325 MHz) radio continuum data from the GMRT data archive (Proposal Code: 23_024 and PI: Manash Ranjan Samal) for our target area. We have reduced the data using CASA[2] Pipeline-cum-Toolkit for Upgraded GMRT data REduction (CAPTURE[3]) (Kale & Ishwara-Chandra, 2021). Before generating the final image, four rounds of phase-only self-calibration were done in the pipeline. Next, the image was cor-

[1] http://english.dlh.pmo.cas.cn/ic/in/

[2] https://casa.nrao.edu/index_docs.shtml

[3] https://github.com/ruta-k/CAPTURE-CASA6.git

rected for primary beam gain. The beam size and sensitivity of the reduced GMRT band-3 image are $\sim$13.″2 $\times$ 9.″5 and $\sim$0.5 mJy beam^{-1}, respectively. We also obtained the processed radio continuum map at 8.46 GHz for our target area(beam size $\sim$3.″1 $\times$ 2.″3; sensitivity $\sim$36.8 μJy beam^{-1}) from NVAS toward T1 only.

4.3 Results

4.3.1 Physical environment of the target sites T1 and T2

4.3.1.1 Elongated filament

Figure 4.1a presents a three-color composite image from *Herschel* (red: 250 μm, green: 160 μm, blue: 70 μm), overlaid with NVSS 1.4 GHz radio continuum emission contours and the position of the previously identified massive star, cgo115. The locations of two 6.7 GHz MMEs are also marked with triangles. Toward our target area, the GMRT 325 MHz radio continuum emission is shown using contours over the *Herschel* color composite image in Figure 4.1b. The most prominent feature observed in this color composite image is an elongated filamentary structure with a dumbbell-like appearance. Each end of this structure is associated with at least one previously reported star-forming region, where a 6.7 GHz MME is also detected. The NVSS 1.4 GHz and GMRT 325 MHz radio continuum contours[4] trace the ionized gas, outlining the spatial extent of the H II region S247. Notably, the massive star cgo115 appears to be positioned at the center of the radio continuum emission (indicated by an asterisk in Figure 4.1a). The

[4]This GMRT image shows the low-frequency radio continuum emission toward our target area. However, this image is not part of our published work (i.e., Maity et al., 2023). In the future, we plan to analyze the GMRT data in detail to investigate the physical properties of ionized gas.

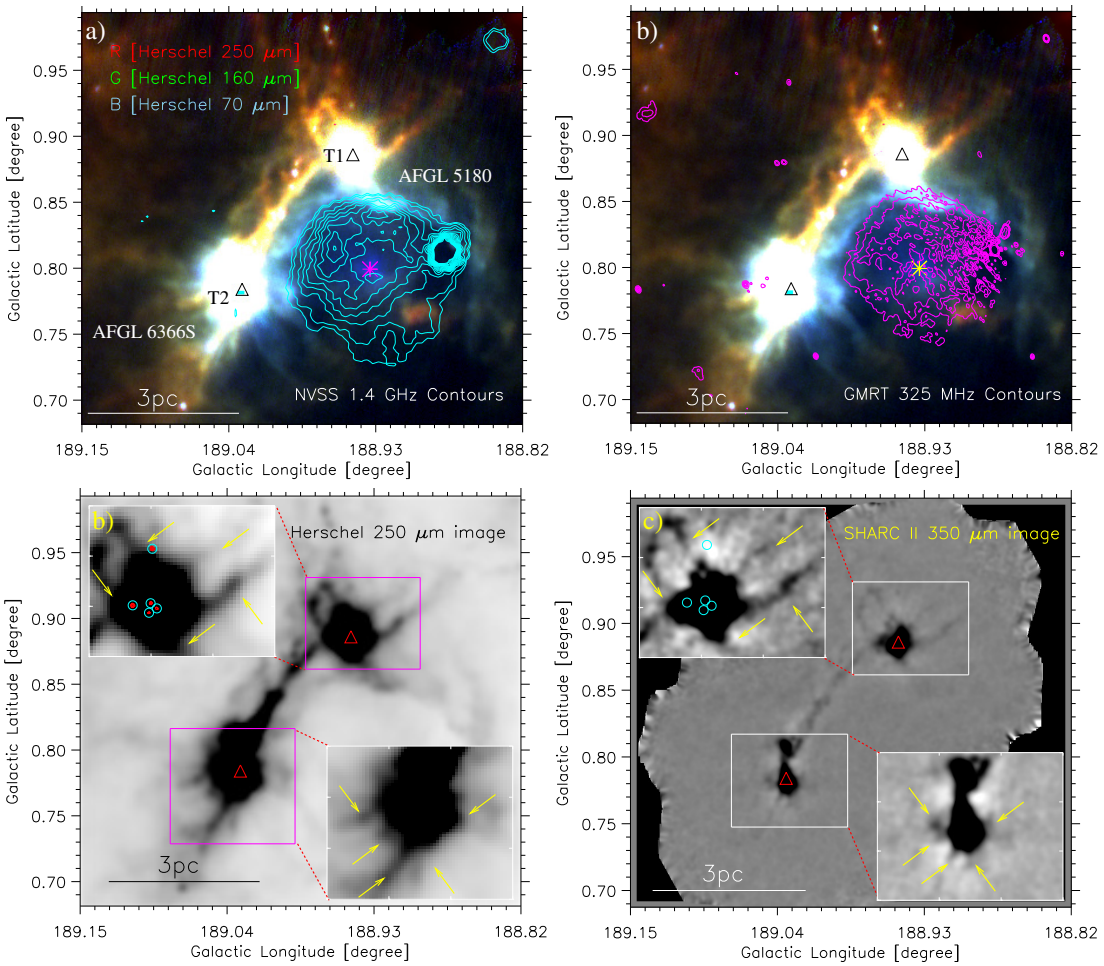

Figure 4.1: (a) Overlay of the NVSS 1.4 GHz radio continuum emission contours on a three-color composite map of an area hosting AFGL 5180 and AFGL 6366S. The color composite map consists of the *Herschel* 250 μm image (in red), 160 μm image (in green), and 70 μm image (in blue). The NVSS radio continuum contours are plotted with levels of 3σ and 5σ to 80σ with an interval of 5σ, where 1σ ~0.45 mJy beam^{-1}. The asterisk indicates the position of an O-type star, which is referred to as cgo115. (b Similar to panel (b), this shows an overlay of the GMRT 325 MHz radio continuum emission contours on the *Herschel* three-color composite image. The GMRT radio continuum contours are plotted with levels of [3, 5, 7, 9, 11, 50] $\times\sigma$, where 1σ ~0.5 mJy beam^{-1}. (c) The panel shows the inverted grayscale *Herschel* image at 250 μm. The insets on the top-left and bottom-right present zoomed-in views of the sites AFGL 5180 (or T1) and AFGL 6366S (or T2), respectively, using the inverted grayscale *Herschel* image at 250 μm. In the direction of T1, the NVAS 8.46 GHz radio continuum contours at 120, 240, and 360 μJy beam^{-1} (where, 1σ ~36.8 μJy beam^{-1}) are shown in red. The peak positions of these radio continuum emissions are indicated by cyan circles (see the inset on the top-left). Arrows highlight sub-filaments toward both target sites. (d) Similar to panel (c), this shows inverted grayscale SHARC-II image at 350 μ. A scale bar of 3 pc is shown for a distance of 1.5 kpc in each panel, with triangles indicating the positions of the 6.7 GHz MMEs.

NVSS 1.4 GHz radio continuum emission is not detected toward the filamentary structure, including both the star-forming sites. The angular separations of the 6.7 GHz MMEs in T1 and T2 with the position of the massive star, cgo115, are determined to be about 5′.3 (2.3 pc) and 5′.9 (2.6 pc), respectively. The angular separation between these two MMEs is about 7′.9 (3.4 pc). We present the *Herschel* 250 μm and SHARC-II 350 μm images in inverted grayscale in Figures 4.1c and 4.1d, respectively. Both the FIR dust continuum images reveal an elongated filamentary structure (of length $\sim$4 pc), hosting T1 and T2 at the opposite edges of the filament.

4.3.1.2 Hub-filament systems

Beyond the elongated filamentary structure, an HFS is identified at both AFGL 5180 and AFGL 6366S, where several small-scale filaments (sub-filaments; length $\sim$1 pc) appear to direct toward the central regions (see Figure 4.1b). To highlight these HFSs, zoomed-in views of T1 and T2 are shown using *Herschel* 250 μm and SHARC-II 350 μm images in inverted grayscale (see the insets in Figure 4.1c and 4.1d, respectively). The NVAS 8.46 GHz radio continuum map is only available for site T1. The NVAS data have greater sensitivity compared to the NVSS and GMRT data. In Figures 4.1c and 4.1d, the cyan circles within the top-left insets show the positions of radio continuum sources identified in the NVAS 8.46 GHz map, revealing a small cluster of radio sources (or massive stars) associated with AFGL 5180.

To further examine the embedded filamentary structures, we utilized *getsf* (Men'shchikov, 2021) on the *Herschel* 160 μm image (resolution $\sim$12″). Details of this algorithm are provided in Section 2.3.3. In this work, the filament skeletons are extracted with the maximum source size and filament width of 20″ and 105″, respectively. The results from the *getsf* utility at a scale of 12″ are shown in Fig-

ure 4.2a, where the filament skeletons are marked in red. Multiple sub-filaments are detected toward both T1 and T2 and are highlighted on the *Herschel* 160 µm image in Figure 4.2a. These sub-filaments converge toward the central regions of T1 and T2, coinciding with the 6.7 GHz MMEs (indicated by green triangles in Figure 4.2a). Therefore, massive star-forming activities are exclusively found at the junctions of sub-filaments. Additionally, two distinct structures are highlighted in Figure 4.2a: a curved feature (F1) and an elongated filament (F2). The curved feature F1 is located at the boundary of the H II region traced in the NVSS 1.4 GHz radio continuum emission map. Meanwhile, T1 and T2 are positioned at opposite ends of filament F2, presenting a new perspective on the presence of HFSs at the edges of an elongated filament in the target region.

4.3.1.3 Feedback of the O-type star

To evaluate the impact of cgo115 (marked by a yellow asterisk in Figure 4.2a) on the curved feature F1 and the filament F2, we have calculated the strength of various pressure components exerted by the massive star on these structures. The equations for the thermal pressure of ionized gas ($P_{\rm H\ II}$), radiation pressure ($P_{\rm rad}$), and stellar wind ram pressure ($P_{\rm wind}$) are obtained from Bressert et al. (2012) and are provided below,

$$P_{\rm H\ II} = \mu m_{\rm H} c_{\rm s}^2 \left(\sqrt{\frac{3 N_{\rm uv}}{4\pi\, \alpha_{\rm B}\, D_{\rm s}^3}} \right); \tag{4.1}$$

$$P_{\rm rad} = L_{\rm bol}/4\pi c D_{\rm s}^2; \tag{4.2}$$

$$P_{\rm wind} = \dot{M}_{\rm w} V_{\rm w}/4\pi D_{\rm s}^2. \tag{4.3}$$

Here, $N_{\rm uv}$ is the number of Lyman continuum photons emitted per second by the ionizing source. The sound speed in the ionized region is $c_{\rm s} = 11\,{\rm km\ s^{-1}}$

(Bisbas et al., 2009) and the radiative recombination coefficient is $\alpha_{\rm B} = 2.6 \times 10^{-13}\,{\rm cm^3\,s^{-1}}$ (Kwan, 1997), assuming the temperature to be around $10^4\,{\rm K}$. The mean molecular weight in the ionized gas is $\mu = 0.678$ (Bisbas et al., 2009), and $m_{\rm H}$ indicates the mass of the hydrogen atom. $\dot{M}_{\rm w}$, $V_{\rm w}$ and $L_{\rm bol}$ are respectively the mass-loss rate through stellar wind, the wind velocity, and the bolometric luminosity of the ionizing source, cgo115. The speed of light (c) is adopted to be $2.9979 \times 10^8\,{\rm m\,s^{-1}}$. $D_{\rm s}$ is the projected distance between the point of our interest and the massive star. For a O9.5V star, we can adopt $L_{\rm bol} \approx 66070\,L_{\odot}$ (Panagia, 1973), $\dot{M}_{\rm w} \approx 1.58 \times 10^{-9}\,M_{\odot}\,{\rm yr^{-1}}$ (Marcolino et al., 2009), $V_{\rm w} \approx 1500\,{\rm km\ s^{-1}}$ (Martins & Palacios, 2017) and $N_{\rm uv} \approx 1.2 \times 10^{48}\,{\rm s^{-1}}$ (Panagia, 1973).

To determine the pressure components mentioned above, 16 positions were selected along structure F1 (see filled hexagons in Figure 4.2a), with the first three positions (#1, #2, and #3) and the last position (#16) following a sequential numbering scheme. Likewise, 25 positions were chosen along filament F2 (see filled crosses in Figure 4.2a). The pressure components $P_{\rm rad}$, $P_{\rm H\,II}$, and the total pressure ($P_{\rm wind} + P_{\rm rad} + P_{\rm H\,II}$) are illustrated in Figures 4.2b and 4.2c for F1 and F2, respectively. Notably, along F1, all pressure components exhibit fluctuations around their mean values (see horizontal lines in Figure 4.2b). For F2, the position closest to the massive star exhibits the highest pressure across all components, with pressure values decreasing symmetrically as the distance from the star increases. The ionized gas pressure dominates the other pressure components in the region of interest. The contribution of wind pressure is negligible, accounting for about 10^{-16} dynes cm^{-2} in the total pressure for both F1 and F2. From Figure 4.2c, it can be inferred that the combined pressure, excluding $P_{\rm H\,II}$ (i.e., the sum of $P_{\rm wind}$ and $P_{\rm rad}$), along F2 is around 10^{-11} dynes cm^{-2}. It is important to highlight that the filaments and the massive star are assumed to be on the same plane as the sky. Consequently, the estimated distances represent

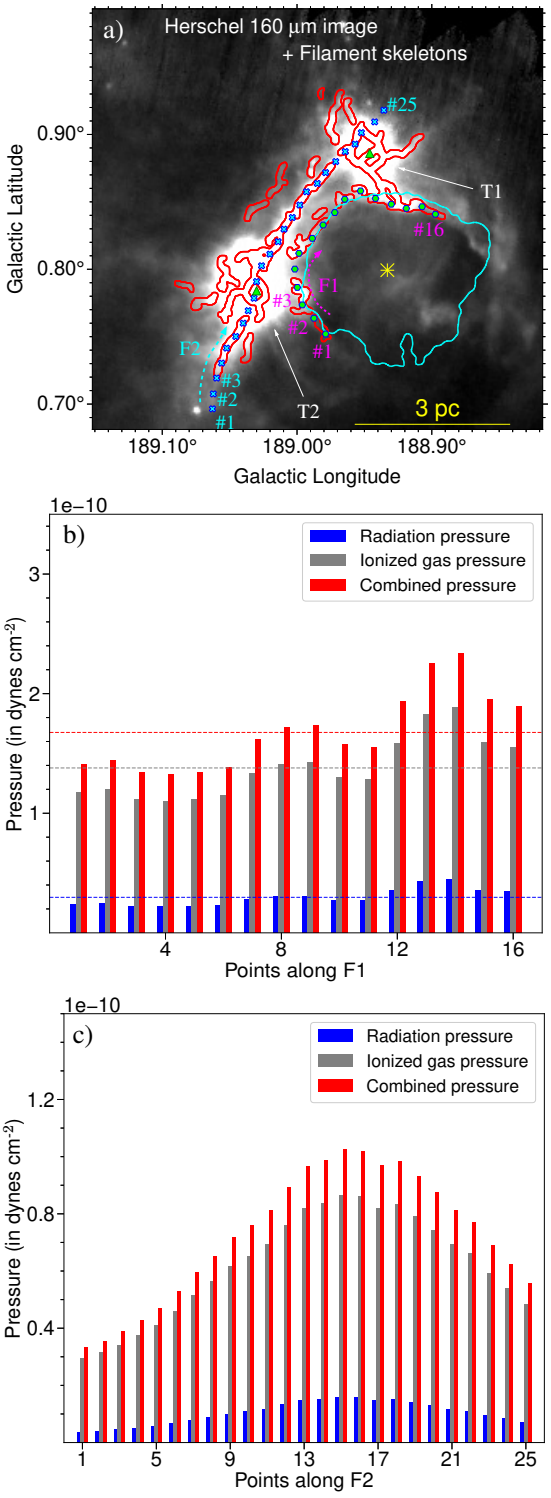

Figure 4.2: (a) *Herschel* 160 μm image overlaid with the NVSS 1.4 GHz radio continuum emission contour at 1.35 mJy beam^{-1} and the *getsf*-identified filament skeletons. This panel shows two distinct structures: the curved feature F1 and filament F2. The filled hexagons and crosses mark several positions along F1 and F2 (see Section 4.3.1.3 for more details), respectively. The asterisk, triangles, and scale bar are the same as in Figure 4.1a. (b) The variation of radiation pressures ($P_{\rm rad}$), ionized gas pressures ($P_{\rm H\,II}$), and combined pressures (i.e., $P_{\rm H\,II}$ + $P_{\rm rad}$ + $P_{\rm wind}$) at the selected positions along F1. The horizontal dashed lines indicate the average values of the pressure distributions. (c) Similar to Figure 4.2b, but displayed for positions along F2.

a lower limit, leading to an upper limit on the calculated pressure values if the projection effect is considered.

4.3.2 Study of embedded protostars

The identification of YSOs serves as a reliable method for tracing ongoing star formation within a given region. To detect embedded YSOs, we follow the procedure of Gutermuth et al. (2009), utilizing photometric data of point-like objects in the area shown in Figure 4.1a. A dereddened color-color diagram ($[[3.6]-[4.5]]_0$ vs. $[K-[3.6]]_0$) is presented in Figure 4.3a, identifying 25 Class I YSOs and 128 Class II YSOs. Additional YSOs are selected using the NIR color-magnitude diagram (H−K vs. K) as shown in Figure 4.3b. To obtain reliable photometric data in the H and K bands from the UKIDSS-GPS survey we used the SQL conditions presented in Lucas et al. (2008). However, since bright sources tend to be saturated in the UKIDSS-GPS survey, we also incorporate 2MASS photometric data for these bands. The color-magnitude analysis of a nearby control field provides a color condition of $H - K > 0.63$ mag, allowing us to find 109 more YSO candidates. After cross-matching sources from both selection methods, a total of 208 YSO candidates are identified. Their spatial distribution is overlaid on the *Herschel* 70 μm image in Figure 4.3c.

The nearest neighbor (NN) surface density analysis is an effective method for identifying groups/clusters of YSOs in star-forming regions (see, e.g., Casertano & Hut, 1985; Bressert et al., 2010; Bhadari et al., 2020). We have employed this technique to generate the surface density map of YSOs in our target region. The area shown in Figure 4.1a is divided into 100 × 100 grid lines with grid spacings of 11.″7 and 11.″1 along the Galactic longitude and latitude, respectively. Considering the distance of 1.5 kpc and NN number of 5, we computed the YSO surface density map, which is presented as contours at the levels of 15–300 YSOs pc^{-2} over the

Herschel 160 μm image in Figure 4.3c. Two prominent YSO clusters, CL1 and CL2, are identified toward sites T1 and T2, respectively, which are highlighted by yellow dotted circles (see Figure 4.3c). Additionally, a significant number of YSOs are distributed along the central region of the filament F2. Therefore, this analysis reveals the ongoing star formation activities toward the entire filament F2, with YSO clusters predominantly located near its edges.

4.3.3 *Spitzer* ratio map and continuum-subtracted H_2 emission

The *Spitzer* ratio map (4.5 μm/3.6 μm) along with the narrow band $H_2(\nu = 1 - 0$ S(1), 2.12 μm) emission are valuable to trace the energetic feedback of star formation activities (including MSF) (see Povich et al., 2007; Dewangan et al., 2017b; Pandey et al., 2020). A comprehensive description of the H_2 emission in MSFRs M 17 UC1–IRS5 is provided in Chen et al. (2015). In this relation, Figure 4.4a presents the *Spitzer* ratio map for our target area. Bright regions in the ratio map present an excess of 4.5 μm emission over 3.6 μm emission, while the dark regions exhibit the opposite condition. The continuum-subtracted $H_2(\nu = 1 - 0$ S(1)) map is produced using the similar approach discussed in Navarete et al. (2015). Figure 4.4b presents the continuum-subtracted $H_2(\nu = 1 - 0$ S(1)) map for the area indicated by a magenta rectangle in Figure 4.4a.

The *Spitzer* 4.5 μm band includes contributions from $H_2(\nu = 0 - 0$ S(9)) emission at 4.693 μm and H I Br-α recombination line emission at 4.05 μm. Conversely, the *Spitzer* 3.6 μm band covers far-ultraviolet heated PAH emission at 3.3 μm, originating from C−H vibrational stretching mode (Allamandola et al., 1989; Draine, 2003; Tielens, 2008), as well as $H_2(\nu = 1 - 0$ O(5)) emission at 3.234 μm. In the *Spitzer* ratio map, bright regions are observed throughout the filament, including T1 and T2 (see Figure 4.4a), due to the excess emission at 4.5

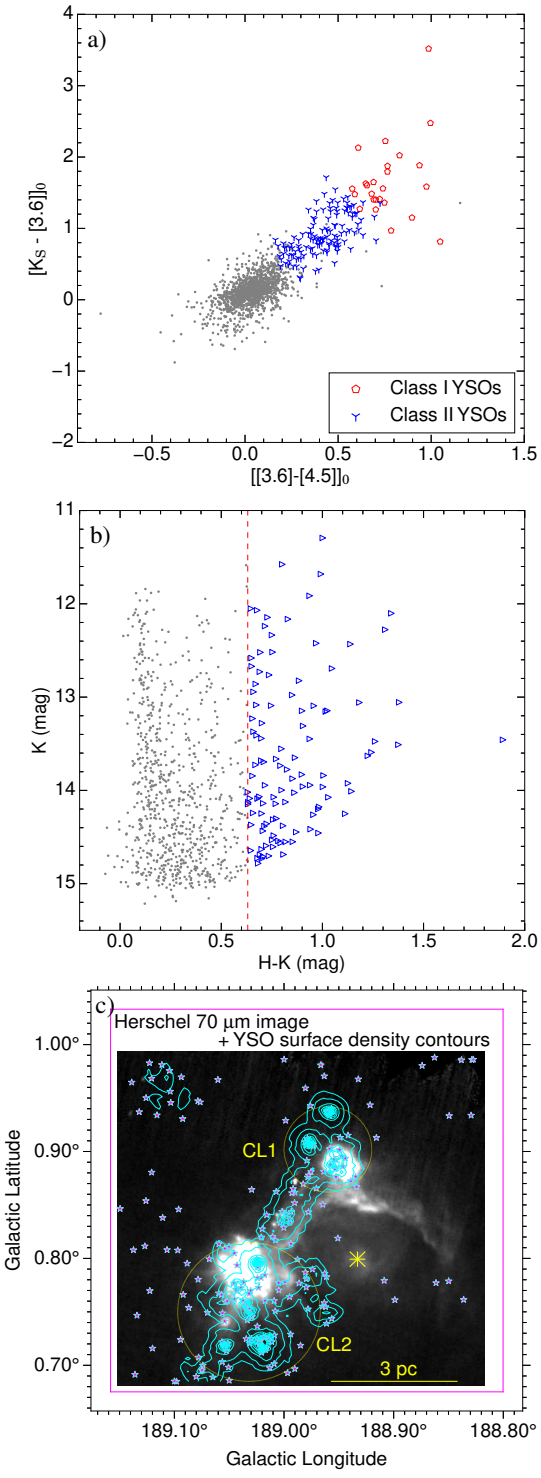

Figure 4.3: (a) The dereddened color-color ($[[3.6]-[4.5]]_0$ vs. $[K-[3.6]]_0$) diagram of the point-like sources distributed toward our target area. Class I and Class II YSOs are presented by red pentagons and blue tri-down symbols, respectively. (b) The color-magnitude (H−K vs. K) diagram of point-like sources. Color-excess sources are highlighted using blue triangle-right symbols. (c) Overlay of the YSO candidates (see magenta stars) and their surface density contours on the *Herschel* 70 μm image. The contours of YSO surface density are at levels of 15, 25, 50, 75, 100, 125, 150, 175, 200, 225, 250, 275, and 300 YSOs pc^{-2}. The yellow circles highlight the clusters of YSOs toward the edges of the filament. The scale bar and the asterisk are the same as Figure 4.2a. The magenta rectangle indicates the area of the molecular data shown in Figure 4.6.

μm compared to 3.6μm. The radio continuum emission is absent in the NVSS and GMRT data toward the bright regions of the ratio map. In Figure 4.4b, the $H_2(\nu = 1 - 0$ S(1)) emission is also detected toward the filament. Hence, Figures 4.4a and 4.4b together support the presence of outflow activities toward the entire filament (including T1 and T2), indicating the ongoing star-forming activities (see also clusters of YSOs in Section 4.3.2). Interestingly, the dark features in the ratio map traced at the periphery of the H II region, S247, indicate an excess of PAH-dominated 3.3 μm emission. A similar characteristic is also detected at the boundary of the Galactic H II region S305 using the *Spitzer* ratio map (Dewangan et al., 2020b; Bhadari et al., 2021). Therefore, the dark areas in the ratio map may display the photo-dissociation regions (PDRs), suggesting the influence of the massive star on its surroundings.

4.3.4 *Herschel* column density and dust temperature maps

The multi-wavelength *Herschel* images allow the computation of the column density ($N(H_2)$) and the dust temperature (T_d) maps. As described in Section 2.3.2, pixel-by-pixel SED fitting with a modified blackbody spectrum provides $N(H_2)$ and T_d. Using *Herschel* images (i.e., 70–500 μm) in the tool *hires* (Men'shchikov, 2021), we have produced $N(H_2)$ and T_d maps at resolutions 6″–37″. However, the $N(H_2)$ and T_d maps at ∼6″ resolution are quite noisy, possibly due to insignificant features present in the *Herschel* 70 μm image itself. Hence, we have used the $N(H_2)$ and T_d maps at resolution ∼12″ in this work, which are presented in Figures 4.4c and 4.4d, respectively. In the direction of the HFSs, the hubs or junctions of the sub-filaments hosting the 6.7 GHz MMEs are found with higher column densities ($N(H_2)$ ∼10^{23} cm^{-2}) and elevated dust temperatures ranging from 22 to 26 K (see Figure 4.4d). Figure 4.4e shows a two-color composite image using the $N(H_2)$ (in red) and T_d maps (in cyan). In Figure 4.4e, the filament F2

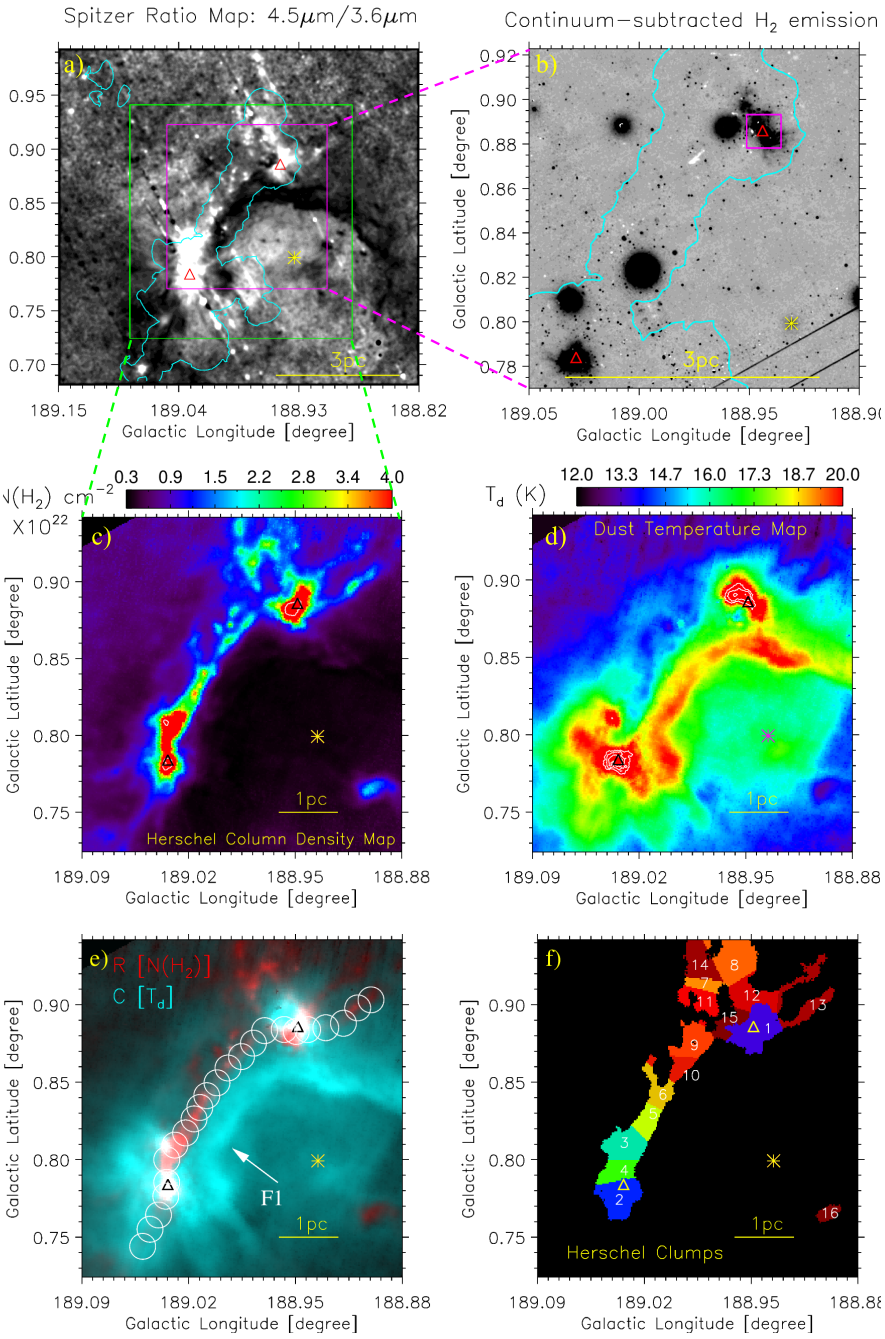

Figure 4.4: (a) *Spitzer* ratio map (4.5 μm/3.6 μm) overlaid with the YSOs surface density contour at 15 YSOs pc^{-2}. (b) The continuum-subtracted H_2 emission map at 2.12 μm for an area highlighted by a magenta rectangle in Figure 4.4a. The rectangle plotted over AFGL 5180 presents the area utilized for the zoomed-in view in Figure A.2. (c) The *Herschel* $N(H_2)$ map, with a white contour at $N(H_2) = 10^{23}$ cm^{-2}. (d) The *Herschel* T_d map (for the same area as Figure 4.4c), with white contours at T_d = 22, 24, and 26 K. (e) A two-color composite image using the *Herschel* $N(H_2)$ map (in red) and T_d map (in cyan). Several circles of radius 30″ are marked in this panel, where average values of various physical parameters are calculated (see Figure 4.7 and Section 4.3.5.1 for details). (f) The panel shows the clumps identified using the IDL-based algorithm *clumpfind* over *Herschel* $N(H_2)$ map. The last four panels display a scale bar of 1 pc. All other symbols are the same as those in Figure 4.1a.

and the curved feature F1 are distinctly identified in the *Herschel* temperature map (see also Figure 4.4d). The curved feature F1 exhibits a relatively higher dust temperature than the filament F2, except for its edges. To put it differently, the elongated filament F2 exhibits a higher column density and lower dust temperature, but the curved structure F1 shows a higher dust temperature and lower column density.

4.3.4.1 Study of *Herschel* clumps and their physical parameters

To analyze fragmentation and detect clumps in the column density map, we used the *clumpfind* algorithm (see Section 2.3.4 for details). In total, 16 clumps are identified in the column density map, as illustrated in Figure 4.4f. The mass of each clump ($M_{\rm clump}$) can be estimated using Equation 2.16,

$$M_{\rm clump} = \mu_{\rm H_2}\, m_{\rm H}\, {\rm Area}_{\rm pixel} \Sigma N({\rm H_2})$$

All the parameters have been defined previously in Section 2.3.5. The value of $\mu_{\rm H_2}$ is adopted to be 2.8 (Kauffmann et al., 2008) for estimating mass of the clumps. Including the mass, various other physical parameters of these 16 clumps are listed in Table 7.1. The mass of these clumps is found to vary between 27 to 498 $M_{\odot}$. The two most massive clumps (IDs: #1 and #2) are located toward the MSFRs T1 and T2, respectively. Additionally, multiple fragments or clumps (IDs: #3, #4, #5, #6, #9, and #10) are distributed along their connecting filament F2 (see Figure 4.4f).

4.3.4.2 The physical parameters of the sub-filaments

To comprehend the changes in column density and dust temperature along the sub-filaments toward AFGL 5180 and AFGL 6366S, we have selected multiple circular regions with a radius of 7″ along the sub-filaments. In Figure 4.5a,

Table 4.1: The list of the physical parameters of the *Herschel* clumps. $R_{\rm clump}$ is the effective radius and $[N(H_2)]_{\rm peak}$ presents the peak column density. $[T_{\rm d}]_{\rm peak}$ and $[T_{\rm d}]_{\rm avg}$ are peak and average dust temperature, respectively.

ID	l	b	$R_{\rm clump}$	$M_{\rm clump}$	$[N(H_2)]_{\rm peak}$	$[T_{\rm d}]_{\rm peak}$	$[T_{\rm d}]_{\rm avg}$
	(degree)	(degree)	(pc)	($M_\odot$)	($\times 10^{22}$ cm^{-2})	(K)	(K)
1	188.951	0.882	0.39	498	36.48	26	19
2	189.030	0.781	0.35	274	22.30	36	21
3	189.032	0.808	0.32	261	12.69	22	18
4	189.032	0.790	0.25	128	7.10	27	20
5	189.014	0.826	0.24	91	3.72	17	15
6	189.007	0.839	0.25	74	3.66	17	15
7	188.975	0.911	0.19	46	3.21	15	14
8	188.966	0.922	0.37	156	3.19	15	13
9	188.991	0.871	0.30	97	3.03	16	15
10	188.992	0.859	0.21	51	2.70	16	15
11	188.977	0.904	0.26	70	2.63	16	15
12	188.953	0.903	0.30	105	2.55	24	17
13	188.910	0.897	0.32	101	2.53	17	14
14	188.974	0.918	0.30	106	2.43	15	13
15	188.958	0.889	0.22	54	2.43	26	20
16	188.902	0.762	0.16	27	1.83	14	14

the sub-filaments identified by *getsf* toward AFGL 5180 and AFGL 6366S are outlined in gray on the *Herschel* column density map. The selected circular regions along the sub-filaments have also been overplotted. The average values of column density and dust temperature for these circular regions are displayed as a function of distances along the sub-filaments from their corresponding hubs in Figures 4.5b and 4.5c, respectively. For AFGL 5180 and AFGL 6366S, lengths of their corresponding filaments range from 1 to 2 pc. The sub-filaments associated with AFGL 6366S exhibit higher dust temperatures (∼16–23 K) and lower column density (∼5×10^{21}–3×10^{22} cm^{-2}) compared to the sub-filaments of AFGL 5180 ($T_{\rm d}$ ∼13–19 K and $N(\rm H_2)$ ∼1×10^{22}–4×10^{22} cm^{-2}). For sub-filaments, the average values of dust temperature and column density are highest at their junctions or hubs and gradually decrease along their lengths as one moves away from the hubs. The pattern of increasing column density along the filaments toward the hub has also been observed in one of the most notable HFSs in the literature, Mon R2 (see Figures 2 and 3 in Kumar et al., 2022).

4.3.5 Probing the distribution of molecular gas

In this section, we have analyzed the CO line data to investigate the gas distribution in both the spatial and velocity space. The details of the molecular data utilized in this work are provided in Section 4.2.

4.3.5.1 Distribution and kinematics of molecular gas

In this section, we have presented the moment maps of ^{12}CO, ^{13}CO, and C^{18}O emission for an area highlighted by a magenta rectangle in Figure 4.3c. The boundary of the H II region (S247), the locations of 6.7 GHz MMEs, and massive O-type (cgo115) are indicated in all the moment maps. Typically, C^{18}O data is optically thin compared to ^{12}CO and ^{13}CO data and traces relatively denser

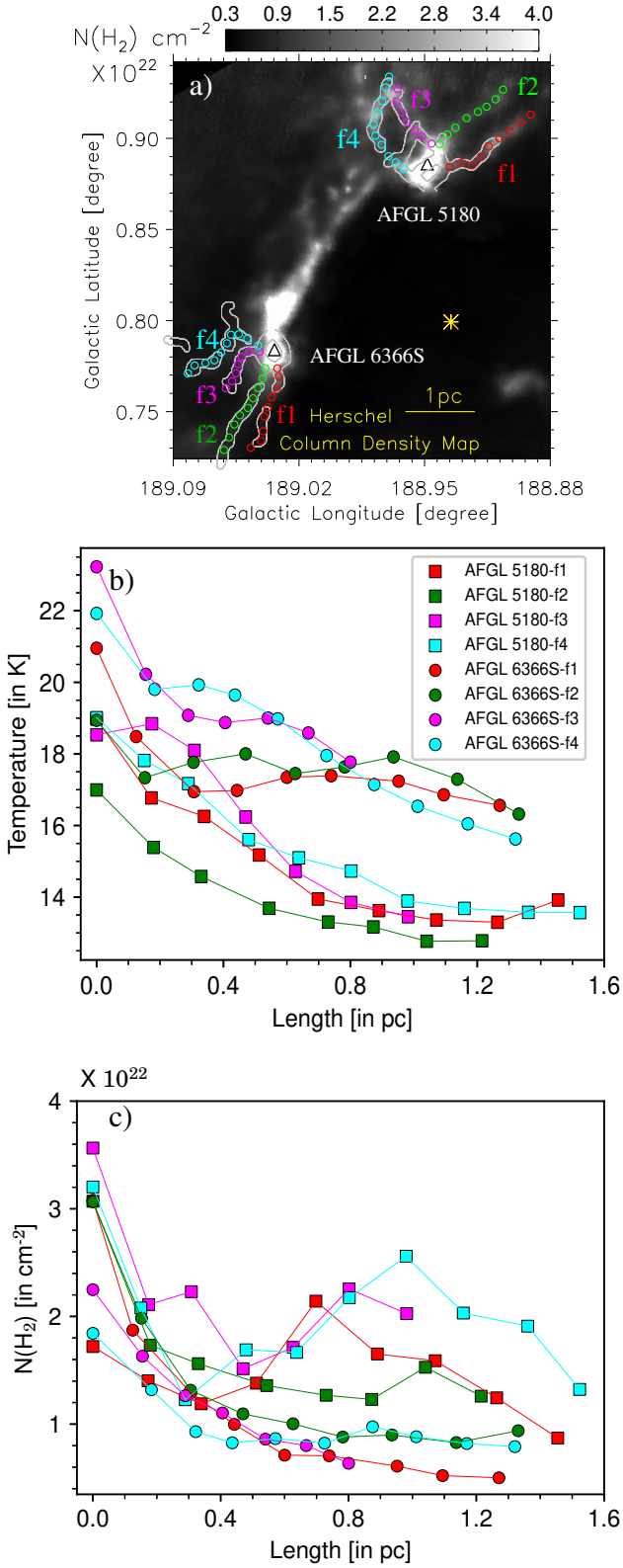

Figure 4.5: (a) *Herschel* column density map same as in Figure 4.4c, presented in grayscale. The sub-filaments (such as f1, f2, f3, and f4) toward AFGL 5180 and AFGL 6366S are outlined in gray. The other symbols are consistent with those in Figure 4.4c. Panels (b) and (c) present changes in the average dust temperature and column density along the sub-filaments for the circular regions highlighted in panel (a).

regions of the molecular cloud. All the moment-0 maps exhibit nearly identical morphology and support the existence of an elongated molecular cloud that hosts T1 and T2 at its two ends. Both T1 and T2 show intense molecular emission in ^{12}CO/^{13}CO/C^{18}O data compared to their filamentary connection. Figures 4.6b, 4.6e, and 4.6h display the moment-1 maps of ^{12}CO, ^{13}CO, and C^{18}O, respectively. Significant variations in velocity (of about 1-2 km s^{-1}) are noted between the MSFRs (i.e., T1 and T2) and the filament connecting them. The filaments identified from the dust continuum emission are overplotted on the moment-1 map for the ^{13}CO and C^{18}O emission in Figures 4.6e and 4.6h, respectively. The filamentary connection between T1 and T2 is primarily identified in the velocity range of [1.3, 2.7] km s^{-1} as shown in Figures 4.6e and 4.6h. Although the molecular line data have coarse beam size compared to the *Herschel* 160 μm image used to detect the filaments, the moment-0 maps reveal an elongated morphology spatially coexisting with filament F2. Nevertheless, sub-filaments are not observed in the moment-0 maps. In Figures 4.6c, 4.6f, and 4.6i, we illustrate the line-width maps for the ^{12}CO, ^{13}CO, and C^{18}O data, respectively. Overall, the line-width map for ^{12}CO exhibits the largest values, while C^{18}O shows the least in the same. However, across all lines, relatively higher line-width values are observed toward the edges of the filament, particularly towards T1 and T2, compared to the rest of the filament.

We have marked several circular regions with a radius of 30″ along the filament F2 in Figure 4.4e, and various physical parameters along the filament have been extracted for those regions. The average values of column density and dust temperature for the circular regions are shown in Figures 4.7a and 4.7b, respectively. These values are calculated using the *Herschel* column density and dust temperature maps, illustrated in Figures 4.4c and 4.4d, respectively. Higher values of column density and dust temperature are observed toward T1 and T2. Utilizing

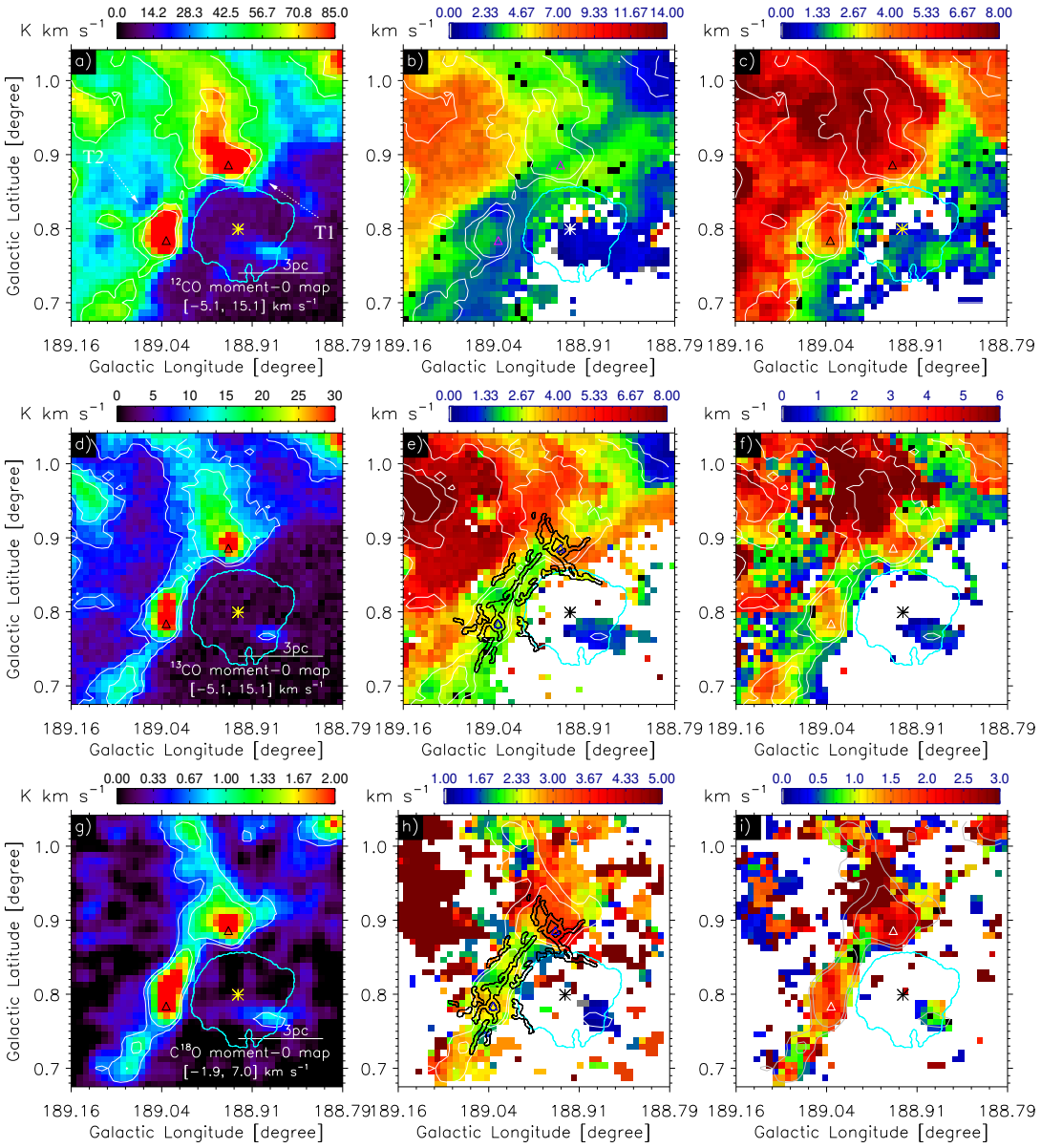

Figure 4.6: The moment maps for ^{12}CO/^{13}CO/C^{18}O($J = 1$–0) line data. Panels (a), (d), and (g) show moment-0 maps for ^{12}CO, ^{13}CO, and C^{18}O data, respectively. The velocity ranges of integration are given in each moment-0 map. Panels (b), (e), and (h) show moment-1 maps for ^{12}CO, ^{13}CO, and C^{18}O data, respectively. The line-width (FWHM) maps of ^{12}CO, ^{13}CO, and C^{18}O data are shown in panels (c), (f), and (i), respectively. All the moment maps of ^{12}CO data in the top row are overplotted with ^{12}CO moment-0 contours at 30% and 40% of the peak value (i.e., ∼174 K km s^{-1}). Similarly, the moment maps of ^{13}CO data in the middle row and those for C^{18}O data in the bottom row are overplotted with their moment-0 contours at 20% and 30% of their respective peak values (i.e., ∼43 K km s^{-1} and ∼3.3 K km s^{-1}, respectively). The moment-1 maps of ^{13}CO and C^{18}O emission are overlaid with the *getsf*-identified filament skeletons in black. In all panels, the NVSS 1.4 GHz radio continuum contour at 1.35 mJy beam^{-1} is displayed in cyan, and other symbols are consistent with those shown in Figure 4.1a.

the ^{13}CO and C^{18}O molecular line data, we have also calculated the average velocity, thermal sound speed ($c_{\rm s} = (kT_{\rm kin}/\mu m_{\rm H})^{1/2}$), non-thermal velocity dispersion ($\sigma_{\rm NT}$), and the ratio of thermal to non-thermal pressure ($P_{\rm TNT} = c_{\rm s}^2/\sigma_{\rm NT}^2$) for the same circular regions. Here, $T_{\rm kin}$ refers to the kinetic gas temperature and to calculate thermal sound speed, we have assumed $T_{\rm kin}$ to be equivalent to the average dust temperatures. The mean molecular weight per particle μ is adopted to be 2.37 (Kauffmann et al., 2008). The thermal and non-thermal velocity dispersion (denoted as $\sigma_{\rm T}$ and $\sigma_{\rm NT}$, respectively) for a molecular gas can be estimated using,

$$\sigma_{\rm T} = (kT_{\rm kin}/\chi m_{\rm H})^{1/2}, \tag{4.4}$$

$$\sigma_{\rm NT} = \sqrt{\frac{\Delta V^2}{8\ln 2} - \frac{kT_{\rm kin}}{\chi m_{\rm H}}} = \sqrt{\frac{\Delta V^2}{8\ln 2} - \sigma_{\rm T}^2}, \tag{4.5}$$

where χ represents the mass of the molecules in units of hydrogen atomic mass, while ΔV indicates the measured line-width (FWHM) for the molecular line data. Therefore, χ ~29 and ~30 for ^{13}CO and C^{18}O, respectively. By analyzing the average velocity and non-thermal velocity dispersion profiles for ^{13}CO and C^{18}O, as illustrated in Figures 4.7c and 4.7d respectively, it is clear that T1 and T2 are associated with higher velocity and non-thermal velocity dispersion. Moreover, T1 exhibits higher velocity than T2, and both ^{13}CO and C^{18}O data reveal an oscillatory pattern in their velocity profiles. The profiles for Mach number ($\frac{\sigma_{\rm NT}}{c_{\rm s}}$) and thermal to non-thermal pressure ratio are shown in Figures 4.7e and 4.7f, respectively. From the Mach number profile, derived using C^{18}O, we can find that the star-forming sites T1 and T2 are supersonic (with Mach number $>$ 3). However, Mach number profile for the C^{18}O data drops down to ~2 toward the filamentary connection between T1 and T2 (see Figure 4.7e). Mach number profile extracted using the ^{13}CO line data reveals the supersonic nature of the filament (i.e., Mach number $>$ 3; see Figure 4.7e). The filamentary structure F2 is traced with lower non-thermal velocity dispersion, leading to higher thermal

to non-thermal ratios compared to T1 and T2 in $C^{18}O$ data. In Figure 4.7f, the values of P_{TNT} are different in the ^{13}CO and $C^{18}O$ emissions. Because the $C^{18}O$ data is optically thin compared to the ^{13}CO emission. Therefore the $C^{18}O$ emission is less affected by the opacity broadening (Phillips et al., 1979; Hacar et al., 2016; Yang et al., 2022).

4.3.5.2 Identification of the molecular cloud components

To gain a comprehensive understanding of the molecular gas distribution toward our target sites, we analyzed ^{13}CO data for an extended area of $\sim 1^\circ \times 1^\circ$ (or $\sim 26\,\mathrm{pc} \times 26\,\mathrm{pc}$). The moment-0 map of ^{13}CO data for the extended area is displayed in Figure 4.8a for a velocity integration range of $[-5.1, 15.1]$ km s^{-1}. The moment-0 map reveals a complex morphology of the molecular cloud. Figure 4.8b presents *Hersechel* 250 μm image for the same area. The *Hersechel* FIR image exibits the elongated filamentary structure embedded in the molecular cloud, which hosts 6.7 GHz MMEs at opposite edges. In Figure 4.8c, the moment-1 map for the ^{13}CO data reveals two different velocity ranges in colors blue and red. The average intensity profile extracted from the rectangular region highlighted in Figure 4.8c is presented in the inset. This profile reveals two velocity components, with their peaks observed at the velocities ~ 2.7 km s^{-1} and ~ 6.4 km s^{-1} for the blue- and red-shifted components, respectively (see the blue and red vertical lines). The blue- and red-shifted components have a relative velocity of about 3.7 km s^{-1}. To ascertain the velocity ranges for the cloud components, the Galactic latitude–velocity (b–v) diagram is presented in Figure 4.8d. This b–v diagram corresponds to the area shown by a white dotted rectangle in Figure 4.8a. This diagram reveals two cloud components: the blue-shifted component in the velocity range of $[-3.1, 4.8]$ km s^{-1} and the red-shifted component in the velocity range of $[5.8, 12.9]$ km s^{-1}. Both the cloud components are observed to be con-

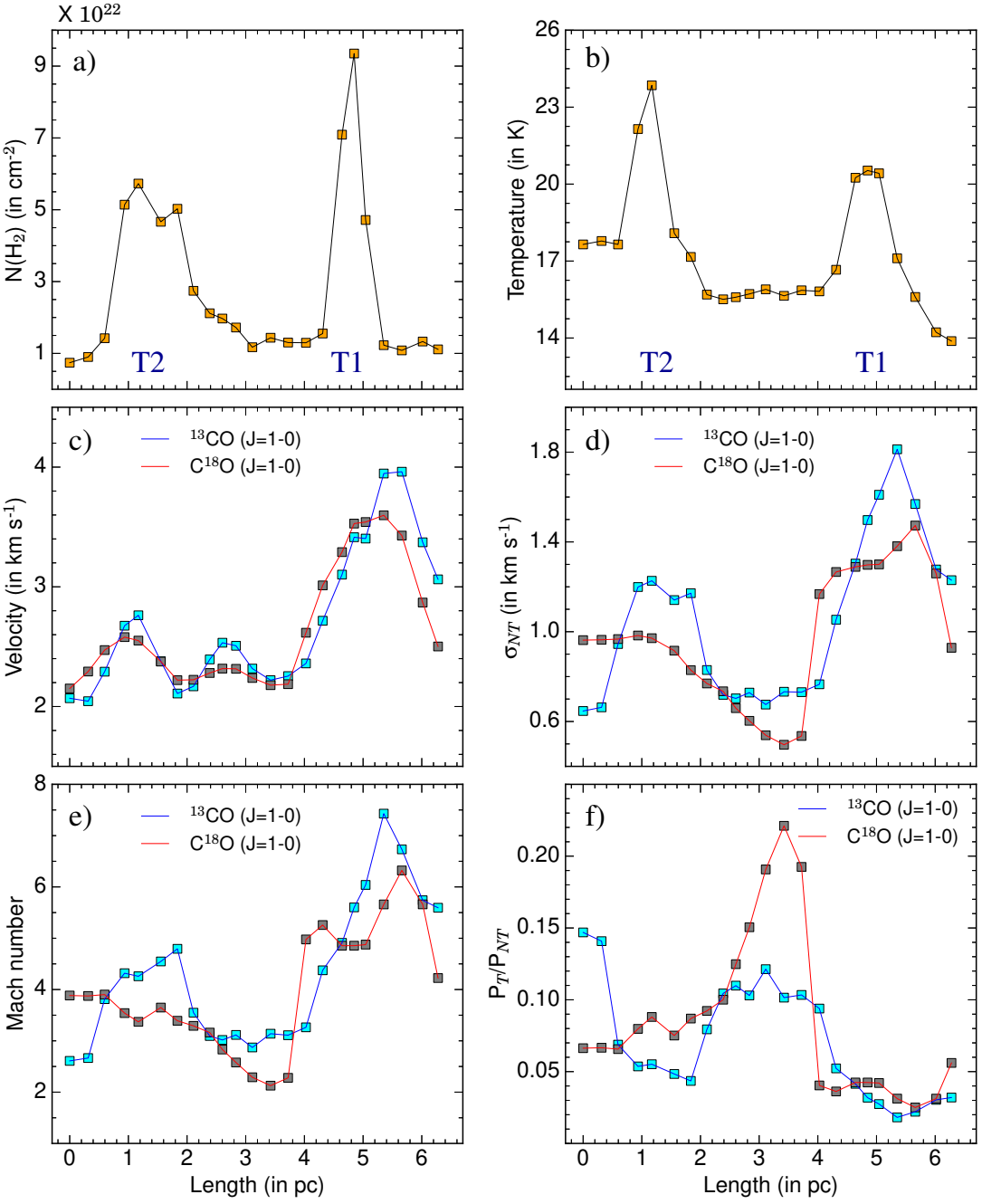

Figure 4.7: Plot of (a) average column density, (b) average dust temperature, (c) radial velocity, (d) non-thermal velocity dispersion, (e) Mach number, and (f) ratio of thermal to non-thermal gas pressure for the circular regions shown in Figure 4.4e. In panels (c)–(f), physical parameters are shown for ^{13}CO and C^{18}O line data.

nected with weak molecular emission in an intermediate velocity range of [4.8, 5.8] km s^{-1}, which is denoted by two yellow dashed lines in Figure 4.8d.

4.3.5.3 Spatial distribution of molecular cloud components

The moment-0 maps for the blue- and red-shifted cloud components are shown using cyan and red colors, respectively, as a two-color composite image in Figure 4.9a. The red-shifted cloud component is displayed within the rectangular region highlighted in yellow. A complementary spatial distribution between two cloud components is visible in Figure 4.9a. However, a more convincing picture of their complementary spatial distribution is achieved by shifting the red-shifted cloud component toward the south-west direction by about 2.3 pc as presented in Figure 4.9b. The positions of the red-shifted cloud component before and after the shift/displacement are indicated by the dashed and solid yellow rectangles, respectively. The MSFRs, represented by the triangles depicting the locations of the 6.7 GHz MMEs, are observed toward the interface of the two cloud components (see in Figure 4.9b).

Section 4.4 presents the implication of these observed results.

4.4 Discussion

Using the *Herschel* image at 160 μm, the results from the *getsf* utility reveal two noteworthy structures in our area of interest: the curved feature F1 and the filament F2. The curved feature F1 corresponds with the PAH emission at 3.3 μm and is located at the boundary of the H II region (S247). Both T1 and T2 host HFSs, which are located at the edges of filament F2. Evidence of outflow activities and YSOs are found toward the entire filament F2. Notably, groups of

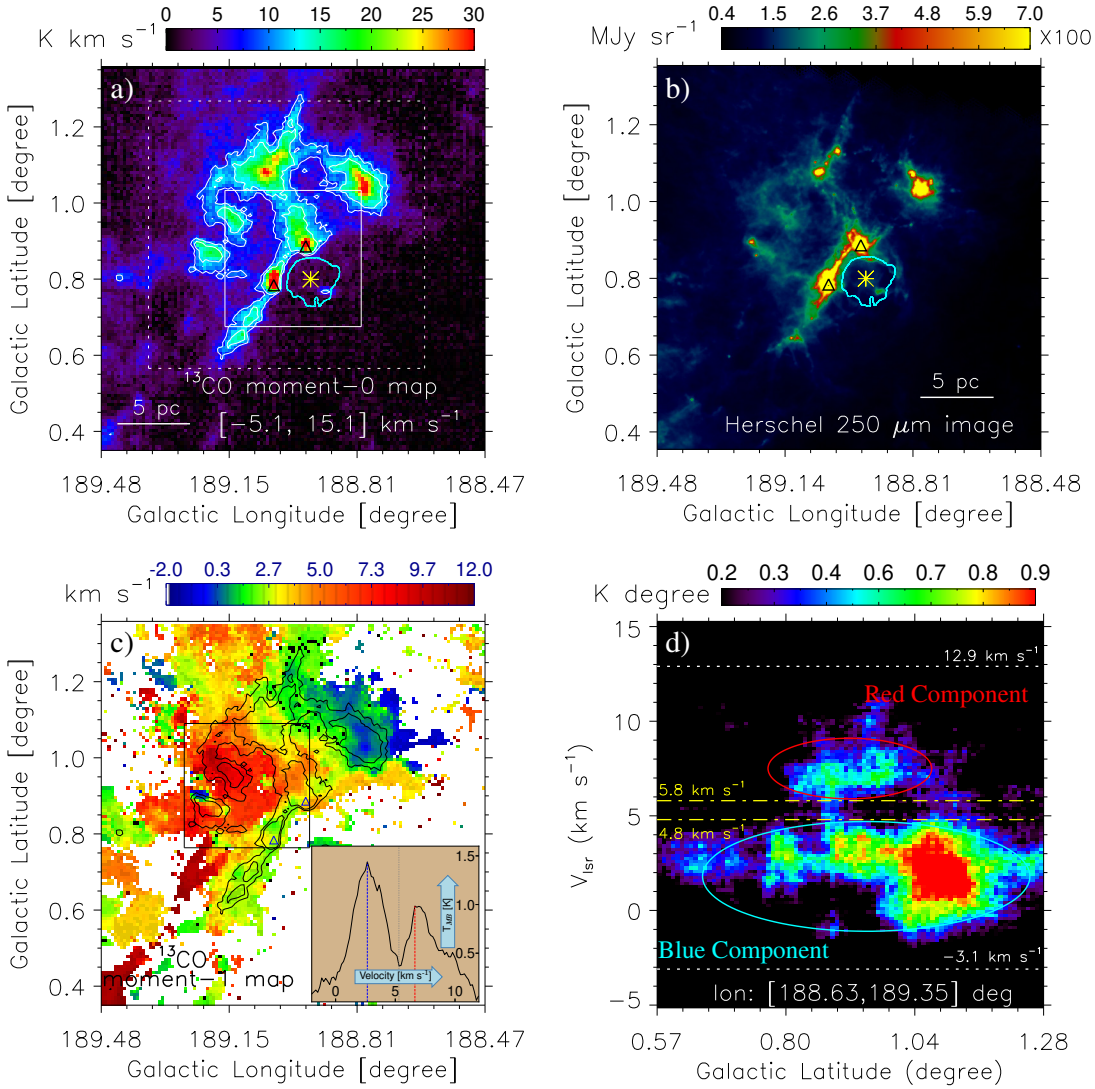

Figure 4.8: (a) Moment-0 map of ^{13}CO emission toward our target sites for an area about 1° × 1° and a velocity integration range of [-5.1, 15.1] km s^{-1}. The contours represent 20% and 30% of the peak value (i.e., ∼43 K km s^{-1}). A scale bar of 5 pc is added in this panel, along with other symbols identical to Figure 4.6. The solid white rectangle represents the area of the molecular data depicted in Figure 4.6. The dotted white rectangle highlights the portion of the molecular data used for the Galactic latitude–velocity diagram shown in Figure 4.8d. (b) *Herschel* 250 μm image for the same area as shown in Figure 4.8a. (c) Moment-1 map for ^{13}CO data with the same contours as presented in Figure 4.8a. The black rectangle indicates the area used to extract the average intensity profile displayed in the inset. (d) Galactic latitude–velocity diagram corresponds to the integration range of Galactic longitude [188.°63, 189.°35]. The dashed and dotted horizontal lines indicate different V_{lsr} values, as mentioned in the figure. The cyan and red ellipses highlight the blue-shifted and red-shifted cloud components, respectively.

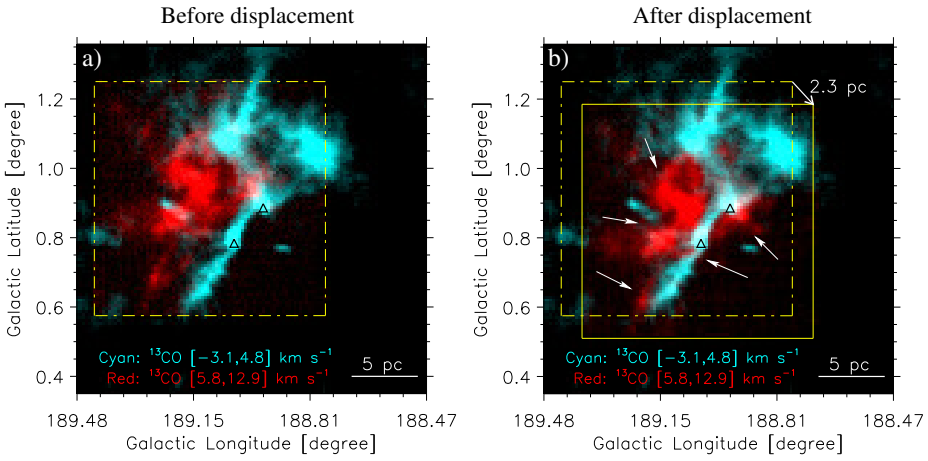

Figure 4.9: (a) The two-color composite image presents the spatial distribution of the blue- and red-shifted cloud components. The blue- and red-shifted components are shown in cyan and red on the linear scales from 2 to 14 and 0 to 8 K km s^{-1}, respectively. The red-shifted component is confined in the yellow dashed rectangle. (b) Spatial distribution of the blue- and red-shifted cloud components with a spatial shift of about 2.3 pc. The dashed and solid yellow rectangle presents the initial and final positions of the red-shifted cloud component, respectively. The white arrows indicate the complementary distribution between the cloud components. The velocity integration ranges for the blue- and red-shifted cloud components are mentioned in both panels. The scale bar and other symbols are same as Figure 4.8a.

YSOs and the 6.7 GHz MMEs are primarily concentrated at the opposite edges of F2. The examination of ^{12}CO, ^{13}CO, and C^{18}O line data reveals supersonic and non-thermal gas motions toward both the HFSs (see Figure 4.7). The velocity dispersion is found to be higher at the edges of the filament compared to its central region, suggesting intense star-forming activities at the edges. Earlier studies suggested both CCC and triggered star formation scenarios in our selected target area. In light of our observational findings, we have carefully assessed these scenarios and the role of filaments in the subsequent sections.

4.4.1 Impact of the massive star on its environment

Massive stars emit Lyman continuum photons that ionize the surrounding medium and create an H II region. This H II region expands supersonically into

the surrounding neutral gas, generating a shock wave. Based on this property, two main scenarios have been proposed in the literature to explain triggered star formation: the "collect and collapse" (C&C; Elmegreen & Lada, 1977) and the radiatively driven implosion (RDI; Bertoldi, 1989). In the RDI model, star formation occurs due to the compression of pre-existing dense clumps by the shock wave. Meanwhile, in the C&C scenario, the shock wave sweeps up cooler neutral gas, forming a massive and dense shell surrounding the H II region (Deharveng et al., 2005; Dale et al., 2007). Over time, this shell of collected gas becomes gravitationally unstable and collapsesto to form new stars.

In our target area, a cavity in the molecular gas distribution is observed in all the moment-0 maps. This cavity in molecular gas distribution indicates an interaction between molecular gas and the ionizing photons from the massive O-type star (cgo115). The curved feature F1, which lacks molecular emission, is positioned near cgo115. In contrast, filament F2 traced in dust continuum maps, as well as in the molecular emission, is located farther away from both F1 and cgo115. The excess of PAH 3.3 μm emission in the *Spitzer* 3.6 μm band suggests that the O-type star possibly has a notable impact on F1. The calculated pressure components (i.e., $P_{\rm wind}$, $P_{\rm rad}$, and $P_{\rm H\,II}$) have consistent values along F1, with $P_{\rm H\,II}$ being the most dominant and $P_{\rm wind}$ having the least contribution. The combined pressure value along F1 is about 10^{-10} dynes cm^{-2}, well above the typical molecular gas pressure ($\sim$$10^{-11}$ dynes cm^{-2}; see Table 7.3 in Dyson & Williams, 1997). Therefore, the feedback from cgo115 seems sufficient to form the feature F1 and may be responsible for its curved appearance. Similar pressure analysis along the filament F2 (see Figure 4.2c) shows that all pressure components decrease as one moves away from the central part of the filament. Notably, since the H II region is not directly connected with F2 (see the cyan contour in Figure 4.2a), we can disregard $P_{\rm H\,II}$ while computing combined pressure. The

total of wind and radiation pressure along F2 peaks at around 1.5×10^{-11} dynes cm^{-2}, which can be counterbalanced by the molecular gas pressure. When $P_{H\,II}$ is included, we observe that the peak of the combined pressure is around 10^{-10} dynes cm^{-2}. Including $P_{H\,II}$, we find the peak of the combined pressure around 10^{-10} dynes cm^{-2}. Consequently, cgo115 has the potential to influence F2 in the future. However, the current pressure values along F2 and its linear morphology do not allow us to connect its origin due to the feedback of cgo115. The combined pressure values of cgo115 at the MSFRs T1 and T2 are also insignificant in affecting the massive star-forming activity. Therefore, the triggered star formation scenarios are not feasible in these MSFRs. This finding agrees with the previously reported work of Vasyunina (2010). By analyzing NIR spectroscopic data of the AFGL 5180 cluster, Vasyunina (2010) revealed that the more evolved stars are located further away from the H II region, whereas the younger sources that are driving outflows are situated closer to the H II region. This signature contradicts the prediction of the triggered star formation scenarios (Dale et al., 2007, 2015).

4.4.2 Role of filaments toward our target sites

The 6.7 GHz MMEs toward T1 and T2 and a small cluster of radio continuum sources toward T1 support the ongoing massive star-forming activity in both HFSs. Hubs or junctions of the sub-filaments toward T1 and T2 show higher column density and dust temperature. We suggest that the mass accumulation through sub-filaments from the large-scale to the dense core-scale is the possible scenario for MSF toward T1 and T2 (e.g., Myers, 2009; Tigé et al., 2017; Motte et al., 2018; Treviño-Morales et al., 2019; Rosen et al., 2020). Previously, Minier et al. (2001) proposed that the 6.7 GHz MMEs are likely indicators of the massive protostellar phase during the early stages of MSF. The massive protostellar phase aligns with the high-mass protostellar phase in the evolutionary paradigm of MSF

from HFS (discussed in Section 1.6) suggested by Motte et al. (2018).

As mentioned in Section 1.6, a recent study by Kumar et al. (2020) aimed to identify HFSs in the Galactic plane within the Galactic longitude and latitude range of $-72^{\circ} \leq l \leq 68^{\circ}$ and $|b| \leq 1^{\circ}$. They detected nearly 3,700 HFS candidates by analyzing *Herschel* 250 μm images toward the Hi-GAL clumps listed in Elia et al. (2017). In addition, their findings revealed that all clumps with luminosities exceeding $10^4\,L_{\odot}$ (within 2 kpc) and $10^5\,L_{\odot}$ (within 5 kpc) are situated at the hubs of HFSs. Interestingly, they observed that HFSs typically consist of 3–7 filaments, with the average filament length ranging between 10 and 20 pc. In this context, the identification of HFSs in AFGL 5180 and AFGL 6366S provides further insights into the nature and properties of these structures. The Hi-GAL clumps toward AFGL 5180 and AFGL 6366S have luminosities of $\sim 10^3$ and $\sim 10^4\,L\odot$ (Elia et al., 2021), respectively. Both the clumps host 6.7 GHz MMEs as the signpost of massive star-forming activity, and they are associated with at least 4 filaments detected based on *Herschel* 160 μm image. The column density and dust temperature values increase along the filaments in the direction to the hubs. The flow of dust and gas through the filaments amplifies the column density of the hub, suiting it for MSF (Myers, 2009; Kumar et al., 2020; Dewangan et al., 2023a). The length of the filaments participating in the formation of HFSs toward our target sites is nearly 1–2 pc. Therefore, for nearby regions ($d \lesssim$ 2 kpc), one can expect more HFSs with parsec-scale filaments. This proposal also agrees with the filament selection criteria of Kumar et al. (2020) because the length scale associated with the image's resolution increases with distance. It is also noticeable that, though the Hi-GAL clump at AFGL 5180 has a luminosity of $\sim 10^3\,L\odot$, it is an observed massive star-forming site. Therefore, we can also expect more such sources in the analysis of 360° *Herschel* data. Hence, a similar analysis like Kumar et al. (2020) for the Hi-GAL 360° clumps (Elia et al., 2021)

with *Herschel* 160/250 μm images can reveal more details about HFSs.

In star formation study, it is evident that molecular clouds often create filamentary structures, which further fragment into dense cores (e.g., André et al., 2010). Our molecular gas study shows a similar filamentary structure further fragmented in dense cores toward its edges. Recently, Clarke et al. (2020) found that the filaments are more prone to fragment into sub-filaments, which are responsible for the formation of hubs via their merging event, and the cores formed at the filament's edges are more massive than the interior ones. The coarse beam sizes of the molecular line data are one of the key obstacles in studying such aspects. Therefore, such a study is beyond the scope of this work. In the last chapter, we discussed the possible connection between HFSs and CCC (see Section 3.4.2) based on our observational work on the W31 complex. Therefore, the next section will focus on the possible CCC scenario for our target sites, AFGL 5180 and AFGL 6366S, where we have detected one HFS in each site.

4.4.3 Cloud-cloud collision scenario

The CCC scenario is an effective triggering mechanism of MSF. Based on the analysis of ^{12}CO(J = 2–1) data (beam size $\sim$2.″7), earlier Shimoikura et al. (2013) proposed CCC as a possible triggering mechanism in our target sites (see Figures 3b and 4 in their paper). They reported two cloud components at the velocities of [−3, 5] and [5, 13] km s^{-1}. In Section 4.3.5.2, we have also found the existence of two cloud components (around [−3.1, 4.8] and [5.8, 12.9] km s^{-1}), which are connected by a bridge feature in velocity space. Additionally, we have investigated a spatial fit of "key/intensity-enhancement" and "cavity/keyhole/intensity-depression" features (i.e., complementary distribution) of two clouds, which is further strengthened after a spatial shift of about 2.3 pc in the red-shifted cloud component. As previously discussed in Section 1.7, Fukui et al. (2018b) detected

similar signature of CCC (i.e., complementary distribution with a spatial shift) toward M43 for the formation of massive stars in the Orion Nebula Cluster (see Figure 1.11). The PV diagrams depend upon the angle ($\theta_{\rm col}$) between the axis of collision and the line of observation, which is thoroughly explained in Section 1.7. In the last chapter, we assumed $\theta_{\rm col} = 10°$ based on minute skewness of the "V" like feature in PV diagram for the CCC scenario in the W31 complex. It is important to note that the PV diagram also depends upon the spatial morphology of the molecular cloud components. Now, the detection of two cloud components toward our target sites in the PV diagram suggests that $\theta_{\rm col}$ is below 90° (Fukui et al., 2018b, 2021a). On the other hand, the requirement of spatial shift for the complementary distribution indicates $\theta_{\rm col}$ to be greater than 0°. Therefore, it is logical to use $\theta_{\rm col}$ values ranging from 30° to 60° for estimating the collision time scale. If the observed velocity difference between the colliding clouds is $V_{\rm obs}$, then along the collision axis it would be, $V_{\rm loc} = \frac{V_{\rm obs}}{\cos\theta_{\rm col}}$. Similarly, spatial shift along the collision axis would be, $l_{\rm loc} = \frac{l_{\rm obs}}{\sin\theta_{\rm col}}$, for the observed spatial shift of $l_{\rm obs}$ in the sky plane. Finally, the collision time scale can be obtained by, $t_{\rm collision} = \frac{l_{\rm loc}}{V_{\rm loc}}$. In case of present study, the observed velocity and spatial shift are $V_{\rm obs} = 3.7\,{\rm km\ s^{-1}}$ and $l_{\rm obs} = 2.3\,{\rm pc}$, respectively. Thus for various values of $\theta_{\rm col}$, i.e., $\theta_{\rm col} = 30°$, 45°, and 60°, $t_{\rm collision}$ is found to be 1.05, 0.60, and 0.35 Myr, respectively. Hence, a collision between molecular clouds about 1 Myr ago initiated the massive star-forming activity toward our target sites. However, it is interesting to note that previous studies determined the age of the NIR cluster to be ∼2.5 Myr (Devine et al., 2008; Vasyunina, 2010). This infers that the colliding clouds were active in low-mass star formation well before the collision took place. As earlier mentioned, CCC is emerging as a potential mechanism of HFS formation in both theoretical and observational studies (Balfour et al., 2015; Fukui et al., 2019; Tokuda et al., 2019; Maity et al., 2022).

It is interesting to note that our target sites host two HFSs located at the edges of a primary filament F2. To date, only a few such systems have been reported in the literature, including the filamentary clouds G45.1+0.3 (Bhadari et al., 2022), IC 5146 dark streamer (Wang et al., 2019; Dewangan et al., 2023b), and NGC 6334 (Zernickel et al., 2013; Arzoumanian et al., 2021). These findings thus open a new window for discussing the formation of HFSs at the edges of a filament.

4.4.4 End-dominated collapse scenario

Wang et al. (2019) proposed an idea for forming HFSs at the opposite edges of a filament in their study of IC 5146 dark Streamer, considering the role of magnetic field and gravitational instability of an isolated filament. Filament gravitationally collapses along its major axis once it becomes thermally and magnetically supercritical. Due to the effect of end-dominated collapse (EDC), massive fragments are exclusively formed at the edges of the filament. According to Bastien (1983); Pon et al. (2012); Clarke & Whitworth (2015), the differential gravitational acceleration along the major axis of an isolated filament drives EDC depending upon its aspect ratio. During the EDC process, the ram pressure exerted by gas motion is sufficient to pinch the magnetic field lines and form the U-shaped magnetic field (or bending effect; see more details in Gómez et al., 2018; Wang et al., 2019) at the filament's edges. A recent study by Wang et al. (2019) and Chung et al. (2022) suggested that the EDC filament IC 5146 prefers to show the bending effect at its edges. Using *Planck* polarization data, Dewangan et al. (2023b) verified this bending effect in nearby ($d \lesssim 2$ kpc) EDC filaments (i.e., NGC 6334; Zernickel et al. (2013), S242; Dewangan et al. (2019); Yuan et al. (2020), IC 5146; Wang et al. (2019); Chung et al. (2022), and Mon R1; Bhadari et al. (2020)). Finally, the massive components accumulated at the edges of the

filament fragments further along the curved magnetic fields to form HFSs (see Figure 13 in Wang et al., 2019).

In literature, apart from IC 5146, the filamentary clouds G45.1+0.3 (Bhadari et al., 2022) and NGC 6334 (Zernickel et al., 2013; Arzoumanian et al., 2021) serve as the sites where the EDC and HFSs are simultaneously investigated. Although signatures of MSF, massive dust clumps, higher column densities, and clusters of YSOs are mainly depicted toward both the edges of the filament F2, our analysis of *Planck* polarization data (see the details in Appendix A.1) does not clearly show the bending effect (see Figure A.1a) to draw a conclusive statement on the EDC process. New high-resolution polarization data toward our target area can shed more light on the bending effect toward both edges of F2. In addition, we conducted a core-scale study of the AFGL 5180 region to investigate the outflow activity and physical association between the 6.7 GHz MME and NVAS 8.46 GHz radio continuum emission with embedded dust cores. To accomplish this, we utilized high-resolution NIR images and ALMA 1.3 mm dust continuum emission. The results of our study are presented in Appendix A.2.

Altogether, our observational results suggest that CCC initiated the massive star-forming activity around 1 Myr ago toward AFGL 5180 and AFGL 6366S. The CCC can be responsible for the observed HFSs. In addition, the magnetic field and differential gravitational acceleration can also shape the observed HFS morphology in our target sites. In the context of mass accumulation toward our target sites, we suspect that the clumps in the central hub accumulate materials through filamentary accretion. Then, individual cores may grow in mass, sharing the common source of gas and dust within the clump. In other words, the final masses of the stars inside the clump are determined not only by the core/clump-scale mass accretion but also by the larger/cloud-scale filamentary mass accretion.

4.5 Summary

In this chapter, we have presented a multi-scale and multi-wavelength observational investigation of two MSFRs, AFGL 5180 and AFGL 6366S, to unveil star formation processes. This study includes careful analysis of various data sets in NIR, MIR, sub-mm, and cm wavelengths. It also includes the analysis of MWISP ^{12}CO/^{13}CO/C^{18}O(J =1–0) data. The major observational outcomes of this chapter are as follows:

1. AFGL 5180 and AFGL 6366S are nearby (d ∼1.5 kpc) MSFRs in their earlier stages. Both the sites host a Class II 6.7 GHz MME and reside at the opposite edges of a filament F2, traced in dust continuum emission at the periphery of the H II region, S247.

2. Application of the *getsf* on *Herschel* 160 μm image reveals a HFS toward both the sites, AFGL 5180 and AFGL 6366S. The NVAS 8.46 GHz radio continuum map reveals a small cluster of radio sources in the vicinity of the central hub of the HFS toward AFGL 5180.

3. Based on the analysis of the photometric data at 1–5 μm, a total of 208 YSOs are identified toward our target area. The YSOs are found along the filament F2, where outflow signatures are also traced in H_2 emission and *Spitzer* ratio map. Clusters of YSOs are primarily depicted toward the edges of the filamentary cloud.

4. The filamentary cloud seems spatially close to the H II region, S247 excited by a massive O9.5 star, cgo115. Various pressure components exerted by the O-type star (i.e., $P_{\rm H\ II}$, $P_{\rm rad}$, and $P_{\rm wind}$) on its surroundings are estimated. In this connection, the impact of the energetic feedback from the massive star on the filamentary cloud is found to be insignificant.

5. Based on the analysis of MWISP ^{13}CO(J =1–0) data, we suggest the previously proposed CCC scenario seems applicable for AFGL 5180 and AFGL 6366S.

Overall, the collision of two clouds at [−3.1, 4.8] km s^{-1} and [5.8, 12.9] km s^{-1} had occurred about 1 Myr ago. Hence, the CCC process appears to explain the observed star formation activities (including massive stars) and HFSs. The filament connecting to sites AFGL 5180 and AFGL 6366S can be a candidate for EDC. High-resolution polarimetric and spectroscopic observations in sub-mm wavelength will be essential to assess the EDC process further.

Chapter 5

G321.93–0.01: A rare site of multiple hub-filament systems with evidence of collision and merging of filaments[†]

5.1 Introduction

Over the last two decades, HFSs have emerged as potential sites for MSF (Anderson et al., 2021; Dewangan et al., 2024, and references therein). However, their origins are still not well understood. In this relation, the last two chapters of this thesis introduce new HFSs identified in the MSFRs, W31 complex (see Chapter 3) and AFGL 5180 & AFGL 6366S (see Chapter 4). In the case of the W31 complex, both HFSs toward W31-N and W31-S host extended

[†]**A. K. Maity**, L. K. Dewangan, N. K. Bhadari, Y. Fukui, A. Haj Ismail, O. R. Jadhav, Saurabh Sharma, and H. Sano, 2024, *The Astronomical Journal*, Volume 169, Issue 2, https://doi.org/10.3847/1538-3881/ad98ff

H II regions, which represent the evolved stages of MSF. The presence of HFSs in similar evolutionary stages for W31-N and W31-S indicates that they may share a common origin (see details in Section 3.4.2). Interestingly, Chapter 4 also discusses a common formation mechanism for the HFSs found in AFGL 5180 & AFGL 6366S, both of which are in relatively early stages of MSF, hosting 6.7 GHz MMEs. The primary objective of this chapter is to find multiple HFSs within the same MSFR and explore whether they can exist at different evolutionary stages. Additionally, it aims to explore their formation processes in that situation. Studies in recent years have proposed scenarios such as the overlapping/merging of filaments (Kumar et al., 2020) and the collision of molecular clouds (Maity et al., 2024, discussed in the next chapter) to explain the formation of HFSs. The connection between CCC and the presence of HFSs has already been reported in the last two chapters. However, detailed observational studies of new target sites are essential to enhance our understanding of HFS formation in diverse situations. Observational investigations are also crucial for determining how the mass accretion rate through the filaments affects overall star-forming activity, including in MSF.

Massive stars are known for their tremendous radiative and mechanical feedback, which greatly influence their parental molecular environment (e.g., Dale et al., 2014; Geen et al., 2015). Consequently, studying the origin of HFSs and the effect of mass accretion through the filaments on star formation requires thorough investigations during the early stages of MSF to ensure an undisturbed molecular environment. In this context, as previously discussed in Chapter 1, the compactness of the ionized (H II) regions acts as an indicator for detecting the early stages of MSF. To achieve the objectives of this chapter, we conducted a detailed observational study of the molecular cloud G321.93–0.01 (hereafter referred to as G321), active in the early stages of MSF. The target source G321 is

located at a distance of about 1.98 kpc (Urquhart et al., 2018).

In Figure 5.1a, we show a three-color composite map of our target area, with red, green, and blue representing *Herschel* 500, 350, and 250 μm images, respectively. A visual inspection of the FIR images in the color composite map reveals several parsec-scale filaments. The map is overlaid with the Sydney University Molonglo Sky Survey (SUMSS; Bock et al., 1999) 843 MHz radio continuum emission contours and the position of ATLASGAL clumps (Urquhart et al., 2018). Previous studies on G321 has identified 22 GHz H_2O and Class I 95 GHz MME (Walsh et al., 2011; Chen et al., 2011; Yang et al., 2017), denoted by the plus symbol in Figure 5.1a. In addition, Yang et al. (2022) identified outflow signatures in the molecular gas kinematics toward some of the ATLASGAL clumps, which are represented by black asterisks in Figure 5.1a, indicating ongoing star-forming activity in our target site G321. The presence of several filaments in *Herschel* images makes G321 an ideal site to search for multiple HFSs and to investigate their potential formation mechanisms and evolutionary stages. The absence of any extended H II in our target area ensures that the gas kinematics remain unaffected by feedback from massive stars. This allows us to explore the initial conditions of star and structure formation within the parental molecular cloud. Therefore, this source offers a unique opportunity to study the early stages of HFSs, which is a challenging task in star formation research. The proximity of G321 (d ~1.98 kpc) enables the detection and study of filaments using the SEDIGISM molecular line data. This study also helps to determine the mass accretion rate through the filaments and understand their impact on star-forming activity, including MSF.

This chapter is organized as follows: Section 5.2 presents an overview of the data sets utilized in this work. Section 5.3 highlights the key findings, which are then analyzed and discussed in Section 5.4. Finally, Section 5.5 summarizes the significant outcomes of this study.

5.2 Data sets

In this work, we explored several archival data sets from different surveys spanning in wavelengths from NIR to radio, which are listed in Table 5.1. The ionized emission toward our target region is traced with SUMSS 843 MHz (Bock et al., 1999) and SARAO MeerKAT Galactic Plane Survey (SMGPS) 1.28 GHz (Goedhart et al., 2024) radio continuum images. The RMS noise levels (σ) of the SUMSS and SMGPS data are about 1 mJy beam^{-1} and 20 μJy beam^{-1}, respectively (Bock et al., 1999; Goedhart et al., 2024). We used ^{13}CO(J = 2–1) and C^{18}O(J = 2–1) line data from the SEDIGISM survey (Schuller et al., 2017a) to study the gas distribution and kinematics, and to calculate the mass of the molecular gas. The native resolution, velocity separation, and RMS noise of these line data are about 30″, 0.25 km s^{-1} and 1 K, respectively. To reduce noise and enhance the visibility of faint or diffuse features in the molecular line data without significantly distorting the overall structure, the data were smoothed using a Gaussian function with a width of 2 pixels (i.e., ∼19″). The resultant angular resolution and RMS noise are about 36″ and 0.35 K, respectively. The *Herschel* images at 160–500 μm and the ATLASGAL 870 μm image are examined to reveal large-scale (∼1-10 pc) features in the thermal dust emission. In addition, these *Herschel* images are also utilized to produce the column density (i.e., $N(H_2)$) and dust temperature (T_d) maps (see Section 5.3.1 for details). For the core-scale study (∼0.01 pc), high-resolution Band-7 (∼0.88 mm) continuum images from Atacama Large Millimeter/submillimeter Array (ALMA; Proposal Id: 2013.1.00960.S, PI: Csengeri, Timea) at two different resolutions were collected from the ALMA Archive[1] (see Table 5.1). The ALMA observations in two different configurations, the 7 m and 12 m arrays, provided images with different

[1] https://jvo.nao.ac.jp/portal/alma/archive.do

resolutions. The 12 m array provides higher spatial resolution, while 7 m array offer better sensitivity for extended sources. Therefore, the 7 m array and 12 m array together enable detailed studies of both the diffuse and compact components of the target. The photometric magnitudes of point-like sources at 3.6, 4.5, and 5.8 μm were acquired from *Spitzer* GLIMPSE-I Spring '07 catalog. Additionally, we collected Vista Variables in the Vía Líactea (VVV) K_s band image and photometric magnitudes of point-like sources in the H and K_s bands from the VVV Data Release 5 (DR5; McMahon et al., 2021). For bright sources that are saturated in the VVV survey, we used photometric data from Two Micron All Sky Survey (2MASS; Minniti et al., 2017).

Table 5.1: List of archive data sets utilized in this work.

Survey	Wavelength/Frequency /line(s)	Resolution/Beam size (arcsec) (arcsec/arcsec^2)	Reference
SARAO MeerKAT Galactic Plane Survey (SMGPS)	1.28 GHz	~8×8	Goedhart et al. (2024)
Sydney University Molonglo Sky Survey (SUMSS)	843 MHz	~45×63	Bock et al. (1999)
SEDIGISM	^{13}CO/C^{18}O (J = 2–1)	~30	Schuller et al. (2017a)
Atacama Large Millimeter/submillimeter Array (ALMA)	879 μm	~4.9×3.1 and 0.33×0.16	Pro. Id: 2013.1.00960.S
ATLASGAL	870 μm	~18.2	Schuller et al. (2009)
Herschel Infrared Galactic Plane Survey (Hi-GAL)	160, 250, 350, and 500 μm	~12, 18, 25, and 37	Molinari et al. (2010b)
Galactic Legacy Infrared Mid-Plane Survey Extraordinaire (GLIMPSE)	3.6, 4.5, 5.8 μm	~2	Benjamin et al. (2003)
Vista Variables in the Vía Líactea (VVV)	1.6 and 2.2 μm	~0.8	Minniti et al. (2010)
Two Micron All Sky Survey (2MASS)	1.6 and 2.2 μm	~2.5	Skrutskie et al. (2006)

5.3 Results

5.3.1 Physical environment of G321

Star-forming activity is closely related to the density and temperature of the medium. Figures 5.1b and 5.1c present the $N(H_2)$) and T_d maps for our target area, respectively, with a resolution of about 12″. These maps were produced

using *Herschel* FIR images in *hires* (Men'shchikov, 2021). The $N(H_2)$ map clearly shows the presence of filaments in the area of our interest. The $N(H_2)$ value toward the position of the ATLASGAL clumps is above 2×10^{22} cm^{-2}, while the filaments are of relatively lower column density. The dust temperature toward the filamentary structures observed in the $N(H_2)$ map is about 15 K. A relatively higher T_d (i.e., ∼20 K) is observed toward the high-column density regions, which are shown with yellow arrows in Figure 5.1b. The SUMSS radio continuum emission is detected exclusively toward these regions. On the other hand, the high-column density regions, which are marked with cyan arrows in Figure 5.1b, are relatively cooler, and their T_d is about 10 K. The availability of the MeerKAT 1.28 GHz high-resolution radio continuum image reveals the presence of four compact H II regions (see H II-1, H II-2, H II-3, and H II-4 in Figure 5.1c). Their effective radii (R_{HII}), total flux density (S_ν), and dynamical timescale (t_{dyn}) are listed in Table 5.2 (see Appendix B.2 for details).

The large-scale molecular gas distribution toward G321 is presented in Figure 5.2 using SEDIGISM ^{13}CO($J = 2$–1) data. Figure 5.2a is the moment-0 map for the velocity (v_{lsr}) range [−38.25, −27.25] km s^{-1}, showing the morphology of the molecular cloud in the plane of sky. The dotted rectangle highlights the area of *Herschel* images shown in Figure 5.1. The peak emission map is displayed in Figure 5.2b. Both Figures 5.2a and 5.2b reveal intense molecular emission toward the position of the ATLASGAL clumps and the presence of several filamentary structures similar to those observed in *Herschel* dust continuum images (see Figure 5.1a). The moment-1 map and the velocity map corresponding to the peak intensity (referred to as the 'peak velocity map') are presented in Figures 5.2c and 5.2d, respectively. The moment-1 map displays overall gas velocity and provides the first hint about the presence of two velocity components, which appear in colors blue and red. The peak velocity map indicates that the filamentary

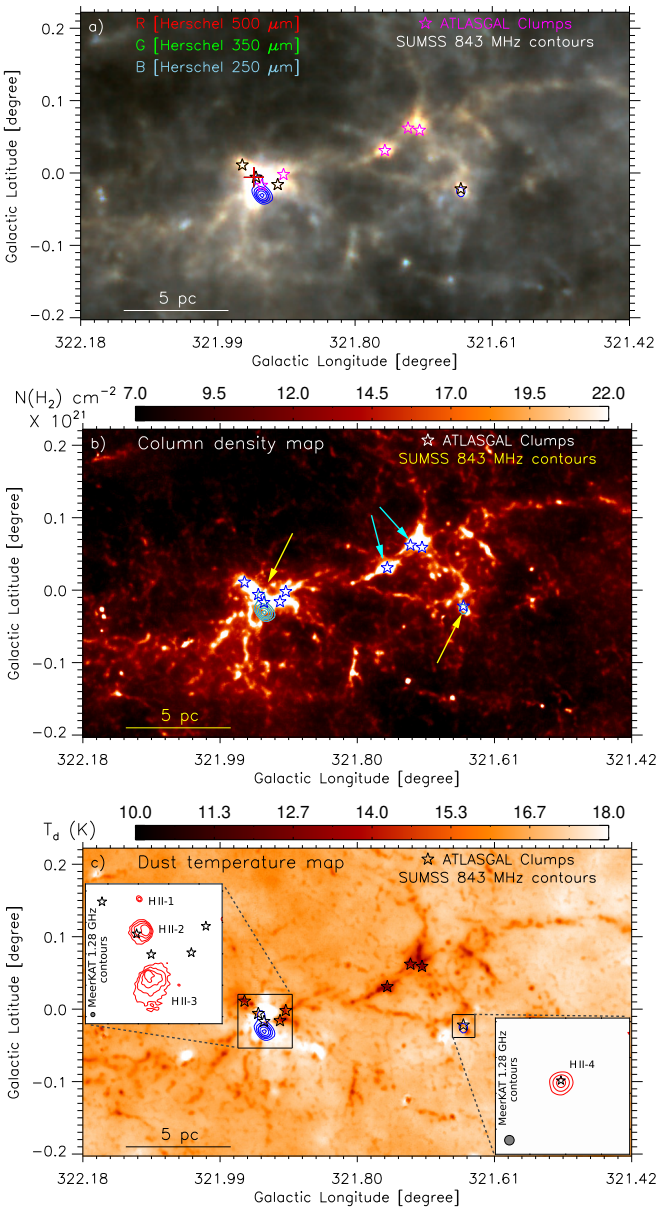

Figure 5.1: (a) *Herschel* three color-composite image. The colors red, green, and blue present *Herschel* 500, 350, and 250 μm continuum images, respectively. The plus symbol indicates the position of the 22 GHz H_2O and Class I 95 GHz MME. The asterisks indicate the locations of ATLASGAL clumps (Urquhart et al., 2018). The clumps exhibiting outflow activity are marked in black (Yang et al., 2022). Panels (b) and (c) show *Herschel* $N(H_2)$ and T_d maps, respectively. The contours in each panel indicate the SUMSS 843 MHz radio continuum emission. The contour levels are at about [3, 6, 9, 12, and 15] $\times$ σ, where 1σ $\sim$1 mJy beam^{-1}. In panel (b), arrows indicate high column density regions. Arrows in yellow highlight areas characterized by higher dust temperatures and the detection of radio emissions, while cyan arrows denote regions with lower dust temperatures and no detectable radio emission. The rectangular regions highlighted in panel (c) are zoomed-in in the insets. The contours in the top-left and bottom-right insets represent MeerKAT 1.28 GHz radio continuum emission at [5, 15, 30, and 50] $\times$ σ and [5, 50, and 160] $\times$ σ, respectively, where 1σ $\sim$20 μJy beam^{-1}. A gray circle at the bottom-left corner of each inset indicates the beam size of the MeerKAT data ($\sim$8$''$$\times$8$''$). A scale bar of 5 pc is shown in each panel.

Table 5.2: Physical parameters of the H II regions.

H II Regions	$R_{\rm HII}$ (pc)	S_ν (mJy)	$\log(N_{\rm uv}$ [s^{-1}])	$t_{\rm dyn}$ (Myr)
H II-1	0.05	0.34	44.02	0.02
H II-2	0.22	13.32	45.61	0.12
H II-3	0.34	25.67	45.89	0.22
H II-4	0.09	6.17	45.27	0.03

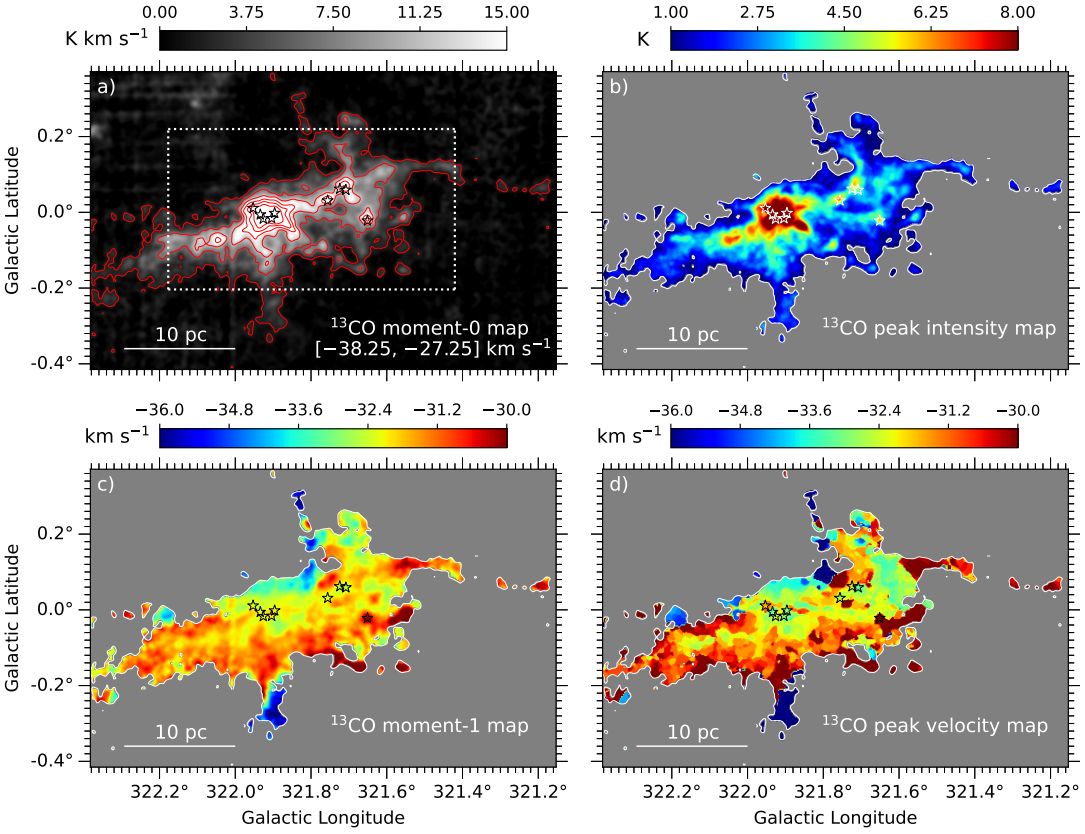

Figure 5.2: (a) SEDIGISM ^{13}CO moment-0 map for $v_{\rm lsr}$ range of [−38.25, −27.25] km s^{-1}. The contour levels are at [3, 11, 19, 27, 35, and 43] × σ, where 1σ ∼0.6 K km s^{-1}. The dotted white rectangle indicates the area of *Herschel* continuum images shown in Figure 5.1. (b) The peak intensity map for the same molecular line data. (c) The moment-1 map. (d) The velocity map corresponding to the peak intensity, referred as the 'peak velocity map.' The images in panels (b), (c) , and (d) are clipped below 3σ level of the moment-0 map. The asterisks are same as Figure 5.1. A scale bar of 10 pc is shown in each panel.

structures observed in the peak intensity map have quite similar velocities across their length. This feature has been well reflected in Figure 5.3, which presents the moment-0 maps of ^{13}CO emission at $v_{\rm lsr}$ from -38.25 to -27.25 km s^{-1}, with an interval of about 0.75 km s^{-1}. This image reveals how the gas velocity changes over cloud structures. The narrow integration range (i.e., < 1 km s^{-1}) ensures that the gaseous structures observed in Figure 5.3 are velocity-coherent features of the molecular cloud.

5.3.2 Detection of filament skeletons and the distribution of color excess sources

The visual inspection of the *Herschel* FIR images in Figure 5.1a and the molecular gas emission in Figures 5.2 and 5.3 indicate the presence of filaments in our target area. To identify the filament skeletons, we utilized *getsf* (Men'shchikov, 2021) on the ^{13}CO moment-0 map, shown in Figure 5.2a. As described in Section 2.3.3, the inputs for *getsf* are the source distance, resolution of the image, and a rough estimation of the widths of the largest filament and core. In this study, the distance of the source and resolution of the image are 1.98 kpc (Urquhart et al., 2018) and 36″, respectively. Through visual inspection of the moment-0 map in DS9, we estimated the widths of the largest filament and core to be 260″ and 160″, respectively. The last two inputs are essential to set a cutoff during successive unsharp masking to prevent decomposition to a very large scale (Men'shchikov, 2021). The *getsf*-identified filament skeletons (on the scale of 204″) are highlighted in Figure 5.4a over the ^{13}CO moment-0 map. Several parsec-scale filaments are found to converge at two distinct junctions, characterized by intense molecular emission and high column density (see the arrows in Figure 5.4a), which perfectly match the definition of HFS (Myers, 2009). Therefore, at least two HFSs, named HFS-1 and HFS-2, are detected using *getsf* in our target area. The hubs corre-

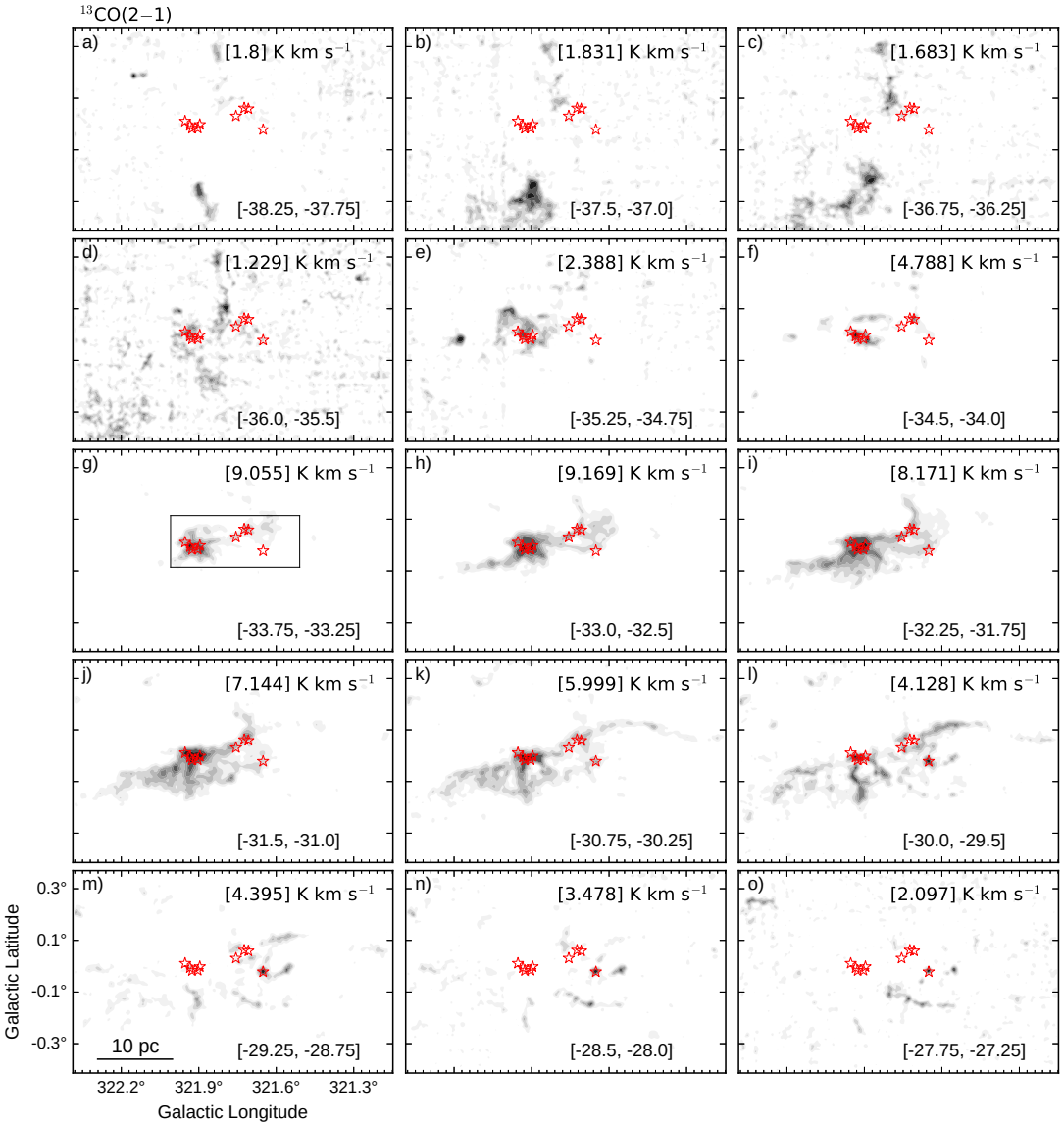

Figure 5.3: Panels (a)–(o) present integrated intensity maps of ^{13}CO emission (using filled contours) for $v_{\rm lsr}$ from −38.25 to −27.25 km s^{-1} with an interval of about 0.75 km s^{-1}. The contour levels are at [0.1, 0.2, 0.3, 0.4, 0.5, 0.6, 0.8, and 1.0] × peak moment-0 values, which are mentioned in the respective panels. The black rectangle shown in panel (g) is zoomed-in using the ATLASGAL 870 μm image in Figure 5.6a. A scale bar of 10 pc is shown in panel (m).

sponding to HFS-1 and HFS-2 are labeled as Hub-1 and Hub-2, respectively, in Figure 5.4a. The detection of two HFSs toward G321 is an interesting finding considering the fact that there are only a few sources reported in the literature with more than one large-scale HFS (> 1 pc) in the same star-forming site, such as IC 5146 (Wang et al., 2019; Dewangan et al., 2023b), G45.3+0.1 (Bhadari et al., 2022), and Galactic 'Snake' (Dewangan et al., 2024).

The high-density regions are susceptible to star-forming activity, which can be inferred from the detection of embedded protostars or Class I YSOs, which show IR color excess due to their envelopes and the dusty circumstellar disks (Povich et al., 2011; Sharma et al., 2017). We have utilized *Spitzer* photometric data (at 3.6–5.8 μm) of point-like sources to detect Class I YSOs in our target site. Previous studies showed that Class I YSOs satisfy the color conditions: [4.5] − [5.8] ≥ 0.7 and [3.6] − [4.5] ≥ 0.7 (Hartmann et al., 2005; Getman et al., 2007). The positions of 61 Class I YSO candidates identified in this work are displayed on the ^{13}CO moment-0 map in Figure 5.4b, within the yellow-dotted region. Several YSO candidates are detected toward both hubs (Hub-1 and Hub-2; see Figure 5.4a) and the filaments. Interestingly, we observe a relatively large number of YSO candidates toward Hub-1 compared to Hub-2. In Figure 5.4c, we have visually marked the extent of Hub-1 and Hub-2 with two blue circles of sky-projected radii about 2.1 and 1.4 pc, respectively. Hub-1 and Hub-2 are zoomed-in using the VVV K_s band image in the top-left and bottom-right insets, respectively. The superior spatial resolution and sensitivity of the VVV K_s band image reveal many point-like sources compared to the *Spitzer* images (not included here) for both hubs. The red rectangles overplotted on the VVV K_s band images in the insets of Figure 5.4c highlight the sources with color excess, $H - K_s > 1.8$. This cutoff value has been obtained from the color-magnitude analysis of a nearby control field (size ∼4.′5 × 4.′5, centered at $l = 321.^{\circ}724$ and

$b = -0.^{\circ}225$). This cutoff value of 1.8 was also utilized to detect the color excess sources for the MSFR toward $l = 345.^{\circ}5$ and $b = 0.^{\circ}3$ in Dewangan et al. (2018a). The better photometric depth of the VVV data allows the detection of 140 color excess sources toward Hub-1 and 32 for Hub-2. Since all these NIR color-excess sources are distributed toward regions of intense molecular emission, it is unlikely that they are background sources; therefore, they can be considered YSO candidates. Use of 2MASS data for bright sources adds 6 more unique color excess sources for Hub-1, while it does not contribute any additional color excess sources for Hub-2.

5.3.3 The physical properties of the molecular cloud, hubs, and the filaments

In this section, we estimate the mass of the molecular cloud, hubs, and filaments. We also determine the line-mass of the filaments and the mass accretion rate along them to the hubs in HFS-1 and HFS-2.

5.3.3.1 Mass estimation using SEDIGISM ^{13}CO(J = 2–1) and C^{18}O(J = 2–1) data

Following Equation 2.8, the ^{13}CO column density (i.e., $N(^{13}\mathrm{CO})$) can be estimated as,

$$N(^{13}\mathrm{CO}) = \frac{3h}{8\pi^3\mu_{\rm dm}^2 S}\frac{Q_{\rm rot}}{g_J}\frac{\exp\left(\frac{E_{\rm up}}{kT_{\rm ex}}\right)}{\exp\left(\frac{h\nu}{kT_{\rm ex}}\right)-1} \times\frac{1}{J(T_{\rm ex})-J(T_{\rm bg})}\frac{\tau_{13}}{1-\exp(-\tau_{13})}\int T_{\rm mb}\,dv, \quad (5.1)$$

where, $T_{\rm mb}$ and τ_{13} represent the main beam temperature and optical depth for the ^{13}CO emission. All other parameters are defined in Section 2.3.1. For

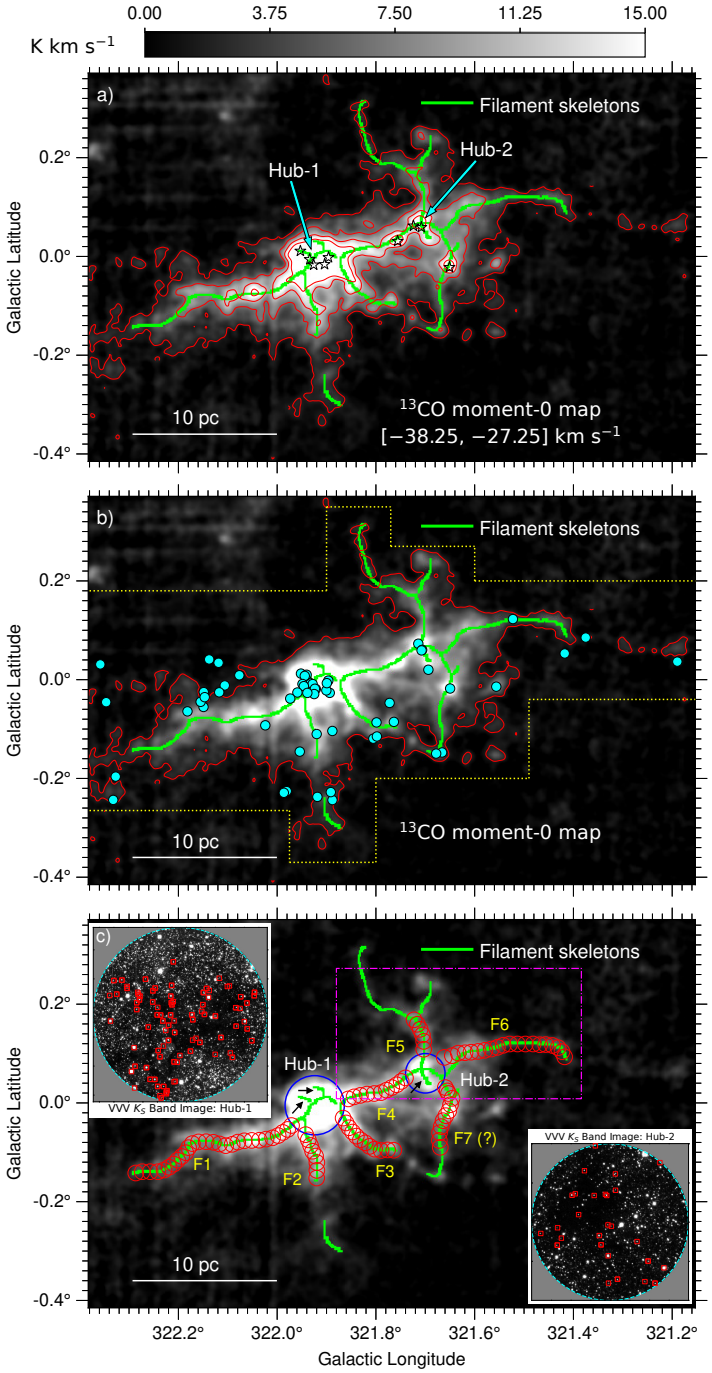

Figure 5.4: (a) The *getsf*-identified filament skeletons are marked over the moment-0 map of ^{13}CO emission. The moment-0 map is identical to Figure 5.2a, and the contour is at 3σ level. (b) The distribution of Class I YSO candidates is shown in the region bounded by dotted yellow lines, with solid cyan circles outlined in black. (c) Two blue circles over the moment-0 map indicate the possible extent of Hub-1 and Hub-2. Black arrows indicate small-scale ($\lesssim$ 1 pc) filaments within the hubs. Both the hubs are zoomed-in using VVV K_s band image in the insets. The red rectangles in the insets indicate the embedded color excess sources with H − K_s > 1.8. The red circular regions over the filament skeletons are utilized to extract the average velocity and velocity dispersion along the filaments, which are shown in Figure 5.5. The area of the magenta dashed-dotted rectangular region is shown using a two-color composite image in Figure 5.10a.

$J = 2 - 1$ transition, the degeneracy $(g_J) = 2J_u + 1 = 5$, and line strength $(S) = J_u/(2J_u + 1) = 2/5$, respectively. The rotational partition function $(Q_{\rm rot})$ is approximated to be $KT/hB + 1/3$ (McDowell, 1988; Yuan et al., 2016), where B is the the rotational angular momentum constant. From the Jet Propulsion Laboratory (JPL) spectroscopic database[2] (Pickett et al., 1998), we obtained $B =$ 55101.011 MHz and the dipole moment, $\mu_{\rm dm} = 0.11046$ Debye for ^{13}CO molecule. The optical depth, τ_{13} can be estimated from the ratio of the line peak intensities of ^{13}CO and C^{18}O data (see Miettinen, 2012; Mangum & Shirley, 2015; Liu et al., 2020),

$$\frac{T_{\rm mb}(^{13}{\rm CO})}{T_{\rm mb}({\rm C}^{18}{\rm O})} \approx \frac{1 - \exp(-\tau_{13})}{1 - \exp(-\tau_{13}/R)}, \tag{5.2}$$

where, R (= 7.4; Areal et al., 2018) is the isotopic ratio of ^{13}CO and C^{18}O. The τ_{13} values are numerically calculated using Equation 5.2 for pixels with peak intensities greater than 3σ, where $1\sigma = 0.35$ K for both the ^{13}CO and C^{18}O data (see Section 5.2). The τ_{13} map and its statistics are included in Appendix B.1 (see Figure B.1a). Then, we obtained the $N(^{13}{\rm CO})$ values using the cosmic microwave background temperature $(T_{\rm bg}) = 2.73$ K, excitation temperature $(T_{\rm ex}) = 15$ (20) K, the integrated ^{13}CO emission, and the τ_{13} values in Equation 5.1. The $N(^{13}{\rm CO})$ values are then converted to $N({\rm H_2})$ for $N({\rm H_2})/N(^{13}{\rm CO}) = 7 \times 10^5$ (e.g., Frerking et al., 1982). The $N({\rm H_2})$ map and its statistics for $T_{\rm ex} = 15$ K can be found in Figure B.1b in Appendix B.1. Figure B.1 shows that estimations of τ_{13} and the corresponding $N({\rm H_2})$ are unavailable for many pixels due to the absence of C^{18}O emission above 3σ. Hence, we have established the relationship, $N({\rm H_2}) \sim 1.173(1.176) \times 10^{21}$ cm^{-2} (K km s^{-1})$^{-1}$ for $T_{\rm ex} = 15(20)$ K, by comparing the total $N({\rm H_2})$ and ^{13}CO moment-0 values for pixels where $N({\rm H_2})$ values are available. This relationship between $N({\rm H_2})$ and ^{13}CO moment-0 value is in agreement with the result of Schuller et al. (2017a) and is used to derive the $N({\rm H_2})$ values for

[2] https://spec.jpl.nasa.gov/ftp/pub/catalog/catdir.html

the entire molecular cloud. However, it is important to note that our estimated $N(H_2)$ values are uncertain by a factor of a few, which will propagate to all the physical parameters calculated based on this $N(H_2)$ values.

The knowledge of $N(H_2)$, the mean molecular weight (μ; assumed to be 2.8 m_H from Kauffmann et al. (2008)), and the distance of the the molecular cloud (i.e., $d = 1.98$ kpc) allows for the calculation of its total mass. The computed mass will have an uncertainty of a factor of a few, mainly due to the uncertainty in $N(H_2)$. For the moment-0 values above 3σ (see Figure 5.2), the total mass of the molecular cloud is about $7.93(7.91) \times 10^4\,M_\odot$ for $T_{ex} = 15$ (20) K, respectively. Similarly, the total mass of Hub-1 and Hub-2 are estimated to be nearly $1.60 \times 10^4\,M_\odot$ and $3.81 \times 10^3\,M_\odot$, respectively. There is no significant difference in the masses of the hubs for $T_{ex} = 15$ and 20 K, up to two decimal places. The red circles[3] with a diameter of about 12 pixels (i.e., ∼1.1 pc; see Figure 5.4c) along the filaments are utilized to extract the velocity profile along the length of the filaments, which are detailed in Section 5.3.3.2. We calculated the mass of these filaments (i.e., F1–F7) for $T_{ex} = 15$ K, using the total ^{13}CO moment-0 values, covered with the red circles. The length (L^{Fil}), mass (M^{Fil}), and line-mass (i.e., $(M/L)^{Fil}$) of the filaments are listed in Table 5.3. Based on the $(M/L)^{Fil}$ values, the stability of the filaments is discussed in Section 5.4.1.

5.3.3.2 Estimation of the mass accretion rate through the filaments to the hubs

The mass accretion rate ($\dot{M}_{||}$) along the filament is a key parameter for the HFSs. Hence, we calculated $\dot{M}_{||}$ using Equation 1.6 depending upon mass of the filaments

[3]By comparing the filament F6 observed in Figures 5.3k and 5.3l, we noticed that the *getsf*-identified skeleton for F6 is not accurate. Consequently, we manually selected the first four circular regions of F6 toward Hub-2.

(M), observed velocity gradient along their length ($\nabla V_{||}^{\rm obs}$) and their angle (α) relative to the plane of the sky. The average velocity for the circular regions of filaments F1–F7 (see Figure 5.4c) is estimated by fitting Gaussians to their velocity profiles and is shown as a function of distance from their hubs in Figure 5.5. We then applied a linear fit (see the red lines) to the average velocity distribution along the length of the filaments to estimate $\nabla V_{||}^{\rm obs}$. The velocity dispersion for these regions is indicated using a color scale, and the average velocity dispersion ($\sigma_{\rm avg}^{\rm Fil}$) for F1–F7 is listed in Table 5.3. The physical association of filament F4 with both Hub-1 and Hub-2, along with the presence of a dense fragment (as detailed in Section 5.3.4), complicates the velocity distribution along the filament, making it impractical to apply the simple mass accretion model proposed by Kirk et al. (2013). The moment-0 maps for narrow velocity integration ranges (see Figure 5.3) do not show a clear signature of filament F7; hence, the detection of this filament is highly doubtful. Therefore, the velocity gradients for filaments F4 and F7 have not been calculated. The finite $L^{\rm Fil}$ and $\nabla V_{||}^{\rm obs}$ indicate that α is neither close to 0° nor 90° for the filaments F1, F2, F3, F5, and F6. Hence, assuming $\alpha = 45°$ and using $M^{\rm Fil}$ and $\nabla V_{||}^{\rm obs}$ in Equation 1.6, we obtained their $\dot{M}_{||}$ values, which are listed in Table 5.3. The $\dot{M}_{||}$ varies from 1.61×10^{-3} to 11.25×10^{-3} $M_\odot$ yr^{-1} for the filaments F5 and F3, respectively. The combined $\dot{M}_{||}$ in Hub-1 through filaments, F1, F2, and F3 is about 26.35×10^{-3} $M_\odot$ yr^{-1}. However, for Hub-2, combined $\dot{M}_{||}$ through filaments, F5, and F6 is about 4.17×10^{-3} $M_\odot$ yr^{-1}. Our estimated mass accretion rate can vary by a factor of 0.58 to 1.73 for $\alpha = 30°$ to 60°. It is important to note that the *getsf*-estimated average width of the filaments is about 1.8 pc. However, to avoid contamination from the surrounding molecular gas and to better determine the average velocity, we selected circular regions with a relatively smaller diameter (∼1.1 pc). This same width was used to calculate the total mass of the filaments. It is important to note

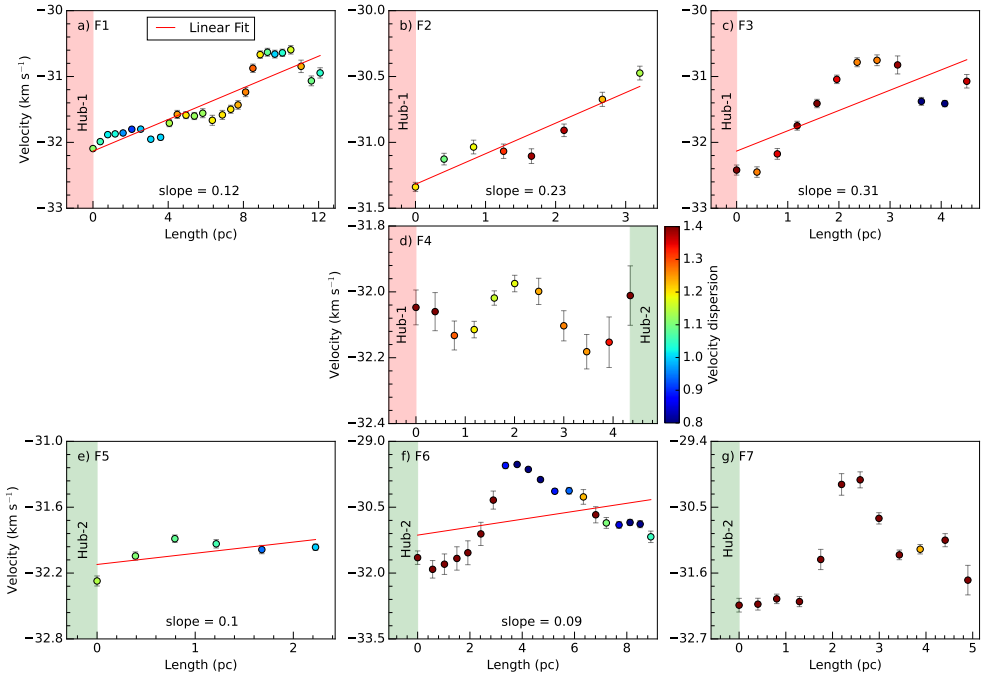

Figure 5.5: Panels (a)–(g) show the average velocity variation along the filaments F1–F7 for the circular regions depicted in Figure 5.4c. The velocity dispersion for these regions is shown using the color scale. The red straight lines indicate the best linear fit to the average velocity distributions. The slopes of the best-fit lines for filaments F1, F2, F3, F5, and F6 are provided in their respective panels.

Table 5.3: The physical properties of the filaments.

IDs	Associated with	$L^{\rm Fil}$	$M^{\rm Fil}$	$(M/L)^{\rm Fil}$	$\sigma^{\rm Fil}_{\rm avg}$	$\nabla V^{\rm obs}_{||}$	$\dot{M}_{||}$	$\frac{(M/L)^{\rm Fil}}{(M/L)^{\rm tur}_{\rm crit}}$
		(pc)	($\times 10^3 M_\odot$)	($\times 10^2 M_\odot$ pc^{-1})	(km s^{-1})	(km s^{-1}pc^{-1})	($\times 10^{-3} M_\odot$ yr^{-1})	
F1	Hub-1	12.08	6.88	5.70	1.11	0.12	8.43	1.0
F2	Hub-1	3.20	2.84	8.88	1.24	0.23	6.67	1.2
F3	Hub-1	4.50	3.55	7.89	1.25	0.31	11.25	1.1
F4	Hub-1 & 2	4.35	4.53	10.41	1.29	—	—	1.3
F5	Hub-2	2.23	1.58	7.09	1.05	0.10	1.61	1.4
F6	Hub-2	8.92	2.78	3.12	1.27	0.09	2.56	0.4
F7	Hub-2	4.90	2.90	5.92	1.79	—	—	0.4

that the analytical model by Kirk et al. (2013) is simplistic, assuming filaments as cylinders of uniform density and neglecting the effects of core formation and stellar feedback. Hence, the varying density of the filament, the formation of its core, and the influence of stellar feedback can impact the velocity profile along the length of the filament. Furthermore, any deviation from the ideal cylindrical shape will result in different projection angles at various points along the filament, thus affecting its velocity profile. These factors prevent a perfect linear fit of the average velocity plot, as observed in Figure 5.5. Therefore, a better model is necessary for more precise results.

5.3.4 Study of the hierarchical structures form clump- to the core-scale

Molecular clouds often exhibit hierarchical density structures. To reveal the same in our target site, we performed a dendrogram analysis using the Python-based tool *astrodendro*. It provides a hierarchical tree with branches that divide into smaller branches and indivisible leaves at the tips of the tree (see details in Section 2.3.4).

5.3.4.1 Clump-scale hierarchical structures in ATLASGAL 870 μm image

We performed the dendrogram analysis on the ATLASGAL 870 μm image to study clump-scale ($\sim$1 pc) structures in the rectangular area highlighted in Figure 5.3g. The input parameters for *astrodendro* were `min_value` = 3σ and `min_delta` = 1σ ($\sim$60 mJy beam^{-1}). The `npix` value was set to be 22, corresponding to twice the beam area of the ATLASGAL data. The hierarchical structures, i.e., the branch and leaves identified in the ATLASGAL continuum image, are highlighted using red and cyan contours in Figure 5.6a, respectively.

The radii of these structures are calculated as $R = \sqrt{A/\pi}$, where A is the exact area. After correcting R for the ATLASGAL beam size, we have listed the deconvolved radii as $R_{\rm eff}$ in Table 5.4, along with the values of A and S_ν. $R_{\rm eff}$ ranges from 0.24 to 0.92 pc. The extent of the hubs (as shown in Figure 5.4c) is marked using dotted circles in Figure 5.6a. Hub-1 hosts the largest structure (i.e., ATLASGAL Branch (ATB)-1; $R_{\rm eff} = 0.92$ pc), which is further fragmented into two leaves, namely ATLASGAL Leaf (ATL)-3 and ATL-4. ATL-6 resides within Hub-2, and ATL-5 is projected over filament F4, which connects both the hubs. We have estimated the average $T_{\rm d}$ for the branch and the leaves (for their area depicted in Figure 5.6a) from the *Herschel* dust temperature map, which are specified in Table 5.4.

The knowledge of S_ν, $T_{\rm d}$, and d of these structures allows the estimation of their total mass using Equation 2.15. For ATLASGAL 870 μm (i.e., 344.59 GHz) emission, $k_{344.59\ \rm GHz}^{870\mu m}$ is about 1.54 cm^2 g^{-1}, derived from the relation $k_\nu = 10\,(\nu/1.2\ [\rm THz])^{1.5}$ (Hildebrand, 1983; Li et al., 2020). Using average $T_{\rm d}$ values, $d = 1.98$ kpc, and $R_t = 100$ (e.g., Weingartner & Draine, 2001a; Mutie et al., 2021) in Equation 2.15, we estimated the mass of the dendrogram structures. The M–$R_{\rm eff}$ plot for the *astrodendro*-identified structural components are shown in Figure 5.6b. The blue dashed line indicates the Kauffmann & Pillai (hereafter, KP-10) condition for MSF, i.e., $M(R) > 870\,M_\odot\ (R/{\rm pc})^{1.33}$ (Kauffmann & Pillai, 2010). For the dust opacity value used in this paper, the mass coefficient provided by Kauffmann & Pillai (2010) is reduced by a factor of 1.249. Hence, the modified KP-10 (hereafter, mKP-10) condition for MSF is $M(R) > 697\,M_\odot\ (R/{\rm pc})^{1.33}$ (Kauffmann & Pillai, 2010). The white region above the gray-shaded area in Figure 5.6b satisfies the mKP-10 condition. ATB-1 and its associated ATL-3 significantly exceed the mKP-10 limit, while ATL-4, ATL-5, and ATL-6 are positioned near the threshold for MSF. On the other hand, ATL-2 signifi-

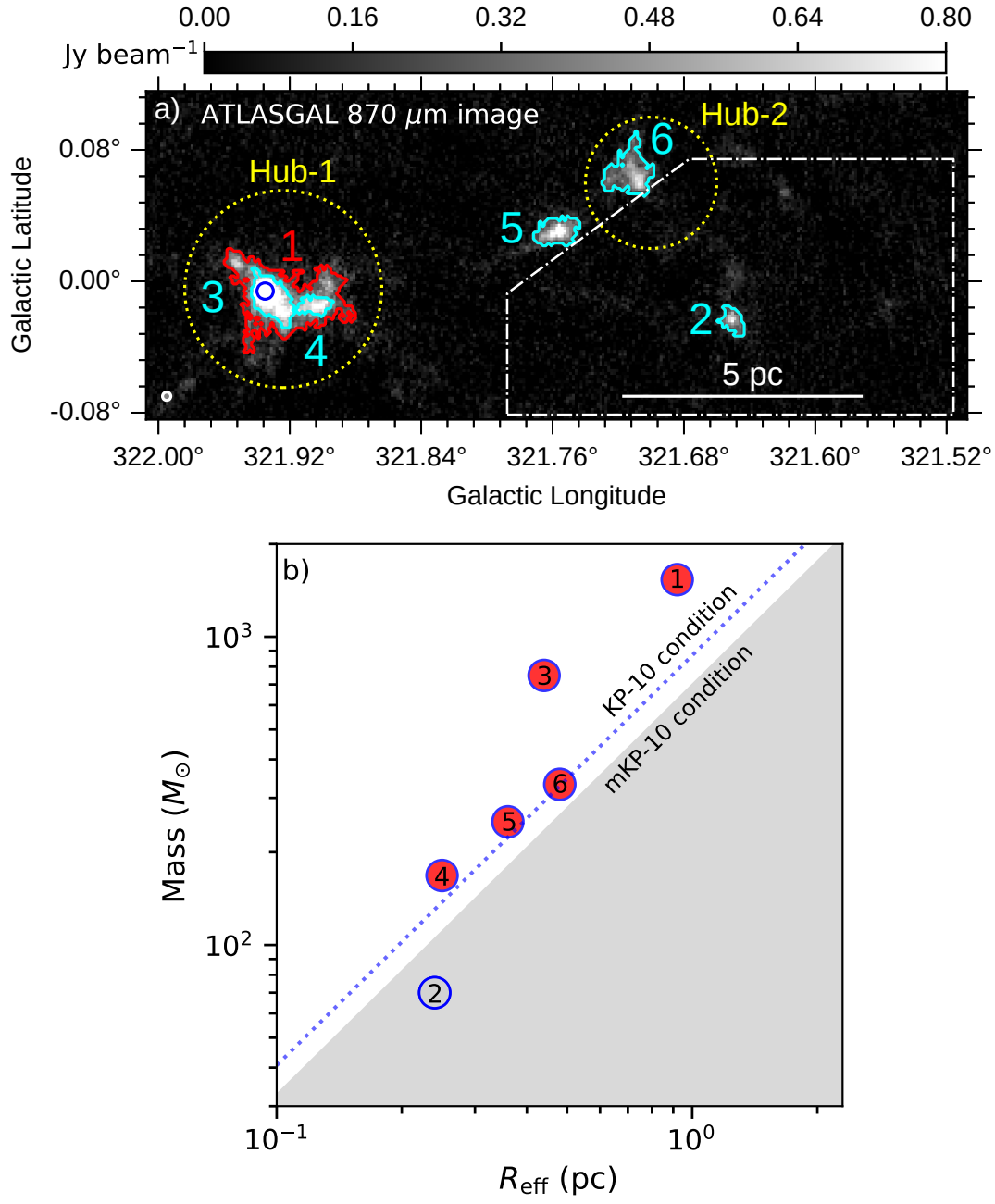

Figure 5.6: (a) The panel shows *astrodendro*-identified hierarchical structures in ATLASGAL 870 μm image. The branch is highlighted with a red contour, while the leaves are presented in cyan. The yellow dotted circles indicate the extent of Hub-1 and Hub-2, as shown in Figure 5.4c). The blue circle inside Leaf-3 is further zoomed-in using the ALMA Band-7 continuum image in Figure 5.7a. The area of the white polygon is shown using a two-color composite image in Figure 5.10b. The white circle at the bottom-left corner of the image presents the beam size ($\sim$18$''$.2 $\times$ 18$''$.2) of the ATLASGAL data. A scale bar of 5 pc is added to this panel. (b) The mass–effective radius plot of the *astrodendro*-identified structures. The blue dotted line presents the KP-10 condition for MSF (Kauffmann & Pillai, 2010). The white region above the gray shaded area corresponds to the mKP-10 condition for MSF, and the structural components that satisfy this condition are shaded in red.

Table 5.4: The physical parameters for the *astrodendro*-identified hierarchical structures in ATLASGAL 870 μm continuum image.

IDs	Type	Exact Area ($\times 10^3$ arcsec^2)	$R_{\rm eff}$ (pc)	S_ν (Jy)	$T_{\rm d}$ (K)	Mass ($M_\odot$)	Density ($\times 10^3$ cm^{-3})	$\log(N(\rm H_2)$ [cm^{-2}])
1	Branch	29.1	0.92	46.10	17	1532	6.8	22.41
2	Leaf	2.2	0.24	2.09	17	70	17.3	22.23
3	Leaf	7.0	0.44	24.64	18	749	29.6	22.73
4	Leaf	2.3	0.25	4.15	15	168	38.7	22.59
5	Leaf	4.7	0.36	5.52	14	251	18.6	22.44
6	Leaf	8.0	0.48	7.27	14	332	10.7	22.32

cantly falls below the mKP-10 limit. Furthermore, assuming the structures to be spherical, we can derive their density and column density using the formulas: $n = 3M/4\pi\mu \rm m_H R_{\rm eff}^3$ (Li et al., 2020) and $N(\rm H_2) = M/\pi\mu \rm m_H R_{\rm eff}^2$ (Bhadari et al., 2023), respectively. The mass, density, and column density of all the dendrogram structures are listed in Table 5.4. These structures have a density of about 10^4 cm^{-3}, with $N(\rm H_2) > 10^{22}$ cm^{-2}. The typical error in the mass estimation is about 20%, considering the uncertainties in $T_{\rm d}$, S_ν, and d are about 10%, 15% (Schuller et al., 2009), and 6% (Urquhart et al., 2018), respectively. The density and column density have similar uncertainties as the mass of the structures. Given that k_ν and $R_t = 100$ can have significant uncertainties (see Li et al., 2020), the 20% error should be considered a lower limit, and the actual error could be several times larger.

5.3.4.2 Core-scale hierarchical structures in ALMA Band-7 continuum data

The area covered by the blue circle within ATL-3 (see Figure 5.6a) is zoomed-in in Figure 5.7a using ALMA Band-7 continuum data (beam size $\sim$4$''$.9 $\times$ 3$''$.1). A single structure is traced in the ALMA data at this angular resolution above the 3σ limit (where 1σ $\sim$40 mJy beam^{-1}), which is highlighted with the yellow contour. The star-forming activity of this structure is revealed through the detection of Class I YSO candidates, as well as 22 GHz H_2O and Class I 95 GHz MME toward it (see Figure 5.7a). The total flux density for the structure is calculated to be about 4.43 Jy. Following the formulas described in Section 5.3.4.1, we calculated the basic physical parameters for this structure, which are $R_{\rm eff}$ $\sim$0.07 pc, M $\sim$139 $M_{\odot}$, $n > 10^6$ cm^{-3}, and $N(\rm H_2) > 10^{23}$ cm^{-2}. Here, $R_{\rm eff}$ is the geometric mean of the semi-major and semi-minor axis corresponding to the exact area of the structure, after being corrected for the beam size. For the mass estimation, we used $k^{880\mu m}_{341.06\ \rm GHz} = 1.52$ cm^2 g^{-1} and the average dust temperature of ATL-3 (i.e., $T_{\rm d} = 18$ K). The availability of ALMA Band-7 continuum data with a better resolution (beam size $\sim$0$''$.33 $\times$ 0$''$.16) allowed us to further zoom-in on the area covered by the red dotted circle in Figure 5.7a. The zoomed-in image is shown in Figure 5.7b. To explore the hierarchical structures at the core scale (i.e., $\lesssim$ 0.01 pc), we utilized *astrodendro* on the ALMA Band-7 continuum high-resolution data. The input parameters for the *astrodendro* analysis were `min_value` = 3σ, `min_delta` = 1σ ($\sim$2 mJy beam^{-1}), and `npix` = 138, corresponding to twice the beam area of the ALMA data. Similar to Figure 5.6a, the *astrodendro*-identified branches and leaves are highlighted in the ALMA Band-7 image using red and cyan contours, respectively (see Figure 5.7b). The positions of the Class I YSO candidates, 22 GHz H_2O, and 95 GHz Class I MME are overlaid in Figure 5.7b. This overlay emphasizes the spatial association between the ALMA branches and

leaves, the YSO candidates, and the maser emissions. The dendrogram tree obtained from the *astrodendro* analysis of the ALMA data is shown in Figure 5.7c.

This tree illustrates how the branches are further fragmented into branches and/or leaves. We have estimated physical parameters for the branches and leaves using the same input parameters as earlier for the low-resolution ALMA data, and these parameters are listed in Table 5.5. The mass of the branches varies from 8 to 33 $M_{\odot}$, while the mass of the leaves is less than 10 $M_{\odot}$. The density of these structures is about 10^7 cm^{-3}, and $N(\mathrm{H_2}) > 10^{24}$ cm^{-2}. The uncertainties in $T_{\rm d}$, S_{ν}, d, k_{ν}, and R_t propagate to a minimum uncertainty of $\sim$50% in the estimation of mass, density, and column density of the ALMA cores (see Sanhueza et al., 2017; Barnes et al., 2021, for details). The M–$R_{\rm eff}$ plot of the *astrodendro*-identified structural components from the ALMA low- and high-resolution data is shown in Figure 5.7d, along with their host ATLASGAL Branch (i.e., ATB-1) and Leaf (i.e., ATL-3). All the structures, from ATB-1 to the ALMA leaves/cores, satisfy the mKP-10 condition for MSF.

5.3.5 Identification of different velocity components and their spatial distribution

As mentioned earlier in Section 5.3.1, the moment-1 map of ^{13}CO emission indicates the presence of two distinct velocity components, represented in colors blue and red (see Figure 5.2c). To identify the different velocity components of the molecular cloud, the Galactic longitude–velocity (i.e., l–v) diagram is produced using the ^{13}CO(J = 2–1) data, which is displayed in Figure 5.8a. The integration range in the Galactic latitude is [$-0\overset{\circ}{.}41$, $0\overset{\circ}{.}37$], while extracting the l–v diagram. The dotted yellow line in Figure 5.8a separates two velocity components at about -35.25 km s^{-1}. The velocity range and peak velocity of the

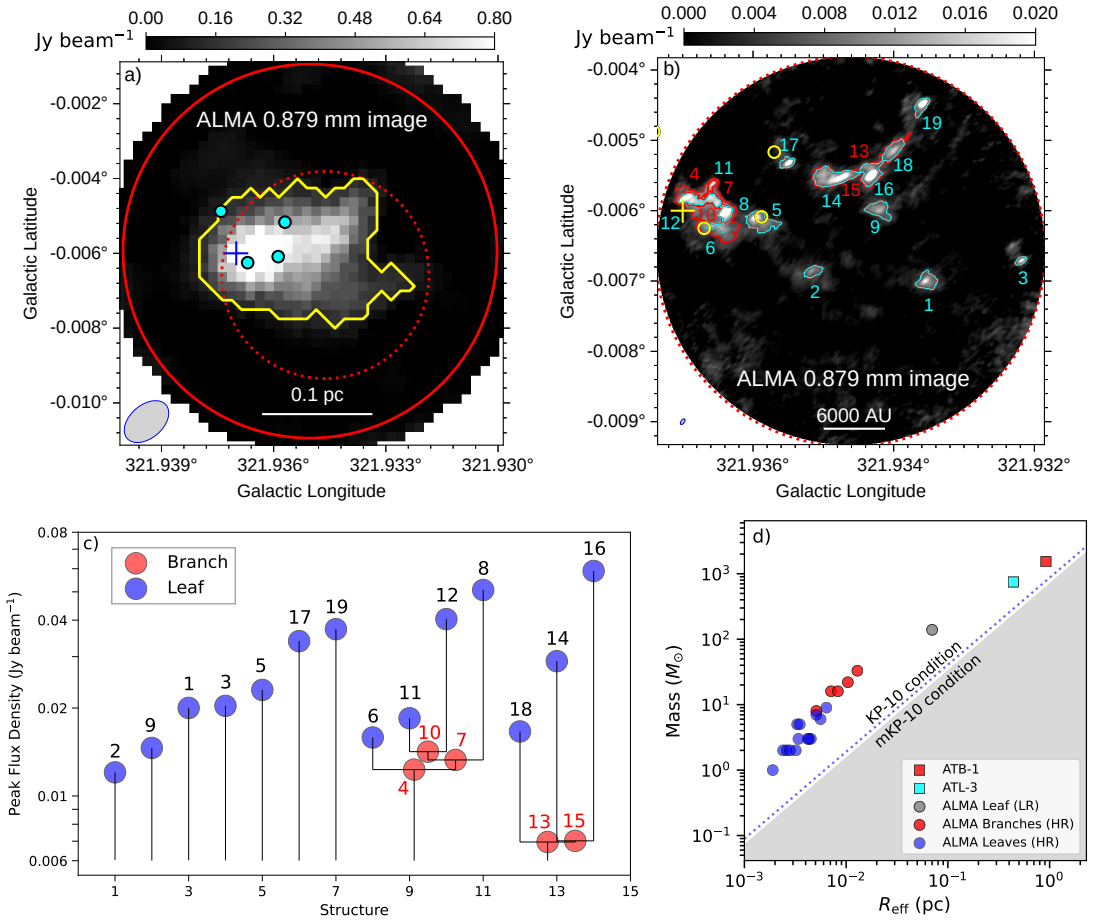

Figure 5.7: (a) ALMA Band-7 continuum image (beam size ∼4.″9×3.″1) of the area highlighted in Figure 5.6a obtained with ALMA 7 m array. The solid red circle represents the extent of the blue circle in Figure 5.6a. The yellow contour presents the *astrodendro*-identified structure. A scale bar of 0.1 pc is marked in the panel. The area under the dotted red circle is further zoomed-in in the next panel. (b) Zoomed-in view of the target area using ALMA Band-7 continuum image of beam size ∼0.″33×0.″16 obtained with ALMA 12 m array. The *astrodendro*-identified structures, i.e., the branches and leaves are marked in colors red and cyan, respectively. A scale bar of 6000 AU is shown on the panel. In panels (a) and (b), the plus symbol indicates the position of the 22 GHz H_2O and Class I 95 GHz MME, and the circles represent Class I YSO candidates. The ellipses in the bottom-left corners of panels (a) and (b) indicate the beam size of the data. (c) The *astrodendro*-identified dendrogram tree for the structural components shown in panel (b). (d) The mass–effective radius plot of the *astrodendro*-identified structural components from ATB-1 to ALMA leaves/cores. For ALMA, "LR" and "HR" stand for low- and high-resolution data. The blue dotted line and the gray shaded area are identical to Figure 5.6b.

Table 5.5: The physical parameters for the *astrodendro*-identified hierarchical structures in ALMA Band-7 continuum image. Dust temperature for ATL-3 (i.e., $T_{\rm d}$ = 18 K) is utilized for the determination of mass of all the structures (i.e., branches and leaves).

IDs	Type	Exact Area	$R_{\rm eff}$	S_ν	Mass	Density	$\log(N(\rm H_2)$ [cm^{-2}])
		(arcsec^2)	($\times$ 10^{-3} pc)	(Jy)	($M_\odot$)	($\times$ 10^6 cm^{-3})	
1	Leaf	0.67	4.3	0.10	3.0	14.0	24.39
2	Leaf	0.38	3.2	0.05	2.0	16.9	24.34
3	Leaf	0.17	1.9	0.03	1.0	45.8	24.57
4	Branch	5.68	12.9	1.07	33.0	5.4	24.46
5	Leaf	1.10	5.6	0.18	6.0	11.1	24.40
6	Leaf	0.24	2.4	0.05	2.0	42.3	24.61
7	Branch	1.78	7.1	0.50	16.0	15.0	24.64
8	Leaf	0.41	3.3	0.15	5.0	46.4	24.79
9	Leaf	0.75	4.5	0.11	3.0	12.3	24.36
10	Branch	0.94	5.1	0.26	8.0	21.3	24.65
11	Leaf	0.27	2.6	0.07	2.0	44.5	24.67
12	Leaf	0.46	3.5	0.15	5.0	36.5	24.72
13	Branch	3.71	10.4	0.69	22.0	6.7	24.46
14	Leaf	1.43	6.4	0.29	9.0	12.2	24.50
15	Branch	2.39	8.3	0.52	16.0	10.0	24.53
16	Leaf	0.92	5.1	0.22	7.0	18.7	24.59
17	Leaf	0.31	2.8	0.07	2.0	31.6	24.56
18	Leaf	0.65	4.2	0.10	3.0	15.0	24.41
19	Leaf	0.43	3.4	0.10	3.0	26.5	24.57

blue-shifted component are [−38.25, −35.50] and −36.75 km s^{-1}, respectively, while for the red-shifted component, the velocity range is [−35.25, −27.25] km s^{-1}, with a peak velocity of −32.25 km s^{-1}. The spatial distribution of the blue- and red-shifted components is shown using their integrated intensity maps in a two-color composite image in Figure 5.8b. It is evident from the integrated emission map of the red-shifted component (shown in red in Figure 5.8b) that both the HFSs are part of this cloud component. Interestingly, the integrated intensity map of the blue-shifted component reveals the presence of a filamentary cloud. Based on the total moment-0 values of the blue-shifted cloud component for the areas bounded by the yellow lines, the total mass of this component is calculated to be about 3.2 $\times 10^2\, M_\odot$. The red-shifted component shows a spatial fit between its high-intensity region and the low-intensity regions of the blue-shifted filamentary cloud. This feature is referred to as complementary distribution in the literature (see Maity et al., 2023, and references therein). To obtain a more compelling demonstration of this complementarity, we moved the red-shifted cloud component in various directions. Based on visual inspection, the best alignment is achieved by shifting the red-shifted component about 4.2 pc to the south-west, as shown in Figure 5.8c. The shift estimation is uncertain due to the error in the source distance and our limited knowledge of the exact morphology of the cloud components at the time of collision. The former contributes an uncertainty of 6% in the shift estimation, while the latter is difficult to quantify. Overall, our estimated shift has a minimum uncertainty of 6%.

To better understand the molecular gas distribution toward Hub-1 and Hub-2 in position-velocity (PV) space, we extracted the PV diagrams for the arrows A1–A7 shown in Figure 5.8b. Arrows A1–A6 are associated with Hub-1, while A7 extends to Hub-2, passing through Hub-1. The width of the slices used to extract the PV diagrams is 3 pixels for A1–A6, and 10 pixels for A7 to cover a larger

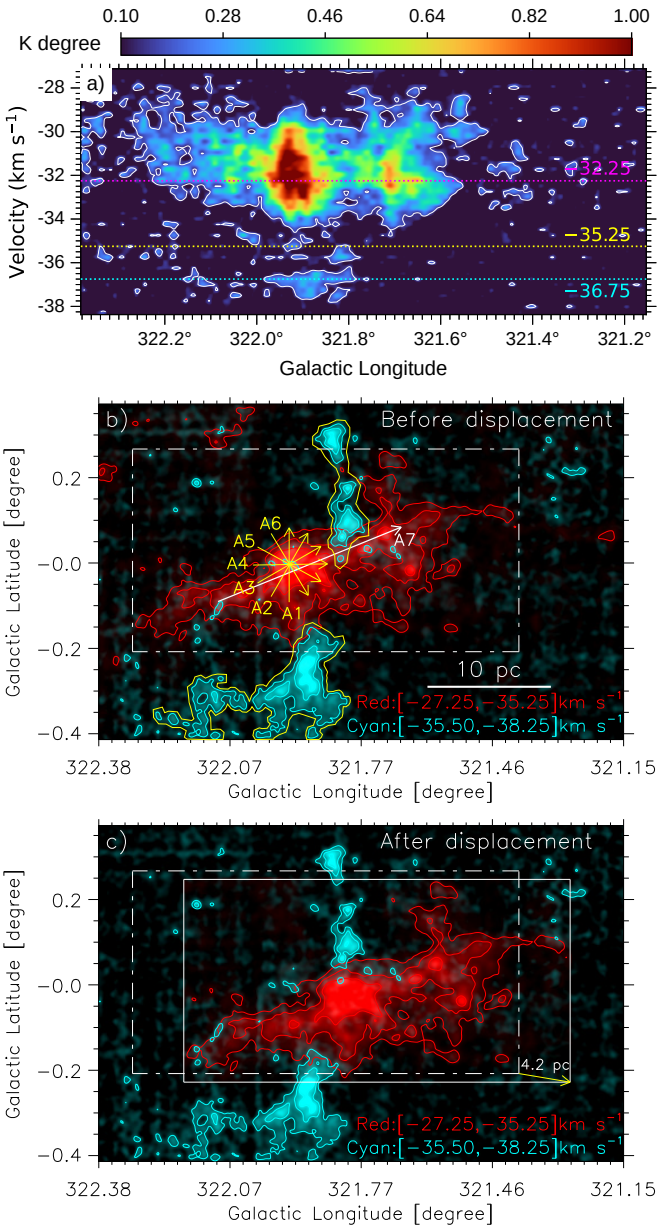

Figure 5.8: (a) The Galactic longitude-velocity (i.e., l–v) diagram for ^{13}CO data. The contour is at 10σ, where 1σ ∼0.016 K degree. The integration range for the Galactic latitude is [−0°.41, 0°.37]. The yellow dotted line separates two velocity components at about −35.25 km s^{-1}. The peak velocities for the blue- and red-shifted components are shown with cyan and magenta dotted lines, respectively. (b) The spatial distribution of the blue- and red-shifted components. The blue- and red-shifted components are integrated for the velocity ranges [−38.25, −35.50] and [−35.25, −27.25] km s^{-1}, respectively. The contour levels for the blue- and red-shifted components are at [3σ, 6σ, 9σ] and [6σ, 15σ, 30σ], respectively. The 1σ values are 0.3 and 0.5 K km s^{-1} for integrated intensity maps of the blue- and red-shifted components, respectively. The areas bounded by the yellow lines are considered for calculating the total mass of the blue-shifted component. The position-velocity diagrams are extracted along the arrows highlighted in the panel (b), which are shown in Figure 5.9. (c) Same as panel (b), with red-shifted component shifted by about 4.2 pc. The dashed-dotted and solid white rectangles present the initial and final positions of the red-shifted cloud component, respectively.

area. The extracted PV diagrams for the arrows are presented in Figure 5.9. The PV diagrams corresponding to A1–A6 show a mixed distribution of two velocity components (see the blue and red arrows). However, for A7, Hub-1 again shows a mixed distribution of two velocity components (see the cyan and red arrows), while other regions, including Hub-2, exhibit only one velocity component (see the white arrows).

5.4 Discussion

We carried out a detailed multi-scale, multi-wavelength observational study of G321. Based on our results, we discuss the role of filaments in mass accumulation and star formation, the massive star-forming activity in G321, and the origin of HFSs.

5.4.1 Role of filaments in mass accumulation and star formation in G321

G321 hosts two HFSs (i.e., HFS-1 and HFS-2; see Figure 5.4), where the hubs (i.e., Hub-1 and Hub-2) are connected with several parsec-scale filaments. As mentioned earlier, filaments are thought to channel molecular gas and dust to their hub, making the hub suitable for MSF (Myers, 2009; Kumar et al., 2020). In the case of G321, the total mass accretion rate to Hub-1 through the filaments is $\sim 2.64 \times 10^{-2}$ $M_{\odot}$ yr^{-1}. For Hub-2, combined mass accretion rate through the filaments is $\sim 4.17 \times 10^{-3}$ $M_{\odot}$ yr^{-1}. In both cases, the mass accretion rates are comparable to or higher than those observed in other MSFRs, such as $\sim 1 \times 10^{-3}$ $M_{\odot}$ yr^{-1} for DR 21 ridge (Schneider et al., 2010), 1–3 $\times 10^{-4}$ $M_{\odot}$ yr^{-1} for Serpens (Kirk et al., 2013), 4–7 $\times 10^{-4}$ $M_{\odot}$ yr^{-1} for Monoceros R2 (Treviño-Morales et al., 2019), $\sim 7.40 \times 10^{-4}$ $M_{\odot}$ yr^{-1} for G310.142+0.758 (Yang et al., 2023), $\sim 6.75 \times$

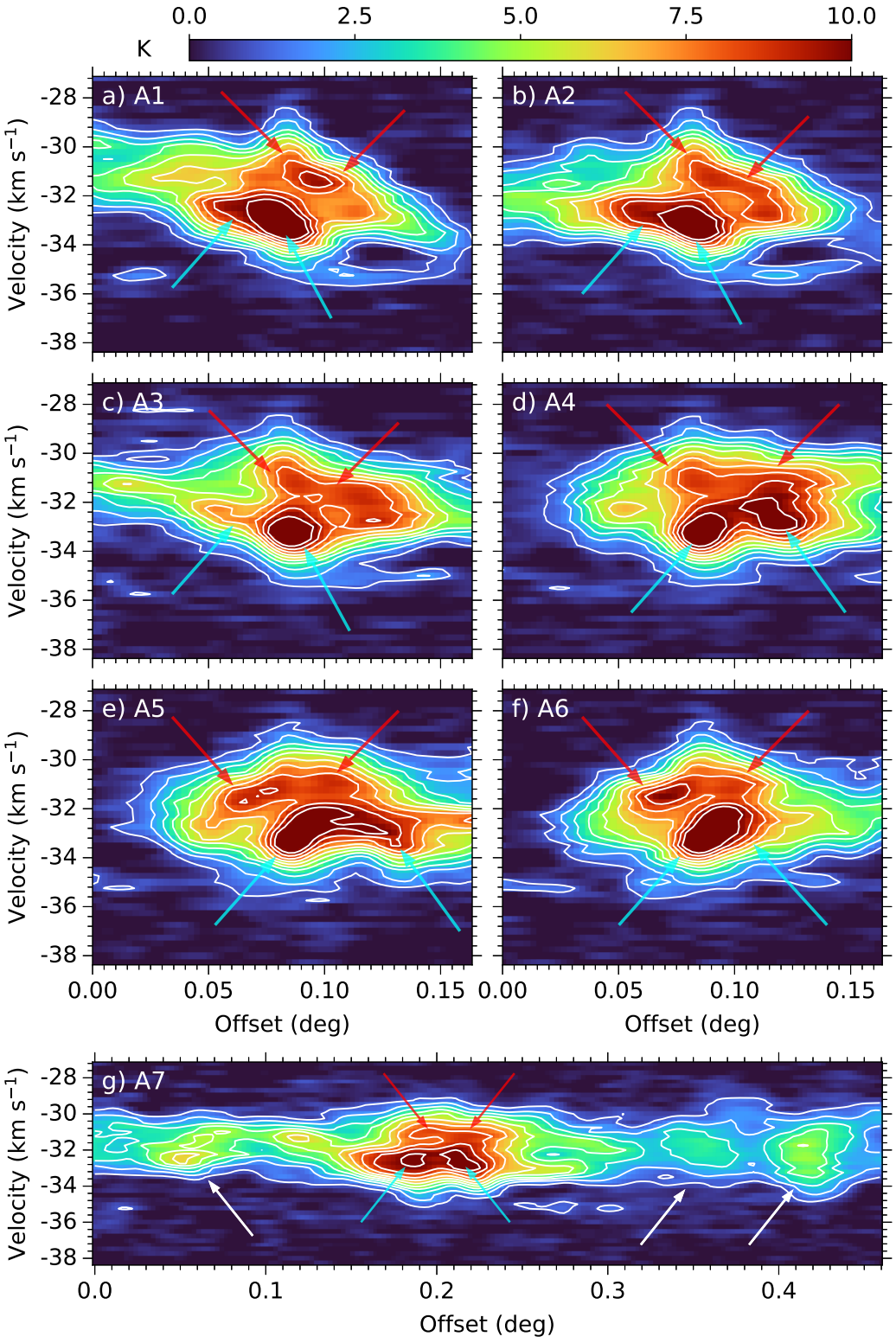

Figure 5.9: Panels (a)–(g) present the PV diagrams along the arrows A1–A7, as indicated in Figure 5.8b. The contour values range from 1 to 10 K, with intervals of 1 K. The red and cyan arrows in each panel indicate two separate velocity components mixed together. The white arrows for A7 point to a single velocity component.

10^{-4} $M_\odot$ yr^{-1} for G148.24+00.41 (Rawat et al., 2024), and ∼1.72 × 10^{-3} $M_\odot$ yr^{-1} for the HFS of RCW 117 (Seshadri et al., 2024). The mass accretion rate for Hub-1 is several times higher than that of Hub-2. It is important to note that the potential contribution from filament F4 has not been included in the comparison between the hubs. Moreover, the simple mass accretion model by Kirk et al. (2013) does not apply to F4 because it is connected to both hubs (see Section 5.3.3.2). As proposed by Liu et al. (2019), the oscillations observed in the average velocity plot along F4 are likely due to its fragmentation process, which is supported by the detection of ATL-5 toward F4. Although no YSO candidate has been detected toward ATL-5, we expect star-forming activity to occur later due to the filament's ongoing fragmentation. The $(M/L)^{\rm Fil}$ values for filaments in G321 varies from about 312 to 1041 $M_\odot$ pc^{-1}, which are comparable to or higher than the values for other filaments, such as ∼385 $M_\odot$ pc^{-1} for Orion (Bally et al., 1987), ∼600 $M_\odot$ pc^{-1} for the G11.11 IRDC (Kainulainen et al., 2013), ∼115 $M_\odot$ pc^{-1} for a subfilament in the G35.39 region (Henshaw et al., 2014), and ∼1000 $M_\odot$ pc^{-1} for filamentary IRDC 18223 (Beuther et al., 2015). The $(M/L)^{\rm Fil}$ values greatly exceeds the isothermal critical line-mass of about 25 $M_\odot$ pc^{-1} for 15 K (Ostriker, 1964). Hence, critical line-mass considering both thermal and non-thermal velocity dispersion, $(M/L)^{\rm tur}_{\rm crit}$ is estimated using Equation 1.5. The line-mass ratio (LMR) between $(M/L)^{\rm Fil}$ and $(M/L)^{\rm tur}_{\rm crit}$ for the filaments is listed in Table 5.3. LMR ∼1 suggests that turbulence provides major support against the gravitational collapse of the filaments. LMR ∼1.3 for F4 implies that it is prone to fragmentation and which is in agreement with our detection of the ongoing filament fragmentation.

Hub-1 is more massive than Hub-2, and its higher mass accretion rate suggests a dependence of the mass accretion rate on the hub's mass. Based on this, we propose the relation $\dot{M}_{||} \propto M^{\beta}_{\rm hub}$, with $\beta \sim 1.28$ in our case. This finding

indicates that the hub's gravitational influence plays a significant role in determining the total mass accretion rate through the filaments. The concept of gas flowing through filaments under the influence of gravity is supported by both observations (e.g., Williams et al., 2018; Wang et al., 2022; Zhou et al., 2022, 2023) and simulations (e.g., Maity et al., 2024). Although the uncertainties in both $M_{\rm hub}$ and $\dot{M}_{||}$ are likely systematic and will not affect the ratio of $M_{\rm hub}$ and $\dot{M}_{||}$ between Hub-1 and Hub-2, our estimation of β is limited to only two data points. Therefore, the value of β could be more precisely constrained with a larger sample of Galactic HFSs. The ratio of the total number of YSO candidates observed in VVV data toward Hub-1 to Hub-2 is about 4.5, which closely corresponds to the ratio of their masses. Previously, we found that the mass of the hub influences its total mass accretion rate. Thus, this study highlights a potential connection between the mass of the hub, its mass accretion rate, and its star-forming activity. The total mass of Hub-1 and Hub-2 is about $2 \times 10^4\,M_{\odot}$, which is about 25% of the total mass of the molecular cloud. The combined mass accretion rate for Hub-1 and Hub-2 is about $3.1 \times 10^{-2}\ M_{\odot}\ {\rm yr}^{-1}$. Given that the mass accretion rate increases with the mass of the hub, they are expected to accumulate an additional 25% of the cloud's total mass in less than 0.6 Myr unless disrupted by the feedback from the newly formed massive stars. This underscores the significant role of filaments in mass accumulation and in creating high-density regions that are conducive to MSF.

Interestingly, we have detected several small-scale ($\lesssim 1$ pc) filament candidates within Hub-1 and Hub-2, indicated by black arrows (see Figure 5.4c). As proposed by Dewangan et al. (2024), the presence of such small-scale filaments can be further confirmed through James Webb Space Telescope (JWST) NIR images in absorption. The detection of small-scale filaments, along with large-scale (> 1 pc) filaments connected to hubs, is important for assessing the self-similar hierarchical

HFS scenario introduced by Zhou et al. (2022), which proposes filamentary mass accretion occurring across multiple scales. Therefore, JWST NIR observations of Hub-1 and Hub-2 will be valuable for further investigation.

5.4.2 The massive star-forming activity in G321

The presence of four compact H II regions, two HFSs with high mass accretion rates (i.e., $> 10^{-3}$ $M_{\odot}$ yr^{-1}) to their hubs, along with evidence of filament fragmentation in F4, makes this region particularly intriguing for studying its potential for MSF. As shown in Figure 5.6, Hub-1 hosts ATB-1, which further fragments into ATL-3 and ATL-4. ATB-1 and Leaf-3 satisfy mKP-10 condition for MSF (Kauffmann & Pillai, 2010). Therefore, HFS-1 is actively engaged in MSF, which is further supported by the detection of three compact H II regions within Hub-1. By comparing the $N_{\rm uv}$ values for these H II regions (see Table 5.2) with the theoretical predictions from Panagia (1973), we determined that the ionizing sources are massive stars of spectral type B1V–B3V. Furthermore, we estimated the minimum stellar mass for a massive star that could be expected from the ATL-3 using the formula from Sanhueza et al. (2017):

$$M_{\rm exp} = \left(\frac{0.3}{\epsilon_{\rm sfe}} \frac{17.3}{M_{\rm clump}} + 1.5 \times 10^{-3} \right)^{-0.77} , \tag{5.3}$$

where $\epsilon_{\rm sfe}$ is the star formation efficiency. This formula was derived assuming the range of stellar masses between 0.08 and 150 $M_{\odot}$ and adopting the initial mass function from Kroupa (2001). The study by Wells et al. (2022) determined that $\epsilon_{\rm sfe}$ = 0.2–0.3 for a clump of a few hundred solar masses. Hence, using $\epsilon_{\rm sfe}$ = 0.2–0.3, and $M_{\rm clump}$ = 749 $M_{\odot}$ for ATL-3 in Equation 5.3, we found $M_{\rm exp}$ ∼13–17 $M_{\odot}$. Given the high mass accretion rate of Hub-1, this can be considered a lower limit for the maximum stellar mass within Hub-1, and we may expect a small cluster of O-type stars to form in Hub-1.

We have estimated the thermal Jeans mass for ATL-3 to be about 3 $M_{\odot}$ using Equation 6 from the study of Palau et al. (2015). This estimate is in agreement with the masses of the ALMA leaves/cores detected within ATL-3, which range from 1–9 $M_{\odot}$, with an average of about 4 $M_{\odot}$ (see Table 5.5). Subsonic/transonic turbulence is sufficient to explain the existence of the ALMA leaves above the Jeans mass (i.e., $> 3\,M_{\odot}$). However, the thermal Jeans mass estimated for the ALMA branches, which is in the range of 0.1–0.2 $M_{\odot}$, does not match the masses of their substructures (i.e., further branches and leaves). Therefore, the ALMA branches may represent ensembles of their substructures that evolve as the substructures themselves evolve, not through step-by-step thermal fragmentation, but rather through a simultaneous formation process as discussed in Morii et al. (2024). It is important to note that the lack of molecular line data compatible with the resolution of the ALMA Band-7 continuum image prevents us from conducting any analysis related to turbulence at the core-scale.

Although ATL-4 (in Hub-1), ATL-5 (toward Filament F4), and ATL-6 (in Hub-2) marginally satisfy mKP-10 condition for MSF, the large errors (at least ∼20%; see Section 5.3.4.1) associated with the mass estimation cast doubt on their potential for MSF. Additionally, the absence of radio continuum emission from these leaves suggests that they are not currently active in MSF. However, since ATL-4 and ATL-6 are part of Hub-1 and Hub-2, respectively, and both actively accumulating material through the filaments, these leaves may evolve into potential MSF sites. Similarly, ATL-5, being part of a fragmenting filament, has the potential to become active in MSF at a later stage. The presence of a compact H II region (driven by a B1V type source) toward ATL-2 clearly indicates ongoing massive star-forming activity. Interestingly, ATL-2 falls below the mKP-10 limit for MSF, a result that aligns with approximately 10% of the MSF sites listed in Beuther et al. (2002), as noted by Kauffmann & Pillai (2010). This

suggests that the mKP-10 limit serves as an approximate threshold for MSF, and follow-up studies are required for such sources, including ATL-2.

In the case of Hub-1, all the structures from ATB-1 and ATL-3 to the ALMA leaves/cores satisfy the mKP-10 condition for MSF. Interestingly, two ALMA branches (IDs: 4 and 13) have masses above 20 $M_{\odot}$; however, they are further fragmented into low-mass cores. The detection of YSO candidates, along with 22 GHz H_2O and Class I 95 GHz MME, indicates ongoing star-forming activity in some of the ALMA low-mass cores. Thus, the presence of only low-mass cores actively forming stars within a hub that satisfies the condition for MSF supports the applicability of the idea proposed by Motte et al. (2018). It is important to note that the ALMA data cover a small area of ATL-3, which is located at the edge of the H II-2 region (not shown in the figure). As a result, it appears that the main driving source of the H II-2 region is beyond the coverage of the ALMA observations. Therefore, a high-resolution ALMA observation covering the entire area of ATB-1 would be beneficial for revealing the complete core mass function, including the cores associated with the H II regions. The absence of H II regions toward Hub-2 indicates that HFS-2 can be in the early stages of Motte's scheme. However, the presence of H II regions toward Hub-1 and the ATL-2 suggests that they are in the later stages of evolution. Hence, we observe significant differences in the evolutionary stages of MSF at our target site, G321.

5.4.3 Origin of the hub-filament systems

Despite being part of the same cloud component (see Section 5.3.5), HFS-1 and HFS-2 show significant differences in terms of the mass of their hubs, mass accretion rate through the filaments, number of color excess sources present in the hubs, and their potential for MSF. In this section, we attempt to explain the origin of these HFSs. As earlier mentioned, a convincing picture of the complementary

spatial distribution between the blue-shifted filamentary cloud component and the red-shifted component was achieved by shifting the red-shifted component toward the south-west direction (see Figure 5.8c). The complementary distribution of two cloud components with a spatial shift in the plane of sky is a well-recognized signature of CCC (e.g., Tsuge et al., 2021; Maity et al., 2023). The intriguing feature of the l–v diagram for G321 is the presence of two cloud components and the absence of the bridge feature. Several studies based on numerical simulations demonstrated the temporal evolution of PV diagrams in the context of CCC (Takahira et al., 2014; Haworth et al., 2015b). Haworth et al. (2015b) argued that the bridge feature may disappear if one cloud component punches through the other. In such cases, the compressed layer will mix with the cloud component passing through the other in the velocity space. The observed morphology of the blue- and red-shifted cloud components toward HFS-1 is consistent with the scenario in which one cloud component punches through the other. Specifically, the red-shifted component appears to have passed through the blue-shifted filamentary cloud, creating a cavity or low-intensity region in the filament. As a result, this scenario does not align with the proposal by Kumar et al. (2020), where HFSs form through the merging or overlapping of filaments. In addition, the detection of the mixing of two velocity components in the PV diagrams along A1–A7 toward Hub-1 (see Figure 5.9) suggests that the compressed layer created during the collision has merged with the red-shifted cloud component in velocity space. Therefore, this study suggests that the formation of HFS-1 was possibly triggered by the collision of the red-shifted cloud component with the blue-shifted filamentary cloud. The collision timescale can be estimated using the formula, $t_{\rm collision} = l_{\rm loc}/v_{\rm loc}$ (see Chapter 4). In this expression, $l_{\rm loc}$ and $v_{\rm loc}$ denote the spatial shift along the collision axis and the intrinsic collision velocity, respectively. The detection of two cloud components in the l–v diagram

for our target sites, along with the necessity of spatial shift for complementary distribution, indicates that $\theta_{\rm col}$ is significant and less than 90°. Hence, we assume $\theta_{\rm col}$ to be within the range of 30° to 60°. Using $l_{\rm obs}$ = 4.2 pc, $v_{\rm obs}$ = 4.5 km s^{-1}, and $\theta_{\rm col}$ = 30°, 45°, and 60°, the corresponding collision timescales ($t_{\rm collision}$) are estimated to be 1.58, 0.91, and 0.53 Myr, respectively. These timescales are consistent with the dynamical timescales of the H II regions (i.e., $t_{\rm dyn} < 0.25$ Myr) and the mean age of the Class I YSOs, which is about 0.44 Myr (Evans et al., 2009). This study, therefore, suggests that a CCC event approximately 1 Myr ago triggered star-forming activity in the region of the collision (i.e., toward Hub-1). The collision also contributed to an increase in the total mass and density of the gas in the collision region, leading to its high mass accretion rate and massive star-forming activity.

The filaments connected to Hub-2 (i.e., F4, F5, and F6) have a relative velocity of about 1.5 km s^{-1} as shown in the two-color composite image in Figure 5.10a. Interestingly, we detected at least three filaments toward ATL-2 through visual inspection of the moment-0 maps of ^{13}CO emission for the velocity ranges [−32.25, −31.75] and [−29.25, −28.75] km s^{-1}. These filaments are marked using dashed-dotted lines over the two-color composite image in Figure 5.10b. These filaments were not visible in Figure 5.4 due to their weak emission strength in the integrated intensity map for the wide velocity range (i.e., [−38.25, −27.25] km s^{-1}). ATL-2 is located precisely at the junction of these filaments, making the entire configuration a candidate HFS (C-HFS). The differing velocities of the filaments for the HFS-2 and C-HFS support the idea proposed by Kumar et al. (2020), where HFSs form through the merging or overlapping of filaments. Further insights into this candidate HFS can be gained through molecular line observations with improved sensitivity and resolution.

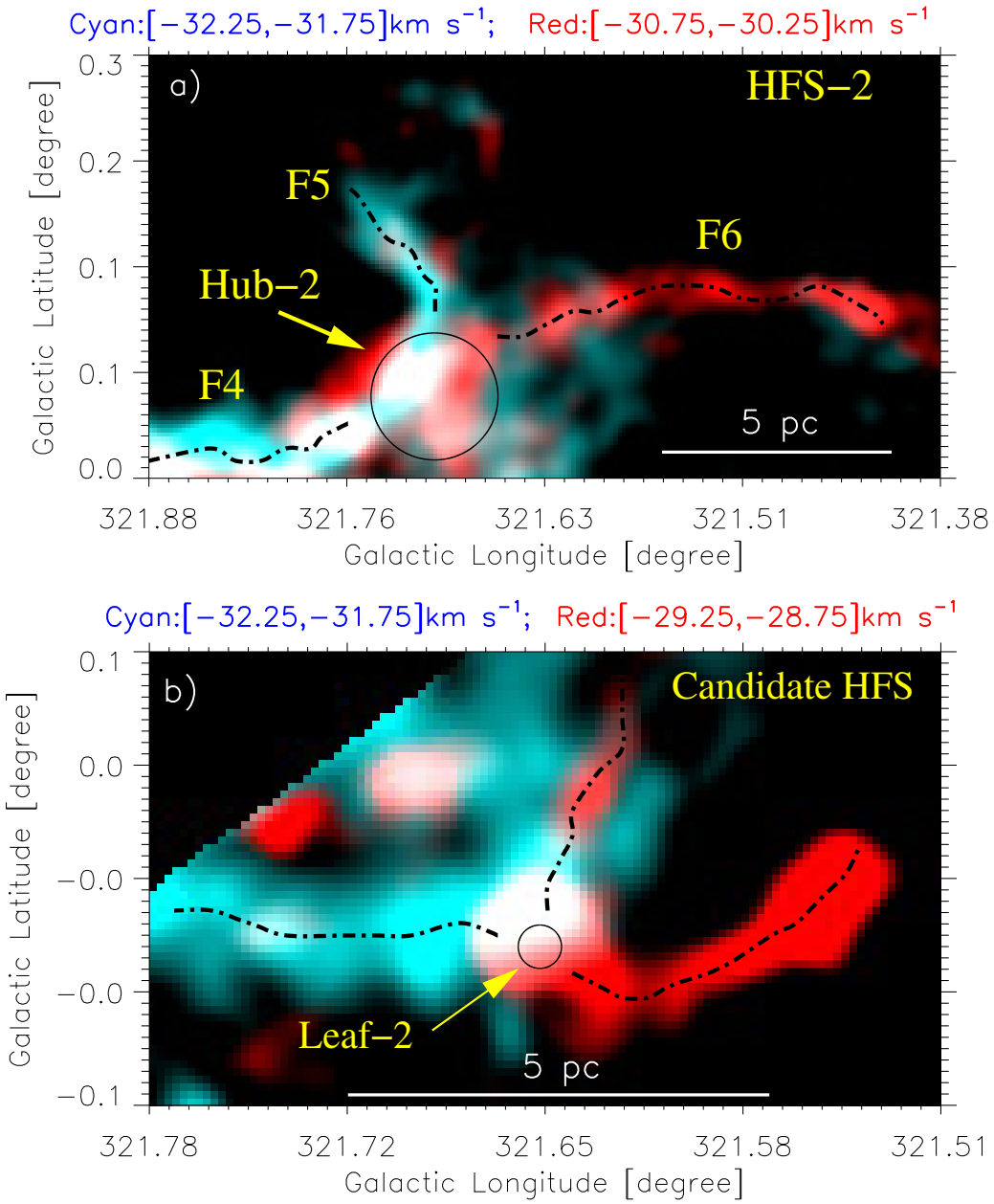

Figure 5.10: (a) The two-color composite image presents the ^{13}CO integrated intensity maps shown in Figures 5.3i (in cyan) and 5.3k (in red) for the region highlighted by the dashed-dotted rectangle in Figure 5.4c. The moment-0 maps in cyan and red are displayed on a linear scale from 3σ to 18σ and 3σ to 10σ, respectively, where 1σ ∼0.15 K km s^{-1}. The black circle, indicated by a yellow arrow, is Hub-2 as shown in Figure 5.4c. The dashed-dotted lines trace the filaments (i.e., F4, F5, and F6) connected to Hub-2. (b) Similar two-color composite image showing ^{13}CO integrated intensity maps displayed in Figures 5.3i (in cyan) and 5.3m (in red) for the area covered by the dashed-dotted polygon in Figure 5.6a. The moment-0 maps in cyan and red are displayed on a linear scale from 6σ to 15σ and 3σ to 7σ, respectively. The black circle, situated at the peak emission of ATL-2 (indicated by a yellow arrow), has a radius equal to the leaf's effective radius. The dashed-dotted lines indicate the filaments connected to Leaf-2. A scale bar of 5 pc is shown in each panel.

5.5 Summary

In this chapter, we conducted a multi-scale and multi-wavelength observational investigation of G321 to search for multiple HFSs within the same MSFR and explore their evolutionary stages and origins. Additionally, we calculated the mass accretion rate for the HFSs and assessed the overall star-forming activity of G321, including MSF. The key findings of this chapter are summarized below.

1. G321 hosts multiple HFSs: HFS-1, HFS-2, and a C-HFS. HFS-1 and HFS-2 are connected by a filament (i.e., F4), which shows clear signs of fragmentation. This is a unique result, considering that such complex sites are rare in the literature.

2. HFS-1 and HFS-2 exhibit high mass accretion rates (i.e., $\dot{M}_{||} > 10^{-3}$ $M_{\odot}$ yr^{-1}). We found $\dot{M}_{||} \propto M_{\rm hub}^{\beta}$ with $\beta \sim 1.28$, suggesting the gravitational influence of the hub on mass accretion through filaments. The study of IR color excess sources demonstrates a possible connection among the mass of the hub, its mass accretion rate, and its star-forming activity.

3. Considering the presence of three compact H II regions driven by B1V–B3V type stars in Hub-1 and its high $\dot{M}_{||}$ values, we may expect a small cluster of O-type stars to form in Hub-1.

4. The analysis of ALMA Band-7 continuum data inside Hub-1/ATL-3 revealed several high-mass branches (M ∼8–33 $M_{\odot}$), which are further fragmented into branches and leaves. We have calculated the mass of these leaves/cores to be about 1–9 $M_{\odot}$, which is in agreement with the thermal Jeans mass of ATL-3 with subsonic/transonic turbulence.

5. A significant difference in the evolutionary stages of MSF is observed in

G321. The absence of H II regions toward Hub-2 indicates that HFS-2 can be in the early stages of Motte's scheme (Motte et al., 2018). However, the presence of compact H II regions toward Hub-1 and the ATL-2 suggests that they are in the later stages of evolution.

6. HFS-1 shows a clear signature of collision with a filamentary cloud about 1 Myr ago, suggesting that the CCC may have triggered the formation of HFS-1. In the cases of HFS-2 and C-HFS, their constituent filaments exhibit relative velocities ($\gtrsim$1 km s^{-1}), indicating possible formation through the merging or overlapping of filaments.

Overall, we have found G321 to be an interesting MSFR, hosting several HFSs. This study clearly shows that interacting filaments (either by collision or merging/overlapping) can form high-density regions susceptible to MSF. It is important to note that we have not explored the formation mechanisms of the individual filaments in this study, which can be addressed in future work.

Chapter 6

Cloud-cloud collision: Formation of hub-filament systems and associated gas kinematics[†]

6.1 Introduction

EARLIER works have well established that MSF requires a high-density region, having a H_2 column density, $N(H_2) \gtrsim 10^{22}$ cm^{-2} (Krumholz et al., 2007b; Zinnecker & Yorke, 2007; Fukui et al., 2021a). Such high column density regions are commonly found at the junction of several filaments or the interface of colliding molecular clouds (e.g., Myers, 2009; Motte et al., 2018; Fukui et al., 2021a; Maity et al., 2022, 2023, 2025a). In the literature, the former scenario is based on accretion through filaments to their common junctions (i.e., hubs), and such systems are known as HFSs (Myers, 2009). The latter scenario is based

[†]**A. K. Maity**, T. Inoue, Y. Fukui, L. K. Dewangan, H. Sano, R. I. Yamada, K. Tachihara, N. K. Bhadari, and O. R. Jadhav, 2024, *The Astrophysical Journal*, Volume 974, Issue 2, https://doi.org/10.3847/1538-4357/ad7098

on the collision of molecular clouds, which is referred to as CCC (Habe & Ohta, 1992). Both scenarios are well described in the previous chapters of this thesis. Interestingly, our recent observational work on Galactic MSFRs, W31 complex (Maity et al., 2022, presented in Chapter 3), AFGL 5180 & 6366S (Maity et al., 2023, presented in Chapter 4), and G321.93–0.01 (Maity et al., 2025a, presented in Chapter 5) reveals simultaneous signatures of CCC and the presence of HFSs. Similar results have also been reported for SDC13 (Peretto et al., 2014; Wang et al., 2022), W33 complex (Zhou et al., 2023) and some extragalactic MSFRs, such as N159E-Papillon (Fukui et al., 2019), N159W-South (Tokuda et al., 2019), and 30 Dor (Wong et al., 2022) in LMC. Although the literature provides limited instances of MSFRs exhibiting concurrent signatures of CCC and the presence of HFSs, this raises two important questions regarding MSF: Can CCC lead to the formation of HFS? If so, how do filaments precisely converge toward a common junction after the collision, resulting in the observed morphology of the HFSs?

In this context, a connection between CCC and the formation of a network of filaments was reported in smoothed particle hydrodynamics simulation by Balfour et al. (2015, 2017). Balfour et al. (2015) demonstrated that collisions between molecular clouds of uniform density and subsonic turbulence result in the formation of radially converging filaments, which are referred to as a "hub-and-spoke" system. In contrast, higher collision velocities lead to the creation of a complex network of filaments resembling a spider's web. Furthermore, (Balfour et al., 2017) showed that when the colliding clouds have internal substructure, the distinction between the "hub-and-spoke" system and the spider's web structure becomes less clear. Their works, however, did not delve deeply into the formation of HFSs. In addition, the absence of magnetic fields in their research can be recognized as a major limitation. Inoue & Fukui (2013) and Inoue et al. (2018) incorporated magnetic fields in their works and thoroughly investigated

the development of filaments in the CCC scenario using MHD simulations. They demonstrated that shock compression of a turbulent and inhomogeneous cloud leads to the rapid development of filaments. However, it remains to be explored whether these filaments gradually converge to form an HFS and how factors such as turbulence, collisional compression, magnetic fields, and gravity influence this process. Hence, this chapter aims to analyze the MHD simulation data generated by Inoue et al. (2018) to unravel the formation mechanism of HFSs through CCC. Additionally, this simulation data provide valuable insights into the intricate gas kinematics involved in CCC, aiding in understanding the observational challenges in detecting CCC sites. Furthermore, this study intends to search for new signatures to identify them at $\theta_{\rm col} = 90°$, which is one of the major objectives of this thesis.

This chapter is organized as follows: Section 6.2 describes the details of the simulation data utilized in this work. Section 6.3 presents the results of our analysis, which are further discussed in Section 6.4. Finally, Section 6.5 summarizes the key findings of this work.

6.2 The model description

The simulation of CCC, conducted by Inoue et al. (2018), incorporated ideal MHD with self-gravity and utilized adaptive mesh refinement and sink particle techniques (developed by Matsumoto, 2007; Matsumoto et al., 2015). The ideal MHD equations with self-gravity are described in Section 2.2.1. Gravity was present in the system from the beginning of the simulation. The molecular gas was approximated to be isothermal, corresponding to the sound speed ($c_{\rm s}$) of about 0.3 km s^{-1}. The cubical numerical domain has each side of 6 pc, with its center at the origin ($x = 0$, $y = 0$, $z = 0$). As an initial setup, a spherical

molecular cloud with a radius (R) of 1.5 pc was placed at (0, 0, 0.5 pc) with a z-component of velocity (v_z) of about -5 km s^{-1}, as shown in Figure 6.1a. The initial density (n) distribution of the spherical cloud was a Gaussian with an amplitude of 10^3 cm^{-3} and a FWHM of about 2.5 pc.

The mean molecular mass of gas particles was set to be 2.4 times the proton mass. Hence, the total mass of the spherical cloud was about 477 $M_\odot$. Turbulence is a common feature in molecular clouds (Larson, 1981), potentially arising from larger-scale flow collisions, Galactic shear, supernova explosions, expanding H II regions, protostellar outflows, and stellar winds (e.g., Vázquez-Semadeni et al., 2003; Hennebelle & Falgarone, 2012; Kim & Ostriker, 2015; Padoan et al., 2016; Orkisz et al., 2017). Therefore, in addition to the bulk motion of the spherical cloud, a turbulent velocity field (v_t) with an FWHM, $\Delta v_t \sim 1$ km s^{-1} was incorporated. As the second cloud component, a sea of dense gas with $n = 10^3$ cm^{-3} was set in the region $z \lesssim -1.5$ pc (see Figure 6.1a) with v_z of about 5 km s^{-1}. The remaining space was filled with relatively less dense gas with $n = 10^2$ cm^{-3}. The histogram of CCC events with the relative velocity between the colliding clouds (i.e., the collision velocity; see Figure 9b in Fukui et al., 2021a) reveals the mean collision velocity to be about 5 km s^{-1}. However, the cloud components observed in all the CCC sites are in collisional interaction, which decreases the velocity separation between the cloud components (Takahira et al., 2014). In addition, the projection effect can reduce the observed velocity separation between the cloud components. Hence, the actual collision velocity will be larger, so a collision velocity of about 10 km s^{-1} is used in this work. This CCC model resembles a scenario in which a larger cloud collides with a smaller one or a cloud undergoes compression by a plane-parallel shock wave[1]. The initial

[1]The interaction of the molecular cloud with an expanding bubble can act as a source of plane-parallel shock (Inutsuka et al., 2015).

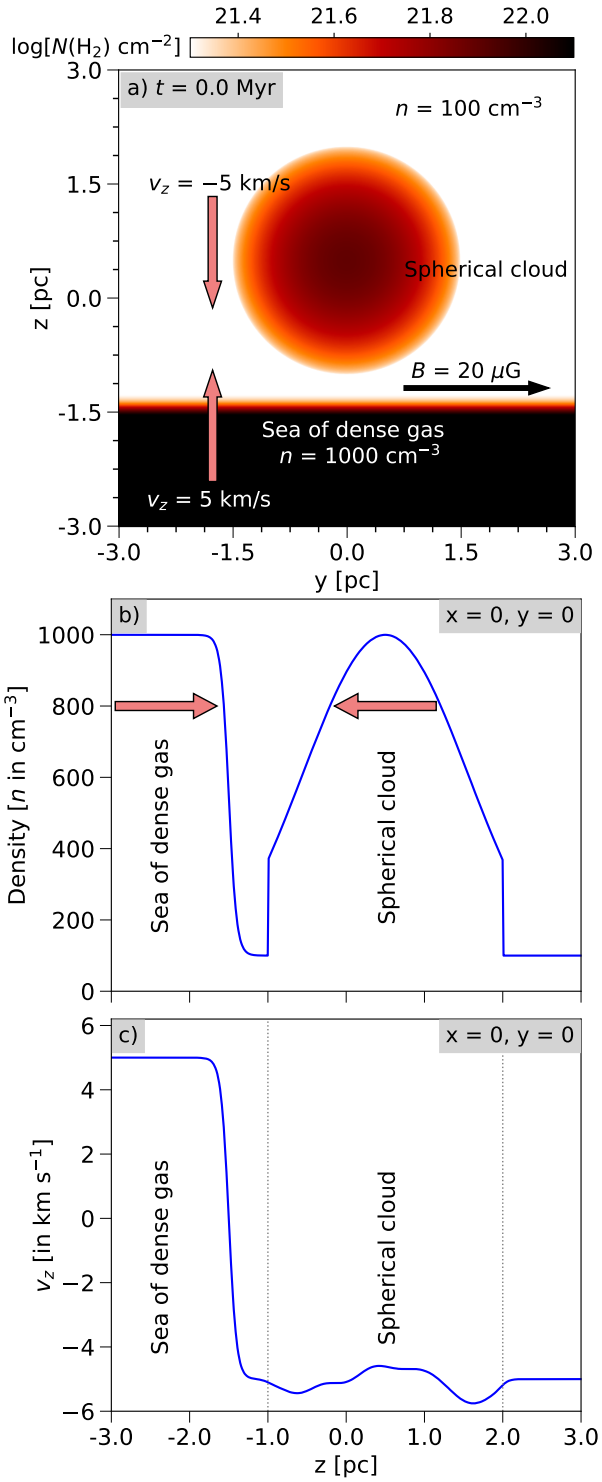

Figure 6.1: An illustration of the initial setup for CCC, similar to Inoue et al. (2018): (a) The H_2 column density (i.e., $N(H_2)$) map in the y–z plane. The arrows in color light-coral point out the directions of movement for the cloud components. The black arrow indicates the direction of the magnetic field. Panels (b) and (c) present the density and z-component of the velocity distribution of the molecular gas along the z-axis, respectively. The spherical cloud component and the sea of dense gas are specified in each panel. In panel (b), the directions of movement of the cloud components are shown with two arrows. In panel (c), the extent of the spherical cloud component is marked with gray dotted lines.

magnetic field, $\vec{B} = [0, 20\,\mu\mathrm{G}, 0]$, was oriented perpendicular to the direction of the collision. The input density and z-component of velocity distributions along the z-axis are shown in Figures 6.1b and 6.1c, respectively. These distributions can be mathematically described as follows:

$$n(0,0,z) = \begin{cases} 550 - 450\ \tanh\left(\frac{z+1.5}{0.1}\right) & \text{if } z < -1 \text{ and } z > 2, \\ 1000 \exp\left(-\frac{(z-0.5)^2}{2\sigma_z^2}\right) & \text{if } -1 \leq z \leq 2, \end{cases} \tag{6.1}$$

and

$$v_z(0,0,z) = -5\ \tanh\left(\frac{z+1.5}{0.1}\right) + v_t(0,0,z), \tag{6.2}$$

where, $\sigma_z = \frac{2.5\,\mathrm{pc}}{\sqrt{(8\ln 2)}}$ is the dispersion of the spherical cloud. Equations 6.1 and 6.2 are in the units of cm^{-3} and km s^{-1}, respectively, with z measured in pc in both cases. For the x and y boundary planes at $\pm$3.0 pc, periodic boundary conditions were used, while free boundary conditions were applied to the z boundary planes at $\pm$3.0 pc. The numerical results of the simulation were recorded from time, t = 0 to 0.7 Myr at an interval of 0.1 Myr. The data utilized in this work have a resolution of about $\frac{6}{512}$ pc = 0.0117 pc $\sim$2400 AU, which is sufficient for the study of HFSs and the associated gas kinematics.

6.3 Results

6.3.1 The physical environment of the shock-compressed layer and distribution of the sink particles

The evolution of the system from t = 0.1 to 0.7 Myr is presented in Figure 6.2 using the $N(\mathrm{H_2})$ maps in the x–z, x–y, and y–z planes. The $N(\mathrm{H_2})$ maps are calculated using Equation 2.17. The simulation introduces sink particles to follow star formation (see Section 2.2.2 for details). The positions of the sink particles

created in this simulation are displayed on the column density maps using the plus (+) symbols. In the x–z and y–z planes, the column density maps show

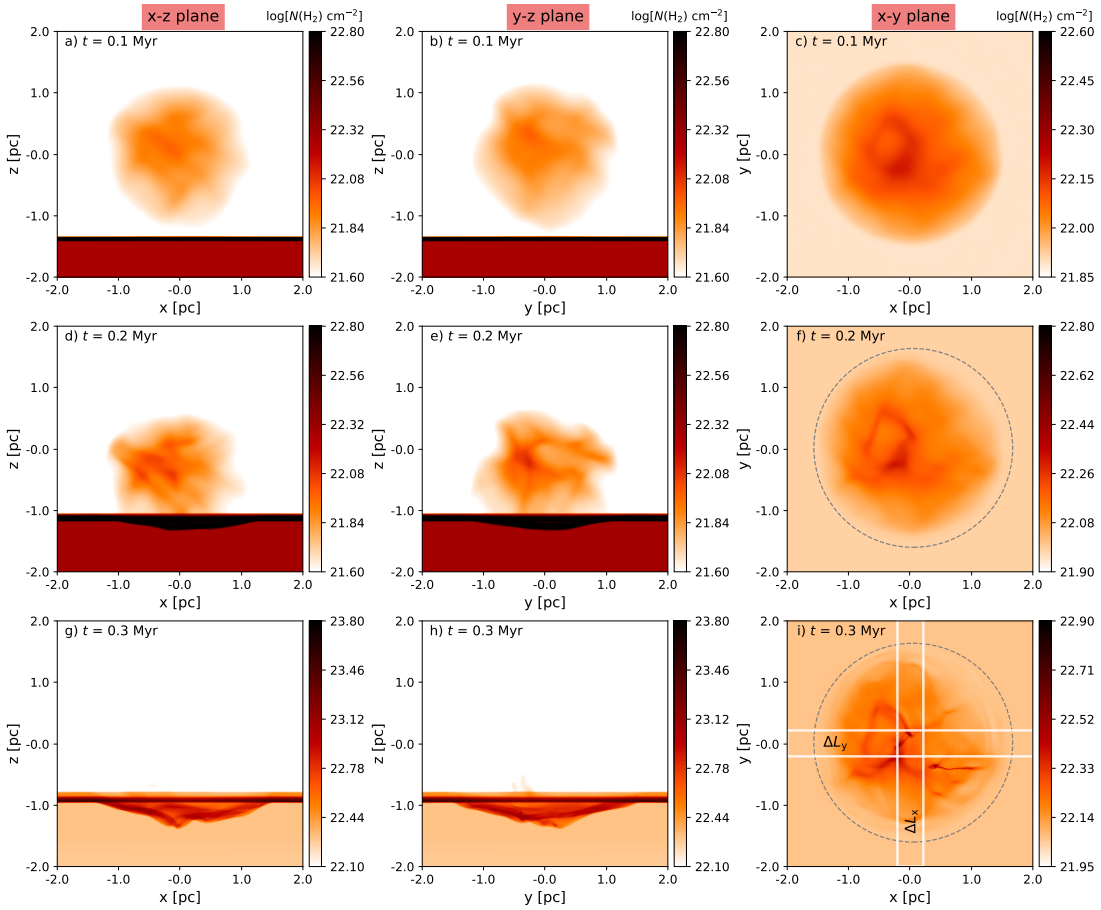

Figure 6.2: Continued.

the development of the shock-compressed layer. As both planes are parallel to the direction of the collision, they present similar gas distribution. Hereafter, we mostly used the y–z plane to show the gas distribution from a perpendicular direction to the collision axis (i.e., the z-axis). The x–y projected maps reveal structural components (i.e., filaments and cores) of the compressed layer. Here, the term 'core' refers to gaseous condensations that do not meet the selection criteria for the sink particles. The structural components and the sink particles

are mostly confined within the circular regions, as shown with the gray dashed circles in Figure 6.2. These circular areas are selected for further examination (see Sections 6.3.2, 6.3.3 and Figures 6.8, 6.9). The pair of white lines overlaid on the x–y projected column density map at $t = 0.3$ Myr along the x- and y-axes are employed to extract the PV diagrams (see Section 6.3.4 and Figure 6.11). The histograms of the gas density for each pixel within z: $[-2, 2]$ pc and n: $[5{\times}10^1, 10^7]$ cm^{-3} are displayed in Figure 6.3, with $t = 0$ Myr showing the input distribution. A low-density gas distribution below the lowest input density (i.e., 10^2 cm^{-3}, marked with blue dotted lines in Figure 6.3) is observed for $t = 0.1$ to 0.7 Myr. Turbulence is responsible for the creation of these low-density regions (Fukui et al., 2021b). Several numerical studies have shown that supersonic turbulence in an isothermal uniform density molecular cloud leads to a lognormal density distribution (e.g., Federrath et al., 2010; Auddy et al., 2018, and references therein), which has densities both above and below the initial density. Initially, the cloud was geometrically symmetrical, moving with uniform velocity and in a uniform magnetic field. Hence, gravity and the magnetic field will not be responsible for the production of low-density regions. Therefore, turbulence is the only factor responsible for the production of those low-density regions. At the same time, the collision of cloud components produces high-density regions, characterized by a power-law tail above $\sim 2 \times 10^4$ cm^{-3}, expressed as $N_{\rm pix} \propto n^{-p}$. Here, $N_{\rm pix}$ presents the pixel number at a given density n, and p is the power-law index. It is evident in Figure 6.3 that the value of p decreases from 7.54 at $t =$ 0.2 Myr to 1.99 at $t = 0.7$ Myr. Consequently, the high-density tail gradually flattens over time.

The temporal change in the cone-shaped[2] compressed layer is displayed in

[2]In reality, molecular clouds are not perfect Gaussians. As long as the central region of a molecular cloud is the densest and the cloud collides with a larger cloud component, a conical

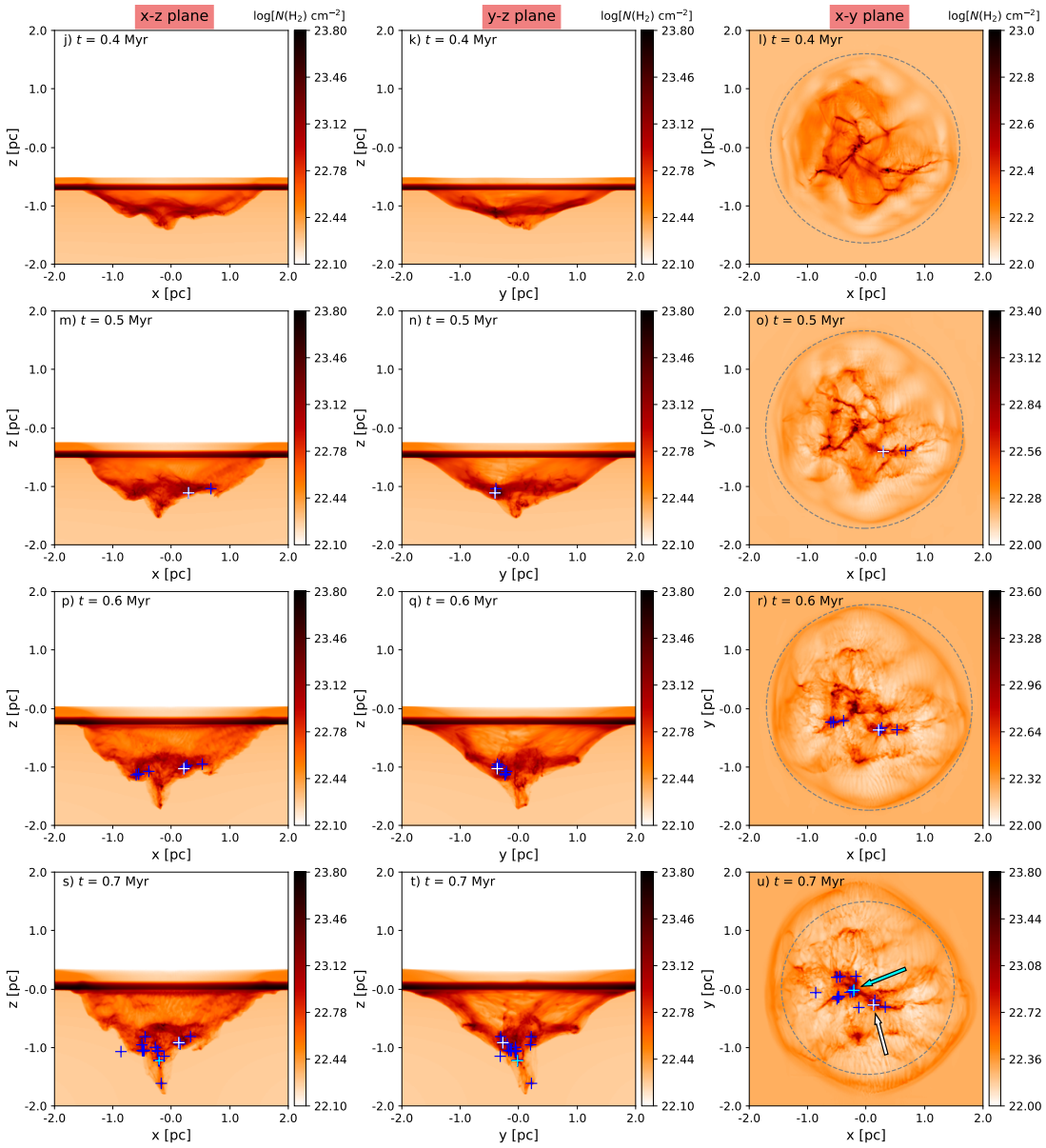

Figure 6.2: The $N(H_2)$ maps for $t = 0.1$ to 0.7 Myr in the x–z (left), y–z (middle), and x–y (right) planes, respectively. The plus (+) symbols present the positions of the sink particles. The white plus symbol shows the heaviest sink particle. The positions of two massive sink particles at $t = 0.7$ are marked in white and cyan, with two arrows pointing toward them in panel (u). The gray dashed circular regions overlaid on the $N(H_2)$ maps in the x–y plane from $t = 0.2$ to 0.7 Myr are zoomed-in in Figure 6.8 with identical color scales. Identical circular regions and color scales from $t = 0.3$ to 0.7 Myr are presented in Figure 6.9. The pair of horizontal and vertical white lines highlighted on panel (i) are utilized to extract the PV diagrams, which are shown in Figure 6.11.

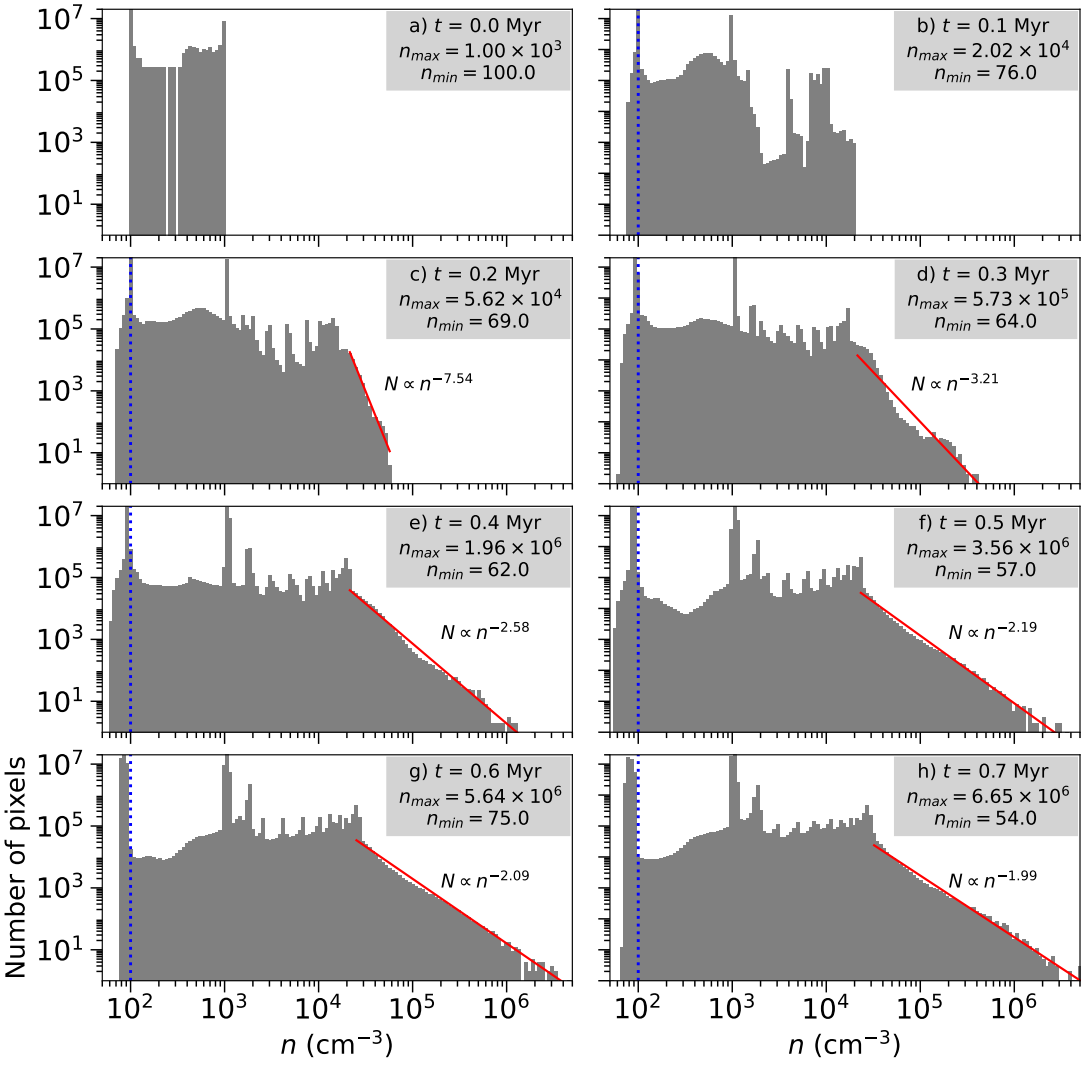

Figure 6.3: Panels (a)–(h) present histograms of H_2 density for each pixel within the range of z: $[-2, 2]$ pc, for t = 0.0 to 0.7 Myr, respectively. Each panel also includes the maximum and minimum density values (i.e., $n_{\rm max}$ and $n_{\rm min}$, respectively) at the corresponding time. The blue dotted line on the panels (b)–(h) is at $n = 10^2$ cm^{-3}.

the y–z projected column density maps for an integration range of x: $[-1, 1]$ pc in Figure 6.4. The compressed layer at each time exhibits symmetry about the collision axis and its angle (θ) with the z-axis decreases from θ $\sim$84° at t = 0.2 Myr to θ $\sim$52° at t = 0.7 Myr due to the collisional impact (see the angles in Figure 6.4). All the cones presented in Figure 6.4 are divided into thin conical shells having a width of 3 pixels. These thin shells (in 3D) are utilized to calculate the mass-weighted average density, z-component of velocity, and the gravitational acceleration using Equation 2.18. The results of this analysis are shown in Figure 6.5, which demonstrate the rapid development of high-density and intermediate-velocity regions. The width and density of the compressed layer increase over time, which leads to an increase in the gravitational acceleration with time. Finally, the compressed layer grows to a thickness of about 1 pc at t = 0.7 Myr. The detected z-component of velocity magnitudes above the highest input value, i.e., $|v_z| \gtrsim 5$ km s^{-1} result from gravitational acceleration.

The high-density gas distribution for the conical geometries of the compressed layers along the z-direction from t = 0.2 to 0.7 Myr is shown in Figure 6.6. At t = 0.3 and 0.4 Myr, the maximum gas density reaches more than 10^5 and 10^6 cm^{-3}, respectively, which can also be inferred from the $n_{\rm max}$ values mentioned in Figure 6.3 and the detection of sink particles after t = 0.4 Myr. A smooth development of the high-density region with $n > 10^4$ cm^{-3} along the z-direction can be seen. However, the distribution of gas with the density, $n > 10^5$ cm^{-3} along the z-direction shows large variations due to the formation of structural components, which are described later. Table 7.1 presents the total mass of the gas within the compressed layer with the density exceeding 10^3 cm^{-3}. We observe an increase in the fraction of dense gas over time. Specifically, the fraction

structure can be expected. The resulting cones, though, may be imperfect or distorted based on the initial structure of the molecular cloud.

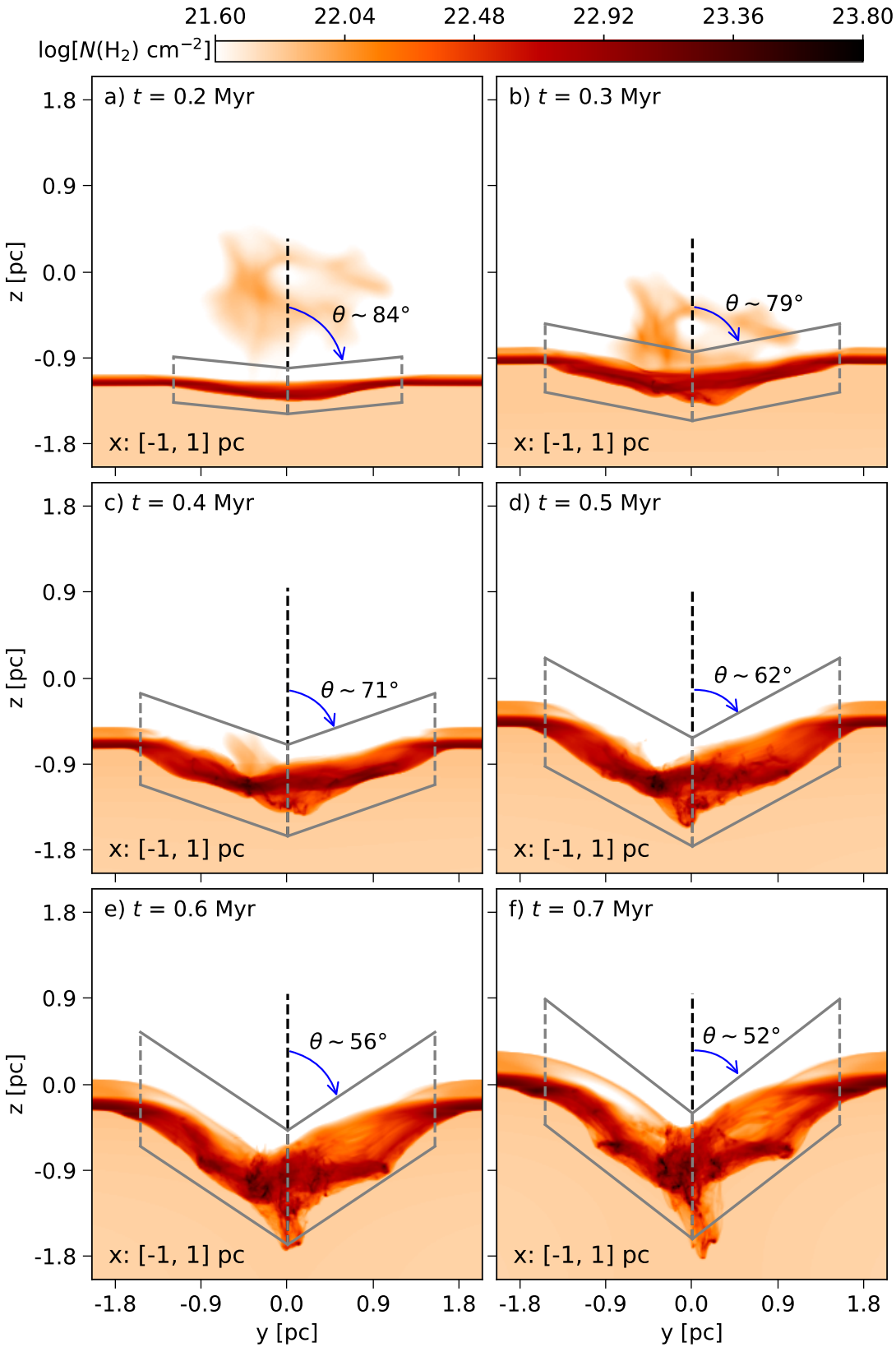

Figure 6.4: Panels (a)–(f) display the $N(H_2)$ map in the y–z plane for the range of x: $[-1, 1]$ pc. In each panel, the overlaid cone illustrates the conical structure of the shock-compressed layer, and a blue arrow indicates its angle with respect to the z-axis. The angle is also mentioned in each panel.

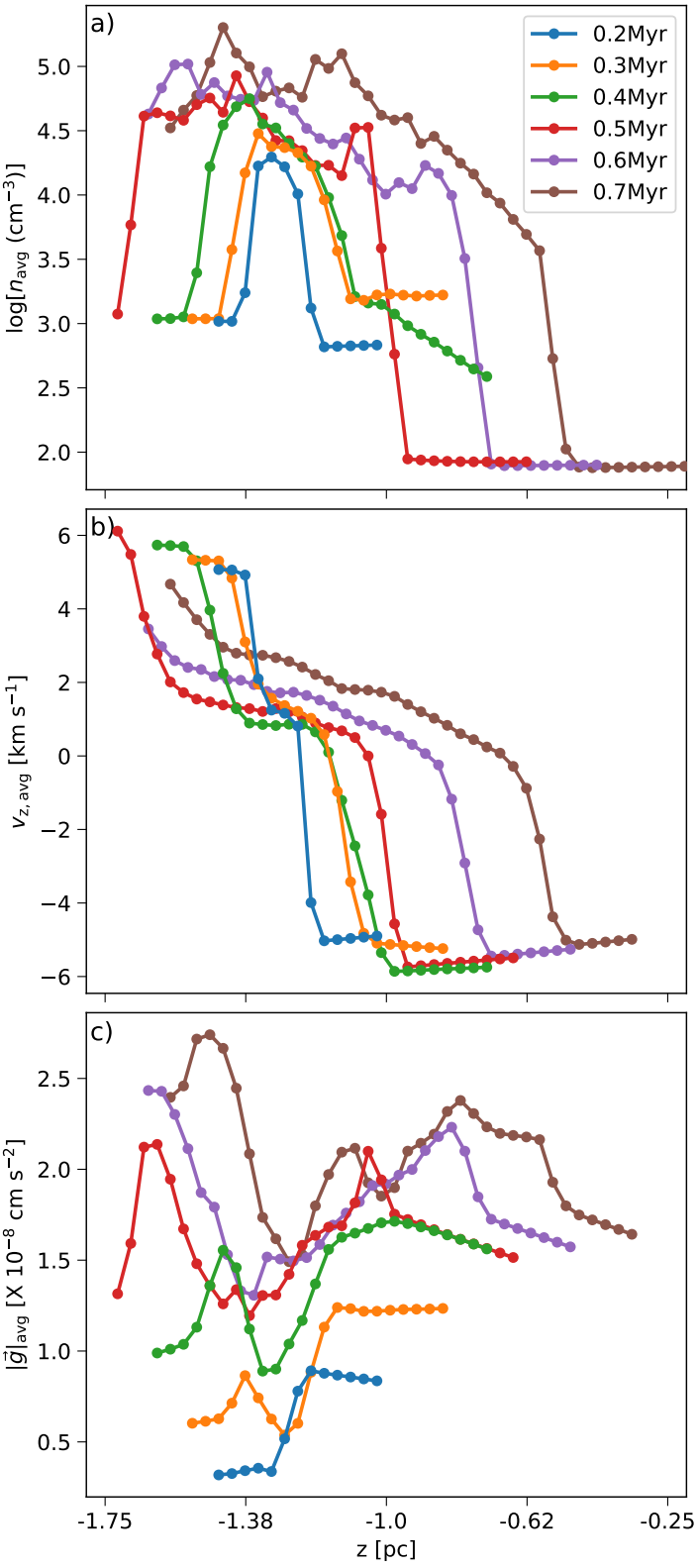

Figure 6.5: The mass-weighted average (a) density, (b) z-component of velocity, and (c) gravitational acceleration of the cone-shaped compressed layers for $t = 0.2$ to 0.7 Myr as highlighted in Figure 6.4.

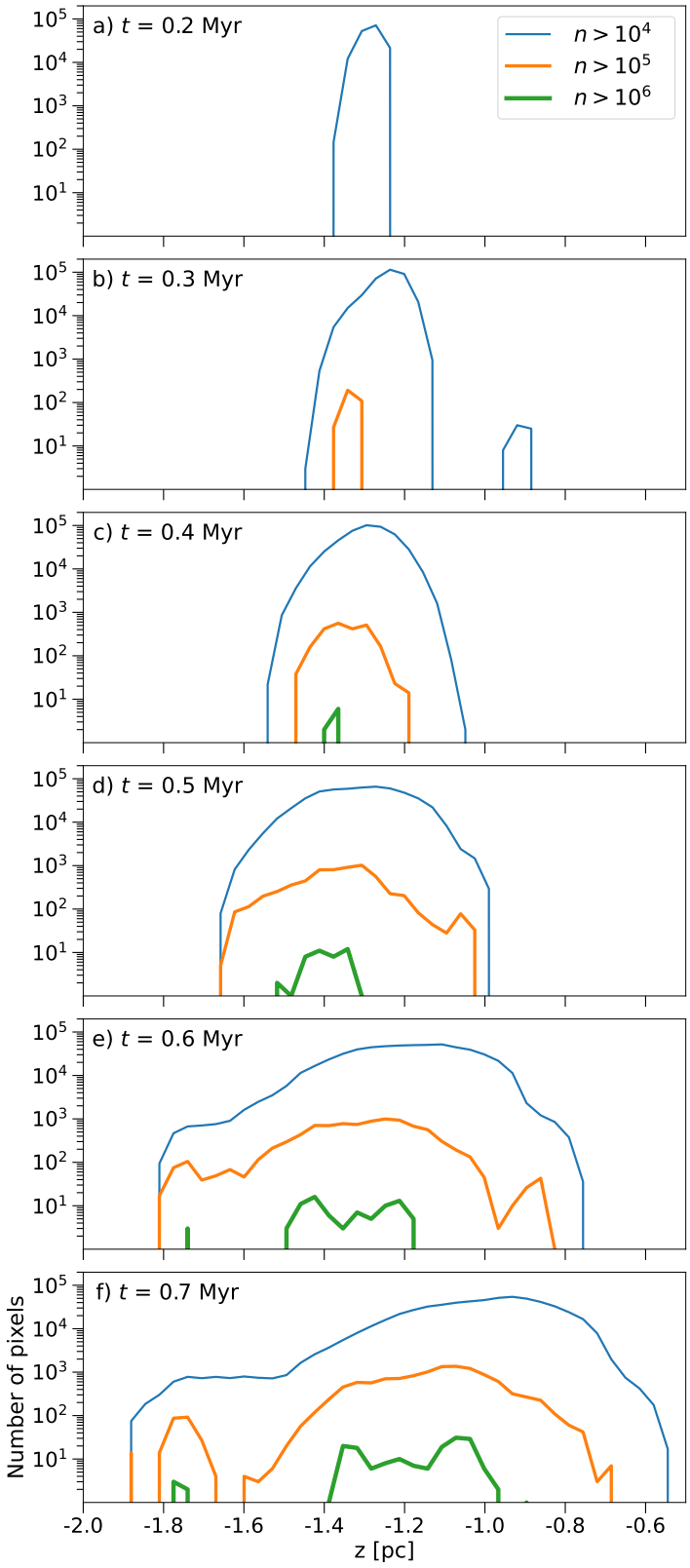

Figure 6.6: Panels (a)–(f) depict the distribution of dense molecular gas along the z-direction for t = 0.2 to 0.7 Myr for the cone-shaped compressed layers shown in Figure 6.4. However, the z-axis range is extended and made identical for each time. The thinnest, intermediate, and thickest lines represent density thresholds of $n > 10^4$, $n > 10^5$, and $n > 10^6$ cm^{-3}, respectively.

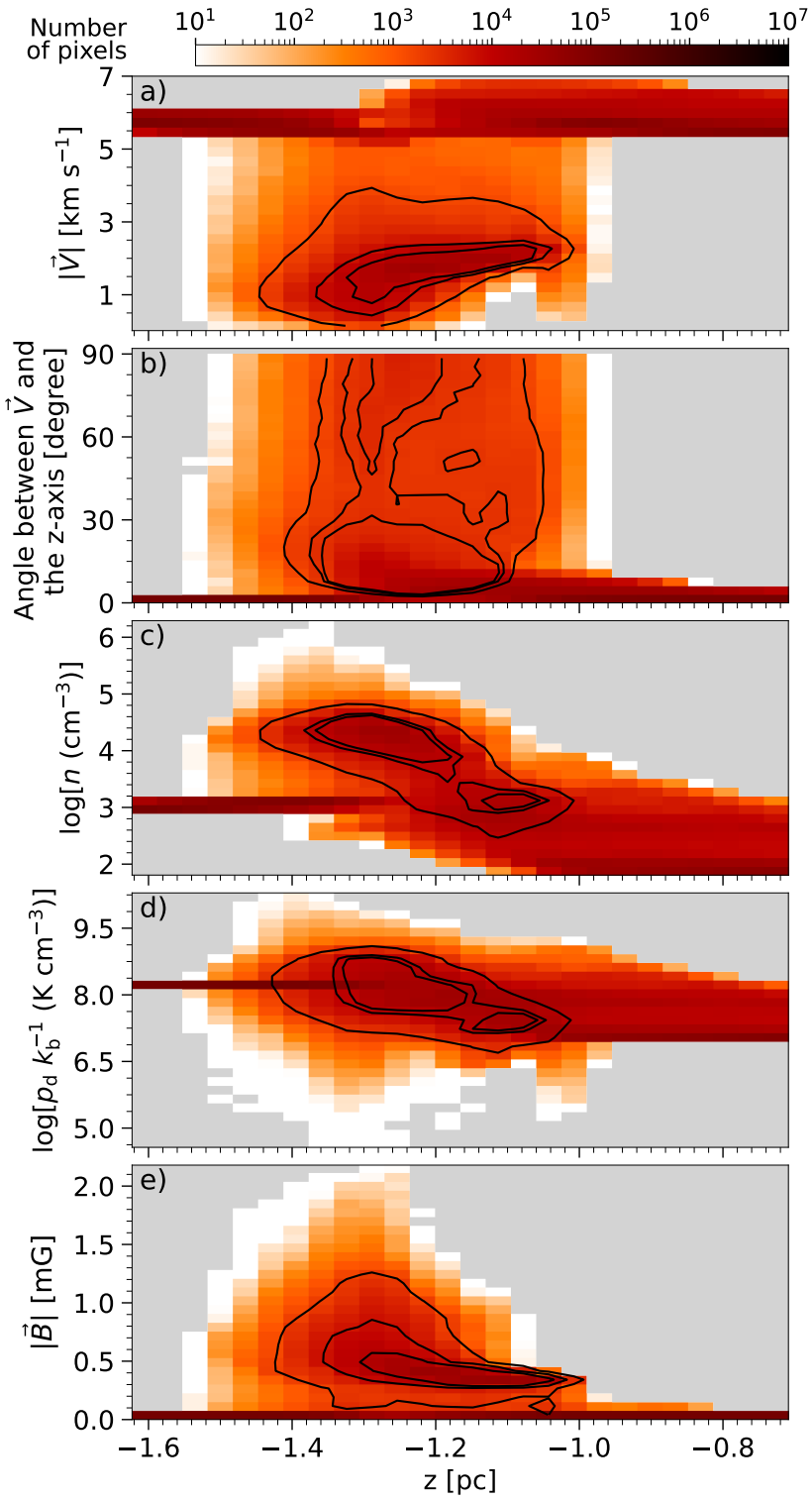

Figure 6.7: The distributions of (a) velocity magnitude ($|\vec{V}|$), (b) angle between $\vec{V}$ and the z-axis, (c) density, (d) dynamic pressure, and (e) magnitude of the magnetic field ($|\vec{B}|$) in the compressed layer at $t = 0.4$ Myr, corresponding to the conical region shown in Figure 6.4c. The contours in each panel represent 30%, 60%, and 90% of the total number of pixels, excluding contributions from the initial gas distribution and gravitationally accelerated gas ($|\vec{V}| \geq 5$ km s^{-1} and angle between $\vec{V}$ and the z-axis $\leq 5°$).

Table 6.1: Total mass of the dense gas. Density, n is in cm^{-3}.

	Mass ($M_\odot$)			
t (Myr)	$n > 10^3$	$n > 10^4$	$n > 10^5$	$n > 10^6$
0.2	337	262	—	—
0.3	937	668	5	—
0.4	1335	1037	40	1
0.5	1743	1196	117	6
0.6	1959	1302	178	13
0.7	2149	1439	260	27

of dense gas with $n > 10^5$ cm^{-3} to the total mass of gas with $n > 10^4$ cm^{-3} rises from about 0.1% at $t = 0.3$ Myr to approximately 18% at $t = 0.7$ Myr. This ratio will increase further if the contributions of the sink particles are added to the calculation.

Figure 6.7 presents the distribution of various physical parameters throughout the compressed layer at $t = 0.4$ Myr. The parameters include velocity magnitude ($|\vec{V}|$), the angle between the velocity vector and the z-axis, density, dynamic pressure, and the magnitude of the magnetic field ($|\vec{B}|$). As a result of the collision, a high-density compressed layer emerges, characterized by a small velocity ($|\vec{V}| \lesssim 2$ km s^{-1}), having a wide range of angles with respect to the axis of collision. This transformation is attributed to shock dissipation and momentum exchange between the colliding components (Fukui et al., 2021b). However, a significant amount of gas is moving at large angles relative to the collision axis (see the black contours), which is also consistent with Figure 6.4. The black contours rep-

resent 30%, 60%, and 90% of the total number of pixels, excluding contributions from the initial gas distribution and gravitationally accelerated gas. Additionally, the compressed layer exhibits a broad range of dynamic pressure and magnetic fields. The colliding motion pinches the magnetic field lines, amplifying the field strength to around 0.3–1 mG.

6.3.2 Detection of the filaments and cores

As the clouds collide along the z-axis, the shock-compressed layer develops primarily in the x–y plane. The dense gas distributions, similar to those in Figure 6.6 but along the x- and y-axes (corresponding plots are not included here), show spike-like features for $n > 10^5$ and $> 10^6$ cm^{-3}. This suggests that the structural components forming in the compressed layer are distinctly visible in the x–y plane. Hence, the x–y projected column density maps were used for detecting filaments and cores embedded in the compressed layer from $t = 0.2$ to 0.7 Myr. Firstly, the column density maps were smoothed to a 3-pixel resolution using *convolve*[1]. Then, we applied the *getsf* algorithm (Men'shchikov, 2021) to the smoothed column density maps to extract embedded filaments and cores. In this case, the structural components are extracted from the column density maps, with maximum filament and core sizes of 8 and 6 pixels, respectively.

The filament skeletons and the cores detected on global-scale in the *getsf* utility are highlighted over the column density maps in Figure 6.8. Multiple filament skeletons are identified from $t = 0.2$ to 0.7 Myr within our target regions (see the gray dashed circles in Figure 6.2). Notably, no cores are detected at $t = 0.2$ Myr or earlier. The high-density skeletons with $N(\mathrm{H_2})^{\mathrm{crest}}_{\mathrm{med}} \geq 10^{21.7}$ cm^{-2} are marked in green, while the low-density skeletons are in white. The column density threshold for the high-density skeletons is set based on the studies of Planck Col-

[1]The *convolve* task is available with *getsf* (Men'shchikov, 2021).

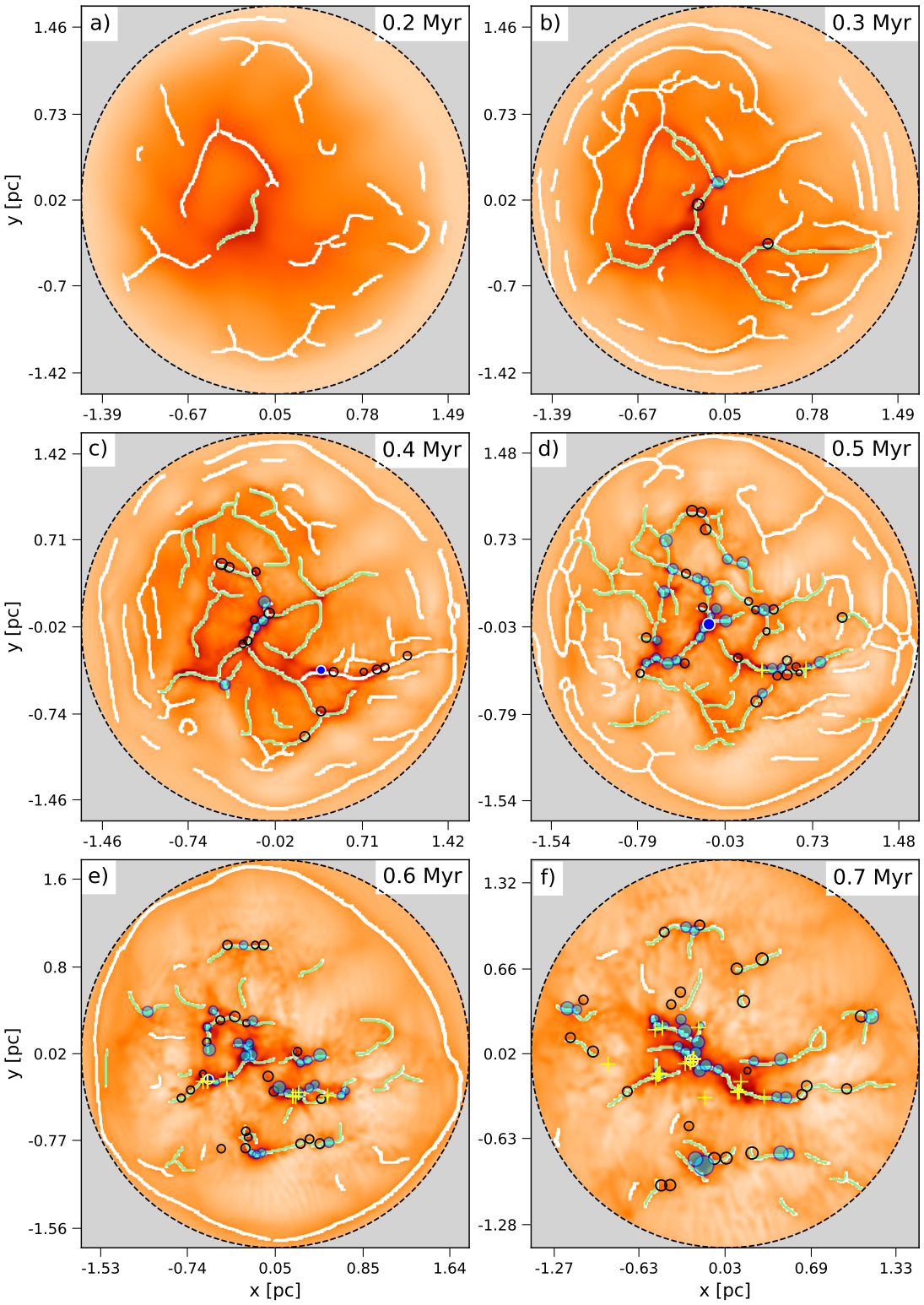

Figure 6.8: Panels (a)–(f) display the distribution of *getsf*-identified filament skeletons and cores for $t = 0.2$ to 0.7 Myr over the $N(H_2)$ maps, respectively. Filament skeletons are primarily presented in white; however, those with $N(H_2)^{crest}_{med} \geq 10^{21.7}$ cm^{-2} are marked in green. Cores with subsolar masses (i.e., $M < M_\odot$) are represented by black circles; those heavier are indicated with filled cyan circles, and the heaviest one is shown with a blue circle outlined in white. The size of the circles represents the actual size of the cores. The position of the sink particles is highlighted with yellow plus symbols.

laboration et al. (2016a) and Cox et al. (2016a). Here, $N(H_2)^{crest}_{med}$[2] is the median column density value along the filament skeleton. The cores and the sink particles are primarily found to be projected either over the spine of the high-density filaments or at their common junctions (see Figure 6.2 for the sink particles). Such distributions are detected toward several star-forming regions, including IC 5146 Dark Streamer (Dewangan et al., 2023b) and RCW 117 (Seshadri et al., 2024). Hence, in particular these high-density filaments are involved in the star formation activity. The details of the high-density filaments from t = 0.2 to 0.7 Myr are summarized in Table 6.2. Their number and combined length increase until t = 0.5 Myr, after which a significant decrease occurs. This trend is also evident in the total mass of these filaments. The projection effect will result in a maximum increase of about 27% in the calculated length for $\theta \sim 52^{\circ}$ at t = 0.7 Myr. We introduced a quantity, denoted as $\frac{\mathrm{Length}_{x}^{Fil}}{\mathrm{Length}_{y}^{Fil}}$, to indicate the orientation of the high-density filaments relative to the initial magnetic field. Here, $\frac{\mathrm{Length}_{x}^{Fil}}{\mathrm{Length}_{y}^{Fil}}$ represents the ratio of the total projected length of the high-density filaments along the x- and y-axis, i.e., perpendicular and parallel to the initial magnetic field, respectively. Therefore, if $\frac{\mathrm{Length}_{x}^{Fil}}{\mathrm{Length}_{y}^{Fil}} \ll 1$, filaments are largely oriented along the initial magnetic field, and for $\frac{\mathrm{Length}_{x}^{Fil}}{\mathrm{Length}_{y}^{Fil}} \gg 1$, filaments are mainly perpendicular to the initial magnetic field. At t = 0.3, 0.6, and 0.7 Myr, $\frac{\mathrm{Length}_{x}^{Fil}}{\mathrm{Length}_{y}^{Fil}} > 1.5$ indicates that the dense filaments are more aligned perpendicular to the initial magnetic field. The possible reasons and implications of the variation of $\frac{\mathrm{Length}_{x}^{Fil}}{\mathrm{Length}_{y}^{Fil}}$ are discussed in detail in Section 6.4.1. The collective properties of the *getsf*-identified cores and the sink particles from t = 0.2 to 0.7 Myr are presented in Table 6.3. The total mass of the cores and the sink particles steadily increases as

[2]The *getsf*-catalogs provide $N(H_2)^{crest}_{med}$, length, mass, and position angle of the filaments, as well as the size and mass of the cores. We adjusted the mass values using a mean molecular mass of 2.4, which was initially set at 2.8.

Table 6.2: Physical parameters for the high-density filaments with $N(\mathrm{H_2})^{\mathrm{crest}}_{\mathrm{med}} \geq 10^{21.7}$ cm^{-2}.

t (Myr)	N^{Fil}	$\mathrm{Length}^{\mathrm{Fil}}_{\mathrm{tot}}$ (pc)	$\mathrm{Mass}^{\mathrm{Fil}}_{\mathrm{tot}}$ ($M_\odot$)	$\frac{\mathrm{Length}^{\mathrm{Fil}}_{\mathrm{x}}}{\mathrm{Length}^{\mathrm{Fil}}_{\mathrm{y}}}$
0.2	2	0.62	51	0.80
0.3	8	4.74	466	1.51
0.4	19	10.35	864	1.03
0.5	31	13.15	1189	1.17
0.6	24	8.81	780	1.54
0.7	23	8.50	983	1.60

time progresses. The spectrum of mass for both the cores and the sink particles broadens over time. At each time step, the mass of the heaviest core, depicted by a blue circle with a white edge in Figure 6.8, increases, ultimately yielding a massive core of about 15 $M_\odot$ at $t = 0.7$ Myr. The mass of the heaviest sink particle also increases over time and reaches about 40 $M_\odot$ at $t = 0.7$ Myr (see the white plus symbol in Figure 6.2). Additionally, at $t = 0.7$ Myr, the heaviest sink particle is accompanied by a massive companion of about 11 $M_\odot$, located at the junction of the filaments (see the cyan plus symbol in Figure 6.2).

6.3.3 The relative orientation of the filament, velocity, magnetic field and gravitational field vectors

To comprehend the formation mechanism of HFS, it is essential to understand the influence of turbulence, magnetic field, and gravity on the flow of materials

Table 6.3: Details of the *getsf*-identified cores and the sink particles.

t (Myr)	$N^{\rm core}$	$M^{\rm core}_{\rm min}$ ($M_\odot$)	$M^{\rm core}_{\rm max}$ ($M_\odot$)	$M^{\rm core}_{\rm total}$ ($M_\odot$)	$N^{\rm sink}$	$M^{\rm sink}_{\rm min}$ ($M_\odot$)	$M^{\rm sink}_{\rm max}$ ($M_\odot$)	$M^{\rm sink}_{\rm total}$ ($M_\odot$)	$M^{\rm core}_{\rm total} + M^{\rm sink}_{\rm total}$ ($M_\odot$)
0.2	—	—	—	—	—	—	—	—	—
0.3	3	0.71	1.06	2.58	—	—	—	—	2.58
0.4	19	0.24	3.88	17.05	—	—	—	—	17.05
0.5	46	0.21	7.72	80.17	3	0.16	5.04	7.60	87.77
0.6	50	0.36	9.81	104.74	9	0.28	20.25	31.89	136.63
0.7	50	0.19	15.39	123.78	25	0.04	40.25	101.5	225.28

through the filaments. Hence, the x–y projected mass-weighted average velocity ($\vec{V}$), magnetic field ($\vec{B}$), and gravitational field vectors ($\vec{g}$) toward the filaments are depicted in Figure 6.9 from $t = 0.3$ to 0.7 Myr. These vectors are overlaid on the column density maps for the circular regions highlighted in Figure 6.2. The vectors precisely at the skeleton (i.e., the spine) of the high-density filaments are shown in black. In contrast, those in the immediate surrounding pixels of the skeletons, selected based on column density thresholds on the *getsf*-identified filament images, are shown in white. To obtain a clear picture of their orientations, $\vec{B}$, $\vec{V}$, and $\vec{g}$ are plotted at intervals of a few pixels in both the x- and y-directions in Figure 6.9. A parallel velocity vector along the filament skeleton (see the black arrows) indicates material flow through the filaments, while perpendicular white arrows depict materials from the surrounding area being fed into the filaments (e.g., Gómez et al., 2018; Wang et al., 2022). However, a perpendicular velocity field at the spine of the filaments reflects their overall bulk motion. Both types of

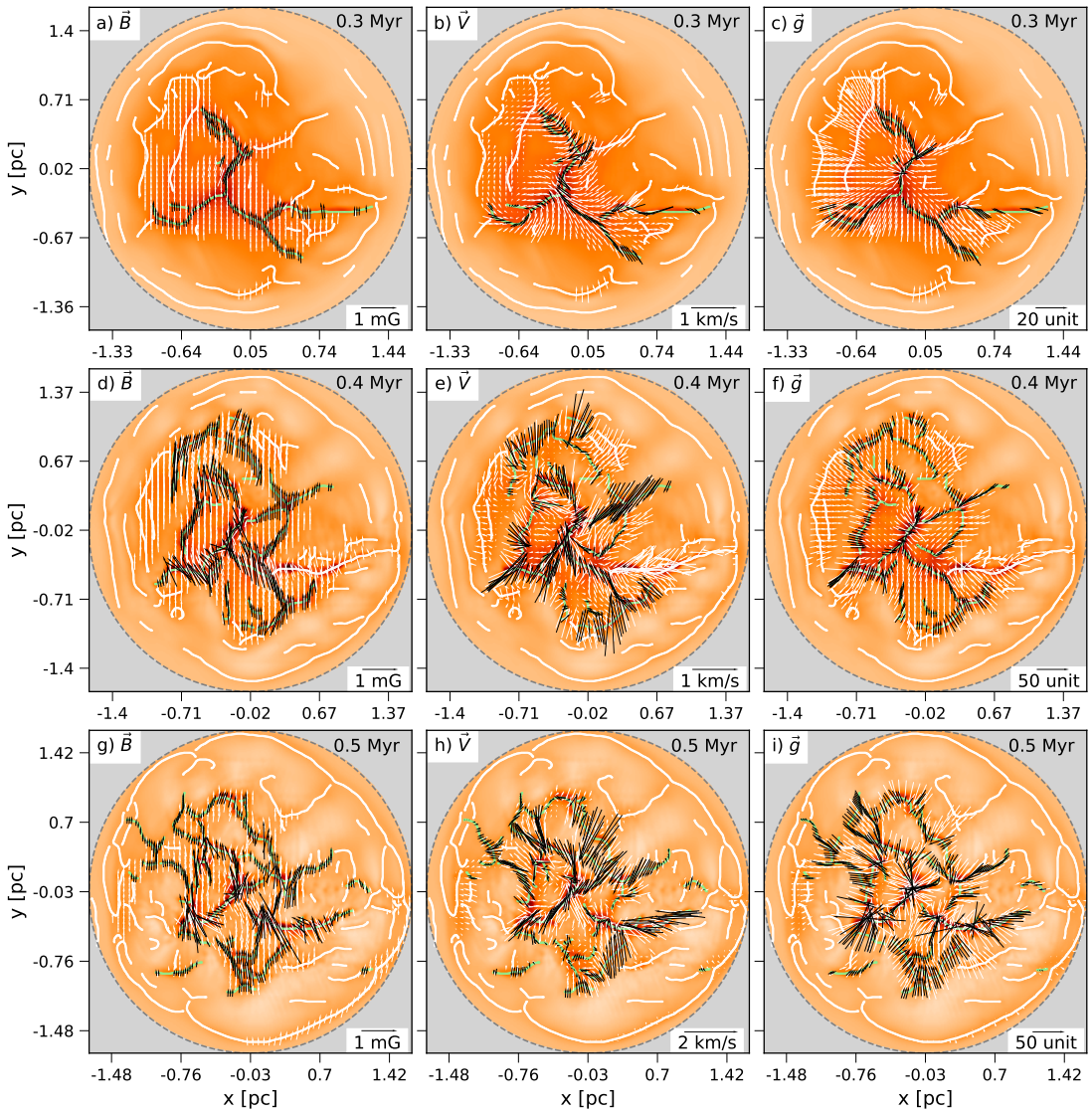

Figure 6.9: Continued.

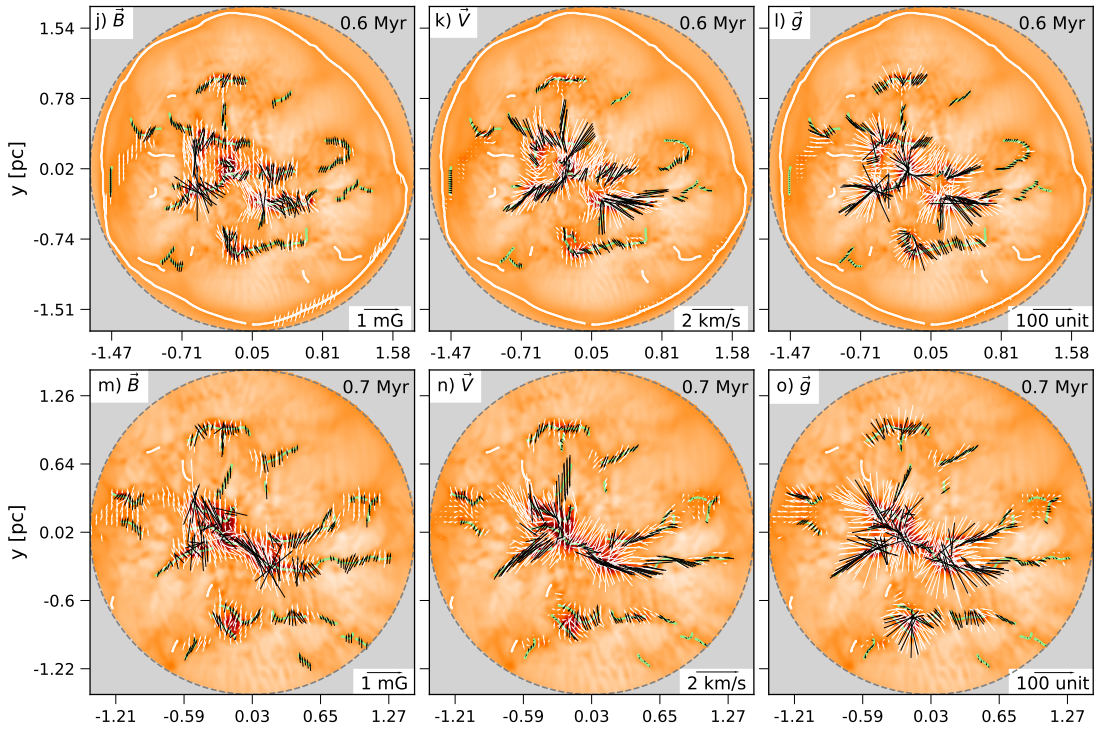

Figure 6.9: The left, middle, and right panels depict the mass-weighted average projected magnetic field, gas velocity, and gravitational field vectors in the x–y plane, respectively. Progressing from top to bottom, the temporal variation of the vectors is illustrated from t = 0.3 to 0.7 Myr. Vectors precisely at high-density filament skeletons (in green) are represented in black, while those in the surrounding regions of the skeletons are depicted in white. Surrounding pixels have column densities above the thresholds of [3, 3, 4, 6, and 6] $\times$ 10^{21} cm^{-2} in the *getsf*-identified filament images for t = 0.3, 0.4, 0.5, 0.6, and 0.7 Myr, respectively.

configurations can be observed through visual examination of the velocity vectors in Figure 6.9. We observe a gradual increase in the strength of the $\vec{B}$ and $\vec{g}$. The magnetic field vectors, which typically make large angles with the filaments, reflect their significant role in filament formation (e.g., Inoue & Fukui, 2013; Pillai et al., 2015; Inoue et al., 2018; Wang et al., 2022). The small angles between $\vec{V}$ and $\vec{g}$ indicate the considerable influence of gravity on the gas kinematics.

In this context, it is essential to perform a quantitative measurement of the relative orientations (i.e., the difference in the position angle, ΔPA) among the filaments, $\vec{B}$, $\vec{V}$, and $\vec{g}$. Hence, Figure 6.10 presents histograms of the relative

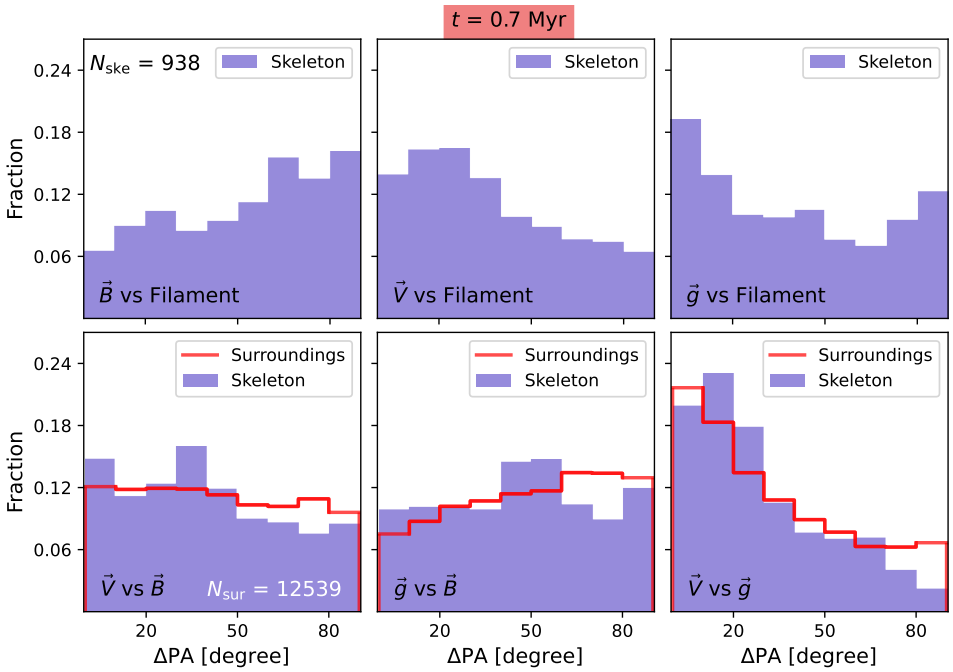

Figure 6.10: Normalized histograms of the relative orientations among the filament skeleton, projected magnetic field, gas velocity, and gravitational field vectors at $t = 0.7$ Myr. The top row depicts pairs between high-density filament skeletons and the magnetic field, gas velocity, and gravitational field vectors. The bottom row illustrates the relative orientations among the magnetic field, gas velocity, and gravitational field vectors for both the skeletons (in light-slate blue) and their surroundings (in red). The total number of pixels in the filament skeletons ($N_{\rm ske}$) and their surroundings ($N_{\rm sur}$) are mentioned at each time step. Figure C.1 in Appendix C contains similar plots for $t = 0.3$ to 0.6 Myr.

orientation among the filaments, $\vec{B}$, $\vec{V}$, and $\vec{g}$ at $t = 0.7$ Myr. The supplementary plots for $t = 0.3$ to 0.6 Myr can be found in Figure C.1 in Appendix C. All pixels from the high-density skeletons and their surroundings (as mentioned for Figure 6.9) are used in Figures 6.10 and C.1. The large ΔPA between the filament skeletons and $\vec{B}$ supports the idea that filaments easily grow perpendicular to the magnetic field (e.g., Inoue & Fukui, 2013; Cox et al., 2016a; Inoue et al., 2018). However, the smaller ΔPA values arise from the dragging of the magnetic field lines, resulting in more parallel components due to the material flowing through the filaments (e.g., Gómez et al., 2018). Thus, the ΔPA between $\vec{B}$ and the

filament skeletons varies over a wide range at t = 0.7 Myr. At the same time (i.e., t = 0.7 Myr), similar wide angular ranges for ΔPA between $\vec{V}$ and the filament skeleton are observed due to two factors: first, gas flow along the spine of the filament, resulting in a parallel relative configuration; and second, the bulk motion of the filaments. The ΔPA between $\vec{g}$ and the filament skeleton shows a clear bimodal distribution at t = 0.7 Myr, contrasting with their distribution at t = 0.3 Myr. The bimodal distribution of ΔPA between the filament skeleton and $\vec{g}$ arises because, toward the central region, materials flow through the filaments toward the hub, giving rise to the parallel component. However, filaments in the outer regions flow as a whole toward the hub, but their orientations are perpendicular to the gravitational field vectors. In Figure C.1, it is evident that $\vec{B}$ forms large angles with $\vec{V}$ for the high-density filaments but appears randomly oriented for the surrounding gas. However, with time, $\vec{V}$ and $\vec{B}$ increasingly align, both for the high-density filaments and their surroundings. This suggests the role of the magnetic field in guiding gas motions in the surroundings and in the bending of magnetic fields due to gas flow through the filaments. Similar findings were reported in studies by Pillai et al. (2015); Juárez et al. (2017); Klassen et al. (2017); Liu et al. (2018); Gómez et al. (2018); Koch et al. (2022). The random distribution of $\vec{B}$ with respect to $\vec{g}$ indicates that the magnetic field does not have a significant role compared to gravity. At t = 0.3 Myr, $\vec{V}$ forms large angles with respect to $\vec{g}$ for the high-density filament skeletons and is nearly randomly distributed with $\vec{g}$ for the surrounding regions. This suggests that gravity does not significantly influence gas kinematics in the initial stages. However, shortly after that, $\vec{V}$ aligns with $\vec{g}$ for both the skeleton and the surrounding regions (see Figure 6.10 and C.1), implying that gravity becomes dominant in governing gas kinematics during later stages of evolution, as observed toward MSFR SDC13 (Wang et al., 2022).

One of the major objectives of this study is to investigate the influence of magnetic fields and gravity on gas flow within filaments. To achieve this, we selected high-density filament skeletons and their surrounding regions at each time step to analyze ΔPAs among the filaments, $\vec{B}$, $\vec{V}$, and $\vec{g}$. Core formation activities may alter the ΔPAs on scales smaller than 0.1 pc, but this is not expected to impact the filament scale (e.g., Wang et al., 2022). In their observational studies, Wang et al. (2022) and Liu et al. (2023) emphasized that the gravitational field may have a very different orientation than the magnetic field and velocity in the diffuse regions far from the filament skeletons, suggesting that the magnetic field, rather than gravity, influences the low-density areas.

6.3.4 The gas kinematics and the spatial distribution of different velocity components

As outlined in Section 1.5, several theoretical and numerical studies estimated the CCC rate to be once every 100 years for our Galaxy (e.g., Tasker & Tan, 2009; Dobbs et al., 2015). However, observational evidence of CCC remains limited, with fewer than 100 cases documented by Fukui et al. (2021a). Therefore, this analysis aims to understand the observational difficulties in the detection of CCC. Using the simulation data, we generated a position(x)-position(y)-velocity($v_{\rm z}$) data cube for t = 0 to 0.7 Myr. The velocity interval between the channels is set to be 0.5 km s^{-1}, which is consistent with several Galactic CO Surveys as listed in Park et al. (2023). These data cubes are analogous to the observed molecular line data used for tracing molecular gas kinematics. The data cubes are utilized to extract the PV diagrams along the x- and y-axes for the regions shown in Figure 6.2i. The PV diagrams at t = 0, 0.2, 0.4, 0.5, and 0.7 Myr are shown in Figure 6.11. The integration range in the y-direction, $\Delta L_{\rm y}$ = 0.4 pc, and in the x-direction, $\Delta L_{\rm x}$ = 0.4 pc while extracting PV diagrams along the

x- and y-directions, respectively. At t = 0 Myr, i.e., before the collision, two cloud components are distinctly visible in the PV diagrams (see Figure 6.11). However, the growth of the compressed layer can be observed at t = 0.2 Myr, marked by a gray shaded region for v_z: [−2.25, 3.75] km s^{-1} (see the panel on the right). The compressed layer lies between the blue- and red-shifted cloud components, shaded in blue and red for v_z: [−6.75,−3.75] km s^{-1} and [4.25, 5.75] km s^{-1}, respectively. At t = 0.5 Myr, one component of the colliding cloud is entirely embraced within the compressed layer. The red-shifted component and the compressed layer are distinguished by the red and gray shaded regions for v_z: [5.25, 7.25] and [−3.25, 4.25] km s^{-1}, respectively. To observe the distribution of the cloud components in the PP space at t = 0.2 and 0.5 Myr, integrated density maps are generated for the previously defined velocity ranges. The integrated density maps are analogous to the integrated intensity (i.e., moment-0) map of the molecular line data analysis. The integrated density map at t = 0.2 Myr is shown in Figure 6.12a. The image corresponds to the red-shifted cloud component, while the blue-shifted component and the compressed layer are presented with blue and black contours, respectively. The complementary spatial distribution between the "intensity-depression" in the integrated density map for the red-shifted component and the 'intensity-enhancement' in integrated density contours for the blue-shifted component is very apparent at t = 0.2 Myr. At the same location, the intermediate-velocity compressed layer is detected in black contours, which is a clear result of CCC. However, at t = 0.5 Myr, when one of the cloud components is completely transformed into the compressed layer, a complementary distribution between the red-shifted cloud component and the compressed layer is observed in Figure 6.12b. Based on these results, we have discussed the observational challenges in the detection of CCC in Section 6.4.3.

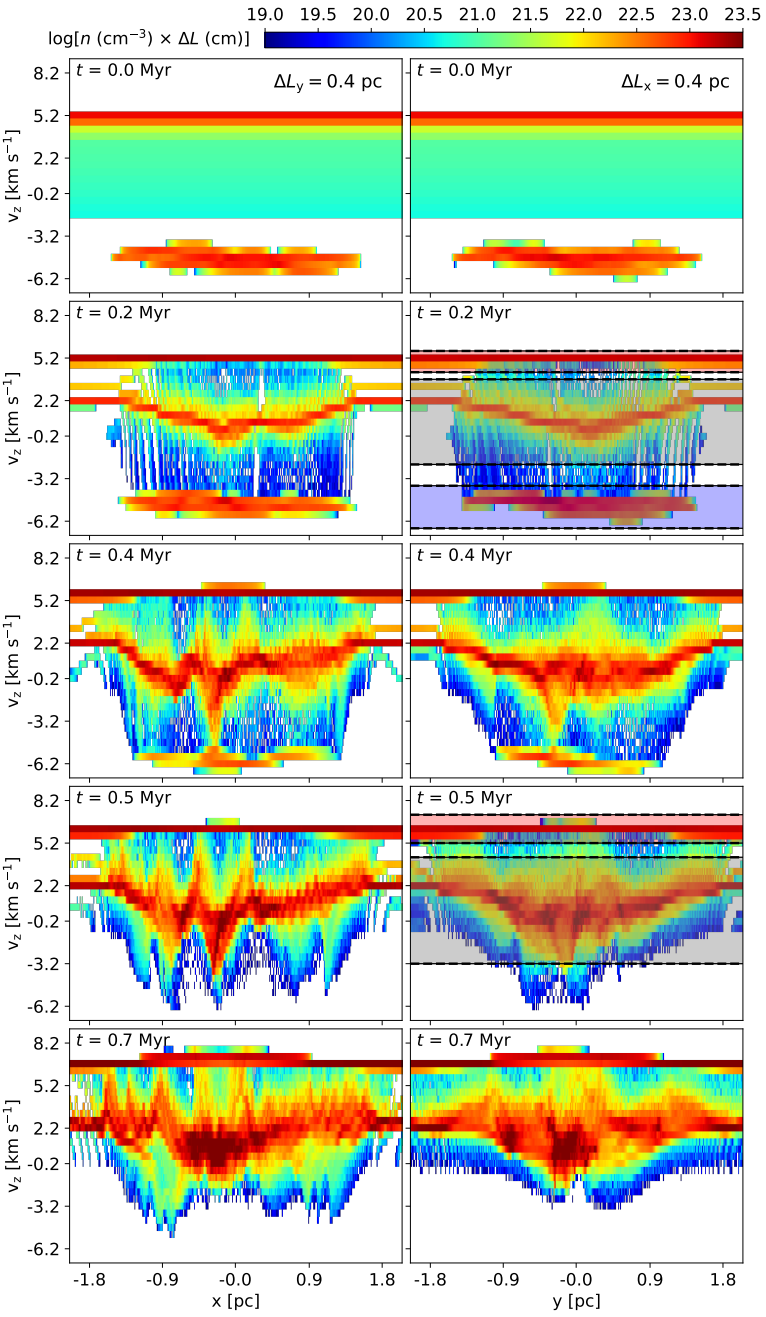

Figure 6.11: The PV diagrams for the regions highlighted in Figure 6.2i. The left and right panels are oriented along the x- and y-axes, respectively. Progressing from top to bottom, it covers $t = 0$, 0.2, 0.4, 0.5, and 0.7 Myr. Three velocity ranges are highlighted with shaded regions in blue, gray, and red on the PV diagram along the y-axis at $t = 0.2$ Myr. Similarly, two velocity ranges are indicated with shaded regions in gray and red on the PV diagram along the y-axis at $t = 0.5$ Myr. These velocity ranges are utilized to generate integrated density maps, which are presented in Figures 6.12.

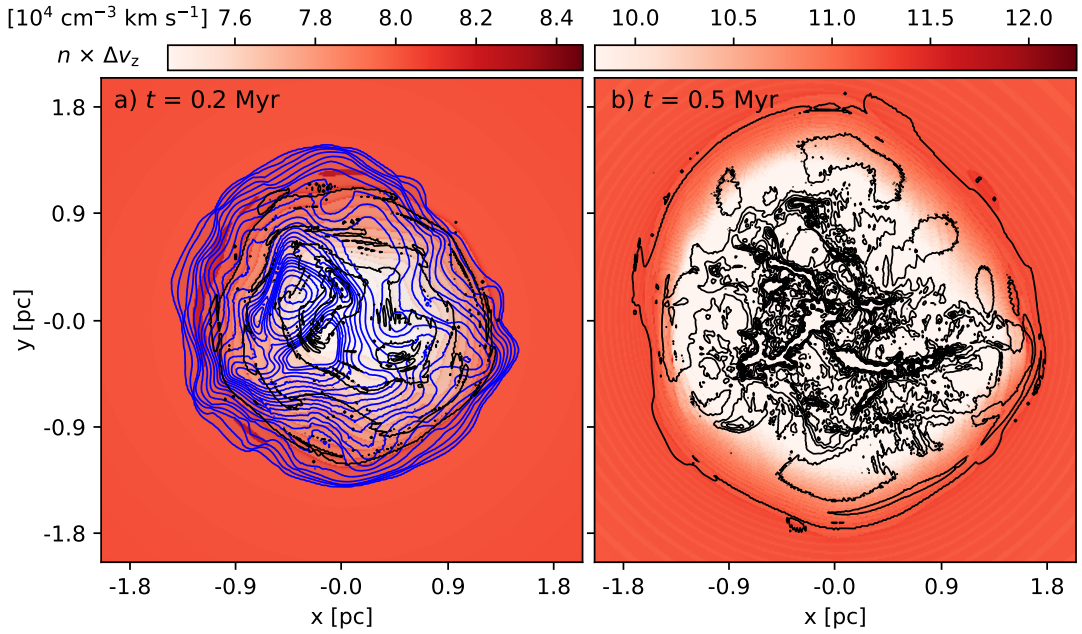

Figure 6.12: The spatial distribution of different velocity components in the x–y plane at $t = 0.2$ and 0.5 Myr. (a) The red-shifted integrated density image at $t = 0.2$ Myr is displayed for the velocity range v_z: [4.25, 5.75] km s^{-1}. The spatial distributions of the blue-shifted component (for v_z: [−6.75, −3.75] km s^{-1}) and the compressed layer (for v_z: [−2.25, 3.75] km s^{-1}) are overlaid on the image using blue and black contours, respectively. A total of 20 equispaced contours ranging from 10^3 to 10^5 cm^{-3} km s^{-1} are shown for the blue-shifted component. Similarly, 10 equispaced contours from 10^4 to 10^5 cm^{-3} km s^{-1} are shown for the compressed layer. (b) The red-shifted integrated density image at $t = 0.5$ Myr is presented for the velocity range v_z: [5.25, 7.25] km s^{-1}. The spatial distribution of the compressed layer (for v_z: [−3.25, 4.25] km s^{-1}) is overlaid on the image using 10 equispaced black contours from 8×10^2 to 4×10^5 cm^{-3} km s^{-1}.

6.4 Discussion

To address the questions introduced in Section 6.1, we explored numerical simulation data of a head-on collision incorporating ideal MHD and self-gravity. This collision creates a high-density region at the interface of the colliding clouds, characterized by an intermediate-velocity distribution. Along with the sink particles, several filaments and cores are detected in the high-density interface. The relative orientations of the filament skeletons, $\vec{B}$, $\vec{V}$, and $\vec{g}$ toward the filaments indicate

the gas motion and its influencing factors. The PV diagrams demonstrate how the signatures of CCC change over time. All the results are thoroughly discussed in this section. In addition, new observational signatures of CCC at $\theta_{\rm col} = 90°$ are proposed in Section 6.4.4.

6.4.1 The impact of the collision on the molecular cloud components and the formation of filaments

A supersonic collision between molecular clouds creates a shock-compressed layer at their interface (e.g., Furukawa et al., 2009; Sano et al., 2018; Nishimura et al., 2021). The final density of the interface depends primarily on the initial density of the cloud components and their collisional velocities (see Equation 1 in Inoue & Fukui, 2013). A positive correlation between the collision velocity and the peak column density is presented in Fukui et al. (2021a) for the observational sites of CCC (see Figure 10 in their work). The width and density of the compressed layer, characterized by an intermediate-velocity relative to the colliding cloud components (e.g., Takahira et al., 2014; Baug et al., 2016; Dewangan et al., 2018c), increase over time due to shock waves propagating through the cloud components, as discussed in detail by Inoue & Fukui (2013). This increase leads to a rise in the total mass of the high-density gas (see Table 7.1) and explains the flattening nature of the high-density tail observed in the histograms of the gas density, as indicated by the red lines in Figure 6.3. The rapid decrease in the slope (i.e., the flattening nature) of the high-density tail suggests the swift development of high-density pixels in the initial stages after the collision. However, the rate of growth of the high-density region slows down in the later stages due to shock dissipation (e.g., Inoue et al., 2018; Fukui et al., 2021b). This phase was described as the 'dissipation stage' in the study by Navarrete et al. (2024). They demonstrated the presence of higher numbers at the beginning of the collision. However, the number

of shocked cells and their Mach numbers decrease in the later stages. Hence, the production of high-density regions slows down over time in the case of CCC. The compressed layer is conducive to the development of structural components, which are favorable environments for star formation (e.g., Shima et al., 2018; Fukui et al., 2021b). The initial density distributions, the collision velocity, and the presence of a magnetic field can have a huge impact on the core and filament formation and their properties (e.g., Inoue & Fukui, 2013; Takahira et al., 2014; Arreaga-García et al., 2014; Balfour et al., 2015, 2017; Inoue et al., 2018; Sakre et al., 2021, 2023). When the colliding clouds have a pre-collision substructure (i.e., inhomogeneous density distribution), it causes an inhomogeneous shock-compressed layer (Inoue & Fukui, 2013; Balfour et al., 2017; Inoue et al., 2018). In that case, higher collision velocities create more massive cores/sink particles. Balfour et al. (2015, 2017) studied particularly low-velocity collisions without considering magnetic fields. The magnetic field strength in our work reaches the order of mG in the plane of the compressed layer, as shown in Figure 6.7. Therefore, the role of the magnetic field cannot be ignored in the evolution of the system. After Inoue & Fukui (2013) and Inoue et al. (2018), this work presents the important roles of magnetic field and high-velocity collision in the formation of filaments. The initial supersonic turbulence (with Mach number > 1) within the spherical cloud creates pre-collision substructure (see Figures 6.2a, 6.2c, and 6.4b) and opposes centralized collapse (Arzoumanian et al., 2011; Federrath, 2016; Shima et al., 2018). Later, the shock compression of the inhomogeneous density structures from the supersonic collision plays a crucial role during/after the collision in the filament formation at the CCC sites. Interestingly, Inoue et al. (2018) found that comparable filament patterns were formed even in the absence of self-gravity, proving that gravity does not play a role in filament formation, especially if the initial clouds are highly turbulent (see Figure 2 in their paper).

Earlier works (e.g., Inoue & Fukui, 2013; Inoue et al., 2018) demonstrated that shock compression is efficient when it is parallel to the magnetic field, which preferentially orients the filaments perpendicular to the initial magnetic field (see Figure 3 in Inoue et al., 2018). Abe et al. (2021) discussed the filament formation mechanisms associated with shock-compressed layers of the molecular clouds and classified the mechanism proposed by Inoue & Fukui (2013) as the type-O mechanism (see also Pineda et al., 2023, for a review). The turbulence-driven inhomogeneous density structures can be randomly oriented with respect to the magnetic field, and the oblique shock effect (for more details see Fukui et al., 2021a) will attempt to compress all of them. This results in randomly oriented filaments with respect to the magnetic field. However, as the gas flows along the magnetic fields effortlessly, filaments perpendicular to the magnetic field gain high density quickly, resulting in a ratio of $\frac{\mathrm{Length}_{\mathrm{x}}^{\mathrm{Fil}}}{\mathrm{Length}_{\mathrm{y}}^{\mathrm{Fil}}} > 1.5$ for the high-density filaments at $t = 0.3$ Myr. The shock compression perpendicular to the magnetic field continues slowly. Consequently, the filaments parallel to the magnetic field enter the high-density regime at $t = 0.4$ Myr, causing the ratio $\frac{\mathrm{Length}_{\mathrm{x}}^{\mathrm{Fil}}}{\mathrm{Length}_{\mathrm{y}}^{\mathrm{Fil}}}$ to decrease to about 1. However, filaments parallel to the magnetic field are mostly dispersed at $t = 0.6$ after the dissipation of shock compression. Therefore, the ratio $\frac{\mathrm{Length}_{\mathrm{x}}^{\mathrm{Fil}}}{\mathrm{Length}_{\mathrm{y}}^{\mathrm{Fil}}}$ increases again. The dispersion of these filaments is also responsible for the sudden decrease in the total mass and length of the high-density filaments after $t = 0.5$ Myr. One possible reason for the dispersion of these filaments is that the magnetic field lines were pinched by the shock compression, resulting in higher field strength and leading to a higher critical line mass (see Equation 28 in Fiege & Pudritz, 2000). Consequently, these filaments disperse as soon as the shock compression dissipates. The stability analysis for individual filaments, both aligned parallel and perpendicular to the magnetic field, is beyond the scope of this chapter and can be addressed in future work.

6.4.2 The formation of HFS

As introduced in Section 6.1, HFSs are assemblies of filaments that transport molecular gas and dust toward the hub (Myers, 2009). Thus, hub emerges as the densest region, conducive to MSF (e.g., Dewangan et al., 2023a, 2024; Seshadri et al., 2024). Previously, this data was utilized by Inoue et al. (2018) to investigate the origin of the most massive sink particle through the gravitational collapse of a massive filament. However, the present work reveals the presence of a massive sink particle and a massive core exactly at the junction of the filaments, indicating that CCC can lead to the formation of HFSs. At t = 0.3 Myr and before, the average velocity of the longitudinal gas flow along the filaments (see the black arrows for $\vec{V}$ in Figure 6.9) is slower ($\sim$0.3 km s^{-1}) than the turbulent velocity dispersion (as $\Delta v_{\rm t}$ $\sim$1.0 km s^{-1}). The gas flow is also not influenced by gravity, as $\vec{V}$ are randomly oriented with respect to $\vec{g}$ (see Figure C.1). Hence, initially, gas flow along the filaments is driven by turbulence. As time progresses, the total mass of the high-density gas increases, allowing gravity to take control of the system's evolution. This shift is reflected in the relative orientations of $\vec{V}$ and $\vec{g}$ at t = 0.4 Myr and beyond. Gravity induces both the mass accumulation of filaments from the surrounding environment and the transport of accumulated gas and dust toward the gravitational center, leading to the convergence of filaments to form HFS (e.g., Gómez et al., 2018; Wang et al., 2022). Therefore, initially, the system's evolution is driven by turbulence, followed by a transition dominated by gravity. Overall, the formation of HFSs from CCC is a three-step process: Step I - Pre-collision phase: molecular clouds acquire an inhomogeneous density structure driven by turbulence (e.g., Federrath, 2016; Shima et al., 2018; Padoan et al., 2020), Step II - Shock-compression during collision: filaments are formed due to the oblique shock effect guided by magnetic fields (e.g., Inoue & Fukui, 2013;

Inoue et al., 2018), and Step III - Convergence of the filaments: gravity controls the gas kinematics and makes the filaments converge to form a HFS (e.g., Wang et al., 2022). Therefore, the formation of HFS from CCC is a combined effect of turbulence, shock compression, magnetic fields, and gravity. It is important to note that only supersonic CCCs are capable of shock compression; therefore, our model for the formation of HFS from CCC holds exclusively for supersonic collisions. Earlier, Inoue & Fukui (2013) and Inoue et al. (2018) tested cases where gravity was not incorporated and found that filaments were produced even in the absence of gravity (see Figure 2 in their works). This indicates that the collision process, along with turbulence and the magnetic field, is sufficient for the filament formation. However, in the later stages, gravity becomes more significant as density increases and attracts gas to form cores within the filaments. A key difference between this study and that of Inoue & Fukui (2013) is the initial spherical cloud geometry, which shapes the filaments into a cone and drives inward flows among them. These inward flows along the filaments merge at the vertex of the cone, leading to the substantial accumulation of high-density gas and the formation of massive star(s).

According to Balfour et al. (2015, 2017), gravity plays the dominant role in the formation of a network of filaments from CCC, especially when turbulence is subsonic in the colliding molecular clouds. However, our simulation used supersonic turbulence, consistent with the findings of Larson (1981). In general, the formation of HFSs aligns with the conceptual frameworks proposed in GHC (Vázquez-Semadeni et al., 2009, 2017, 2019) or inertial-inflow (Padoan et al., 2020) scenarios. Both of these scenarios emphasize the longitudinal inflow of gas along filaments, yet they are driven by distinct mechanisms. GHC is primarily propelled by gravity (Vázquez-Semadeni et al., 2019), whereas inertial inflow is a result of turbulence (Padoan et al., 2020). According to Padoan et al. (2020), the

inertial-inflow model predicts that the net inflow velocity along the filaments is usually significantly smaller than the turbulent velocity and is not primarily controlled by gravity. The GHC model (Vázquez-Semadeni et al., 2009, 2017, 2019), on the other hand, predicts anisotropic gravitational contraction at all scales, which is characterized by longitudinal flow along filaments. However, upon recognizing the distinct roles of turbulence and gravity in our model, it becomes evident that neither scenario alone is sufficient to fully explain the formation of HFSs from CCC. Instead, an interplay between turbulence- and gravity-driven theories emerges alongside the effect of collision.

Although the analysis of projected column density maps and field vectors allows for easy comparison with observational works, it is worth noting that some of the correlations between the filament skeletons and the field vectors discussed in this chapter may be influenced by the projection effect and mass-weighted averaging process of the vectors. Interestingly, the impact of mass-weighted averaging in our case is minimal for several reasons. The density in the compressed layer ($n > 10^4$ cm^{-3}) greatly exceeds that of both the ambient medium and the dense cloud components, and we have selected only high-density filaments. The x- and y-components of the velocities are zero outside the compressed layer, thus not affecting the direction of the mass-weighted x–y projected velocity components. Although the initial magnetic field strength was 20 μG, it increased to over 0.3 mG in the compressed layer. Additionally, the gravitational acceleration in the x–y plane is significantly stronger in the compressed layer compared to other regions. Consequently, mass-weighted averaging has a negligible effect on the direction of the x-y projected $\vec{B}$, $\vec{V}$ and $\vec{g}$. However, to eliminate the projection effect, a more comprehensive analysis would require the use of a simultaneous filament and core identification tool (such as *getsf*) for 3D (position-position-position) datasets. This approach would enable the utilization of $\vec{B}$, $\vec{V}$, $\vec{g}$, and

their relative orientations for filaments detected in 3D.

6.4.3 Difficulties in observational detection of CCC

As described in Section 1.7, the primary challenge in observing CCC lies in the angle ($\theta_{\rm col}$) of the relative motion of the clouds to the line of sight. At $\theta_{\rm col} = 90°$, distinguishing colliding clouds is not feasible, making CCC detection impractical (e.g., Takahira et al., 2014; Priestley & Whitworth, 2021). Notably, even under the optimal condition for observing CCC, i.e., at $\theta_{\rm col} = 0°$, our study reveals that within a timescale, $t_{\rm col} = \frac{2R}{v_{\rm col}} = \frac{3\,{\rm pc}}{10\,{\rm km\,s^{-1}}} \approx 0.3$ Myr, the smaller cloud will be entirely transformed into the intermediate-velocity compressed layer, thereby reducing the velocity separation between the cloud components. According to Larson's law, the velocity dispersion of molecular clouds increases with their size (Larson, 1981) and the typical FWHM for a cloud with $R = 10$ pc is about 7 km s^{-1} (Ward-Thompson & Whitworth, 2015). The increasing velocity dispersion of molecular clouds with their size makes it difficult for observers to distinguish the shock-compressed layer and the larger cloud component in the velocity space. Therefore, even if a cloud of $R = 1.5$ pc collides with another cloud of $R = 10$ pc at a relative velocity of 10 km s^{-1}, and it is observed from a perfect viewing angle (i.e., $\theta_{\rm col} = 0°$), these two cloud components will be indistinguishable after a timescale of about 0.3 Myr irrespective of the velocity resolution of the molecular line data. Furthermore, when colliding clouds exhibit significant size differences, the collision process will result in a minute decrease in the integrated intensity map at the collision site for the larger cloud component. Hence, it is challenging to detect this subtle decrease in emission due to limited instrumental sensitivity. A rough estimate for the minimum detectable cavity size for the SEDIGISM ^{13}CO(2–1) data can be achieved using the relation, $N({\rm H_2}) \sim 10^{21}$ cm^{-2} (K km s^{-1})$^{-1}$ from the studies of Schuller et al. (2016, 2017b) and Maity

et al. (2025a). For SEDIGISM ^{13}CO(2–1) data, sensitivity per channel is about 1 K and the velocity interval is $\sim$0.25 km s^{-1} (Schuller et al., 2021). Now, considering a cloud of radius $R = 10$ pc with a velocity distribution spanning about 18 km s^{-1} (equivalent to an extension of 6σ for an FWHM of about 7 km s^{-1}), a cavity of at least 2 pc is required to detect a 3σ (where 1σ $\sim$2 K km s^{-1}) dip in the moment-0 map for a density of 10^3 cm^{-3}. Therefore, confirming the complementary distribution and identifying CCC is also challenging for such sites within the timescale of $t_{\rm col}$. Considering that collisions of molecular clouds with different mass/size scales and similar mass/size scales happen at a similar rate (Inoue et al., 2018), and $\theta_{\rm col}$ can have a wide range of values, it is natural that many CCC sites go undetected. This provides a natural explanation for why the detected CCC sites predominantly consist of clouds of similar sizes (Fukui et al., 2021a). It is important to note that synthetic molecular line data of CCC will be helpful to search for new observational signatures at $\theta_{\rm col} = 0°$ when the compressed layer is mixed in velocity space with the larger cloud component.

6.4.4 The cone: A mass-collecting machine

The initial spherical cloud geometry shapes the filaments into a cone, which is best observed at $\theta_{\rm col} = 90°$. Therefore, the column density maps in the x–z and y–z planes reveal the clearest view of the cone at $t = 0.7$ Myr in Figure 6.13a and 6.13b, respectively. As discussed in Section 6.4.3, the bridge feature appears in the early phases of the collision, and the detection of complementary distribution can also be challenging if the clouds have a larger size difference. However, the cone shape lasts longer and may be more useful over a much longer time scale (about a few Myr) to test for CCC at $\theta_{\rm col} = 90°$. The bending of the magnetic field observed in the y–z plane serves as an observational footprint of the CCC or shock compression for an observer at higher viewing angles. Interestingly,

such curved magnetic field morphology is not observed in the x–z plane (see Figure 6.13a) because the initial magnetic field was parallel to the y-axis, i.e., to the line of sight for an observer in that plane. However, an initial magnetic field making some angle with the line of sight for an observer will always show the curved morphology toward the direction of the collision.

As displayed by the projected mass-weighted gas velocity vectors in Figure 6.13c, materials on the surface of the cone flow toward its vertex. The total mass of the compressed layer within a cylinder, having its symmetry along the z-axis and radius of 1.5 pc is about 1975 $M_{\odot}$ (including low-density gas and the sink particles). With a density cutoff of 4×10^3 cm^{-3}, the compressed layer contains about 91% (i.e., $\sim$1805 $M_{\odot}$) of its total mass in a total volume of about 1.63 pc^3. The high-density layer is divided using cylindrical shells C1, C2, C3, C4, and C5 with radii of 0.3, 0.6, 0.9, 1.2, and 1.5 pc, respectively (see Figure 6.13c). Table 6.4 lists the total mass of the high-density gas, volume fraction, average density, total mass of the sink particles, and the fraction of the total mass for the compressed layer within the cylindrical shells. The vertex of the cone is the densest region of the compressed layer, which is active in star-forming activity as the sink particles are mostly distributed toward it. Hence, the star cluster, including the massive stars, will reside toward the vertex of the cone. Therefore, the distribution of the stars relative to the cone is another observational signature of CCC for higher viewing angles. The key feature of this model lies in its capability to accumulate materials rapidly. Initially, the gas of 1805 $M_{\odot}$ was distributed in a volume of about 36.5 pc^3, but it is compressed into a volume of about 1.6 pc^3 within a few 0.1 Myr. The variations in the dynamic pressure, gravitational acceleration, and the magnetic fields in the compressed layer at t = 0.7 Myr, along the z-direction, are shown in Figures 6.13d, 6.13e, and 6.13f, respectively. The regions, L1–L6, marked in Figures 6.13c,6.13d, 6.13e and 6.13f,

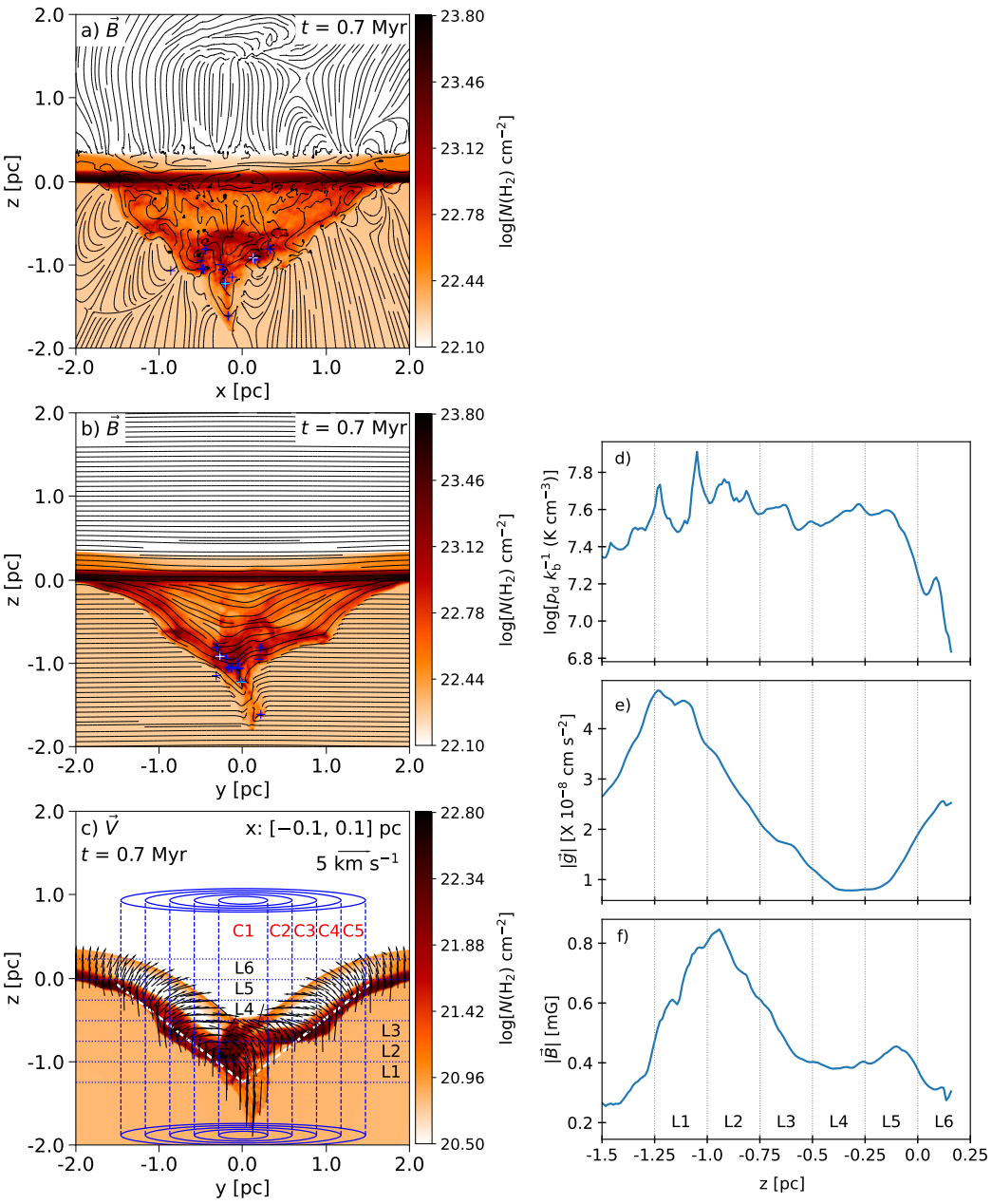

Figure 6.13: The magnetic field streamlines are shown over the (a) x–z and (b) y–z projected column density maps at t = 0.7 Myr. The plus symbols are sink particles, identical to Figure 6.2s and 6.2t, respectively. (c) The y–z projected mass-weighted average gas velocity vectors for the compressed layer are displayed over the column density map for an integration range of x:[−0.1, 0.1] pc. The horizontal cuts, L1–L6 (having a width, ΔL_z = 0.25 pc), are used to extract the PV diagrams shown in Figure 6.14. The pair of white dashed lines show a cone (with $\theta \sim 52°$). Panels (d), (e), and (f) show the changes in dynamic pressure, gravitational acceleration, and the magnetic fields in the compressed layer at t = 0.7 Myr. The regions, L1–L6, are marked in the last three panels with gray dotted lines.

Table 6.4: The mass distribution of the compressed layer and the sink particles at $t = 0.7$ Myr.

Cylindrical shell	$M^{\rm gas}$ ($M_\odot$)	Volume fraction (%)	$n_{\rm avg}$ (cm^{-3})	$M^{\rm sink}$ ($M_\odot$)	$\frac{M^{\rm gas}+M^{\rm sink}}{M_{\rm total}}$[1]
C1	233	8.1	29571	69	0.17
C2	355	15.6	23561	25	0.21
C3	327	20.0	16915	8	0.19
C4	353	25.2	14432	–	0.19
C5	436	31.1	14469	–	0.24

[1] $M_{\rm total}$ represents the combined mass of the gas and sink particles across all cylindrical shells.

indicate that the strengths of the dynamic pressure, gravitational acceleration, and the magnetic fields increase as we move toward the vertex of the cone from its base. At the vertex of the cone (i.e., within C1), the total collected mass is about 307 $M_\odot$ within a volume of about 0.13 pc^3, making it highly favorable for the formation of massive star(s).

The PV diagrams toward the cone reveal unique features that can hint at the origin of such conical structures from a CCC or shock compression event. The PV diagrams along the y-direction for the regions L1–L6 of the compressed layer are shown in Figures 6.14a–6.14f, respectively. The velocity interval between the channels is set to be 0.25 km s^{-1} (for a y–z–v_x data cube) and the integration range in the z-direction, ΔL_z is 0.25 pc. The positive (i.e., red-shifted) and negative (i.e., blue-shifted) velocity components in the PV diagrams arise from

the near- and far-sides of the cone, respectively, due to the projection effect. The

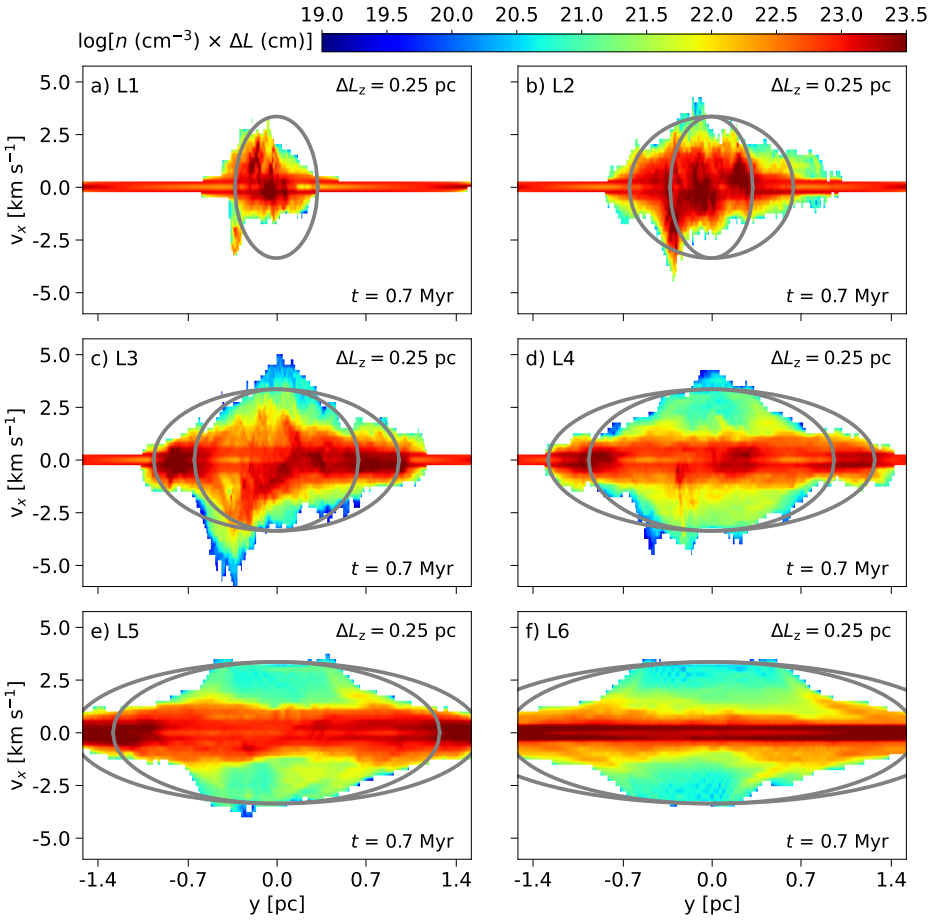

Figure 6.14: Panels (a)–(f) present the PV diagrams extracted for the regions, L1–L6, which are highlighted in Figure 6.13c. The gray curves on the PV diagrams present a cone (with $\theta \sim 52°$) with a constant gas velocity of about 4.25 km s^{-1} directed toward its vertex. The cone is shown by white dashed lines in Figure 6.13c.

gray curves on the PV diagrams represent a constant gas velocity of approximately 4.25 km s^{-1} for a cone with an angle of about 52°. The deviation of the PV diagrams from our simulated data and the simple analytical model is because the flow velocity is not constant, and the compressed layer has a finite width. This study reveals that the velocity extent increases as one moves from the base of the cone (i.e., from L6) toward the vertex, due to the gravitational attraction of a

large amount of gas collected at the vertex, reaching its maximum at L3. At the vertex, as gas from different directions accumulates, the velocity extent decreases due to the conservation of momentum. Altogether, these signatures in the PV diagrams, the curved morphology of the magnetic field, and the position of the stars in the cone can be utilized to test the CCC scenario at $\theta_{\rm col} = 90°$.

Fukui et al. (2017b) conducted a detailed analysis of the H I gas in the south-east region of the LMC and confirmed that the region has two velocity components, labeled as L and D, separated by about 50 km s^{-1}. The authors found complementary distributions with a spatial displacement between them and suggested that they are colliding with a collision timescale of about 2 Myr. They also discovered H I bridge features between them spanning over a kpc size and interpreted that the collision triggered the formation of the young massive cluster R136 as well as other star-forming regions including N159, located at 500 pc south of 30 Dor. Subsequently, Fukui et al. (2019), Tokuda et al. (2019, 2022), and Wong et al. (2022) conducted high-resolution CO observations with ALMA toward N159E, N159W-S, and N159W-N, and 30 Dor, respectively. The common properties of these clouds include filamentary cone/fan shapes with north-south elongation ranging from a few pc to a few 10 pc, having a vertex at their southern ends. It is remarkable that most active high-mass star formation in each case takes place near the vertex, in addition to scattered star formation along the filaments. These aspects seem to be in accordance with the MHD simulations of Inoue et al. (2018), where the initial setup involves the injection of a spherical cloud onto an extended plane-like gas layer, leading to the formation of filaments into a cone/fan-shaped gas distribution. The present chapter extends the model of Inoue et al. (2018) by revealing detailed physical properties of the gas distribution and kinematics and by elucidating how filaments form and merge at the vertex of the cone to drive massive star-forming activity. We expect to see many

more cone/fan-shaped Galactic and extragalactic sources, which will contribute to a better understanding of the model.

6.5 Summary

We have analyzed the MHD simulation data of Inoue et al. (2018) to understand the connection between two theories of MSF: Accretion through filaments to the hub in case of HFSs and CCC. This study includes a detailed investigation of the shock-compressed layer, the detection of filaments and cores, and an exploration of the gas kinematics involved in CCC. The major outcomes of this work are summarized as follows.

1. A supersonic CCC creates a shock-compressed layer in the interface of the colliding cloud components. Depending on the initial parameters of the colliding clouds, the morphology of the network of filaments and the core mass spectrum can vary (Balfour et al., 2017). However, with supersonic turbulence or high-density inhomogeneity, the shock compression rapidly leads to the formation of filaments, and subsequently, the creation of HFSs, as detected at $t = 0.7$ Myr. Therefore, we found that CCC can lead to the formation of HFSs.

2. The collision of the spherical cloud with the sea of dense gas shapes the filaments into a cone and drives inward flows among them. These inward flow of filaments merge at the vertex of the cone, rapidly accumulating high-density gas. Consequently, the vertex of the cone becomes favorable for the formation of a massive star(s). The cone functions as a mass-collecting machine, involving a non-gravitational early process of filament formation, followed by gravitational gas attraction to complete the formation of the HFS.

3. Apart from the angle of the relative motion of the clouds to the line of sight, observational detection of CCC faces two major challenges: I. Identifying the two cloud components in the PV space after the timescale $t_{\rm col}$ and II. Detecting a minute dip in the emission of the larger cloud component to verify complementary distribution if the cloud components have larger size differences, which is equally probable as mentioned in Inoue et al. (2018).

4. CCC events at $\theta_{\rm col} = 90^\circ$ can be confirmed by the position-velocity diagrams presenting gas flow toward the vertex of the cone, which hosts stars/young stellar objects, and by the magnetic field morphology curved toward the direction of collision.

Altogether, this work indicates a strong connection between CCC and the formation of HFSs. Turbulence, shock compression, magnetic fields, and gravity each contribute to the formation of HFSs through CCC. In addition, this work also highlights the challenges in observing CCC signatures and proposes new possible signatures for $\theta_{\rm col} = 90^\circ$.

Chapter 7

Investigating Embedded Structures and Gas Kinematics in the IRDC Hosting Bubble N59-North[†]

7.1 Introduction

To demonstrate how the MHD simulation results from the previous chapter enhance our understanding of molecular gas distribution, large-scale gas motion, and observed MSF activity, this chapter presents a multi-scale and multi-wavelength observational study of an extended area encompassing the MIR bubble N59 (Churchwell et al., 2006; Deharveng et al., 2010; Hattori et al., 2016; Hanaoka et al., 2019) and its northern edge, known as N59-North (Chen et al.,

[†]**A. K. Maity**, L. K. Dewangan, O. R. Jadhav, Saurabh Sharma, Ram Kesh Yadav, Y. Fukui, H. Sano, and T. Inoue, *The Astronomical Journal*, Volume 169, Issue 6, https://doi.org/10.3847/1538-3881/adcedd

2024). The bubble N59 is located toward the Galactic coordinates (l, b) = (33.°071, −0.°075) and exhibits a broken ring or shell-like structure in both molecular line data and dust continnum emission (e.g., Paulson et al., 2024). Anderson & Bania (2009) estimated a kinematic distance of 5.6±2 kpc for N59. However, using Gaia parallax measurements (Gaia Collaboration et al., 2016, 2021), Paulson et al. (2024) refined this to a more accurate distance of 4.66±0.70 kpc, which is adopted in this study. The N59-North region contains several Class II 6.7 GHz MMEs and UC H II regions, which serve as the indicators of early stages of MSF (e.g., Deharveng et al., 2010; Paulson et al., 2024). Using a multi-wavelength approach, Paulson et al. (2024) identified a HFS candidate associated with N59-North. However, additional studies are needed to validate the existence of this proposed HFS candidate.

Using MWISP ^{12}CO/^{13}CO(J = 1–0) line data, Chen et al. (2024) reported multiple velocity components toward the N59 bubble, specifically [65, 79], [79, 86], [86, 95], and [95, 108] km s^{-1} (see Figure 2 in their work). Based on this, they suggested that multiple collision events have occurred among these velocity components over the past 2 Myr. However, the physical connections between these velocity components and their respective distances are not thoroughly addressed in their study. Among these, the velocity component in the range of [95, 108] km s^{-1} appears to correspond to the major cloud associated with N59/N59-North, exhibiting a filamentary structure (see Figure 6 in Chen et al., 2024). Despite the availability of extensive observational datasets and several studies focusing on N59/N59-North, the full extent of this filamentary structure remains unexplored, pointing to physical processes that are yet to be fully investigated. In Figure 7.1a, we highlight the extended IRDC, visible in the *Spitzer* 8.0 μm image (indicated by arrows), appearing as a filamentary structure in absorption. The locations of N59 and N59-North are also indicated in Figure 7.1a (see also Chen

et al., 2024). In general, IRDCs are known to host dense, cold molecular gas and dust that block IR radiation from background sources. They are regarded as important sites for studying the earliest phases of MSF (e.g. Ragan et al., 2009, and references therein). Interestingly, the IRDC hosting N59-North has not been the focus of any previous studies. As a result, the formation and evolution of the filament, along with its associated massive star-forming activity, remain unexplored. In this study, we employ a multi-wavelength observational approach to investigate the physical environment and star formation processes in the IRDC. We present a detailed kinematic analysis of the structures embedded in the IRDC using ^{13}CO(J = 1–0) and ^{13}CO(J = 3–2) molecular line data.

The outline of this chapter is as follows: In Section 7.2, we describe the observational data sets utilized in this research. The outcomes of this work are detailed in Section 7.3. The significance of these outcomes related to MSF in the IRDC is discussed in Section 7.4. Finally, Section 7.5 summarizes the key results of this study.

7.2 Data sets

In this work, we utilized multi-wavelength archival data sets (i.e., from NIR to radio) as listed in Table 7.1. The MAGPIS and SMGPS radio continuum data have RMS noise levels (σ) of about 0.4 mJy beam^{-1} and 20 μJy beam^{-1}, respectively (Helfand et al., 2006; Goedhart et al., 2024). The ^{13}CO(J = 1–0) line data from the Boston University-Five College Radio Astronomy Observatory GRS are calibrated in the antenna temperature ($T_{\rm A}$) scale. The $\sigma(T_{\rm A})$, velocity separation between the channels, and angular resolution of the GRS ^{13}CO(J = 1–0) line data are about 0.13 K, 0.21 km s^{-1}, and 46″, respectively (see Jackson et al., 2006, for more details). The CHIMPS ^{13}CO(J = 3–2) line data (having critical

density $\geq 10^4$ cm^{-3} at temperature ≤ 20 K; Rigby et al., 2016) were also examined toward the selected target area. The $\sigma(T_A)$, the velocity separation between the channels, and the angular resolution of the CHIMPS ^{13}CO($J = 3$–2) line data are about 0.6 K, 0.5 km s^{-1}, and 15″, respectively. To enhance the visibility of faint or diffuse features, the CHIMPS line data were smoothed using a Gaussian function, resulting in an angular resolution of ∼27″ and $\sigma(T_A)$ ∼0.15 K. In the direction of the selected target area, the ATLASGAL clumps at 870 μm (from Urquhart et al., 2018) and the positions of YSOs from the *Spitzer*/IRAC Candidate YSO (SPICY) Catalog (Kuhn et al., 2021) were collected. The *Herschel* dust temperature (T_d) and H_2 column density ($N(H_2)$) maps (resolution ∼12″) were obtained from Marsh et al. (2017). The photometric magnitudes of point-like sources at 3.6, 4.5, and 5.8 μm were obtained from the *Spitzer* GLIMPSE-I Spring ′07 catalog (Benjamin et al., 2003).

Table 7.1: The list of multi-wavelength surveys utilized in the present work.

Survey	Wavelength/Frequency/line(s)	Resolution (″)	Reference
SARAO MeerKAT Galactic Plane Survey (SMGPS)	1.3 GHz	∼8	Goedhart et al. (2024)
Multi-Array Galactic Plane Imaging Survey (MAGPIS)	20 cm	∼6	Helfand et al. (2006)
Galactic Ring Survey (GRS)	2.7 mm; ^{13}CO($J = 1$–0)	∼46	Jackson et al. (2006)
CO Heterodyne Inner Milky Way Plane Survey (CHIMPS)	0.907 mm; ^{13}CO($J = 3$–2)	∼15	Rigby et al. (2016)
APEX Telescope Large Area Survey of the Galaxy (ATLASGAL)	870 μm	∼19.2	Schuller et al. (2009)
Herschel Infrared Galactic Plane Survey (Hi-GAL)	70, 160, 250, 350, 500 μm	∼5.8, ∼12, ∼18, ∼25, ∼37	Molinari et al. (2010b)
Inner Galactic plane survey using the Multiband Infrared Photometer for Spitzer (MIPSGAL)	24 μm	∼6	Carey et al. (2009)
Spitzer Galactic Legacy Infrared Mid-Plane Survey Extraordinaire (GLIMPSE)	3.6, 4.5, 5.8, 8.0 μm	∼2, ∼2, ∼2, ∼2	Benjamin et al. (2003)

7.3 Results

7.3.1 Existence of an extended filamentary structure

Figure 7.1a presents the *Spitzer* 8.0 μm image overlaid with MAGPIS 20 cm continuum emission contours. As mentioned earlier, the *Spitzer* 8.0 μm image

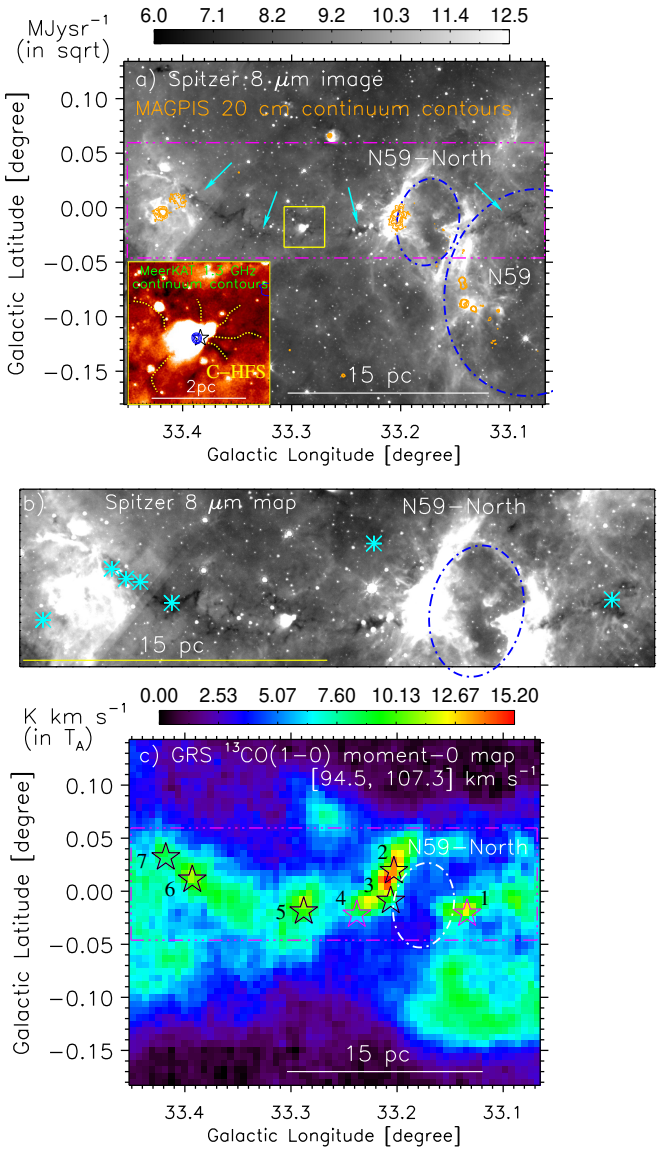

Figure 7.1: (a) *Spitzer* 8 μm image of an area $\sim$0.°39 × 0.°31, centered at (l, b) = (33.°26, −0.°02), covering the IRDC associated with the bubble N59-North. The filamentary IRDC is marked with cyan arrows, while the bubbles N59 and N59-North are outlined by the large and small ellipses, respectively. The orange contours present MAGPIS 20 cm radio continuum emission at levels [5, 8, 10 and 15] $\times\sigma$, with 1σ = 0.4 mJy beam^{-1}. The inset shows a zoomed-in view of the yellow rectangular region outlined over the IRDC. Blue contours indicate MeerKAT 1.3 GHz continuum emission at levels [5, 15, and 25] $\times\sigma$, with 1σ = 20 μJy beam^{-1}. The position of the ATLASGAL clumps (from Urquhart et al. (2018)) is shown with black star symbols. The IR-dark filaments are highlighted by yellow dotted lines in the inset. (b) Same image as panel (a) for the magenta dotted-dashed rectangular region. The position of the IRDC candidates toward the filament obtained from Pari & Hora (2020) is marked using asterisk symbols. (c) GRS ^{13}CO(J = 1–0) integrated intensity (moment-0) map for the velocity range [94.5, 107.3] km s^{-1}. For the moment-0 map 1σ = 0.21 K km s^{-1}. The black and magenta star symbols indicate the position of the ATLASGAL clumps with and without the signature of outflow signatures, respectively. The ellipse corresponding to N59-North is highlighted in panels (b) and (c). A scale bar of 2 pc is provided in the inset of panel (a), while a 15 pc scale bar is shown in each panel for a distance of 4.66 kpc.

reveals an extended IRDC, as indicated by arrows. The MAGPIS radio continuum contours offer information on the distribution of ionized emission toward the IRDC. Previously reported structures, such as N59 and N59-North, are also labeled in the figure. Figure 7.1b offers a closer view of this IRDC, including N59-North. Asterisks mark several IRDC candidates identified by Pari & Hora (2020) through a semi-automated computational analysis of *Spitzer*/GLIMPSE data. This filamentary structure, as observed in absorption, spans about 28 pc at the distance of 4.66 kpc and exhibits a disruption of nearly 3.8 pc at the location of the bubble N59-North. This extended filamentary structure has not been extensively studied to date. To confirm its existence as a single entity, we analyzed the GRS ^{13}CO(J = 1–0) line data and generated the moment-0 map over the velocity range of [94.5, 107.3] km s^{-1}. In Figure 7.1c, the GRS moment-0 map reveals the molecular gas associated with the IRDC and highlights a similar filamentary morphology. The moment-0 map is also overlaid with the positions of the ATLASGAL clumps (see stars in Figure 7.1c), situated at same distance ($\sim$6.5 kpc) and exhibiting velocities between [99.2, 103.9] km s^{-1} (from Urquhart et al., 2018). The alignment in velocity range and distance of the ATLASGAL clumps along the filamentary structure confirm its existence as a single physical entity, despite apparent disruptions near N59-North.

Yang et al. (2018) studied the outflow activity associated with the ATLASGAL clumps using the CHIMPS ^{13}CO/C^{18}O(J = 3–2) line data. Clumps exhibiting outflow activity are indicated by black stars in Figure 7.1c. No outflow activity was detected by Yang et al. (2018) for the ATLASGAL clump at $l = 33.^{\circ}134$. The C^{18}O(J = 3–2) emission observed toward the clump at $l = 33.^{\circ}238$ was insufficient to search outflow activity. These two clumps are marked in magenta in Figure 7.1c. The physical paremeters of these ATLASGAL clumps are listed in Table 7.2.

Table 7.2: The physical properties of the ATLASGAL clumps. The velocity, mass, and effective radius of these clumps are obtained from Urquhart et al. (2018). The mass and effective radius values presented in the table have been rescaled to the adopted distance of $d = 4.66$ kpc. Information on outflow activity associated with these clumps is sourced from Yang et al. (2018).

ID	l (deg)	b (deg)	v (km s^{-1})	$R_{\rm eff}$ (pc)	$\log(M\ [M_\odot])$	Outflow
1	33.134	-0.021	102.8	0.22	2.46	No
2	33.203	0.019	101.2	0.50	2.98	Yes
3	33.206	-0.009	100.0	0.90	2.95	Yes
4	33.238	-0.022	100.4	0.88	3.09	–
5	33.288	-0.019	99.2	0.34	2.40	Yes
6	33.393	0.011	103.9	1.02	3.38	Yes
7	33.418	0.032	103.7	0.20	2.32	Yes

Notably, the ATLASGAL clump located at $l = 33.^{\circ}288$ (hereafter, ATL-5) is situated at the center of the filamentary cloud. To determine whether these clumps satisfy the empirical mass–size criterion for MSF, we have plotted the mass of the ATLASGAL clumps against their effective radius (see Figure 7.2). In Figure 7.2, the blue dashed line represents the Kauffmann & Pillai condition for MSF,expressed as $M(R) = 870\ M_\odot\ (R/\mathrm{pc})^{1.33}$ (Kauffmann & Pillai, 2010). Urquhart et al. (2018) adjusted the mass coefficient by a factor of 1.5 to account for the difference in dust absorption coefficient used in their study.

This modification yields the modified Kauffmann & Pillai criterion (referred to

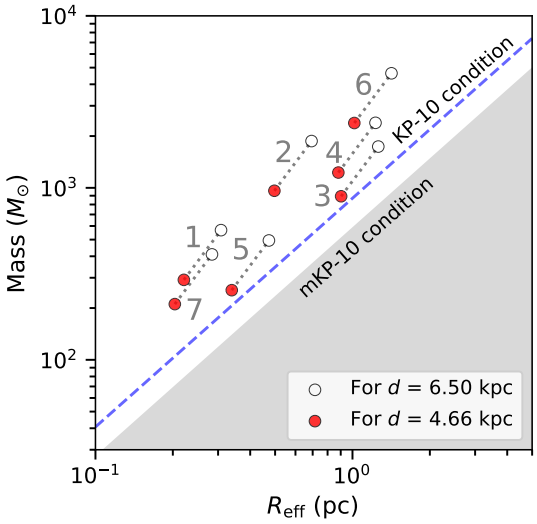

Figure 7.2: The mass–effective radius plot for the ATLASGAL clumps. The data from Urquhart et al. (2018) for $d = 6.5$ kpc are displayed as open circles, while the red solid circles represent the data points scaled to our adopted distance of 4.66 kpc. The KP-10 condition for MSF is indicated by the blue dotted line. The mKP-10 condition for MSF as defined by Urquhart et al. (2018) corresponds to the white region above the gray-shaded area.

as mKP-10) for MSF, defined as $M(R) > 580\ M_\odot\ (R/\mathrm{pc})^{1.33}$ (see Urquhart et al., 2018). The white area above the gray-shaded region in the plot represents clumps that satisfy the mKP-10 condition. It is important to note that all ATLASGAL clumps meet the mKP-10 criterion for MSF, even after their masses and effective radii are adjusted to the distance of 4.66 kpc.

7.3.2 Investigation of a HFS candidate, C-HFS

Figure 7.2 clearly demonstrates that ATL-5 meets the empirical mass–size criterion for MSF. However, no MAGPIS 20 cm continuum emission is detected toward this clump. The bottom left inset in Figure 7.1a is the *Spitzer* 8.0 μm image focusing on the central part of the filamentary structure in absorption (outlined by the solid box in Figure 7.1a), where ATL-5 is located. Overlaid MeerKAT 1.3 GHz continuum emission contours within the inset reveal ionized gas con-

centrated around ATL-5, providing evidence of ongoing MSF activity within the clump. The detection of radio continuum emission is attributed to the higher sensitivity of the MeerKAT data compared to the MAGPIS data. We calculated the total flux density of the UC H II region (radius ∼0.05 pc) from MeerKAT data above the 5σ threshold to be about 0.37 mJy. Using this value and assuming the temperature to be about 10^4 K, we determined the total number of Lyman continuum photons emitted per second (denoted as $N_{\rm UV}$), following Equation B.2. We found that $\log(N_{\rm UV})$ ∼44.8 for the driving source of the H II region. Comparing our calculated value of $N_{\rm UV}$ with the theoretical estimation of Panagia (1973), we infer that the source responsible for ionizing the gas is a B2-type star.

In the central part of the filamentary structure hosting N59-North, several pc-scale IR-dark filaments are identified in the *Spitzer* 8.0 μm image. These filaments seem to converge toward a common junction associated with ATL-5 (see the inset and the solid box in Figure 7.1a). We estimated the background/foreground emission in the *Spitzer* 8 μm image using the median filtering technique (see Simon et al., 2006; Ragan et al., 2009, for details) and found it to be about 70 MJy sr^{-1} toward ATL-5. In contrast, the IR-dark filaments associated with ATL-5 are detected at levels of about 55–65 MJy sr^{-1}. These values indicate that the IR-dark filaments are not random background fluctuations but reliable features, positioning ATL-5 at the center of a HFS candidate (i.e., C-HFS) with an extent of less than 3 pc. The central hub (or ATL-5) is associated with an UC H II region. The identification of the C-HFS is a new and important result, highlighting the potential of *Spitzer* 8 μm image in revealing pc-scale HFSs. Previously, Dewangan et al. (2024) identified multiple such HFSs using absorption features in the *Spitzer* 8 μm image toward the IRDC G11.11−0.12 (see also Bhadari et al., 2025).

7.3.3 Study of ^{13}CO(J = 1–0) and ^{13}CO(J = 3–2) data in the filamentary cloud

We investigate the gas distribution and kinematics in the filamentary cloud using the the GRS ^{13}CO(J = 1–0) and CHIMPS ^{13}CO(J = 3–2) line data.

7.3.3.1 Molecular gas morphology and velocity in the filamentary cloud

Figures 7.3a and 7.3b show the moment-0 map and the moment-1 map of the GRS ^{13}CO(J = 1–0) emission, respectively. In Figures 7.3c and 7.3d, we present the moment-0 and moment-1 maps of the CHIMPS ^{13}CO(J = 3–2) emission, respectively. As mentioned in Section 7.2, CHIMPS ^{13}CO(J = 3–2) data have better resolution and trace relatively higher-density gas as compared to GRS ^{13}CO(J = 1–0) data. By combining both datasets, we obtain a comprehensive view of the gas morphology and velocity for both diffuse ($\sim 10^3$ cm^{-3}) and denser ($\geq 10^4$ cm^{-3}) gas components. Note that Figure 7.3a is identical to Figure 7.1c; however, it has been included in Figure 7.3 alongside other panels for ease of comparison.

The ^{13}CO(J = 3–2) moment-0 map clearly reveals the filamentary morphology of the higher-density gas within the extended molecular emission traced in the ^{13}CO(J = 1–0) moment-0 map. Molecular condensations are traced toward the ATLASGAL clumps in the ^{13}CO(J = 3–2) moment-0 map. Both the moment-1 maps reveal similar velocities at the opposite edges of the filament (see clumps ATL-1, ATL-6, ATL-7). There are significant velocity variations of a few km s^{-1} along the length of the filament, from its edges toward the center. The lowest velocity is observed toward the central region of the filament, where C-HFS or ATL-5 is situated. Notably, intense molecular emission is detected in

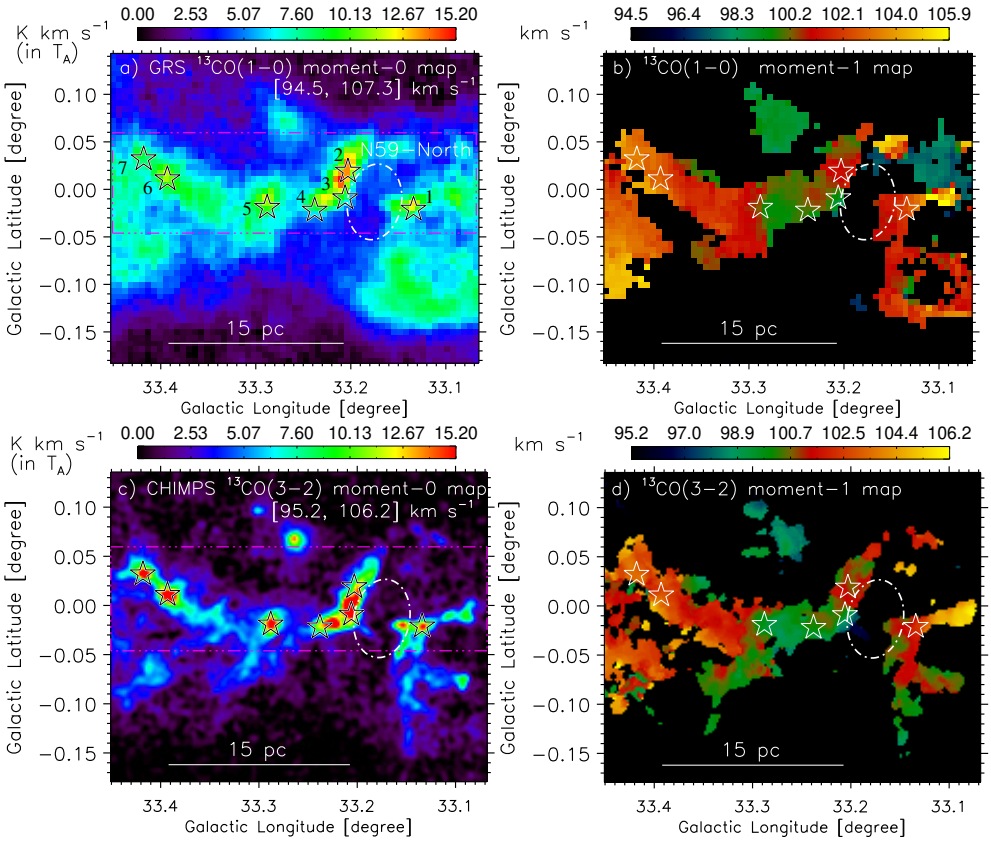

Figure 7.3: (a) GRS ^{13}CO($J = 1$–0) moment-0 map, identical to Figure 7.1b. (b) GRS ^{13}CO($J = 1$–0) moment-1 map. (c) CHIMPS ^{13}CO($J = 3$–2) moment-0 map for the velocity range [95.2, 106.2] km s^{-1}. For the moment-0 map $1\sigma = 0.36$ K km s^{-1}. (d) CHIMPS ^{13}CO($J = 3$–2) moment-1 map. The rectangular region highlighted in panels (a) and (c) is identical to the one shown in Figure 7.1. A scale bar of 15 pc is provided in each panel.

both ^{13}CO($J = 1$–0) and ^{13}CO($J = 3$–2) moment-0 maps toward the bubble N59-North, which is associated with ATL-2 (see Figures 7.3a and 7.3c). The moment-1 maps indicate that the molecular gas toward the bubble N59-North (including ATL-2) exhibits velocity variations compared to its surrounding areas. This suggests that the massive stars responsible for the bubble N59-North might have influenced the morphology and gas kinematics in the filament. This aspect is explored in detail in Section 7.3.3.2.

7.3.3.2 Position-velocity and position-position-velocity diagrams

To reveal the kinematics of the dense gas, we produced the Galactic longitude-velocity (i.e., l-v or position-velocity (PV)) diagram using the ^{13}CO(J = 3–2) data, which is shown in Figure 7.4a. The white arrows in Figure 7.4a represent the velocity gradients identified in the PV diagram toward the eastern and western parts of the filament. We have estimated these gradients to be about -0.32 and 0.36 km s^{-1} pc^{-1}, respectively. In the case of the l-v diagram, the integration range in Galactic latitude is too large (i.e., [$-0.^{\circ}046$, $0.^{\circ}059$]) to properly reveal the gas kinematics toward the bubble N59-North. Therefore, we performed the spectral decomposition of the ^{13}CO(J = 3–2) data using the Python-based tool `SCOUSEPY`[1] (Henshaw et al., 2016, 2019). The process began by defining the size of the 'Spectral Averaging Areas (SAA)' in pixels, with a selected size of 3 × 3 pixel^2. These SAAs are spatially distributed to cover all emission above a specific threshold (∼1.5 K). From each of these SAAs, an averaged spectrum was extracted and fitted with single or multiple Gaussian components. The best-fit parameters from the SAA-averaged spectra were then utilized to fit the spectra at each pixel in the SAA. To visualize the results, the centroid velocity/velocities of the fitted Gaussian(s) is/are plotted for each pixel in position-position-velocity (PPV; here, l-b-v) space. The resulting PPV diagram from our analysis is shown in Figure 7.4b, where the moment-0 map of the filament is displayed using filled contours in the l-b plane. The PPV map is consistent with the PV diagram, revealing opposite velocity gradients toward the eastern and western parts of the filament. Notably, the PPV map clearly highlights the red- and blue-shifted gas components toward the bubble N59-North (see the arrows).

[1] https://scousepy.readthedocs.io/en/latest/index.html

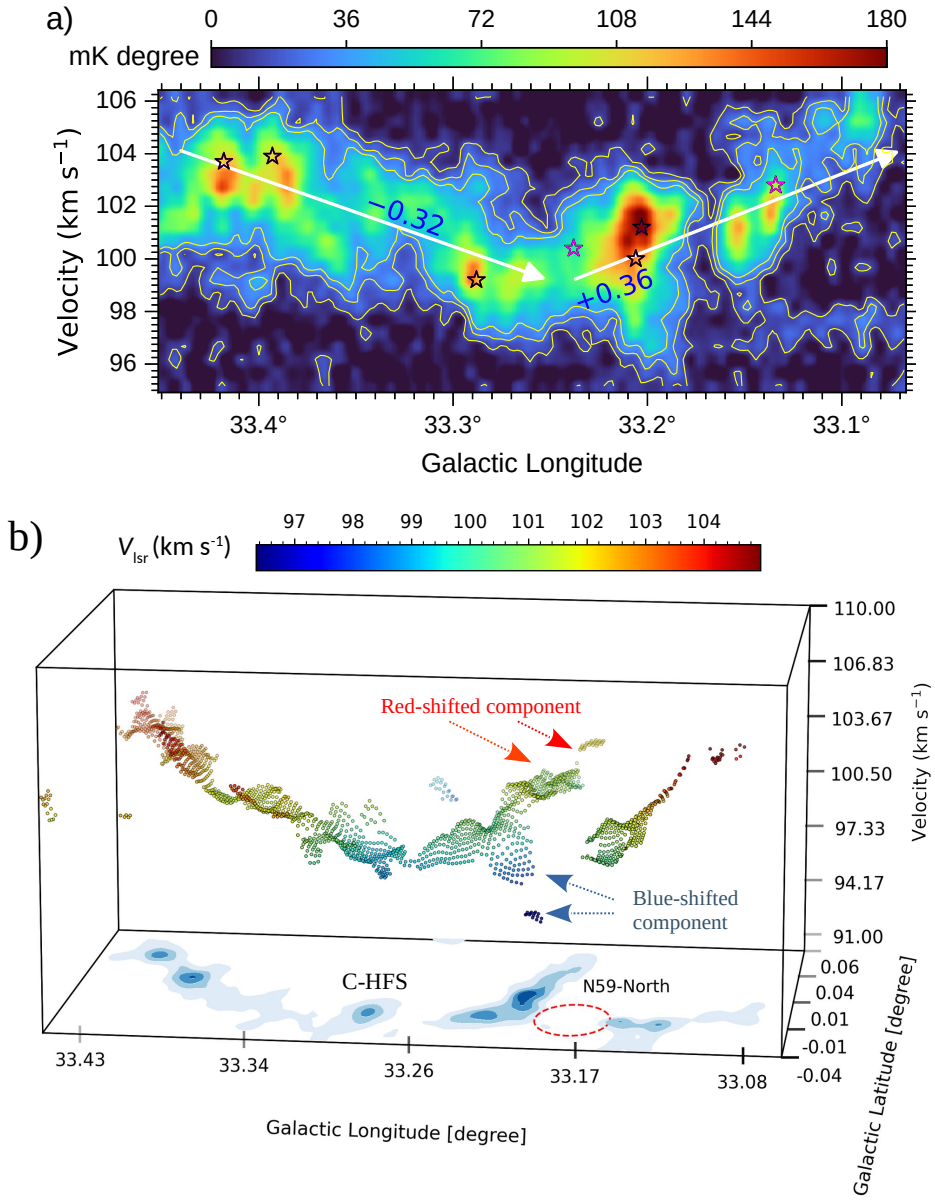

Figure 7.4: (a) The Galactic longitude-velocity (i.e., *l*-*v*) diagram of the ^{13}CO(J = 3–2) data for the integration range in Galactic latitude = [−0.°046, 0.°059]. The contours are drawn at about [6, 12, and 18]×σ, where 1σ = 2 mK degree. White arrows indicate the velocity gradients in the eastern and western parts of the filament, and the corresponding velocity gradient values are provided in the figure in units of km s^{-1} pc^{-1}. (b) The `SCOUSEPY`-generated position-position-velocity (PPV; here, *l*-*b*-*v*) diagram. The data points in the diagram represent the position and centroid velocity of the Gaussian components identified in the ^{13}CO(J = 3–2) emission. The data points are also colored based on their velocity, according to the color scale at the top of the image. The ^{13}CO(J = 3–2) integrated intensity map is shown in the *l*-*b* plane using filled contours at levels [5, 10, 15, 20, and 25] K km s^{-1}. The location of the bubble N59-North is highlighted with a red ellipse in the *l*-*b* plane. The blue- and red-shifted velocity components toward N59-North are indicated with arrows.

7.3.4 Star fomation activities in the filamentary cloud

Figures 7.5a, 7.5b, 7.5c, and 7.5d present overlays of the locations of the ATLASGAL clumps and the ^{13}CO(J = 3–2) emission contour at about 3.7 K km s^{-1} (i.e., $\sim$10σ) on four different maps: the *Spitzer* 8.0 μm image, the MeerKAT 1.3 GHz continuum emission map, the *Herschel* H_2 column density map, and the *Herschel* dust temperature map, respectively. These maps help us to identify the presence of dense molecular gas, dust clumps, ionized emission, cold dust, warm dust, and column density toward the filamentary cloud. The filamentary cloud is linked to material exhibiting column densities exceeding 2.25 $\times$ 10^{22} cm^{-2}, and is assoicated with warm dust ($T_{\rm d}$ = 20.5–24 K) as well as relatively cold dust emission ($T_{\rm d}$ = 17–18.5 K). All the ATLASGAL clumps are seen toward the areas where column densities exceed 3.2 $\times$ 10^{22} cm^{-2}. The radio continuum emission map reveals the association of extended ionized regions with the filamentary cloud, where the presence of warm dust emission is evident. In the filamentary cloud, dust emission at $T_{\rm d}$ = 17–18.5 K is traced in regions within the longitude range of [33.°25–33.°4].

The detection of YSOs within a molecular cloud provides as direct evidence of ongoing star formation. The IR excess observed in YSOs arises from their envelopes and dusty circumstellar disks (Sharma et al., 2017; Kuhn et al., 2021). To analyze the distribution of YSOs within the filamentary structure hosting N59-North (outlined by the magenta dot-dashed lines in Figure 7.1a), we used the SPICY catalog by Kuhn et al. (2021). In the *Spitzer* 8.0 μm image, the positions of Class I, Flat Spectrum, and Class II YSOs from the catalog are highlighed by red, cyan, and green diamonds, respectively (see Figure 7.5a). Using the color conditions [4.5] $-$ [5.8] $\geq$ 0.7 and [3.6] $-$ [4.5] $\geq$ 0.7 (Getman et al., 2007), we have also identified additional Class I YSO candidates, represented by blue

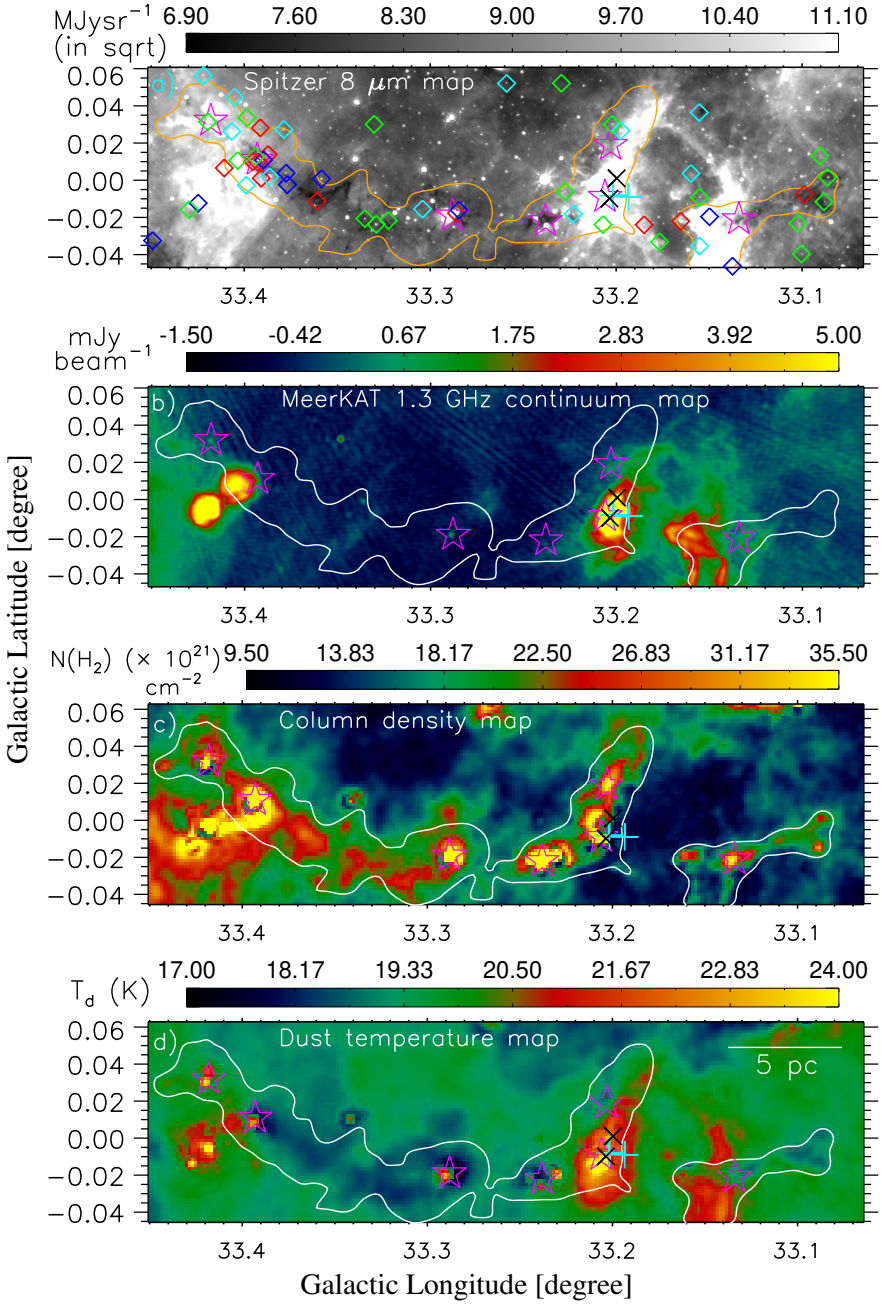

Figure 7.5: (a) *Spitzer* 8 μm image, (b) MeerKAT 1.3 GHz radio continuum emission map, (c) H_2 column density ($N(H_2)$) map, and (d) Dust temperature (T_d) map, corresponding to the region outlined by red dotted-dashed lines in Figures 7.1 and 7.3. In each panel, the ^{13}CO(J = 3–2) emission is shown using a contour at about 3.7 K km s^{-1}. The magenta star, black cross, and cyan plus symbols indicate the position of the ATLASGAL clumps, 6.7 GHz MMEs, and UC H II regions, respectively. The YSO candidates are shown using diamond symbols in panel (a). The Class I, Flat Spectrum, and Class II sources obtained from the SPICY catalog (Kuhn et al., 2021) are colored red, cyan, and green, respectively. The blue diamonds are additional Class I YSO candidates satisfying the color conditions: [4.5] − [5.8] ≥ 0.7 and [3.6] − [4.5] ≥ 0.7 (Getman et al., 2007). A scale bar of 5 pc is marked in panel (d).

diamonds in Figure 7.5a. These YSOs are distinct from those reported in Kuhn et al. (2021). Overall, numerous YSO candidates are detected within the ^{13}CO(J = 3–2) moment-0 contour, indicating the association of higher-density gas with ongoing star-forming activity.

7.4 Discussion

Through a comprehensive multi-wavelength observational investigation, we have gained new insights into the MSF activity toward the bubble N59-North. Our findings include the identification of an extended IRDC/filamentary structure that exhibits significant velocity variation along its length. Additionally, we have revealed several dust clumps as potential candidates for MSF and identified a C-HFS. These results are discussed in this section to infer the ongoing physical processes related to the origin, evolution, and MSF activity of the IRDC hosting the bubble N59-North.

7.4.1 The massive star-forming activity in the filamentary cloud

Massive stars form inside hot molecular cores (Mayra et al., 1999; van der Tak, 2004; Paron, 2024). Later, the intense UV radiation from massive stars, beyond the Lyman limit, ionizes the surrounding gas (Panagia, 1973). The size of H II regions increases over time; thus, the compact H II regions (< 0.5 pc) are associated with the early stages of MSF. In this study, we have detected a pc-scale HFS candidate (i.e., C-HFS) at the center of the filament, which is associated with ATL-5 and an UC H II region. The presence of the UC H II region and the absence of any extended H II regions suggest that C-HFS represents an early stage of HFS. Assuming that the H II region expanding in a uniform medium, we

calculated the dynamical age for the UC H II region to be about 0.01–0.04 Myr for the initial densities $n = 10^4$ to 10^5 cm^{-3}, respectively, using Equation B.1. In this calculation, the sound speed in the ionized region ($\sim$10 km s^{-1}; Bisbas et al., 2009), as well as its effective radius ($\sim$0.05 pc) and Strömgren radius, are provided as inputs. For densities ranging from $n = 10^4$ to 10^5 cm^{-3}, the Strömgren radius of the H II region varies from 0.006 to 0.001 pc. Interestingly, our target IRDC hosts several UC H II regions and 6.7 GHz MMEs toward the edge of the N59-North bubble. Recently, Chen et al. (2024) calculated the dynamical timescale for the extended H II region associated with N59-North to be about 2 Myr and proposed that the expansion of the H II is responsible for the star-forming activity near N59-North. This study supports their proposed idea by revealing the expanding gas motion near the N59-North bubble by detecting blue- and red-shifted velocity components. Therefore, taking all the information together, we find that our target IRDC has been active in MSF for the last few Myr.

The presence of several pc-scale filaments associated with C-HFS at the central part of the large-scale filament indicates the importance of multiple scales filamentary mass accretion related to MSF as proposed by Zhou et al. (2022). The gas flow in the filaments on small scale is primarily driven by gravity, whereas the large-scale gas flow is possibly caused by both turbulence (as inertial flow) and gravitational contraction (e.g., Zhou et al., 2022; Bhadari et al., 2025). Thus, the hubs accumulate a large amount of material and become suitable for MSF. The observed large-scale velocity gradients toward the filament hosting N59-North possibly suggest a converging gas flow, which is providing material to C-HFS (e.g., Kirk et al., 2013). More details about the large-scale gas motion and its possible origin are given in Section 7.4.2. The GRS and CHIMPS line data have insufficient resolution to trace C-HFS; therefore, small-scale gas motion remains

unexplored in this work. It is important to note that although all ATLASGAL clumps satisfy the condition for MSF, we have not observed pc-scale HFS systems associated with them, except for ATL-5. This suggests that, in the case of these clumps, the HFS configuration may arise at later stages or may be too weak to be detected with the current sensitivity of the data. As demonstrated by the recent observational work by Bhadari et al. (2025), a combination of ALMA and JWST observations can be extremely useful for hunting such early stages of massive star-forming regions and understanding the driving mechanisms of gas flow in small-scale.

7.4.2 The possible origin and evolution of the filamentary cloud

The PV/PPV diagrams show significant velocity variation ($\sim$ few km s^{-1}) along the filament, which can be very important for inferring the possible mechanisms driving the large-scale gas motion. In Figures 7.6a, 7.6b, and 7.6c, we provide schematic diagrams explaining how the PV diagrams would appear under different processes of gas flow, such as rotation, central collapse, and EDC, respectively. The PV diagrams are shown for cylindrical filaments and line of observation making significant angle ($\sim 45^{\circ}$) relative to the filament. For a rotating filament with constant angular velocity, the observed velocity will be proportional to the distance along the spine of the filament. A centrally collapsing filament will develop a massive clump toward its central region, exhibiting both blue- and red-shifted velocity components directed toward the filament's center. This kinematic signature can be inferred from the study by Liu et al. (2019). According to Clarke & Whitworth (2015), due to varying gravitational acceleration along the length of the isolated filaments, they undergo EDC. In the EDC process, massive clumps are exclusively found at the opposite edges of the filament, having blue- and

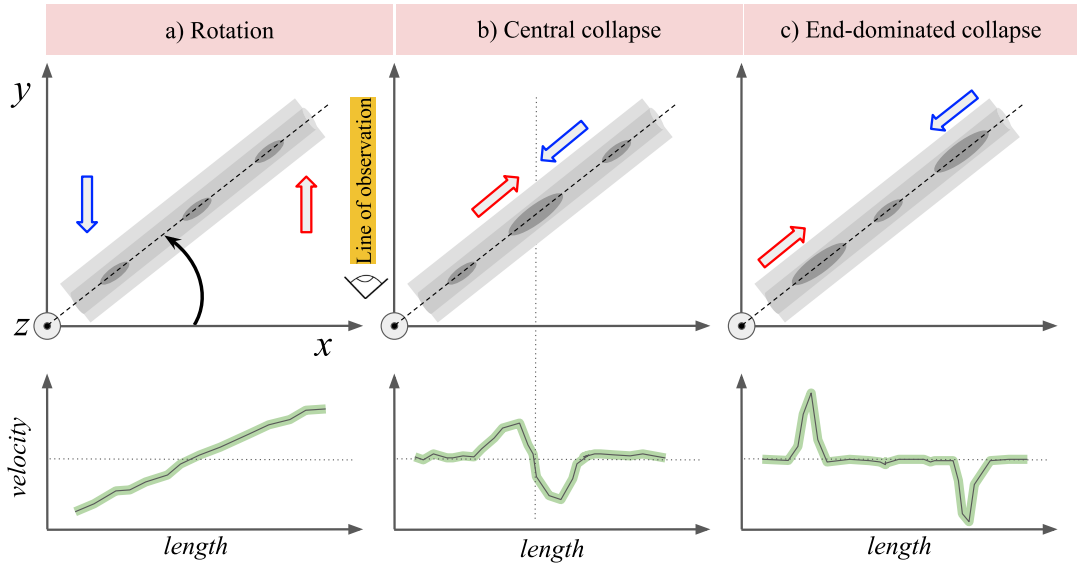

Figure 7.6: A schematic view of the possible PV diagrams for cylindrical filaments in different gas motions. The x–z plane represents the plane of the sky, and the y-direction corresponds to the line of observation, which forms a significant angle ($\sim 45°$) relative to the filament. (a) A rotating filament with a constant angular velocity, indicated by a curved arrow. (b) A filament undergoing central collapse (motivated from Liu et al., 2019). (c) A filament undergoing EDC (motivated from Clarke & Whitworth, 2015). The blue and red arrows in each panels represent the blue- and red-shifted velocity components.

red-shifted velocity components. It is important to note that if the filament is parallel to the line of observation, its filamentary nature will not be observed. Whereas, if the filament is perpendicular to the line of observation, blue- or red-shifted components will only be visible for rotation. The PV/PPV diagrams of the filament hosting N59-North do not correspond to any of the PV diagrams shown in Figure 7.6. Therefore, rotation, central collapse, and EDC are unlikely to be responsible for the large-scale gas flow in this filament.

Interestingly, the PV diagram for the target filament matches perfectly with that of the compressed layer observed in the CCC scenario presented in the last chapter. The CCC model discussed in the last chapter involves the collision of a turbulent molecular cloud (radius of 1.5 pc) and a dense sea of gas, moving

at a relative velocity of 10 km s^{-1}, as shown in Figure 7.7a. The collision resulted in a cone-shaped compressed layer as presented in Figure 7.7b at 0.4 Myr. Since molecular clouds are not ideal spheres in reality, the resulting cones can be imperfect or distorted, influenced by the molecular cloud's initial structure. Figures 7.7c and 7.7d show the PV diagrams at 0.4 Myr along the x- and y-axis for the line of observation toward z-direction, respectively. The area covered by the black lines highlights the compressed layer in the PV diagrams. The opposite signs of the velocity gradients in the left and right part of the PV diagrams indicate converging gas flow toward the vertex of the cone. The similarity of the observed PV diagram for the filament hosting N59-North and the PV diagrams for a converging gas flow in a cone suggests that the filament must have a cone-like shape. This indicates that the gas is converging toward the center of the filament, where C-HFS is situated. Figure 7.7e presents a schematic diagram that illustrates the cone-like shape of the filament and the variation in velocity along its length before the emergence of the N59-North bubble. The converging gas flows toward the center of the filament give rise to C-HFS. The emergence and expansion of bubble N59-North, along with its effect on the PV diagram, is illustrated in Figure 7.7f.

As mentioned earlier in Chapter 6, the model proposed by Inoue et al. (2018) is also applicable in the case of a molecular cloud interacting with a plane-parallel shock front arising from the expansion of an H II region. We examined MeerKAT 1.3 GHz radio continuum data and MIPSGAL 24 μm data for an extended region to investigate this possibility. An extended H II region is evident in both the MeerKAT and MIPSGAL data, as shown in Figures 7.8a and 7.8b, respectively. This H II region is classified as a candidate H II region in Anderson et al. (2014) and is highlighted with a dotted circle in Figure 7.8. However, our target filament extends beyond the boundaries of the H II region, and molecular gas is not traced

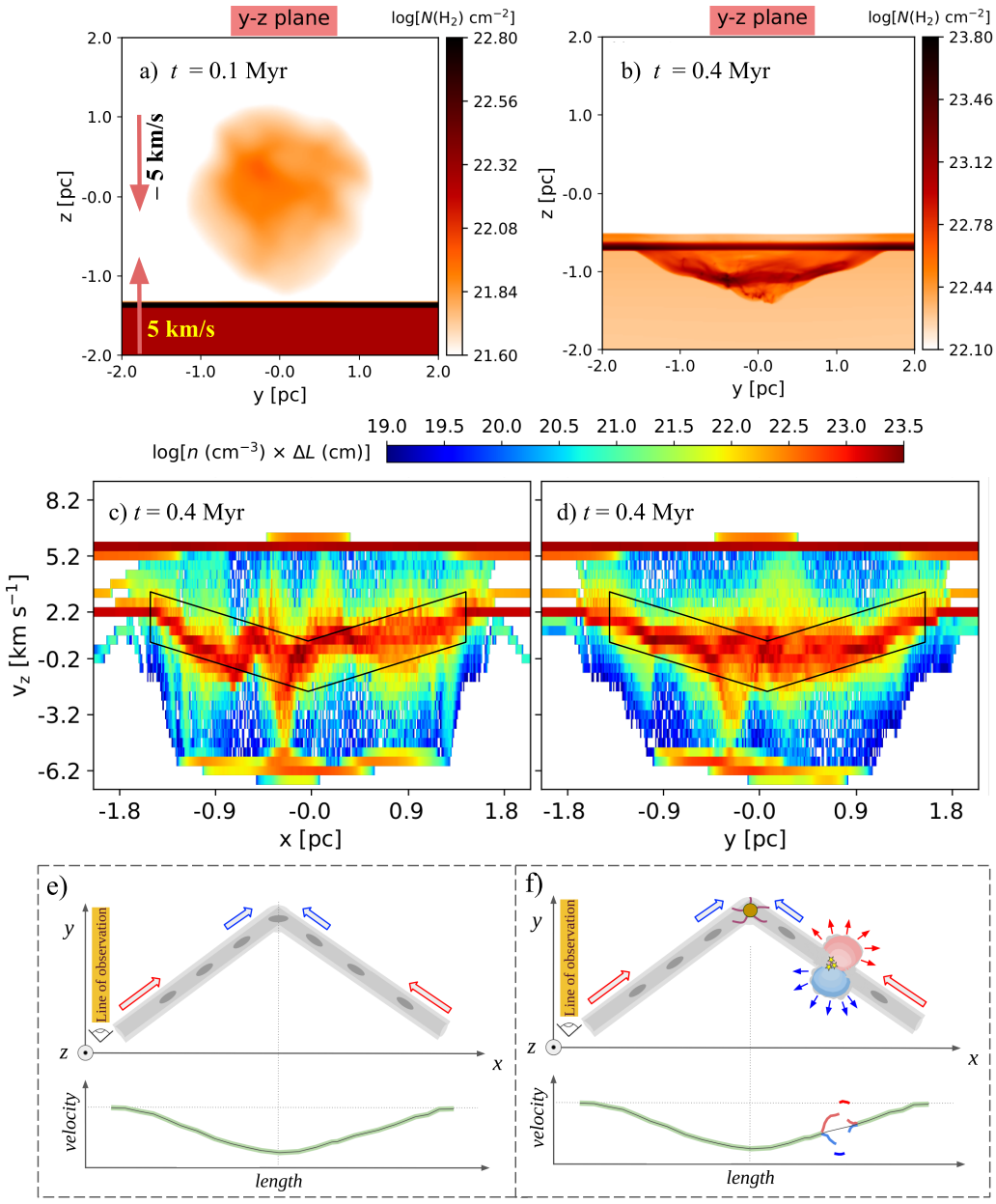

Figure 7.7: (a) The $N(H_2)$ map in the y–z plane at 0.1 Myr, showing the collision of a turbulent molecular cloud (radius = 1.5 pc) and a sea of dense gas moving with a relative velocity of 10 km s^{-1} along the z-direction. (b) The $N(H_2)$ map in the y–z plane at 0.4 Myr. Panels (c) and (d) present the PV diagrams along the x- and y-axis, respectively, for a width of 0.4 pc. The area enclosed by the black lines indicates the velocity of the compressed gas. These figures are taken from Maity et al. (2024). The schematic diagrams in panels (e) and (f) depict the initial and current configurations of our target filament in position and velocity space, respectively. The current configuration shows the presence of a HFS at the center of the filament, bubble N59-North, and its role in creating blue- and red-shifted velocity components. Stars indicate the presence of radio continuum sources toward N59-North. Similar to Figure 7.6, the x–z plane represents the plane of the sky, while the y-direction corresponds to the line of observation. The blue and red arrows represent the blue- and red-shifted velocity components in the filament. Note that the schematic figures are not to scale.

at the edge of this H II region in the velocity range of the filament. Therefore, the H II region is possibly not associated with the filament.

7.4.3 The review of CCC scenario toward N59-North

As mentioned in Section 7.1, a CCC event was reported toward this target site by Chen et al. (2024). They proposed a collision of two cloud components with velocities of [65, 79] and [95, 108] km s^{-1}, having a relative velocity of about 24 km s^{-1}. We found different distances for the ATLASGAL clumps with the velocity ranges [72, 83] and [98, 109] km s^{-1}. The distribution of the ATLASGAL clumps according to their velocities and distances is shown using different symbols in Figure 7.8b. It is important to note that, the histogram of the Galactic CCC events based on their collision velocities shows that the number of CCC events decreases above 5 km s^{-1} and collision with a relative velocity of 24 km s^{-1} is extremely rare (Fukui et al., 2021a). In addition, the origin of the entire filament hosting N59-North is not established based on the collision of the above-mentioned velocity components. Therefore, considering all these points, it is unlikely that the collision of velocity components [65, 79] and [95, 108] km s^{-1} is responsible for the formation of the filament hosting N59-North and its massive star-forming activity.

We can enhance the understanding of the possible CCC event at this target site based on the results of our study presented in Chapter 6. No clear signature of two velocity components is observed in the range [95, 108] km s^{-1} (see Figure 7.4) for the entire filament. As detailed in Section 6.4.3, the absence of two velocity components in CCC sites is very much possible as the signature of the two velocity components, and their connection (known as bridge feature; Torii et al., 2011; Fukui et al., 2014, 2015; Dewangan, 2017; Sano et al., 2018; Fujita et al., 2021) remains for a very short period. From the beginning of the collision,

the timescale is limited by the size of the cloud components and their relative velocity. Beyond that timescale, it becomes impossible to separate the individual velocity components. Therefore, the possibility of CCC toward this target site remains; however, the exact determination of the colliding cloud components within the velocity range [95, 108] km s^{-1} is not feasible with our current understanding of CCC. Such analysis would require new methods.

Several studies based on MHD simulations (e.g., Inoue & Fukui, 2013; Inoue et al., 2018; Fukui et al., 2021b), have demonstrated that the formation of high-density filaments is efficient perpendicular to the magnetic field. While in the case of CCC, the filaments can form parallel to the magnetic field, however, they disperse over time Maity et al. (2024). Therefore, high-resolution dust polarization observations will be helpful in examining the magnetic field morphology for the filament hosting N59-North. Interestingly, the formation and distribution of the massive dense cores suitable for MSF depend upon the inhomogeneous density structures of the colliding molecular clouds before the collision. Thus, the massive star-forming activity is not strictly restricted to the vertex part of the cone/central part of the filament only. The possibility of MSF, apart from the central part of the filament, accounts for the formation of stars which are responsible for the bubble N59-North.

7.5 Summary

To understand the physical processes related to MSF, we conducted a multi-wavelength observational investigation for an extended area hosting N59-North. The major outcomes of this study are summarized below.

1. An elongated IRDC (length ∼28 pc) is investigated in the *Spitzer* 8 μm image, which is not reported in the literature. This IRDC hosts bubble

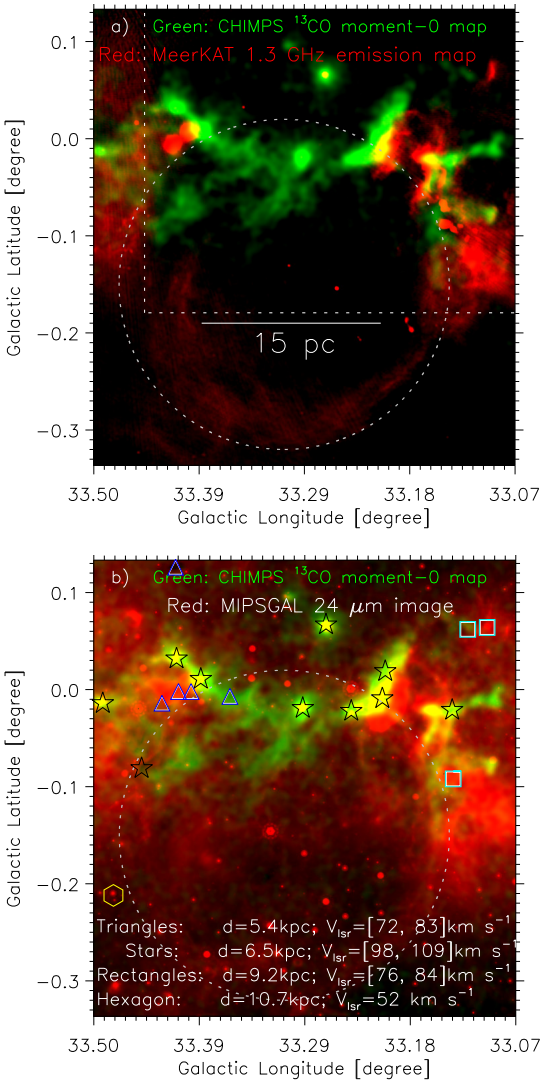

Figure 7.8: (a) A large-scale view of our target site is shown using a two-color composite image. Colors red and green present the MeerKAT 1.3 GHz radio continuum emission and ^{13}CO(J = 3–2) moment-0 map, respectively. The radio continuum emission is displayed on a linear scale from 5σ to 100σ, where 1σ = 20 μJy beam^{-1}. The moment-0 map is shown on a linear scale from 3σ to 30σ, where 1σ = 0.36 K km s^{-1}. The white dotted rectangle indicates the area shown in Figure 7.1a. A scale bar of 15 pc is marked in this panel. (b) This panel presents a similar two-color composite image as panel (a), with red representing the MIPSGAL 24 µm image. The MIPSGAL image is displayed on a logarithmic scale, ranging from 25 to 200 MJy sr^{-1}. The distribution of the ATLASGAL clumps for different velocity ranges and distances is indicated using various symbols, as described in the figure. The extent of a candidate H II region from Anderson et al. (2014) is marked with a dotted circle in each panel.

N59-North, multiple protostars, and seven ATLASGAL dust clumps at the same distance.

2. The GRS ^{13}CO(J = 1–0) and CHIMPS ^{13}CO(J = 3–2) line data confirm the existence of this elongated filamentary structure, which is traced in a velocity range of about [95, 106] km s^{-1}.

3. All ATLASGAL clumps meet the emperical mKP-10 criteria (i.e., $M(R) > 580\ M_{\odot}\ (R/\mathrm{pc})^{1.33}$; Urquhart et al., 2018) for MSF.

4. Using the *Spitzer* 8 μm image, a new C-HFS is investigated toward the ATLASGAL clump located at the central part of the filament. In the direction of C-HFS, we have detected an UC H II region driven by a B2-type star based on MeerKAT 1.3 GHz continuum emission. The lack of extended ionized emission toward C-HFS suggests that it is in the early evolutionary stage with no significant feedback from the young massive star.

5. The study of the observed velocity features in the CHIMPS ^{13}CO(J = 3–2) PV/PPV diagrams toward the filament and the existing theoretical models shows that physical processes such as rotation, central collapse, or EDC are not responsible for the observed gas motion in the filament. Additionally, the comparison of PV/PPV diagrams with the results of MHD simulations (Inoue et al., 2018; Maity et al., 2024) suggests that the filament is possibly conical in shape and exhibits converging gas motion toward its center.

6. The blue- and red-shifted gas velocities observed at the edges of the bubble N59-North in the PPV diagram show an expanding gas motion.

7. The outcomes of this study favor CCC activity in the filament at [95, 106] km s^{-1}, but they contradict previous claims of a collision between the [65, 79] and [95, 108] km s^{-1} components, as they are at different distances.

Although the exact colliding components remain unidentified, comparisons of the outcomes of this study with MHD simulations suggest that CCC contributed to the filament's formation and gas motion.

Taken together all the results, the filament hosting N59-North displays a converging gas motion toward its center, where a pc-scale C-HFS is detected at an early evolutionary stage of HFSs. The converging flow toward C-HFS supports the idea of multi-scale filamentary mass accretion for MSF, likely triggered by CCC.

Chapter 8

Summary and future perspectives

8.1 Summary

This thesis is primarily focused on understanding MSF. To achieve the objectives of this thesis, extensive observational studies were conducted on multiple Galactic MSFRs, including the W31 complex (in Chapter 3), AFGL 5180 & AFGL 6366S (in Chapter 4), G321.93–0.01 (in Chapter 5), and the IRDC associated with the N59-North bubble (in Chapter 7). These regions were carefully selected to cover a range of evolutionary stages and environmental conditions, allowing for a comprehensive analysis of the physical processes governing MSF. Multi-wavelength continuum and molecular line data were utilized to trace H II regions, structures in thermal dust emission, molecular gas distribution & kinematics, and YSOs. In addition to observational investigations, detailed analysis of MHD simulation data were performed to explore the potential link between CCC and the formation of HFSs (in Chapter 6). The simulation data provided valuable insights into the physical mechanisms driving CCC-induced mass accumulation and filament formation, including the interplay of turbulence, magnetic fields, and gravitational forces. Furthermore, the simulations helped assess the

limitations of existing observational CCC signatures, such as the bridge feature and complementary distribution, particularly at higher values of the collision angle ($\theta_{\rm col}$). New diagnostic signatures of CCC are proposed that could be effective in identifying CCC events at higher viewing angles, thereby improving the detectability of this process in real observations. The major outcomes of this thesis work are summarized below:

1. W31 complex hosts two extended H II regions (i.e., W31-N and W31-S) and several Class I protostars and a total of 49 ATLASGAL 870 μm dust clumps (at d ~3.55 kpc). The *Herschel* 250 μm continuum map shows the presence of HFS toward both W31-N and W31-S. The central hubs harbour H II regions and they are depicted with extended structures (with $T_{\rm d} \sim$ 25–32 K) in the *Herschel* dust temperature map. The analysis of the NANTEN2 ^{12}CO(J = 1–0) and SEDIGISM ^{13}CO(J = 2–1) line data toward W31-S supports the presence of two cloud components around 8 and 16 km s^{-1}, and their connection in velocity space. A spatial complementary distribution between the two cloud components is also investigated toward W31-S. These findings favor the applicability of CCC in W31-S. Overall, our observational findings support the theoretical scenario of CCC in W31, which explains the formation of massive stars and the existence of HFS.

2. *Herschel* FIR images reveals a HFS toward AFGL 5180 and AFGL 6366S. These two MSFRs host a Class II 6.7 GHz MME and reside at the opposite edges of an elongated filamentary cloud. Clusters of YSOs are primarily observed toward the edges of the filamentary cloud. The filamentary cloud seems spatially close to the H II region, S247, excited by a massive O9.5 star. To understand the impact of this massive star on AFGL 5180 and AFGL 6366S, we have estimated thermal pressure of the ionized gas of the H II region ($P_{\rm H\ II}$), radiation pressure ($P_{\rm rad}$), and ram pressure of the stellar

wind (P_{wind}). Our analysis indicates that the feedback from the massive star has an insignificant effect on AFGL 5180 and AFGL 6366S. The analysis of MWISP ^{13}CO(J = 1–0) line data suggests the collision of two cloud components at [−3.1, 4.8] and [5.8, 12.9] km s^{-1} about 0.3–0.9 Myr ago to explain the observed massive star-forming activities and HFSs.

3. The SEDIGISM ^{13}CO(J = 2–1) data reveal multiple HFSs, namely, HFS-1, HFS-2, and a candidate HFS toward the molecular cloud G321.93–0.01. HFS-1 and HFS-2 exhibit significantly high mass accretion rates ($\dot{M}_{||} > 10^{-3}$ $M_\odot$ yr^{-1}) to their hubs. Hub-1 is comparatively massive, having higher $\dot{M}_{||}$ than Hub-2. Detection of three compact H II regions within Hub-1 using MeerKAT 1.3 GHz radio continuum data and the presence of a clump, which meets Kauffmann & Pillai's criteria for MSF, confirm the massive star-forming activity in HFS-1. The presence of a compact H II region at the hub of candidate HFS confirms that it is active in MSF. Therefore, HFS-1 and the candidate HFS are in relatively evolved stages of MSF. Conversely, despite a high $\dot{M}_{||}$, the non-detection of radio continuum emission toward Hub-2 suggests it is in the relatively early stages of MSF. Analysis of ^{13}CO data reveals that the formation of HFS-1 was likely triggered by the collision of a filamentary cloud about 0.5–1.5 Myr ago. In contrast, the relative velocities ($\gtrsim$ 1 km s^{-1}) among the filaments of HFS-2 and C-HFS indicate their formation through the merging of filaments.

4. Based on our analysis of the MHD simulation data of CCC from Inoue et al. (2018), we have found that CCC can lead to the formation of HFSs through a three-step process: initially, turbulence creates inhomogeneous density structures in molecular clouds before the collision (e.g., Federrath, 2016; Padoan et al., 2020); next, during the collision, these structures undergo

compression, forming filaments guided by magnetic fields (e.g., Inoue & Fukui, 2013; Inoue et al., 2018); finally, gravity causes the filaments to converge and form an HFS (e.g., Wang et al., 2022). Therefore, the formation of HFSs from CCC is a combined effect of turbulence, shock compression, magnetic fields, and gravity. This study underscores two primary challenges in detecting CCC observationally, aside from the relative motion of clouds along the line of sight. First, distinguishing the two cloud components in PV space becomes difficult after the timescale $t_{\rm col}$. Second, when there is a significant size difference between the cloud components, identifying a slight dip in the emission of the larger cloud to confirm complementary distribution is challenging. After outlining the major challenges in detecting CCC, this study proposes that CCC events at $\theta_{\rm col} = 90^{\circ}$ can be confirmed through their distinct PV diagrams, the distribution of stars/YSOs, and curved magnetic field morphology.

5. The *Spitzer* 8 μm image reveals an elongated IRDC (length $\sim$28 pc) containing the bubble N59-North, several protostars, and seven ATLASGAL dust clumps at same distance. The existence of this filament is confirmed through GRS ^{13}CO(J = 1–0) and CHIMPS ^{13}CO(J = 3–2) data in a velocity range of about [95, 106] km s^{-1}. Using *Spitzer* 8 μm image, a new embedded candidate HFS is investigated toward the filament's central region. MeerKAT 1.3 GHz continuum emission reveals an UC H II region toward candidate HFS driven by a B2-type star, suggesting an early stage of HFS. The PV and PPV diagrams suggest the filament is possibly conical, with gas converging toward its center, where C-HFS is located. The PPV diagram also reveals the expansion of the bubble N59-North through detection of blue- and red-shifted gas velocities. By comparing the results of this study with MHD simulations, we find that CCC may potentially contribute

to the formation of the filament at [95, 106] km s^{-1} and influence its gas motion. However, a collision between the components at [65, 79] and [95, 108] km s^{-1} appears unlikely due to their differing distances, in contrast to earlier claims. These findings support the idea of multi-scale filamentary mass accretion for MSF, likely triggered by CCC.

Overall, our observational investigations of Galactic MSFRs reveal that accretion through filaments in HFSs is an active process of mass accumulation for MSF. Several new HFSs are identified in the early stages of MSF, indicating they are minimally affected by feedback from massive stars. Furthermore, our observations show that multiple HFSs can coexist within a single molecular cloud at different evolutionary stages. Interestingly, we have detected simultaneous signatures of both CCC and HFSs, suggesting that CCC may play a role in HFS formation. Using MHD simulation data, we confirmed that CCC can indeed trigger HFS formation through the combined effects of turbulence, collisional compression, magnetic fields, and gravity. Additionally, this thesis explores the challenges in detecting CCC events observationally and proposes new signatures for identifying CCC at higher viewing angles–an approach that, to our knowledge, is unique in the existing literature. In their recent study, Vázquez-Semadeni et al. (2024b) proposed that CCC and the merging/overlapping of filaments fall under the gravity-driven GHC (Vázquez-Semadeni et al., 2009, 2017, 2019) scenario. However, as shown by Inoue & Fukui (2013) and Inoue et al. (2018), filaments can form in the absence of gravity, where turbulence and shock compression due to collision play a major role. Finally, due to the effect of gravity, the filaments make a common junction to form HFSs. Similarly, the merging of filaments amplifies the mass and density in the overlapping zones, enhancing the gravitational potential and driving gas flow along the filaments (see Kumar et al., 2020). Therefore, gravity plays an evident role in the later stages of evolution for both

scenarios (i.e., CCC and the merging/overlapping of filaments). However, the distinct effects of collisions and merging cannot be ignored.

8.2 Future perspectives

I would like to begin this section with a quote attributed to Albert Einstein: *"As our circle of knowledge expands, so does the circumference of darkness surrounding it."* This sentence succinctly conveys that every advancement in understanding uncovers new challenges, and this thesis is no exception. Therefore, I have outlined a few emerging challenges related to MSF and our future prospects to address them below.

i. **Enhancing our comprehension of the connection between HFS formation and CCC:**

   (a) This thesis has demonstrated that CCC can potentially lead to the formation of HFSs. However, it raises the question: Are all HFSs a result of CCC? To address this, a systematic search for CCC signatures in Galactic HFSs is essential. Such an investigation will be pivotal in uncovering the connection between CCC and the formation of HFSs.

   (b) Our observational investigations show that multiple HFSs can coexist, which cannot be explained by the CCC model described in Chapter 6. This is likely due to the smaller size ($R = 1.5$ pc) of one of the cloud components considered in the simulation. It would be interesting to investigate whether the collision of a relatively larger cloud component ($R >$ 10–50 pc) can explain the origin of multiple HFSs from CCC.

ii. **Investigating mass accretion in MSF and the impact of feedback**

from massive star-forming activity on the surrounding environment:

(a) Since massive stars reach the main sequence while accreting material, further growth of the massive stars relies upon the battle between accretion and their feedback. To understand the connection between mass accretion and feedback in MSF, next, I would like to observationally explore the molecular gas distribution and outflow activity using both ALMA continuum and molecular line observations toward a large number of MSFRs.

(b) The interaction of ionizing photons from newly formed massive stars with the parent filamentary structures is not explored in detail in this thesis. Therefore, based on our uGMRT observations (Proposal Code: 45_115, PI: Arup Kumar Maity), we aim to estimate the rate of advancement of the ionization front, electron density, and the total mass of ionized gas boiled off from the filament based on the model of Whitworth & Priestley (2021). Such studies will enhance our understanding of the evolution of HFSs.

iii. **Investigating the orientation of filaments in the HFS with respect to magnetic field lines:**

(a) Due to unavailability of high-resolution dust polarization data, the potential role of the EDC process in HFS formation toward AFGL 5180 and AFGL 6366S remains inconclusive. Although several proposals (IDs: M23AP032, M24AP059, and M24BP079; PI: Arup Kumar Maity) for JCMT SCUBA-2/POL-2 dust polarization observations were accepted, the observations could not be conducted due to adverse weather conditions. We plan to submit a new proposal to ac-

quire the necessary data. The JCMT dust polarization data will be utilized to explore magnetic field distribution toward AFGL 5180 and AFGL 6366S. It is important to examine the orientation of the filaments associated with the HFS against the magnetic field lines, which will be useful in understanding both the EDC and Wang et al. (2019)'s idea of HFSs formation.

Appendix A

For Chapter 4

A.1 Plane-of-sky magnetic field in our target area

We determined the position angles of the plane-of-sky (POS) magnetic field using the *Planck* 353 GHz Stokes I, Q, and U images. First, we calculated the linear polarization angles (PAs) of dust emission in Galactic coordinates with the conventional formula $\theta_{\rm GAL} = 0.5 \times \arctan2(-{\rm U}, {\rm Q})$. The negative sign in U adheres to the IAU convention (for further details, see Planck Collaboration et al., 2015), and we utilized the two-argument function arctan2 to prevent π-ambiguity in PA estimation. The magnetic field orientations, denoted as $\rm B_{Gal}$, were obtained by adding 90° to the electric field PAs (e.g., Planck Collaboration et al., 2016a,b). $\rm B_{Gal}$ is measured from the Galactic north in an anticlockwise direction (i.e., toward the east).

The *Planck* 353 GHz image for our target region is shown in Figure A.1a. The POS magnetic field distribution is illustrated by the overlaid pseudo-vectors in Figure A.1a. The orientation of the magnetic field is almost perpendicular to the

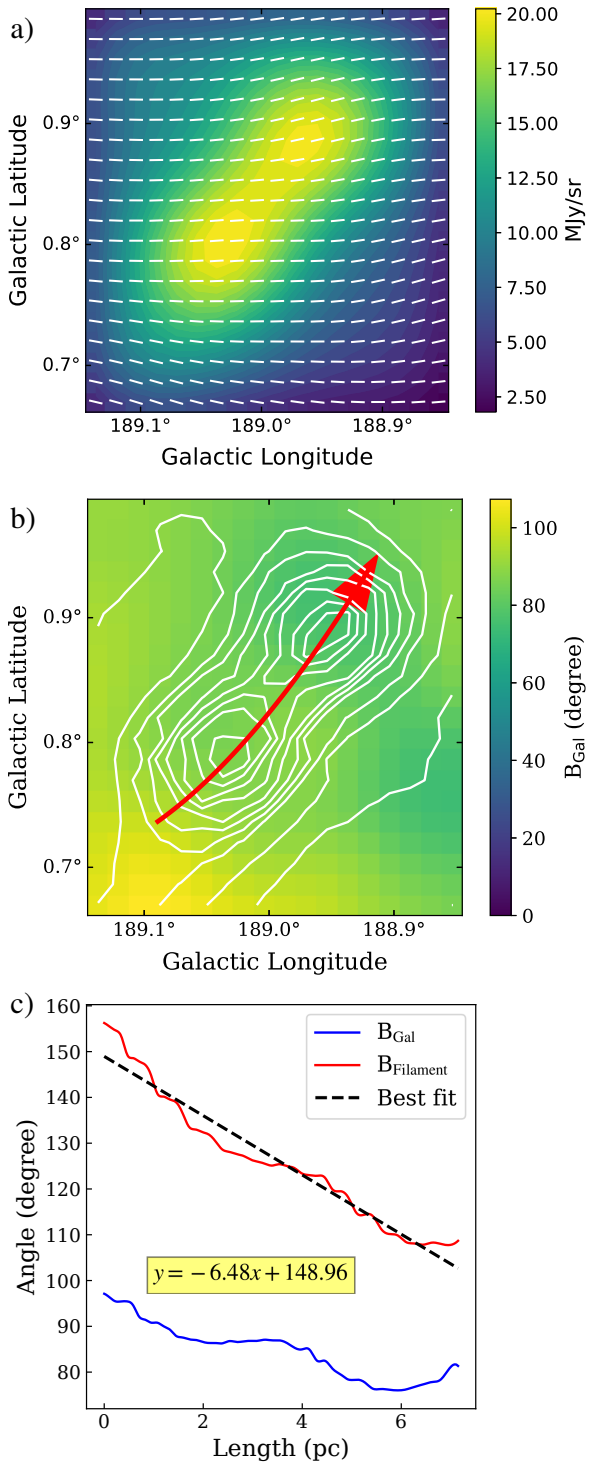

Figure A.1: (a) The *Planck* 353 GHz map is overlaid with the POS magnetic field pseudo-vectors of our target area highlighted by the white dotted rectangle in Figure 4.9a. (b) The spatial distribution of the POS magnetic field position angle (B_{Gal}). The overlaid contours indicate the *Planck* 353 GHz intensity ranging from 4.6 to 27.6 MJy sr^{-1} in linear order. (c) The distributions of B_{Gal} and $B_{Filament}$ along the red curved arrow shown in panel (b). $B_{Filament}$ represents the magnetic field position angle relative to the major axis of the filament (additional details can be found in Appendix A.1). A best-fit line is displayed and labeled for the $B_{Filament}$ distribution.

filament, aligning with findings from other studies (e.g., Palmeirim et al., 2013; Planck Collaboration et al., 2016c; Cox et al., 2016b). Figure A.1b presents the spatial distribution of B_{Gal}. We analyzed how the magnetic field's position angle varies with respect to the filament's major axis (i.e., $B_{Filament}$). The variation of B_{Gal} and $B_{Filament}$ toward our target area is shown in Figure A.1c. A linear trend in $B_{Filament}$ along the filament's primary axis suggests longitudinal mass flow from the edges toward the central part (Dewangan et al., 2023b). However, new high-resolution data on dust polarization in our target region could provide further insights into the influence of the magnetic field on the observed structure.

A.2 A zoomed-in view of the MSFR AFGL 5180

The high-resolution NIR images from UKIDSS and HST allow us to examine the rectangular area highlighted in Figure 4.4b toward AFGL 5180 (T1). In Figure A.2a, we display a two-color composite image that combines the UKIDSS K band image in red with the HST F160W band image in cyan. This image is overlaid with NVAS 8.46 GHz radio continuum emission contours in green, highlighting three compact radio sources in the vicinity of AFGL 5180. In the direction of AFGL 5180 one of the radio continuum sources is exclusively associated with the Class II 6.7 GHz MME and one of them (at the top) spatially coexists with a B4V–B8V type star (Vasyunina, 2010).

Following the method outlined by Long et al. (2020), we produced the continuum-subtracted [Fe II] image at 1.64 μm using the HST images from F164N and F160W bands. The [Fe II] emissions in star-forming regions arise from shock-excited material due to outflows and jets Fedriani et al. (2019). We present the continuum-subtracted [Fe II] emission in the direction of AFGL 5180 using red contours over the HST F110W band image in Figure A.2b. Interestingly, NVAS

8.46 GHz radio continuum emission and 6.7 GHz MME are detected at the center of the bipolar outflow morphology.

The area highlighted by the cyan box in Figure A.2b is further zoomed-in using the ALMA 1.3 mm dust continuum emission as shown in Figure A.2c, which has a resolution of about $0''.18 \times 0''.28$. In this figure, the existence of at least two cores (i.e., core-1 and core-2) is evident. The cyan arrow points to an extended area of dust emission surrounding one of these cores, while the pink arrows indicate the candidate cores located along the line connecting the primary cores. Using Equation 2.15, we calculated the masses of the core-1 and core-2 to be about 5.4 $M_{\odot}$ and 1.3 $M_{\odot}$, respectively. We selected a 6σ contour to determine the total flux density using the *clumpfind* tool. The source's distance and temperature are taken as 1.5 kpc and 25 K, respectively, with a gas-to-dust ratio of 100 and an opacity value of 0.33 cm^2 g^{-1} (Weingartner & Draine, 2001b; Mutie et al., 2021). The core-1 and core-2 identified in the ALMA 1.3 mm continuum emission map (resolution $\sim 0''.18 \times 0''.28$) are illustrated in Figure A.2d. In this figure, we have also included the contours of the 1.3 mm continuum emission in red (resolution $\sim 0''.63 \times 1''.23$), alongside the NVAS 8.46 GHz radio continuum emission contours in black and the location of the 6.7 GHz MME. It can be observed in Figure A.2d that core-1 is associated with both the 6.7 GHz MME and the radio continuum emission. Core-1 is connected to core-2 by dust emission, which spans less than 5000 AU, creating a dumbbell-like shape at this small scale. This configuration is traced within the central hub of the HFS in AFGL 5180. Notably, there is no radio continuum emission detected toward core-2.

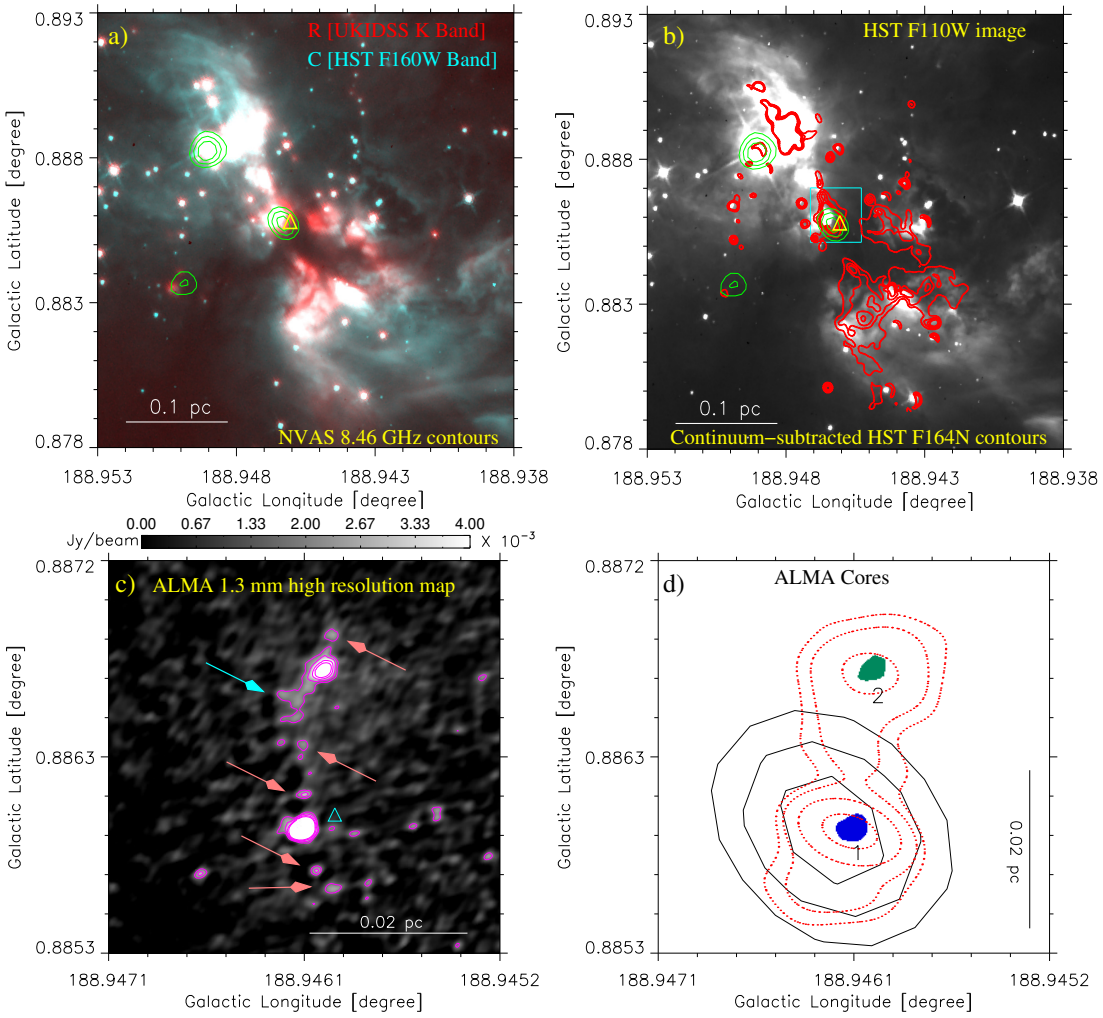

Figure A.2: (a) A zoomed-in view of AFGL 5180 (for the rectangular region indicated in Figure 4.4b) is displayed using a two-color composite image (red: UKIDSS K-band image + cyan: HST F160W band image). The NVAS 8.46 GHz radio continuum emission contours are overlaid on the color composite image. (b) This panel shows the HST F110W band image overlaid with the continuum-subtracted [Fe II] emission contours (at 1.64 μm; in red) and the NVAS 8.46 GHz radio continuum emission contours (in green) overlaid. (c) The panel presents the ALMA 1.3 mm dust continuum map (resolution $\sim$0$''$.18 $\times$ 0$''$.28) for an area highlighted by a rectangle in Figure A.2b. The contours are shown at values 4σ, 6σ, 9σ and 12σ, where 1σ = 0.45 mJy beam^{-1}. The arrows indicate possible low-mass cores and an envelope-like feature (see Appendix A.2 for more details). (d) The panel shows the positions of two cores (i.e., 1 and 2) detected in the ALMA 1.3 mm dust continuum map (resolution $\sim$0$''$.18 $\times$ 0$''$.28). The NVAS 8.46 GHz radio continuum emission contours are also plotted in black. The dotted contours in red show the 1.3 mm dust continuum emission (resolution $\sim$0$''$.63 $\times$ 1$''$.23) with the levels of 8, 14, 20, 26, and 32 mJy beam^{-1}. In panels (a), (b), and (c), the triangle indicates the position of the 6.7 GHz MME, and the radio continuum contours are plotted with the levels of 120, 160, and 200 μJy beam^{-1}, where 1σ = 36.8 μJy beam^{-1}. A scale bar of 0.1 pc and 0.02 pc is shown in panels (a, b) and (c, d), respectively.

Appendix B

For Chapter 5

B.1 The optical depth and column density maps

The τ_{13} and $N(H_2)$ map maps produced from SEDIGISM ^{13}CO/C^{13}O (J =2–1) data are shown in Figures B.1a and B.1b, respectively.

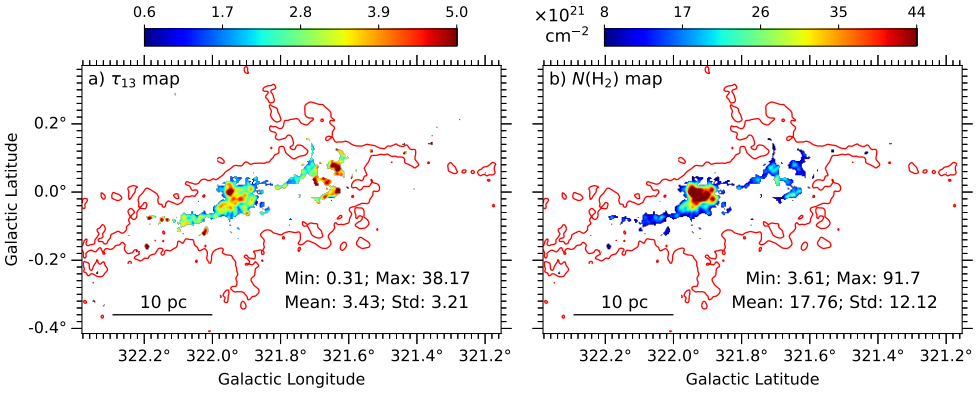

Figure B.1: (a) The optical depth (i.e., τ_{13}) map. The minimum (Min), maximum (Max), mean, and standard deviation (Std) values for the τ_{13} map are provided in the panel. (b) The column density (i.e., $N(H_2)$) map for T_{ex} = 15 K. The Min, Max, mean, and Std values for the $N(H_2)$ map are indicated in the panel in units of 10^{21} cm^{-2}. In both panels, the red contour indicates the extent of the ^{13}CO emission above the 3σ limit, as shown in Figure 5.2. A scale bar of 10 pc is displayed in each panel.

B.2 The estimation of the dynamical age of the H II regions

The dynamical age of the H II regions, which are assumed to be expanding in a uniform medium, can be estimated using the formula from Dyson & Williams (1997):

$$t_{\rm dyn} = \frac{4R_{\rm s}}{7c_{\rm s}} \left[\left(\frac{R_{\rm HII}}{R_{\rm s}} \right)^{7/4} - 1 \right], \tag{B.1}$$

where $c_{\rm s}$ ($\sim$10 km s^{-1}; Bisbas et al., 2009) is the sound speed in the ionized region. $R_{\rm HII}$ is the effective radius of the H II region, which was calculated based on their area above 5σ in the MeerKAT 1.28 GHz radio continuum data (see Figure 5.1c). The $R_{\rm HII}$ value for each H II region is listed in Table 5.2. $R_{\rm s}$ is the Strömgren radius, given by $R_{\rm s} = (3N_{\rm uv}/4\pi n_{\rm i}^2 \alpha_{\rm B})^{1/3}$, where $N_{\rm uv}$ is the number of photons emitted by the ionizing source beyond the Lyman limit, $n_{\rm i}$ is the initial H number density, and $\alpha_{\rm B}$ ($\sim 2.6\times10^{-13}$ cm^3 s^{-1}; Kwan, 1997) is the recombination coefficient. We used $n_{\rm i} = 10^4$ cm^{-3} based on the average H_2 density for the ATLASGAL leaves (see Table 5.4). We calculated $N_{\rm uv}$ using the formula (Matsakis et al., 1976):

$$N_{\rm uv}\ [s^{-1}] = 7.54 \times 10^{46} \left(\frac{\nu}{\rm GHz} \right)^{0.1} \left(\frac{T_{\rm eff}}{10^4\,\rm K} \right)^{-0.45} \left(\frac{S_\nu}{\rm Jy} \right) \left(\frac{d}{\rm kpc} \right)^2, \tag{B.2}$$

where, $\nu = 1.28$ GHz, $d = 1.98$ kpc, $T_{\rm eff}$ is the effective electron temperature (assumed to be 10^4 K), S_ν is the total flux density for the H II regions. Our calculated S_ν (above $> 5\sigma$) and corresponding $\log(N_{\rm uv}\ [s^{-1}])$ values are included in Table 5.2. Finally, using all the input parameters in Equation B.1, we estimated the dynamical time scale for the H II regions and listed in Table 5.2.

Appendix C

For Chapter 6

C.1 The $\triangle$PA distributions for t = 0.3 to 0.6 Myr

Normalized histograms of the relative orientations among the filament skeleton, projected magnetic field, gas velocity, and gravitational field vectors at t = 0.3 to 0.6 Myr are shown in Figure C.1.

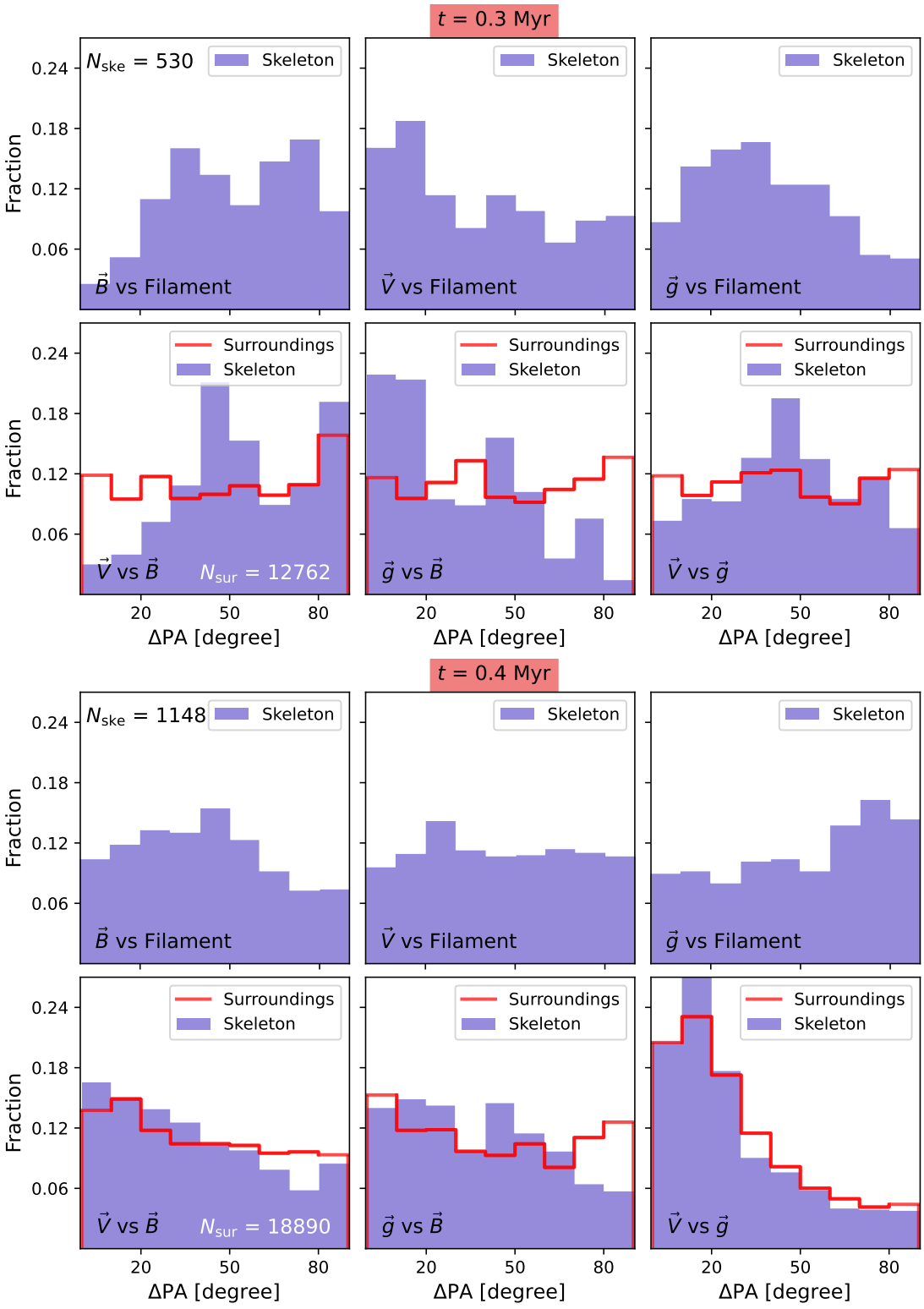

Figure C.1: Continued.

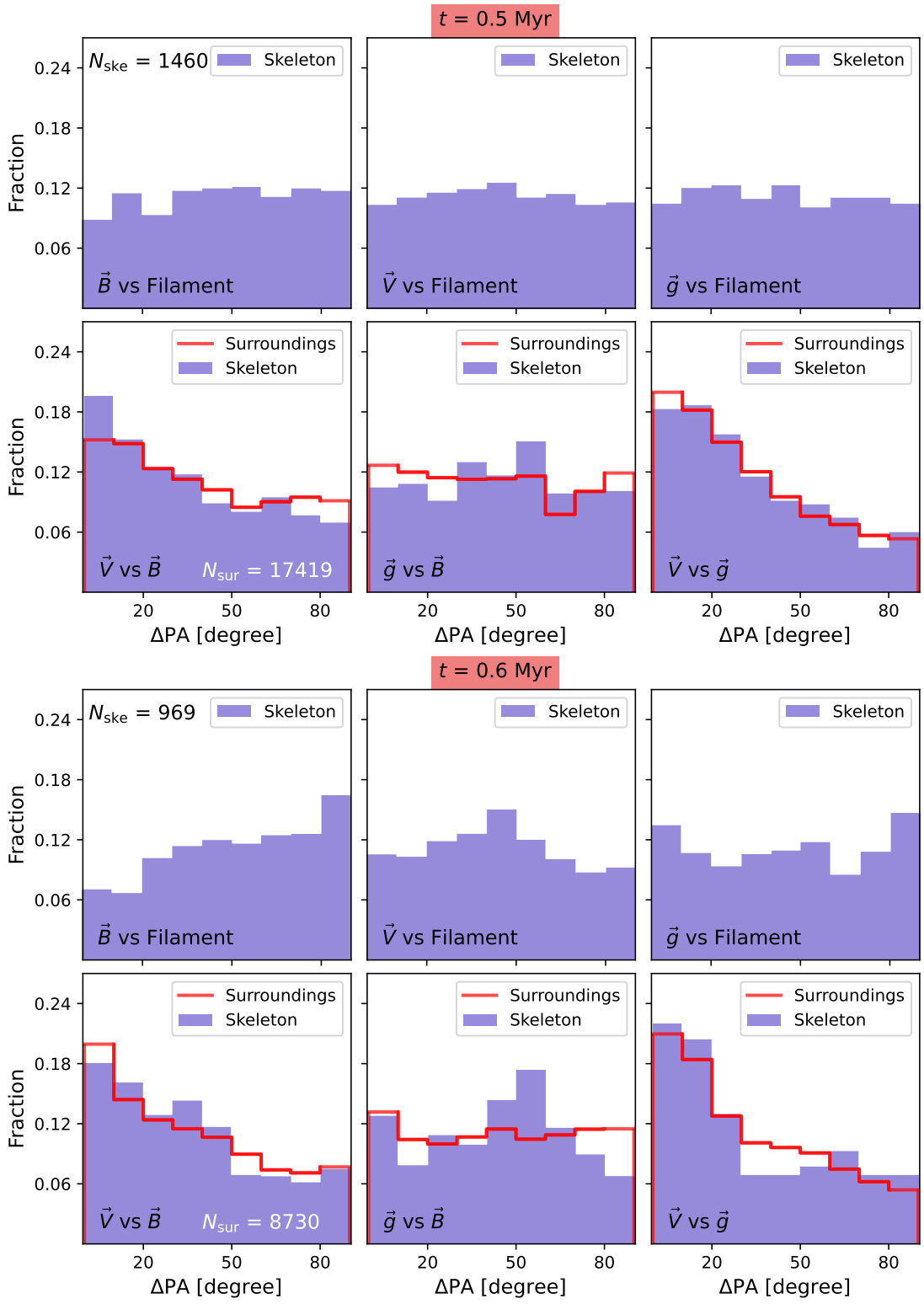

Figure C.1: Same as Figure 6.10, but for t = 0.3 to 0.6 Myr, respectively.

Bibliography

Abe, D., Inoue, T., Inutsuka, S.-i., & Matsumoto, T. 2021, ApJ, 916, 83, doi: 10.3847/1538-4357/ac07a1 [Cited on page 190.]

Allamandola, L. J., Tielens, A. G. G. M., & Barker, J. R. 1989, ApJS, 71, 733, doi: 10.1086/191396 [Cited on page 94.]

Anathpindika, S. V. 2010, MNRAS, 405, 1431, doi: 10.1111/j.1365-2966.2010.16541.x [Cited on page 20.]

Anderson, L. D., & Bania, T. M. 2009, ApJ, 690, 706, doi: 10.1088/0004-637X/690/1/706 [Cited on page 204.]

Anderson, L. D., Bania, T. M., Balser, D. S., et al. 2014, ApJS, 212, 1, doi: 10.1088/0067-0049/212/1/1 [Cited 2 times on pages 222 and 226.]

Anderson, M., Peretto, N., Ragan, S. E., et al. 2021, MNRAS, 508, 2964, doi: 10.1093/mnras/stab2674 [Cited on page 119.]

André, P. 2015, in Encyclopedia of Astrobiology, ed. M. Gargaud, W. M. Irvine, R. Amils, H. J. J. Cleaves, II, D. L. Pinti, J. C. Quintanilla, D. Rouan, T. Spohn, S. Tirard, & M. Viso, 2308–2313, doi: 10.1007/978-3-662-44185-5_504 [Cited on page 10.]

André, P., Men'shchikov, A., Bontemps, S., et al. 2010, A&A, 518, L102, doi: 10.1051/0004-6361/201014666 [Cited 4 times on pages 3, 17, 71, and 113.]

Arce, H. G., Shepherd, D., Gueth, F., et al. 2007, in Protostars and Planets V, ed. B. Reipurth, D. Jewitt, & K. Keil, 245, doi: 10.48550/arXiv.astro-ph/0603071 [Cited on page 15.]

Areal, M. B., Paron, S., Celis Peña, M., & Ortega, M. E. 2018, A&A, 612, A117, doi: 10.1051/0004-6361/201732067 [Cited on page 132.]

Arreaga-García, G., Klapp, J., & Morales, J. S. 2014, International Journal of Astronomy and Astrophysics, 4, 192, doi: 10.4236/ijaa.2014.41018 [Cited on page 189.]

Arzoumanian, D., André, P., Didelon, P., et al. 2011, A&A, 529, L6, doi: 10.1051/0004-6361/201116596 [Cited on page 189.]

Arzoumanian, D., Furuya, R. S., Hasegawa, T., et al. 2021, A&A, 647, A78, doi: 10.1051/0004-6361/202038624 [Cited 2 times on pages 115 and 116.]

Auddy, S., Basu, S., & Kudoh, T. 2018, MNRAS, 474, 400, doi: 10.1093/mnras/stx2740 [Cited on page 166.]

Balfour, S. K., Whitworth, A. P., & Hubber, D. A. 2017, MNRAS, 465, 3483, doi: 10.1093/mnras/stw2956 [Cited 7 times on pages 20, 28, 78, 160, 189, 192, and 201.]

Balfour, S. K., Whitworth, A. P., Hubber, D. A., & Jaffa, S. E. 2015, MNRAS, 453, 2471, doi: 10.1093/mnras/stv1772 [Cited 6 times on pages 28, 78, 114, 160, 189, and 192.]

Bally, J., Langer, W. D., Stark, A. A., & Wilson, R. W. 1987, ApJL, 312, L45, doi: 10.1086/184817 [Cited 2 times on pages 17 and 148.]

Barnes, A. T., Henshaw, J. D., Fontani, F., et al. 2021, MNRAS, 503, 4601, doi: 10.1093/mnras/stab803 [Cited on page 141.]

Bartkiewicz, A., & van Langevelde, H. J. 2012, in IAU Symposium, Vol. 287, Cosmic Masers - from OH to H0, ed. R. S. Booth, W. H. T. Vlemmings, & E. M. L. Humphreys, 117–126, doi: 10.1017/S1743921312006771 [Cited on page 38.]

Bastien, P. 1983, A&A, 119, 109 [Cited 2 times on pages 18 and 115.]

Basu, S. 1998, The Astrophysical Journal, 509, 229, doi: 10.1086/306494 [Cited on page 7.]

Baug, T., Dewangan, L. K., Ojha, D. K., & Ninan, J. P. 2016, ApJ, 833, 85, doi: 10.3847/1538-4357/833/1/85 [Cited on page 188.]

Beltrán, M. T., Rivilla, V. M., Kumar, M. S. N., Cesaroni, R., & Galli, D. 2022, A&A, 660, L4, doi: 10.1051/0004-6361/202243361 [Cited on page 78.]

Benjamin, R. A., Churchwell, E., Babler, B. L., et al. 2003, PASP, 115, 953, doi: 10.1086/376696 [Cited 4 times on pages 40, 58, 123, and 206.]

Bertoldi, F. 1989, ApJ, 346, 735, doi: 10.1086/168055 [Cited on page 110.]

Beuther, H., Kuiper, R., & Tafalla, M. 2025, arXiv e-prints, arXiv:2501.16866, doi: 10.48550/arXiv.2501.16866 [Cited on page 9.]

Beuther, H., Ragan, S. E., Johnston, K., et al. 2015, A&A, 584, A67, doi: 10.1051/0004-6361/201527108 [Cited on page 148.]

Beuther, H., Schilke, P., Menten, K. M., et al. 2002, ApJ, 566, 945, doi: 10.1086/338334 [Cited on page 151.]

Beuther, H., Linz, H., Henning, T., et al. 2011, A&A, 531, A26, doi: 10.1051/0004-6361/201116686 [Cited 4 times on pages 30, 56, 76, and 78.]

Bhadari, N. K., Dewangan, L. K., Ojha, D. K., Pirogov, L. E., & Maity, A. K. 2022, ApJ, 930, 169, doi: 10.3847/1538-4357/ac65e9 [Cited 6 times on pages 17, 18, 23, 115, 116, and 129.]

Bhadari, N. K., Dewangan, L. K., Pirogov, L. E., & Ojha, D. K. 2020, ApJ, 899, 167, doi: 10.3847/1538-4357/aba2c6 [Cited 3 times on pages 18, 93, and 115.]

Bhadari, N. K., Dewangan, L. K., Pirogov, L. E., et al. 2023, MNRAS, 526, 4402, doi: 10.1093/mnras/stad2981 [Cited on page 139.]

Bhadari, N. K., Dewangan, L. K., Zemlyanukha, P. M., et al. 2021, ApJ, 922, 207, doi: 10.3847/1538-4357/ac2a44 [Cited on page 96.]

Bhadari, N. K., Dewangan, L. K., Jadhav, O. R., et al. 2025, A&A, 694, L18, doi: 10.1051/0004-6361/202452189 [Cited 3 times on pages 211, 219, and 220.]

Bik, A., Kaper, L., Hanson, M. M., & Smits, M. 2005, A&A, 440, 121, doi: 10.1051/0004-6361:20042597 [Cited 3 times on pages 56, 76, and 82.]

Bisbas, T. G., Wünsch, R., Whitworth, A. P., & Hubber, D. A. 2009, A&A, 497, 649, doi: 10.1051/0004-6361/200811522 [Cited 3 times on pages 91, 219, and 244.]

Blum, R. D., Damineli, A., & Conti, P. S. 2001, AJ, 121, 3149, doi: 10.1086/321088 [Cited 4 times on pages 30, 56, 75, and 76.]

Bock, D. C. J., Large, M. I., & Sadler, E. M. 1999, AJ, 117, 1578, doi: 10.1086/300786 [Cited 4 times on pages 40, 121, 122, and 123.]

Bonnell, I. A., Bate, M. R., Clarke, C. J., & Pringle, J. E. 2001, MNRAS, 323, 785, doi: 10.1046/j.1365-8711.2001.04270.x [Cited on page 15.]

Bonnell, I. A., Vine, S. G., & Bate, M. R. 2004, MNRAS, 349, 735, doi: 10.1111/j.1365-2966.2004.07543.x [Cited on page 15.]

Breen, S. L., Ellingsen, S. P., Contreras, Y., et al. 2013, MNRAS, 435, 524, doi: 10.1093/mnras/stt1315 [Cited on page 82.]

Bressert, E., Ginsburg, A., Bally, J., et al. 2012, ApJL, 758, L28, doi: 10.1088/2041-8205/758/2/L28 [Cited on page 90.]

Bressert, E., Bastian, N., Gutermuth, R., et al. 2010, MNRAS, 409, L54, doi: 10.1111/j.1745-3933.2010.00946.x [Cited on page 93.]

Burkhart, B., Lazarian, A., Goodman, A., & Rosolowsky, E. 2013, ApJ, 770, 141, doi: 10.1088/0004-637X/770/2/141 [Cited on page 50.]

Busquet, G., Zhang, Q., Palau, A., et al. 2013, ApJL, 764, L26, doi: 10.1088/2041-8205/764/2/L26 [Cited on page 18.]

Cai, M. J., Shang, H., Lin, H.-H., & Shu, F. H. 2008, ApJ, 672, 489, doi: 10.1086/523788 [Cited on page 7.]

Carey, S. J., Noriega-Crespo, A., Mizuno, D. R., et al. 2009in , 76–97, doi: 10.1086/596581 [Cited 2 times on pages 40 and 206.]

Carpenter, J. M., Snell, R. L., & Schloerb, F. P. 1995a, ApJ, 445, 246, doi: 10.1086/175692 [Cited on page 83.]

—. 1995b, ApJ, 450, 201, doi: 10.1086/176132 [Cited on page 83.]

Casali, M., Adamson, A., Alves de Oliveira, C., et al. 2007, A&A, 467, 777, doi: 10.1051/0004-6361:20066514 [Cited on page 84.]

Casertano, S., & Hut, P. 1985, ApJ, 298, 80, doi: 10.1086/163589 [Cited on page 93.]

Caswell, J. L., Vaile, R. A., Ellingsen, S. P., Whiteoak, J. B., & Norris, R. P. 1995, MNRAS, 272, 96, doi: 10.1093/mnras/272.1.96 [Cited 2 times on pages 12 and 82.]

Cesaroni, R., Felli, M., Jenness, T., et al. 1999, A&A, 345, 949 [Cited on page 15.]

Chen, E., Chen, X., Chen, X., Fang, M., & He, Q. 2024, MNRAS, 535, 419, doi: 10.1093/mnras/stae2394 [Cited 5 times on pages 31, 203, 204, 219, and 224.]

Chen, H.-R. V., Zhang, Q., Wright, M. C. H., et al. 2019, ApJ, 875, 24, doi: 10.3847/1538-4357/ab0f3e [Cited 2 times on pages 21 and 51.]

Chen, X., Ellingsen, S. P., Shen, Z.-Q., Titmarsh, A., & Gan, C.-G. 2011, ApJS, 196, 9, doi: 10.1088/0067-0049/196/1/9 [Cited on page 121.]

Chen, Z., Nürnberger, D. E. A., Chini, R., Jiang, Z., & Fang, M. 2015, A&A, 578, A82, doi: 10.1051/0004-6361/201424895 [Cited on page 94.]

Chung, E. J., Lee, C. W., Kwon, W., et al. 2022, arXiv e-prints, arXiv:2208.07891. https://arxiv.org/abs/2208.07891 [Cited on page 115.]

Churchwell, E. 1999, in NATO Advanced Study Institute (ASI) Series C, Vol. 540, The Origin of Stars and Planetary Systems, ed. C. J. Lada & N. D. Kylafis, 515. https://www.cfa.harvard.edu/research/rg/massive-star-formation [Cited on page 11.]

Churchwell, E. 2002, ARA&A, 40, 27, doi: 10.1146/annurev.astro.40.060401.093845 [Cited 2 times on pages 13 and 38.]

Churchwell, E., Povich, M. S., Allen, D., et al. 2006, ApJ, 649, 759, doi: 10.1086/507015 [Cited on page 203.]

Clarke, S. D., & Whitworth, A. P. 2015, MNRAS, 449, 1819, doi: 10.1093/mnras/stv393 [Cited 3 times on pages 115, 220, and 221.]

Clarke, S. D., Williams, G. M., & Walch, S. 2020, MNRAS, 497, 4390, doi: 10.1093/mnras/staa2298 [Cited on page 113.]

Condon, J. J., Cotton, W. D., Greisen, E. W., et al. 1998, AJ, 115, 1693, doi: 10.1086/300337 [Cited 3 times on pages 40, 58, and 86.]

Condon, J. J., & Ransom, S. M. 2016, Essential Radio Astronomy [Cited on page 38.]

Corbel, S., Wallyn, P., Dame, T. M., et al. 1997, ApJ, 478, 624, doi: 10.1086/303807 [Cited on page 56.]

Cox, N. L. J., Arzoumanian, D., André, P., et al. 2016a, A&A, 590, A110, doi: 10.1051/0004-6361/201527068 [Cited 2 times on pages 177 and 182.]

—. 2016b, A&A, 590, A110, doi: 10.1051/0004-6361/201527068 [Cited on page 239.]

Cragg, D. M., Sobolev, A. M., & Godfrey, P. D. 2005, MNRAS, 360, 533, doi: 10.1111/j.1365-2966.2005.09077.x [Cited on page 12.]

Crossley, J. H., Sjouwerman, L. O., Fomalont, E. B., & Radziwill, N. M. 2007, in American Astronomical Society Meeting Abstracts, Vol. 211, American Astronomical Society Meeting Abstracts, 132.03 [Cited on page 40.]

Crutcher, R. M. 2012, ARA&A, 50, 29, doi: 10.1146/annurev-astro-081811-125514 [Cited on page 4.]

Csengeri, T., Belloche, A., Bontemps, S., et al. 2019, A&A, 632, A57, doi: 10.1051/0004-6361/201935226 [Cited 2 times on pages 11 and 12.]

Dale, J. E., Bonnell, I. A., & Whitworth, A. P. 2007, MNRAS, 375, 1291, doi: 10.1111/j.1365-2966.2006.11368.x [Cited 2 times on pages 110 and 111.]

Dale, J. E., Haworth, T. J., & Bressert, E. 2015, MNRAS, 450, 1199, doi: 10.1093/mnras/stv396 [Cited on page 111.]

Dale, J. E., Ngoumou, J., Ercolano, B., & Bonnell, I. A. 2014, MNRAS, 442, 694, doi: 10.1093/mnras/stu816 [Cited on page 120.]

Davis, C. J., Moriarty-Schieven, G., Eislöffel, J., Hoare, M. G., & Ray, T. P. 1998, AJ, 115, 1118, doi: 10.1086/300259 [Cited on page 82.]

Deharveng, L., Zavagno, A., & Caplan, J. 2005, A&A, 433, 565, doi: 10.1051/0004-6361:20041946 [Cited on page 110.]

Deharveng, L., Schuller, F., Anderson, L. D., et al. 2010, A&A, 523, A6, doi: 10.1051/0004-6361/201014422 [Cited 2 times on pages 203 and 204.]

Devine, K. E., Churchwell, E. B., Indebetouw, R., Watson, C., & Crawford, S. M. 2008, AJ, 135, 2095, doi: 10.1088/0004-6256/135/6/2095 [Cited 4 times on pages 31, 82, 83, and 114.]

Dewangan, L. K. 2017, ApJ, 837, 44, doi: 10.3847/1538-4357/aa5df2 [Cited 3 times on pages 25, 74, and 224.]

—. 2022, MNRAS, 513, 2942, doi: 10.1093/mnras/stac967 [Cited 2 times on pages 17 and 78.]

Dewangan, L. K., Baug, T., Ojha, D. K., & Ghosh, S. K. 2018a, ApJ, 869, 30, doi: 10.3847/1538-4357/aae9db [Cited on page 130.]

Dewangan, L. K., Bhadari, N. K., Maity, A. K., et al. 2024, MNRAS, 527, 5895, doi: 10.1093/mnras/stad3384 [Cited 5 times on pages 119, 129, 149, 191, and 211.]

—. 2023a, Journal of Astrophysics and Astronomy, 44, 23, doi: 10.1007/s12036-022-09907-7 [Cited 4 times on pages 18, 19, 112, and 191.]

Dewangan, L. K., Bhadari, N. K., Men'shchikov, A., et al. 2023b, ApJ, 946, 22, doi: 10.3847/1538-4357/acbccc [Cited 4 times on pages 115, 129, 177, and 239.]

Dewangan, L. K., Dhanya, J. S., Ojha, D. K., & Zinchenko, I. 2018b, ApJ, 866, 20, doi: 10.3847/1538-4357/aadfe3 [Cited on page 74.]

Dewangan, L. K., & Ojha, D. K. 2017, ApJ, 849, 65, doi: 10.3847/1538-4357/aa8e00 [Cited 2 times on pages 25 and 74.]

Dewangan, L. K., Ojha, D. K., & Baug, T. 2017a, ApJ, 844, 15, doi: 10.3847/1538-4357/aa79a5 [Cited 2 times on pages 18 and 19.]

Dewangan, L. K., Ojha, D. K., Grave, J. M. C., & Mallick, K. K. 2015, MNRAS, 446, 2640, doi: 10.1093/mnras/stu2234 [Cited 3 times on pages 56, 76, and 78.]

Dewangan, L. K., Ojha, D. K., Sharma, S., et al. 2020a, ApJ, 903, 13, doi: 10.3847/1538-4357/abb827 [Cited on page 19.]

Dewangan, L. K., Ojha, D. K., Zinchenko, I., & Baug, T. 2018c, ApJ, 861, 19, doi: 10.3847/1538-4357/aac6bb [Cited on page 188.]

Dewangan, L. K., Ojha, D. K., Zinchenko, I., Janardhan, P., & Luna, A. 2017b, ApJ, 834, 22, doi: 10.3847/1538-4357/834/1/22 [Cited on page 94.]

Dewangan, L. K., Pirogov, L. E., Ryabukhina, O. L., Ojha, D. K., & Zinchenko, I. 2019, ApJ, 877, 1, doi: 10.3847/1538-4357/ab1aa6 [Cited on page 115.]

Dewangan, L. K., Sharma, S., Pandey, R., et al. 2020b, ApJ, 898, 172, doi: 10.3847/1538-4357/ab9c27 [Cited on page 96.]

Dobbs, C. L., Pringle, J. E., & Duarte-Cabral, A. 2015, MNRAS, 446, 3608, doi: 10.1093/mnras/stu2319 [Cited 3 times on pages 20, 26, and 184.]

Downes, D., Wilson, T. L., Bieging, J., & Wink, J. 1980, AAPS, 40, 379 [Cited on page 56.]

Draine, B. T. 2003, ARA&A, 41, 241, doi: 10.1146/annurev.astro.41.011802.094840 [Cited 2 times on pages 3 and 94.]

—. 2011, Physics of the Interstellar and Intergalactic Medium [Cited on page 2.]

Du, F. 2021, Research in Astronomy and Astrophysics, 21, 077, doi: 10.1088/1674-4527/21/3/077 [Cited 2 times on pages 1 and 2.]

Dunne, L., Eales, S., Ivison, R., Morgan, H., & Edmunds, M. 2003, Nature, 424, 285, doi: 10.1038/nature01792 [Cited on page 1.]

Dyson, J. E., & Williams, D. A. 1997, The physics of the interstellar medium, doi: 10.1201/9780585368115 [Cited 2 times on pages 110 and 244.]

Elia, D., Molinari, S., Schisano, E., et al. 2017, MNRAS, 471, 100, doi: 10.1093/mnras/stx1357 [Cited on page 112.]

Elia, D., Merello, M., Molinari, S., et al. 2021, MNRAS, 504, 2742, doi: 10.1093/mnras/stab1038 [Cited on page 112.]

Elmegreen, B. G., & Lada, C. J. 1977, ApJ, 214, 725, doi: 10.1086/155302 [Cited on page 110.]

Evans, Neal J., I., Dunham, M. M., Jørgensen, J. K., et al. 2009, ApJS, 181, 321, doi: 10.1088/0067-0049/181/2/321 [Cited 2 times on pages 59 and 154.]

Federrath, C. 2016, MNRAS, 457, 375, doi: 10.1093/mnras/stv2880 [Cited 3 times on pages 189, 191, and 231.]

Federrath, C., Roman-Duval, J., Klessen, R. S., Schmidt, W., & Mac Low, M. M. 2010, A&A, 512, A81, doi: 10.1051/0004-6361/200912437 [Cited 4 times on pages 4, 41, 43, and 166.]

Fedriani, R., Caratti o Garatti, A., Purser, S. J. D., et al. 2019, Nature Communications, 10, 4048, doi: 10.1038/s41467-019-12105-9 [Cited on page 239.]

Fiege, J. D., & Pudritz, R. E. 2000, MNRAS, 311, 85, doi: 10.1046/j.1365-8711.2000.03066.x [Cited 2 times on pages 18 and 190.]

Frerking, M. A., Langer, W. D., & Wilson, R. W. 1982, ApJ, 262, 590, doi: 10.1086/160451 [Cited on page 132.]

Fujita, S., Torii, K., Kuno, N., et al. 2021, PASJ, 73, S172, doi: 10.1093/pasj/psz028 [Cited 4 times on pages 25, 27, 74, and 224.]

Fukui, Y., Habe, A., Inoue, T., Enokiya, R., & Tachihara, K. 2021a, PASJ, 73, S1, doi: 10.1093/pasj/psaa103 [Cited 13 times on pages 20, 25, 26, 27, 74, 114, 159, 162, 184, 188, 190, 195, and 224.]

Fukui, Y., Inoue, T., Hayakawa, T., & Torii, K. 2021b, PASJ, 73, S405, doi: 10.1093/pasj/psaa079 [Cited 5 times on pages 166, 174, 188, 189, and 225.]

Fukui, Y., Tsuge, K., Sano, H., et al. 2017a, PASJ, 69, L5, doi: 10.1093/pasj/psx032 [Cited on page 74.]

—. 2017b, PASJ, 69, L5, doi: 10.1093/pasj/psx032 [Cited on page 200.]

Fukui, Y., Onishi, T., Mizuno, N., et al. 2006, in IAU Special Session, Vol. 1, IAU Special Session, 21 [Cited on page 40.]

Fukui, Y., Ohama, A., Hanaoka, N., et al. 2014, ApJ, 780, 36, doi: 10.1088/0004-637X/780/1/36 [Cited 4 times on pages 20, 25, 74, and 224.]

Fukui, Y., Harada, R., Tokuda, K., et al. 2015, ApJL, 807, L4, doi: 10.1088/2041-8205/807/1/L4 [Cited 2 times on pages 25 and 224.]

Fukui, Y., Kohno, M., Yokoyama, K., et al. 2018a, PASJ, 70, S44, doi: 10.1093/pasj/psx144 [Cited on page 14.]

Fukui, Y., Torii, K., Hattori, Y., et al. 2018b, ApJ, 859, 166, doi: 10.3847/1538-4357/aac217 [Cited 7 times on pages 20, 25, 26, 74, 75, 113, and 114.]

Fukui, Y., Tokuda, K., Saigo, K., et al. 2019, ApJ, 886, 14, doi: 10.3847/1538-4357/ab4900 [Cited 5 times on pages 24, 78, 114, 160, and 200.]

Furukawa, N., Dawson, J. R., Ohama, A., et al. 2009, ApJL, 696, L115, doi: 10.1088/0004-637X/696/2/L115 [Cited on page 188.]

Gaia Collaboration, Prusti, T., de Bruijne, J. H. J., et al. 2016, A&A, 595, A1, doi: 10.1051/0004-6361/201629272 [Cited on page 204.]

Gaia Collaboration, Brown, A. G. A., Vallenari, A., et al. 2021, A&A, 649, A1, doi: 10.1051/0004-6361/202039657 [Cited on page 204.]

Geen, S., Rosdahl, J., Blaizot, J., Devriendt, J., & Slyz, A. 2015, MNRAS, 448, 3248, doi: 10.1093/mnras/stv251 [Cited on page 120.]

Getman, K. V., Feigelson, E. D., Garmire, G., Broos, P., & Wang, J. 2007, ApJ, 654, 316, doi: 10.1086/509112 [Cited 6 times on pages 38, 52, 59, 129, 216, and 217.]

Ghosh, S. K., Iyengar, K. V. K., Karnik, A. D., et al. 2000, Bulletin of the Astronomical Society of India, 28, 515 [Cited 2 times on pages 82 and 83.]

Gilden, D. L. 1984, ApJ, 279, 335, doi: 10.1086/161894 [Cited on page 24.]

Girichidis, P., Offner, S. S. R., Kritsuk, A. G., et al. 2020, SSR, 216, 68, doi: 10.1007/s11214-020-00693-8 [Cited 3 times on pages 2, 3, and 6.]

Goedhart, S., Cotton, W. D., Camilo, F., et al. 2024, MNRAS, 531, 649, doi: 10.1093/mnras/stae1166 [Cited 5 times on pages 40, 122, 123, 205, and 206.]

Goicoechea, J. R., Pety, J., Cuadrado, S., et al. 2016, Nature, 537, 207, doi: 10.1038/nature18957 [Cited on page 13.]

Gómez, G. C., & Vázquez-Semadeni, E. 2014, ApJ, 791, 124, doi: 10.1088/0004-637X/791/2/124 [Cited on page 17.]

Gómez, G. C., Vázquez-Semadeni, E., & Zamora-Avilés, M. 2018, MNRAS, 480, 2939, doi: 10.1093/mnras/sty2018 [Cited 5 times on pages 115, 179, 182, 183, and 191.]

Goodman, A. A., Rosolowsky, E. W., Borkin, M. A., et al. 2009, Nature, 457, 63, doi: 10.1038/nature07609 [Cited on page 50.]

Gutermuth, R. A., Megeath, S. T., Myers, P. C., et al. 2009, ApJS, 184, 18, doi: 10.1088/0067-0049/184/1/18 [Cited 3 times on pages 38, 52, and 93.]

Habe, A., & Ohta, K. 1992, PASJ, 44, 203 [Cited 3 times on pages 20, 24, and 160.]

Hacar, A., Alves, J., Burkert, A., & Goldsmith, P. 2016, A&A, 591, A104, doi: 10.1051/0004-6361/201527319 [Cited on page 105.]

Haemmerlé, L., Eggenberger, P., Meynet, G., Maeder, A., & Charbonnel, C. 2016, A&A, 585, A65, doi: 10.1051/0004-6361/201527202 [Cited on page 8.]

Hanaoka, M., Kaneda, H., Suzuki, T., et al. 2019, PASJ, 71, 6, doi: 10.1093/pasj/psy126 [Cited on page 203.]

Hartmann, L., Megeath, S. T., Allen, L., et al. 2005, ApJ, 629, 881, doi: 10.1086/431472 [Cited 4 times on pages 38, 52, 59, and 129.]

Hattori, Y., Kaneda, H., Ishihara, D., et al. 2016, PASJ, 68, 37, doi: 10.1093/pasj/psw028 [Cited on page 203.]

Haworth, T. J., Shima, K., Tasker, E. J., et al. 2015a, MNRAS, 454, 1634, doi: 10.1093/mnras/stv2068 [Cited 2 times on pages 25 and 74.]

Haworth, T. J., Tasker, E. J., Fukui, Y., et al. 2015b, MNRAS, 450, 10, doi: 10.1093/mnras/stv639 [Cited on page 153.]

Hayashi, K., Sano, H., Enokiya, R., et al. 2018, PASJ, 70, S48, doi: 10.1093/pasj/psx141 [Cited on page 74.]

Helfand, D. J., Becker, R. H., White, R. L., Fallon, A., & Tuttle, S. 2006, The Astronomical Journal, 131, 2525, doi: 10.1086/503253 [Cited 3 times on pages 40, 205, and 206.]

Hennebelle, P., & Falgarone, E. 2012, A&ARv, 20, 55, doi: 10.1007/s00159-012-0055-y [Cited 2 times on pages 4 and 162.]

Hennebelle, P., & Inutsuka, S.-i. 2019, Frontiers in Astronomy and Space Sciences, 6, 5, doi: 10.3389/fspas.2019.00005 [Cited on page 5.]

Henshaw, J. D., Caselli, P., Fontani, F., Jiménez-Serra, I., & Tan, J. C. 2014, MNRAS, 440, 2860, doi: 10.1093/mnras/stu446 [Cited 2 times on pages 18 and 148.]

Henshaw, J. D., Longmore, S. N., Kruijssen, J. M. D., et al. 2016, MNRAS, 457, 2675, doi: 10.1093/mnras/stw121 [Cited on page 214.]

Henshaw, J. D., Ginsburg, A., Haworth, T. J., et al. 2019, MNRAS, 485, 2457, doi: 10.1093/mnras/stz471 [Cited on page 214.]

Herbst, E., & van Dishoeck, E. F. 2009, ARA&A, 47, 427, doi: 10.1146/annurev-astro-082708-101654 [Cited on page 12.]

Hildebrand, R. H. 1983, QJRAS, 24, 267 [Cited 2 times on pages 51 and 137.]

Hoare, M. G. 2005, APSS, 295, 203, doi: 10.1007/s10509-005-3690-1 [Cited on page 13.]

Hoare, M. G., Kurtz, S. E., Lizano, S., Keto, E., & Hofner, P. 2007, in Protostars and Planets V, ed. B. Reipurth, D. Jewitt, & K. Keil, 181. https://arxiv.org/abs/astro-ph/0603560 [Cited on page 13.]

Hosokawa, T., & Omukai, K. 2009, ApJ, 691, 823, doi: 10.1088/0004-637X/691/1/823 [Cited on page 14.]

Houlahan, P., & Scalo, J. 1992, ApJ, 393, 172, doi: 10.1086/171495 [Cited on page 49.]

Inoue, T., & Fukui, Y. 2013, ApJL, 774, L31, doi: 10.1088/2041-8205/774/2/L31 [Cited 15 times on pages 20, 28, 76, 78, 160, 181, 182, 188, 189, 190, 191, 192, 225, 232, and 233.]

Inoue, T., Hennebelle, P., Fukui, Y., et al. 2018, PASJ, 70, S53, doi: 10.1093/pasj/psx089 [Cited 25 times on pages 20, 28, 33, 39, 78, 160, 161, 163, 181, 182, 188, 189, 190, 191, 192, 195, 200, 201, 202, 222, 225, 227, 231, 232, and 233.]

Inutsuka, S.-i., Inoue, T., Iwasaki, K., & Hosokawa, T. 2015, A&A, 580, A49, doi: 10.1051/0004-6361/201425584 [Cited 2 times on pages 20 and 162.]

Jackson, J. M., Rathborne, J. M., Shah, R. Y., et al. 2006, ApJS, 163, 145, doi: 10.1086/500091 [Cited 2 times on pages 205 and 206.]

Jeans, J. H. 1902, Philosophical Transactions of the Royal Society of London Series A, 199, 1, doi: 10.1098/rsta.1902.0012 [Cited on page 5.]

Jog, C. J., & Ostriker, J. P. 1988, ApJ, 328, 404, doi: 10.1086/166302 [Cited on page 20.]

Juárez, C., Girart, J. M., Zamora-Avilés, M., et al. 2017, ApJ, 844, 44, doi: 10.3847/1538-4357/aa78a6 [Cited on page 183.]

Kainulainen, J., Ragan, S. E., Henning, T., & Stutz, A. 2013, A&A, 557, A120, doi: 10.1051/0004-6361/201321760 [Cited on page 148.]

Kale, R., & Ishwara-Chandra, C. H. 2021, Experimental Astronomy, 51, 95, doi: 10.1007/s10686-020-09677-6 [Cited on page 86.]

Kauffmann, J., Bertoldi, F., Bourke, T. L., Evans, N. J., I., & Lee, C. W. 2008, A&A, 487, 993, doi: 10.1051/0004-6361:200809481 [Cited 4 times on pages 46, 98, 104, and 133.]

Kauffmann, J., & Pillai, T. 2010, ApJL, 723, L7, doi: 10.1088/2041-8205/723/1/L7 [Cited 5 times on pages 137, 138, 150, 151, and 209.]

Keto, E. 2007, ApJ, 666, 976, doi: 10.1086/520320 [Cited on page 13.]

Keto, E., & Wood, K. 2006, The Astrophysical Journal, 637, 850, doi: 10.1086/498611 [Cited on page 9.]

Kim, C.-G., & Ostriker, E. C. 2015, ApJ, 802, 99, doi: 10.1088/0004-637X/802/2/99 [Cited on page 162.]

Kim, K.-T., & Koo, B.-C. 2001, ApJ, 549, 979, doi: 10.1086/319447 [Cited on page 55.]

—. 2002, ApJ, 575, 327, doi: 10.1086/341285 [Cited on page 76.]

Kimble, R. A., MacKenty, J. W., O'Connell, R. W., & Townsend, J. A. 2008, in Society of Photo-Optical Instrumentation Engineers (SPIE) Conference Series, Vol. 7010, Space Telescopes and Instrumentation 2008: Optical, Infrared, and Millimeter, ed. J. M. Oschmann, Jr., M. W. M. de Graauw, & H. A. MacEwen, 70101E, doi: 10.1117/12.789581 [Cited on page 40.]

Kirk, H., Myers, P. C., Bourke, T. L., et al. 2013, ApJ, 766, 115, doi: 10.1088/0004-637X/766/2/115 [Cited 6 times on pages 21, 134, 136, 146, 148, and 219.]

Klassen, M., Pudritz, R. E., & Kirk, H. 2017, MNRAS, 465, 2254, doi: 10.1093/mnras/stw2889 [Cited on page 183.]

Klein, R., Posselt, B., Schreyer, K., Forbrich, J., & Henning, T. 2005, ApJS, 161, 361, doi: 10.1086/496962 [Cited 2 times on pages 82 and 83.]

Koch, E. W., & Rosolowsky, E. W. 2015, Monthly Notices of the Royal Astronomical Society, 452, 3435, doi: 10.1093/mnras/stv1521 [Cited on page 48.]

Koch, P. M., Tang, Y.-W., Ho, P. T. P., et al. 2022, ApJ, 940, 89, doi: 10.3847/1538-4357/ac96e3 [Cited on page 183.]

Koempe, C., Baudry, A., Joncas, G., & Wouterloot, J. G. A. 1989, A&A, 221, 295 [Cited on page 82.]

Kroupa, P. 2001, MNRAS, 322, 231, doi: 10.1046/j.1365-8711.2001.04022.x [Cited on page 150.]

—. 2002, Science, 295, 82, doi: 10.1126/science.1067524 [Cited on page 1.]

Krumholz, M. R. 2008, in Astronomical Society of the Pacific Conference Series, Vol. 387, Massive Star Formation: Observations Confront Theory, ed. H. Beuther, H. Linz, & T. Henning, 200 [Cited on page 16.]

Krumholz, M. R. 2015a, in Astrophysics and Space Science Library, Vol. 412, Very Massive Stars in the Local Universe, ed. J. S. Vink, 43, doi: 10.1007/978-3-319-09596-7_3 [Cited on page 2.]

Krumholz, M. R. 2015b, arXiv e-prints, arXiv:1511.03457, doi: 10.48550/arXiv.1511.03457 [Cited 3 times on pages 4, 41, and 42.]

Krumholz, M. R., & Bonnell, I. A. 2009, Structure formation in astrophysics, 288 [Cited on page 16.]

Krumholz, M. R., Klein, R. I., & McKee, C. F. 2007a, ApJ, 656, 959, doi: 10.1086/510664 [Cited on page 14.]

Krumholz, M. R., McKee, C. F., & Klein, R. I. 2004, The Astrophysical Journal, 611, 399, doi: 10.1086/421935 [Cited on page 43.]

Krumholz, M. R., Stone, J. M., & Gardiner, T. A. 2007b, ApJ, 671, 518, doi: 10.1086/522665 [Cited 2 times on pages 38 and 159.]

Kuhn, M. A., de Souza, R. S., Krone-Martins, A., et al. 2021, ApJS, 254, 33, doi: 10.3847/1538-4365/abe465 [Cited 4 times on pages 206, 216, 217, and 218.]

Kumar, M. S. N., Arzoumanian, D., Men'shchikov, A., et al. 2022, A&A, 658, A114, doi: 10.1051/0004-6361/202140363 [Cited 2 times on pages 18 and 100.]

Kumar, M. S. N., Palmeirim, P., Arzoumanian, D., & Inutsuka, S. I. 2020, A&A, 642, A87, doi: 10.1051/0004-6361/202038232 [Cited 10 times on pages 19, 21, 23, 24, 112, 120, 146, 153, 154, and 233.]

Kurtz, S. 2005, in Massive Star Birth: A Crossroads of Astrophysics, ed. R. Cesaroni, M. Felli, E. Churchwell, & M. Walmsley, Vol. 227, 111–119, doi: 10.1017/S1743921305004424 [Cited on page 13.]

Kurtz, S., Cesaroni, R., Churchwell, E., Hofner, P., & Walmsley, C. M. 2000, in Protostars and Planets IV, ed. V. Mannings, A. P. Boss, & S. S. Russell, 299–326 [Cited on page 12.]

Kurtz, S., Churchwell, E., & Wood, D. O. S. 1994, ApJS, 91, 659, doi: 10.1086/191952 [Cited on page 83.]

Kwan, J. 1997, ApJ, 489, 284, doi: 10.1086/304773 [Cited 2 times on pages 91 and 244.]

Larson, R. B. 1981, MNRAS, 194, 809, doi: 10.1093/mnras/194.4.809 [Cited 4 times on pages 4, 162, 192, and 194.]

Lawrence, A., Warren, S. J., Almaini, O., et al. 2007, MNRAS, 379, 1599, doi: 10.1111/j.1365-2966.2007.12040.x [Cited 2 times on pages 40 and 84.]

Leistra, A., Cotera, A. S., & Liebert, J. 2006, AJ, 131, 2571, doi: 10.1086/500641 [Cited on page 82.]

Lequeux, J. 2005, The Interstellar Medium, doi: 10.1007/b137959 [Cited on page 6.]

Li, S., Zhang, Q., Liu, H. B., et al. 2020, ApJ, 896, 110, doi: 10.3847/1538-4357/ab84f1 [Cited 2 times on pages 137 and 139.]

Liu, H.-L., Sanhueza, P., Liu, T., et al. 2020, ApJ, 901, 31, doi: 10.3847/1538-4357/abadfe [Cited on page 132.]

Liu, H.-L., Stutz, A., & Yuan, J.-H. 2019, MNRAS, 487, 1259, doi: 10.1093/mnras/stz1340 [Cited 3 times on pages 148, 220, and 221.]

Liu, J., Zhang, Q., Koch, P. M., et al. 2023, ApJ, 945, 160, doi: 10.3847/1538-4357/acb540 [Cited on page 184.]

Liu, M., Tan, J. C., Marvil, J., et al. 2021, The Astrophysical Journal, 921, 96, doi: 10.3847/1538-4357/ac0829 [Cited on page 38.]

Liu, T., Li, P. S., Juvela, M., et al. 2018, ApJ, 859, 151, doi: 10.3847/1538-4357/aac025 [Cited on page 183.]

Long, K. S., Blair, W. P., Winkler, P. F., & Lacey, C. K. 2020, ApJ, 899, 14, doi: 10.3847/1538-4357/aba2e9 [Cited on page 239.]

Lucas, P. W., Hoare, M. G., Longmore, A., et al. 2008, MNRAS, 391, 136, doi: 10.1111/j.1365-2966.2008.13924.x [Cited 2 times on pages 52 and 93.]

Lynds, B. T., & Oneil, Jr., E. J. 1985, ApJ, 294, 578, doi: 10.1086/163325 [Cited on page 17.]

Mai, X., Liu, T., Liu, X., et al. 2024, ApJL, 961, L35, doi: 10.3847/2041-8213/ad19c3 [Cited on page 15.]

Maity, A. K., Dewangan, L. K., Bhadari, N. K., et al. 2025a, AJ, 169, 56, doi: 10.3847/1538-3881/ad98ff [Cited 5 times on pages 31, 33, 159, 160, and 194.]

—. 2023, MNRAS, 523, 5388, doi: 10.1093/mnras/stad1644 [Cited 7 times on pages 31, 32, 87, 144, 153, 159, and 160.]

Maity, A. K., Dewangan, L. K., Jadhav, O. R., et al. 2025b, AJ, 169, 325, doi: 10.3847/1538-3881/adcedd [Cited 2 times on pages 31 and 34.]

Maity, A. K., Dewangan, L. K., Sano, H., et al. 2022, ApJ, 934, 2, doi: 10.3847/1538-4357/ac7872 [Cited 5 times on pages 30, 32, 114, 159, and 160.]

Maity, A. K., Inoue, T., Fukui, Y., et al. 2024, ApJ, 974, 229, doi: 10.3847/1538-4357/ad7098 [Cited 6 times on pages 33, 120, 149, 223, 225, and 227.]

Mangum, J. G., & Shirley, Y. L. 2015, PASP, 127, 266, doi: 10.1086/680323 [Cited 2 times on pages 45 and 132.]

Marcolino, W. L. F., Bouret, J. C., Martins, F., et al. 2009, A&A, 498, 837, doi: 10.1051/0004-6361/200811289 [Cited on page 91.]

Marsh, K. A., Whitworth, A. P., & Lomax, O. 2015, MNRAS, 454, 4282, doi: 10.1093/mnras/stv2248 [Cited on page 58.]

Marsh, K. A., Whitworth, A. P., Lomax, O., et al. 2017, MNRAS, 471, 2730, doi: 10.1093/mnras/stx1723 [Cited 2 times on pages 58 and 206.]

Martins, F., & Palacios, A. 2017, A&A, 598, A56, doi: 10.1051/0004-6361/201629538 [Cited on page 91.]

Matsakis, D. N., Evans, N. J., I., Sato, T., & Zuckerman, B. 1976, AJ, 81, 172, doi: 10.1086/111871 [Cited on page 244.]

Matsumoto, T. 2007, PASJ, 59, 905, doi: 10.1093/pasj/59.5.905 [Cited 2 times on pages 41 and 161.]

Matsumoto, T., Dobashi, K., & Shimoikura, T. 2015, ApJ, 801, 77, doi: 10.1088/0004-637X/801/2/77 [Cited 2 times on pages 41 and 161.]

Mayra, O., Susana, L., & Paola, D. 1999, arXiv e-prints, astro, doi: 10.48550/arXiv.astro-ph/9909473 [Cited on page 218.]

McDowell, R. S. 1988, JCP, 88, 356, doi: 10.1063/1.454608 [Cited on page 132.]

McKee, C. F., & Ostriker, E. C. 2007, Annu. Rev. Astron. Astrophys., 45, 565 [Cited on page 7.]

McKee, C. F., & Tan, J. C. 2002, Nature, 416, 59, doi: 10.1038/416059a [Cited on page 14.]

—. 2003, ApJ, 585, 850, doi: 10.1086/346149 [Cited on page 14.]

McMahon, R. G., Banerji, M., Gonzalez, E., et al. 2021, VizieR Online Data Catalog: The VISTA Hemisphere Survey (VHS) catalog DR5 (McMahon+, 2020), VizieR On-line Data Catalog: II/367. Originally published in: 2013Msngr.154...35M [Cited on page 123.]

Men'shchikov, A. 2021, A&A, 649, A89, doi: 10.1051/0004-6361/202039913 [Cited 9 times on pages 46, 48, 49, 62, 89, 96, 124, 127, and 175.]

Menten, K. M. 1991, ApJL, 380, L75, doi: 10.1086/186177 [Cited 3 times on pages 12, 38, and 82.]

Merello, M., Evans, Neal J., I., Shirley, Y. L., et al. 2015, ApJS, 218, 1, doi: 10.1088/0067-0049/218/1/1 [Cited 2 times on pages 40 and 85.]

Miettinen, O. 2012, A&A, 545, A3, doi: 10.1051/0004-6361/201219497 [Cited on page 132.]

Minier, V., Conway, J. E., & Booth, R. S. 2001, A&A, 369, 278, doi: 10.1051/0004-6361:20010124 [Cited 3 times on pages 38, 82, and 111.]

Minniti, D., Lucas, P., & VVV Team. 2017, VizieR Online Data Catalog: VISTA Variable in the Via Lactea Survey DR2 (Minniti+, 2017), VizieR On-line Data Catalog: II/348. Originally published in: Astron. Astrophys., 537, A107 (2002) [Cited on page 123.]

Minniti, D., Lucas, P. W., Emerson, J. P., et al. 2010, NA, 15, 433, doi: 10.1016/j.newast.2009.12.002 [Cited on page 123.]

Molet, J., Brouillet, N., Nony, T., et al. 2019, A&A, 626, A132, doi: 10.1051/0004-6361/201935497 [Cited on page 11.]

Molinari, S., Swinyard, B., Bally, J., et al. 2010a, PASP, 122, 314, doi: 10.1086/651314 [Cited 2 times on pages 17 and 40.]

—. 2010b, A&A, 518, L100, doi: 10.1051/0004-6361/201014659 [Cited 4 times on pages 58, 85, 123, and 206.]

Morii, K., Sanhueza, P., Nakamura, F., et al. 2023, ApJ, 950, 148, doi: 10.3847/1538-4357/acccea [Cited on page 15.]

Morii, K., Sanhueza, P., Zhang, Q., et al. 2024, ApJ, 966, 171, doi: 10.3847/1538-4357/ad32d0 [Cited on page 151.]

Motte, F., Bontemps, S., & Louvet, F. 2018, ARA&A, 56, 41, doi: 10.1146/annurev-astro-091916-055235 [Cited 12 times on pages 1, 2, 11, 19, 22, 23, 71, 111, 112, 152, 157, and 159.]

Motte, F., Bontemps, S., Schilke, P., et al. 2007, A&A, 476, 1243, doi: 10.1051/0004-6361:20077843 [Cited on page 11.]

Mutie, M. M., Chibueze, J. O., El Bouchefry, K., et al. 2021, MNRAS, 506, 4175, doi: 10.1093/mnras/stab1946 [Cited 3 times on pages 83, 137, and 240.]

Myers, P. C. 2009, ApJ, 700, 1609, doi: 10.1088/0004-637X/700/2/1609 [Cited 9 times on pages 3, 18, 71, 111, 112, 127, 146, 159, and 191.]

Navarete, F., Damineli, A., Barbosa, C. L., & Blum, R. D. 2015, MNRAS, 450, 4364, doi: 10.1093/mnras/stv914 [Cited 4 times on pages 40, 82, 85, and 94.]

Navarrete, S., Pinargote, B. J., & Banda-Barragán, W. E. 2024, arXiv e-prints, arXiv:2404.13250, doi: 10.48550/arXiv.2404.13250 [Cited on page 188.]

Nishimura, A., Costes, J., Inaba, T., et al. 2017, arXiv e-prints, arXiv:1706.06002. https://arxiv.org/abs/1706.06002 [Cited on page 74.]

Nishimura, A., Fujita, S., Kohno, M., et al. 2021, PASJ, 73, S285, doi: 10.1093/pasj/psaa083 [Cited on page 188.]

Oh, C. S., Kobayashi, H., Honma, M., et al. 2010, PASJ, 62, 101, doi: 10.1093/pasj/62.1.101 [Cited on page 82.]

Orkisz, J. H., Pety, J., Gerin, M., et al. 2017, A&A, 599, A99, doi: 10.1051/0004-6361/201629220 [Cited 2 times on pages 4 and 162.]

Ostriker, J. 1964, ApJ, 140, 1529, doi: 10.1086/148057 [Cited 2 times on pages 18 and 148.]

Owen, E. R., Wu, K., Inoue, Y., Yang, H. Y. K., & Mitchell, A. M. W. 2023, Galaxies, 11, 86, doi: 10.3390/galaxies11040086 [Cited on page 3.]

Padoan, P., Pan, L., Haugbølle, T., & Nordlund, Å. 2016, ApJ, 822, 11, doi: 10.3847/0004-637X/822/1/11 [Cited 2 times on pages 4 and 162.]

Padoan, P., Pan, L., Juvela, M., Haugbølle, T., & Nordlund, Å. 2020, ApJ, 900, 82, doi: 10.3847/1538-4357/abaa47 [Cited 6 times on pages 4, 16, 17, 191, 192, and 231.]

Palau, A., Ballesteros-Paredes, J., Vázquez-Semadeni, E., et al. 2015, MNRAS, 453, 3785, doi: 10.1093/mnras/stv1834 [Cited on page 151.]

Palla, F., & Stahler, S. W. 1993, The Astrophysical Journal, 418, 414, doi: 10.1086/173402 [Cited on page 9.]

Palmeirim, P., André, P., Kirk, J., et al. 2013, A&A, 550, A38, doi: 10.1051/0004-6361/201220500 [Cited 2 times on pages 46 and 239.]

Panagia, N. 1973, AJ, 78, 929, doi: 10.1086/111498 [Cited 4 times on pages 91, 150, 211, and 218.]

Pandey, R., Sharma, S., Panwar, N., et al. 2020, ApJ, 891, 81, doi: 10.3847/1538-4357/ab6dc7 [Cited on page 94.]

Panja, A., Dewangan, L. K., Baug, T., et al. 2023, ApJ, 958, 17, doi: 10.3847/1538-4357/ad0048 [Cited on page 23.]

Panopoulou, G. V., Tassis, K., Goldsmith, P. F., & Heyer, M. H. 2014, MNRAS, 444, 2507, doi: 10.1093/mnras/stu1601 [Cited on page 17.]

Pari, J., & Hora, J. L. 2020, PASP, 132, 054301, doi: 10.1088/1538-3873/ab7b39 [Cited 2 times on pages 207 and 208.]

Park, G., Currie, M. J., Thomas, H. S., et al. 2023, ApJS, 264, 16, doi: 10.3847/1538-4365/ac9b59 [Cited on page 184.]

Paron, S. 2024, arXiv e-prints, arXiv:2403.13610, doi: 10.48550/arXiv.2403.13610 [Cited on page 218.]

Paulson, S. T., Mallick, K. K., & Ojha, D. K. 2024, MNRAS, 530, 1516, doi: 10.1093/mnras/stae917 [Cited on page 204.]

Peretto, N., Fuller, G. A., André, P., et al. 2014, A&A, 561, A83, doi: 10.1051/0004-6361/201322172 [Cited on page 160.]

Pety, J. 2005, in SF2A-2005: Semaine de l'Astrophysique Francaise, ed. F. Casoli, T. Contini, J. M. Hameury, & L. Pagani, 721 [Cited on page 86.]

Phillips, T. G., Huggins, P. J., Wannier, P. G., & Scoville, N. Z. 1979, ApJ, 231, 720, doi: 10.1086/157237 [Cited on page 105.]

Pickett, H. M., Poynter, R. L., Cohen, E. A., et al. 1998, JQSRT, 60, 883, doi: 10.1016/S0022-4073(98)00091-0 [Cited on page 132.]

Pillai, T., Kauffmann, J., Tan, J. C., et al. 2015, ApJ, 799, 74, doi: 10.1088/0004-637X/799/1/74 [Cited 2 times on pages 181 and 183.]

Pineda, J. E., Arzoumanian, D., Andre, P., et al. 2023, in Astronomical Society of the Pacific Conference Series, Vol. 534, Protostars and Planets VII, ed. S. Inutsuka, Y. Aikawa, T. Muto, K. Tomida, & M. Tamura, 233, doi: 10.48550/arXiv.2205.03935 [Cited 2 times on pages 17 and 190.]

Planck Collaboration, Ade, P. A. R., Aghanim, N., et al. 2014, A&A, 571, A1, doi: 10.1051/0004-6361/201321529 [Cited 2 times on pages 40 and 85.]

—. 2015, A&A, 576, A104, doi: 10.1051/0004-6361/201424082 [Cited on page 237.]

—. 2016a, A&A, 586, A136, doi: 10.1051/0004-6361/201425305 [Cited 2 times on pages 175 and 237.]

—. 2016b, A&A, 594, A19, doi: 10.1051/0004-6361/201525821 [Cited on page 237.]

—. 2016c, A&A, 586, A138, doi: 10.1051/0004-6361/201525896 [Cited on page 239.]

Pon, A., Toalá, J. A., Johnstone, D., et al. 2012, ApJ, 756, 145, doi: 10.1088/0004-637X/756/2/145 [Cited 2 times on pages 18 and 115.]

Povich, M. S., Stone, J. M., Churchwell, E., et al. 2007, ApJ, 660, 346, doi: 10.1086/513073 [Cited on page 94.]

Povich, M. S., Smith, N., Majewski, S. R., et al. 2011, ApJS, 194, 14, doi: 10.1088/0067-0049/194/1/14 [Cited 3 times on pages 10, 52, and 129.]

Priestley, F. D., & Whitworth, A. P. 2021, MNRAS, 506, 775, doi: 10.1093/mnras/stab1777 [Cited 4 times on pages 25, 27, 74, and 194.]

Ragan, S., Henning, T., Krause, O., et al. 2012, Astronomy and Astrophysics, 547, A49, doi: 10.1051/0004-6361/201219232 [Cited on page 11.]

Ragan, S. E., Bergin, E. A., & Gutermuth, R. A. 2009, ApJ, 698, 324, doi: 10.1088/0004-637X/698/1/324 [Cited 4 times on pages 11, 38, 205, and 211.]

Ragan, S. E., Henning, T., Tackenberg, J., et al. 2014, A&A, 568, A73, doi: 10.1051/0004-6361/201423401 [Cited on page 17.]

Rathborne, J. M., Jackson, J. M., & Simon, R. 2006, The Astrophysical Journal, 641, 389, doi: 10.1086/500423 [Cited on page 11.]

Rawat, V., Samal, M. R., Walker, D. L., et al. 2024, MNRAS, 528, 2199, doi: 10.1093/mnras/stae060 [Cited on page 148.]

Reid, M. J., Menten, K. M., Brunthaler, A., et al. 2009, ApJ, 693, 397, doi: 10.1088/0004-637X/693/1/397 [Cited on page 82.]

Ridge, N. A., Di Francesco, J., Kirk, H., et al. 2006, AJ, 131, 2921, doi: 10.1086/503704 [Cited on page 57.]

Rigby, A. J., Moore, T. J. T., Plume, R., et al. 2016, MNRAS, 456, 2885, doi: 10.1093/mnras/stv2808 [Cited 3 times on pages 38, 40, and 206.]

Roelfsema, P. 1989, in Astronomical Society of the Pacific Conference Series, Vol. 6, Synthesis Imaging in Radio Astronomy, ed. R. A. Perley, F. R. Schwab, & A. H. Bridle, 315 [Cited on page 44.]

Roman-Lopes, A., & Roman-Lopes, G. F. 2019, MNRAS, 484, 5578, doi: 10.1093/mnras/stz064 [Cited on page 82.]

Rosen, A. L., Offner, S. S. R., Sadavoy, S. I., et al. 2020, SSR, 216, 62, doi: 10.1007/s11214-020-00688-5 [Cited 4 times on pages 14, 15, 16, and 111.]

Rosolowsky, E. W., Pineda, J. E., Kauffmann, J., & Goodman, A. A. 2008, ApJ, 679, 1338, doi: 10.1086/587685 [Cited on page 50.]

Saito, H., Saito, M., Sunada, K., & Yonekura, Y. 2007, ApJ, 659, 459, doi: 10.1086/512058 [Cited on page 82.]

Sakre, N., Habe, A., Pettitt, A. R., & Okamoto, T. 2021, PASJ, 73, S385, doi: 10.1093/pasj/psaa059 [Cited on page 189.]

Sakre, N., Habe, A., Pettitt, A. R., et al. 2023, MNRAS, 522, 4972, doi: 10.1093/mnras/stad1089 [Cited on page 189.]

Salpeter, E. E. 1955, ApJ, 121, 161, doi: 10.1086/145971 [Cited on page 1.]

Sanhueza, P., Jackson, J. M., Zhang, Q., et al. 2017, ApJ, 841, 97, doi: 10.3847/1538-4357/aa6ff8 [Cited 2 times on pages 141 and 150.]

Sano, H., Enokiya, R., Hayashi, K., et al. 2018, PASJ, 70, S43, doi: 10.1093/pasj/psy006 [Cited 4 times on pages 25, 74, 188, and 224.]

Sano, H., Tsuge, K., Tokuda, K., et al. 2021, PASJ, 73, S62, doi: 10.1093/pasj/psaa045 [Cited on page 74.]

Santos, F. P., Busquet, G., Franco, G. A. P., Girart, J. M., & Zhang, Q. 2016, ApJ, 832, 186, doi: 10.3847/0004-637X/832/2/186 [Cited on page 17.]

Schilke, P. 2015, EAS Publications Series, 75, 227 [Cited on page 8.]

Schneider, N., Csengeri, T., Bontemps, S., et al. 2010, A&A, 520, A49, doi: 10.1051/0004-6361/201014481 [Cited on page 146.]

Schneider, N., Csengeri, T., Hennemann, M., et al. 2012, A&A, 540, L11, doi: 10.1051/0004-6361/201118566 [Cited 3 times on pages 18, 19, and 71.]

Schneider, S., & Elmegreen, B. G. 1979, ApJS, 41, 87, doi: 10.1086/190609 [Cited on page 17.]

Schuller, F., Menten, K. M., Contreras, Y., et al. 2009, A&A, 504, 415, doi: 10.1051/0004-6361/200811568 [Cited 5 times on pages 40, 58, 123, 139, and 206.]

Schuller, F., Urquhart, J., Bronfman, L., et al. 2016, The Messenger, 165, 27 [Cited on page 194.]

Schuller, F., Csengeri, T., Urquhart, J. S., et al. 2017a, A&A, 601, A124, doi: 10.1051/0004-6361/201628933 [Cited 6 times on pages 38, 56, 58, 122, 123, and 132.]

—. 2017b, A&A, 601, A124, doi: 10.1051/0004-6361/201628933 [Cited on page 194.]

Schuller, F., Urquhart, J. S., Csengeri, T., et al. 2021, MNRAS, 500, 3064, doi: 10.1093/mnras/staa2369 [Cited on page 195.]

Schulz, N. S. 2005, From Dust To Stars Studies of the Formation and Early Evolution of Stars, doi: 10.1007/b138917 [Cited 5 times on pages 4, 5, 7, 8, and 38.]

Seshadri, A., Vig, S., Ghosh, S. K., & Ojha, D. K. 2024, MNRAS, 527, 4244, doi: 10.1093/mnras/stad3385 [Cited 4 times on pages 21, 148, 177, and 191.]

Sharma, S., Pandey, A. K., Ojha, D. K., et al. 2017, MNRAS, 467, 2943, doi: 10.1093/mnras/stx014 [Cited 3 times on pages 52, 129, and 216.]

Sharpless, S. 1959, ApJS, 4, 257, doi: 10.1086/190049 [Cited on page 82.]

Shima, K., Tasker, E. J., Federrath, C., & Habe, A. 2018, PASJ, 70, S54, doi: 10.1093/pasj/psx124 [Cited 2 times on pages 189 and 191.]

Shimoikura, T., Dobashi, K., Saito, H., et al. 2013, ApJ, 768, 72, doi: 10.1088/0004-637X/768/1/72 [Cited 3 times on pages 82, 83, and 113.]

Shu, F. H. 1977, ApJ, 214, 488, doi: 10.1086/155274 [Cited 2 times on pages 4 and 7.]

Shu, F. H., Adams, F. C., & Lizano, S. 1987, ARA&A, 25, 23, doi: 10.1146/annurev.aa.25.090187.000323 [Cited on page 5.]

Simon, R., Jackson, J. M., Rathborne, J. M., & Chambers, E. T. 2006, ApJ, 639, 227, doi: 10.1086/499342 [Cited on page 211.]

Skrutskie, M. F., Cutri, R. M., Stiening, R., et al. 2006, AJ, 131, 1163, doi: 10.1086/498708 [Cited 3 times on pages 40, 84, and 123.]

Smith, J. 1980, ApJ, 238, 842, doi: 10.1086/158045 [Cited on page 24.]

Smith, M. 2004, The Origin of Stars, G - Reference,Information and Interdisciplinary Subjects Series (Imperial College Press). https://books.google.co.in/books?id=UVgBoqZg8a4C [Cited 7 times on pages 3, 5, 7, 8, 10, 37, and 38.]

Sobolev, A. M., Cragg, D. M., & Godfrey, P. D. 1997, A&A, 324, 211 [Cited on page 12.]

Sousbie, T. 2011, MNRAS, 414, 350, doi: 10.1111/j.1365-2966.2011.18394.x [Cited 2 times on pages 21 and 48.]

Stahler, S. W. 1983, ApJ, 274, 822, doi: 10.1086/161495 [Cited on page 8.]

Stark, A. A., & Lee, Y. 2005, ApJL, 619, L159, doi: 10.1086/427936 [Cited on page 20.]

Su, Y., Yang, J., Zhang, S., et al. 2019, ApJS, 240, 9, doi: 10.3847/1538-4365/aaf1c8 [Cited 2 times on pages 40 and 86.]

Szymczak, M., Olech, M., Sarniak, R., Wolak, P., & Bartkiewicz, A. 2018, MNRAS, 474, 219, doi: 10.1093/mnras/stx2693 [Cited 2 times on pages 31 and 82.]

Takahira, K., Tasker, E. J., & Habe, A. 2014, ApJ, 792, 63, doi: 10.1088/0004-637X/792/1/63 [Cited 8 times on pages 25, 26, 27, 153, 162, 188, 189, and 194.]

Tan, J. C., Beltrán, M. T., Caselli, P., et al. 2014, in Protostars and Planets VI, ed. H. Beuther, R. S. Klessen, C. P. Dullemond, & T. Henning, 149, doi: 10.2458/azu_uapress_9780816531240-ch007 [Cited on page 2.]

Tan, J. C., Kong, S., Butler, M. J., Caselli, P., & Fontani, F. 2013, ApJ, 779, 96, doi: 10.1088/0004-637X/779/2/96 [Cited on page 11.]

Tasker, E. J., & Tan, J. C. 2009, ApJ, 700, 358, doi: 10.1088/0004-637X/700/1/358 [Cited 2 times on pages 26 and 184.]

Terzian, Y. 1965, ApJ, 142, 135, doi: 10.1086/148268 [Cited on page 38.]

Tielens, A. G. G. M. 2005, The Physics and Chemistry of the Interstellar Medium [Cited on page 4.]

—. 2008, ARA&A, 46, 289, doi: 10.1146/annurev.astro.46.060407.145211 [Cited 2 times on pages 38 and 94.]

Tigé, J., Motte, F., Russeil, D., et al. 2017, A&A, 602, A77, doi: 10.1051/0004-6361/201628989 [Cited 3 times on pages 19, 23, and 111.]

Tokuda, K., Fukui, Y., Harada, R., et al. 2019, ApJ, 886, 15, doi: 10.3847/1538-4357/ab48ff [Cited 4 times on pages 24, 114, 160, and 200.]

Tokuda, K., Minami, T., Fukui, Y., et al. 2022, ApJ, 933, 20, doi: 10.3847/1538-4357/ac6b3c [Cited on page 200.]

Torii, K., Enokiya, R., Sano, H., et al. 2011, ApJ, 738, 46, doi: 10.1088/0004-637X/738/1/46 [Cited 2 times on pages 25 and 224.]

Torii, K., Hattori, Y., Hasegawa, K., et al. 2017, ApJ, 835, 142, doi: 10.3847/1538-4357/835/2/142 [Cited 2 times on pages 25 and 74.]

Torii, K., Hattori, Y., Matsuo, M., et al. 2021, PASJ, 73, S368, doi: 10.1093/pasj/psy098 [Cited on page 74.]

Treviño-Morales, S. P., Fuente, A., Sánchez-Monge, Á., et al. 2019, A&A, 629, A81, doi: 10.1051/0004-6361/201935260 [Cited 6 times on pages 18, 19, 21, 23, 111, and 146.]

Tsuge, K., Fukui, Y., Tachihara, K., et al. 2021, PASJ, 73, S35, doi: 10.1093/pasj/psaa033 [Cited 2 times on pages 74 and 153.]

Tsuge, K., Sano, H., Tachihara, K., et al. 2019, ApJ, 871, 44, doi: 10.3847/1538-4357/aaf4fb [Cited on page 74.]

Urquhart, J. S., König, C., Giannetti, A., et al. 2018, MNRAS, 473, 1059, doi: 10.1093/mnras/stx2258 [Cited 13 times on pages 58, 59, 60, 121, 125, 127, 139, 206, 207, 208, 209, 210, and 227.]

van der Tak, F. F. S. 2004, in Star Formation at High Angular Resolution, ed. M. G. Burton, R. Jayawardhana, & T. L. Bourke, Vol. 221, 59, doi: 10.48550/arXiv.astro-ph/0309152 [Cited on page 218.]

Vasyunina, T. 2010, PhD thesis, Ruprecht-Karls University of Heidelberg, Germany [Cited 4 times on pages 83, 111, 114, and 239.]

Vázquez-Semadeni, E., Ballesteros-Paredes, J., & Klessen, R. 2003, in Astronomical Society of the Pacific Conference Series, Vol. 287, Galactic Star Formation Across the Stellar Mass Spectrum, ed. J. M. De Buizer & N. S. van der Bliek, 81–86, doi: 10.48550/arXiv.astro-ph/0206038 [Cited 2 times on pages 4 and 162.]

Vázquez-Semadeni, E., Gómez, G. C., & González-Samaniego, A. 2024a, MNRAS, 530, 3445, doi: 10.1093/mnras/stae1090 [Cited on page 16.]

Vázquez-Semadeni, E., Gómez, G. C., Jappsen, A. K., Ballesteros-Paredes, J., & Klessen, R. S. 2009, ApJ, 707, 1023, doi: 10.1088/0004-637X/707/2/1023 [Cited 4 times on pages 16, 192, 193, and 233.]

Vázquez-Semadeni, E., González-Samaniego, A., & Colín, P. 2017, MNRAS, 467, 1313, doi: 10.1093/mnras/stw3229 [Cited 4 times on pages 16, 192, 193, and 233.]

Vázquez-Semadeni, E., Palau, A., Ballesteros-Paredes, J., Gómez, G. C., & Zamora-Avilés, M. 2019, MNRAS, 490, 3061, doi: 10.1093/mnras/stz2736 [Cited 4 times on pages 16, 192, 193, and 233.]

Vázquez-Semadeni, E., Palau, A., Gómez, G. C., et al. 2024b, arXiv e-prints, arXiv:2408.10406, doi: 10.48550/arXiv.2408.10406 [Cited on page 233.]

Verma, A., Sharma, S., Dewangan, L., et al. 2023, Journal of Astrophysics and Astronomy, 44, 52, doi: 10.1007/s12036-023-09932-0 [Cited on page 18.]

Walsh, A. J., Burton, M. G., Hyland, A. R., & Robinson, G. 1998, MNRAS, 301, 640, doi: 10.1111/j.1365-8711.1998.02014.x [Cited 2 times on pages 12 and 82.]

Walsh, A. J., Breen, S. L., Britton, T., et al. 2011, MNRAS, 416, 1764, doi: 10.1111/j.1365-2966.2011.19115.x [Cited on page 121.]

Wang, J.-W., Lai, S.-P., Eswaraiah, C., et al. 2019, ApJ, 876, 42, doi: 10.3847/1538-4357/ab13a2 [Cited 5 times on pages 18, 115, 116, 129, and 236.]

Wang, J.-W., Koch, P. M., Tang, Y.-W., et al. 2022, ApJ, 931, 115, doi: 10.3847/1538-4357/ac6872 [Cited 9 times on pages 149, 160, 179, 181, 183, 184, 191, 192, and 232.]

Wang, K., Zhang, Q., Testi, L., et al. 2014, MNRAS, 439, 3275, doi: 10.1093/mnras/stu127 [Cited on page 17.]

Ward-Thompson, D., & Whitworth, A. P. 2015, An Introduction to Star Formation [Cited 4 times on pages 4, 6, 9, and 194.]

Weingartner, J. C., & Draine, B. T. 2001a, ApJ, 548, 296, doi: 10.1086/318651 [Cited 2 times on pages 46 and 137.]

—. 2001b, ApJ, 548, 296, doi: 10.1086/318651 [Cited on page 240.]

Wells, M. R. A., Urquhart, J. S., Moore, T. J. T., et al. 2022, MNRAS, 516, 4245, doi: 10.1093/mnras/stac2420 [Cited on page 150.]

Whitney, B., Benjamin, R., Meade, M., et al. 2011, in American Astronomical Society Meeting Abstracts, Vol. 217, American Astronomical Society Meeting Abstracts #217, 241.16 [Cited 2 times on pages 40 and 84.]

Whitworth, A. P., & Priestley, F. D. 2021, MNRAS, 504, 3156, doi: 10.1093/mnras/stab1125 [Cited on page 235.]

Williams, G. M., Peretto, N., Avison, A., Duarte-Cabral, A., & Fuller, G. A. 2018, A&A, 613, A11, doi: 10.1051/0004-6361/201731587 [Cited on page 149.]

Williams, J. P., de Geus, E. J., & Blitz, L. 1994, ApJ, 428, 693, doi: 10.1086/174279 [Cited on page 50.]

Wilson, T. L. 1974, A&A, 31, 83 [Cited on page 56.]

Wolfire, M. G., & Cassinelli, J. P. 1987, ApJ, 319, 850, doi: 10.1086/165503 [Cited 2 times on pages 8 and 76.]

Wong, T., Oudshoorn, L., Sofovich, E., et al. 2022, ApJ, 932, 47, doi: 10.3847/1538-4357/ac723a [Cited 2 times on pages 160 and 200.]

Wood, D. O. S., & Churchwell, E. 1989, ApJS, 69, 831, doi: 10.1086/191329 [Cited on page 55.]

Wu, Y., Zhang, Q., Chen, H., et al. 2005, AJ, 129, 330, doi: 10.1086/426361 [Cited on page 15.]

Wu, Y. W., Xu, Y., Pandian, J. D., et al. 2010, ApJ, 720, 392, doi: 10.1088/0004-637X/720/1/392 [Cited on page 82.]

Yang, A. Y., Thompson, M. A., Urquhart, J. S., & Tian, W. W. 2018, ApJS, 235, 3, doi: 10.3847/1538-4365/aaa297 [Cited 2 times on pages 208 and 209.]

Yang, A. Y., Urquhart, J. S., Wyrowski, F., et al. 2022, A&A, 658, A160, doi: 10.1051/0004-6361/202142039 [Cited 5 times on pages 58, 59, 105, 121, and 125.]

Yang, D., Liu, H.-L., Tej, A., et al. 2023, ApJ, 953, 40, doi: 10.3847/1538-4357/acdf42 [Cited 2 times on pages 21 and 146.]

Yang, W., Xu, Y., Chen, X., et al. 2017, ApJS, 231, 20, doi: 10.3847/1538-4365/aa6ff3 [Cited on page 121.]

Yuan, J., Wu, Y., Liu, T., et al. 2016, ApJ, 820, 37, doi: 10.3847/0004-637X/820/1/37 [Cited on page 132.]

Yuan, L., Li, G.-X., Zhu, M., et al. 2020, A&A, 637, A67, doi: 10.1051/0004-6361/201936625 [Cited on page 115.]

Zernickel, A., Schilke, P., & Smith, R. J. 2013, A&A, 554, L2, doi: 10.1051/0004-6361/201321425 [Cited 2 times on pages 115 and 116.]

Zhou, J.-W., Liu, T., Evans, N. J., et al. 2022, MNRAS, 514, 6038, doi: 10.1093/mnras/stac1735 [Cited 4 times on pages 21, 149, 150, and 219.]

Zhou, J.-W., Li, S., Liu, H.-L., et al. 2023, MNRAS, 519, 2391, doi: 10.1093/mnras/stac3559 [Cited 2 times on pages 149 and 160.]

Zinnecker, H., & Yorke, H. W. 2007, ARA&A, 45, 481, doi: 10.1146/annurev.astro.44.051905.092549 [Cited 9 times on pages 1, 2, 7, 9, 11, 14, 15, 55, and 159.]